

# Tailoring self-assembly and optoelectronic properties of organic semiconductors via macromolecular engineering.

THÈSE N° 6957 (2016)

PRÉSENTÉE LE 22 AVRIL 2016

À LA FACULTÉ DES SCIENCES DE BASE

LABORATOIRE D'INGÉNIERIE MOLÉCULAIRE DES NANOMATÉRIAUX OPTOÉLECTRONIQUES  
PROGRAMME DOCTORAL EN CHIMIE ET GÉNIE CHIMIQUE

ÉCOLE POLYTECHNIQUE FÉDÉRALE DE LAUSANNE

POUR L'OBTENTION DU GRADE DE DOCTEUR ÈS SCIENCES

PAR

Andrea GASPERINI

acceptée sur proposition du jury:

Prof. S. Gerber, présidente du jury  
Prof. K. Sivula, directeur de thèse  
Prof. R. Chiechi, rapporteur  
Prof. P. Beaujuge, rapporteur  
Prof. A. Boghossian, rapporteuse



ÉCOLE POLYTECHNIQUE  
FÉDÉRALE DE LAUSANNE

Suisse  
2016



## Acknowledgements

I have lived my doctoral thesis as a funny, very productive and enriching experience. Without the few good people I have met on my way till now, this period would have just been a lonely, flat and chasing results ride. My deepest gratitude is owed to Kevin who bet on me as first collaborator for his new experience in the position of lab manager and PhD supervisor. I highly appreciated the trust given to me since the beginning and the space accorded to design and develop my own research projects. I particularly appreciated as well the technical support that he gave to me in all the little problems of the daily routine in the lab and in all the writing that we have gone through together.

The success of the research projects presented in this thesis is also the result of contributions and moments shared with all the group members of LIMNO. I found particular vital the support had by Xavier with the management of the equipment, the measurements and the commitment that he has always shown when discussing my projects. It has been a real pleasure to work with him. I cannot not mention the support and the care that our spiritual guide Nestor, has given to me these years when things were going wrong both inside and outside the lab. I am glad he stayed with us all this time in LIMNO and I really appreciated his efforts in keeping a good atmosphere in the lab. Another central figure of my period here has been Mathieu. I found in him a rare humbleness and a friend with which spend time in conferences, late nights and everything that was happening in the lab after 6:45 pm. I would also like to mention the precious advices I received from Sebastian and the help of our secretary Nadia regarding all my administrative issues.

Finally, I have always received a huge support from Kristel, especially in these last months, Carlo, Alberto, Leo, Adriana, Fei and Victorine. Without the encouragement of my family and in particular of my aunt Ivana, my cousin Valentina and my grandparents I would have never started and finished my PhD.



## Summary

Conjugated polymers and small molecules are a promising class of semiconducting materials for application in macroelectronic and energy conversion devices. The development of high performance devices employing this class of semicrystalline materials ultimately depends on the precise control of crystalline domain size, orientation and connectivity due to the complex nature of their molecular interactions and chemical structure. It is therefore of paramount importance to control self-assembly processes of  $\pi$ -conjugated molecules and polymers into functional microstructures over a wide set of length scales suitable for device optimal operation. In the present thesis, we investigated the effect that novel materials design criteria have on the control of the active layer morphology and long-term stability in organic field effect transistors and bulk heterojunction solar cells. A first strategy to reduce microstructure complexity in semiconducting polymer thin-films is to separate the contributions to morphology and charge transport resulting from different polymer molecular weights. Combined morphological and electronic characterization revealed a high degree of isotropy in charge transport mechanisms in semicrystalline and poorly aggregating conjugated systems as a result of the broad variety of self-assembled microstructures observed at different molecular weights. Next, we designed and synthesized a new class of semiconducting materials based on a flexible linker concept. Initially, we showed the successful preparation and purification of a prototype in a class of semiconducting polymer that allows independent control over the conjugated segment length and overall chain length by covalently linking low-MW conjugated segments with flexible aliphatic linkers. Our flexibly linked polymeric material exhibited improved thin-film formation compared to the low-MW starting polymer and unique thermal properties. Importantly, our linking strategy had a clear effect on the chain self-assembly and allowed structural control between distinct thin film morphologies without altering the chain length. Next we extended the flexible linker design motif to small molecule derivatives that are employed in high performance bulk heterojunction solar cells. In this study we showed, that active layer degradation under continuous thermal stress can be inhibited by the formation of a more robust thin film microstructure with the additive present. Finally, the efficient functionalization of a series of polymeric blocks was successfully used to synthesize a new class of alternated multi-block copolymers. The facile nature of the synthetic procedure enables high degree of polymerization and offers the possibility to include a large number of semiconducting polymers in block copolymer architectures. Ultimately, when our alternating multi-block copolymers are solution processed in thin films, a relatively high degree of self-assembly and micro-domains phase separation is observed at length scale ideal for well-ordered heterojunction needed to improve solar cells efficiency.

## **Keywords**

Organic semiconductors, conjugated polymers, flexible linker, self-assembly, morphology, field effect transistors, organic materials characterization

## Sommario

Polimeri coniugati e piccole molecole sono una promettente classe di materiali semiconduttori per applicazioni in dispositivi elettronici e di conversione di energia. Lo sviluppo di dispositivi ad alte prestazioni che utilizzano questa classe di materiali semicristallini dipende in ultima analisi dal preciso controllo delle dimensioni, orientamento e la connettività dei domini cristallini a causa della complessa natura delle loro interazioni molecolari e della loro struttura chimica. È quindi di fondamentale importanza, controllare i processi di auto-assemblaggio di molecole e polimeri coniugati in microstrutture funzionali in una vasta serie di scale di lunghezza adatta per funzionamento ottimale dei dispositivi. Nella presente tesi, abbiamo studiato l'effetto che nuovi criteri di progettazione di materiali coniugati hanno sul controllo della morfologia dello strato attivo e sulla stabilità a lungo termine nei transistori organici ad effetto di campo e nelle celle solari a eterogiunzione. Una prima strategia per ridurre la complessità microstrutturale nei film sottili di polimeri semiconduttori è quello di separare i contributi alla morfologia e al trasporto di carica derivante dal diverso peso molecolare del polimero. Abbiamo rivelato un alto grado di anisotropia nei meccanismi di trasporto di carica e di auto-assemblaggio in sistemi coniugati semicristallini e semi-amorfi in funzione del loro peso molecolare. Successivamente, abbiamo progettato e sintetizzato una nuova classe di materiali semiconduttori basato sul concetto di linker flessibile. Inizialmente, abbiamo mostrato il successo della preparazione e purificazione del prototipo in una classe di polimeri semiconduttori che consente il controllo indipendente sulla lunghezza del segmento coniugato e sulla lunghezza complessiva della catena da covalentemente collegando corti segmenti coniugati con linker alifatici flessibili. Il nuovo materiale polimerico esibisce una migliore formazione del film sottile rispetto ai croci segmenti polimerici di partenza e uniche proprietà termiche. È importante sottolineare che la nostra strategia di collegamento ha avuto un chiaro effetto sulla auto-assemblaggio delle catene polimeriche e ha permesso il controllo delle diverse morfologie a film sottile senza modificare la lunghezza della catena. Il concetto del linker flessibile è poi stato esteso a derivati di piccole molecole semiconduttori che sono impiegati in dispositivi fotovoltaici ad alte prestazioni. In questo studio abbiamo dimostrato, che il degrado dello strato attivo sotto continuo stress termico può essere inibita dalla formazione di una più robusta microstruttura del film sottile con l'additivo presente all'interno. Infine, la efficiente funzionalizzazione di una serie di segmenti polimerici è stato utilizzata con successo per la sintesi una nuova classe di copolimeri alternati a multiblocco. La facile sintesi consente un alto grado di polimerizzazione e offre la possibilità di includere un gran numero di polimeri semiconduttori in architetture come i copolimeri a blocchi. Infine, quando i copolimeri alternati a multiblocco sono processati in film sottili, un relativamente elevato grado di auto-assemblaggio e di formazioni di micro-domini è osservato a

lunghezze ideali per la formazione di eterogiunzioni ben ordinate che sono necessarie per migliorare l'efficienza delle celle solari

## **Parole chiave**

semiconduttori organici, polimeri coniugati, linker flessibile, auto-assemblamento, morfologia, transistor a effetto di campo, caratterizzazione dei materiali organici







# Table of contents

Acknowledgements.....	v
Summary.....	vii
Sommario.....	ix
List of abbreviations.....	xiii
<b>Chapter 1 Introduction.....</b>	<b>21</b>
1.1 Motivation .....	21
1.2 Molecular engineering and charge transport in organic semiconductors.....	24
1.3 Morphological stability of electronic devices.....	27
1.4 Scope of the thesis .....	30
<b>Chapter 2 Experimeal methods .....</b>	<b>31</b>
2.1 Field effect transistors .....	31
2.2.1 Transistors Fabrication.....	33
2.2.2 Measuring device characteristic.....	34
2.2 Bulk Heterojunction solar cells .....	36
2.2.1 Parameters of a solar cell .....	36
2.2.2 Charge generation in solar cells.....	37
2.2.3 Bulk Heterojunction solar cells fabrication .....	39
2.2.3 Measuring device characteristics .....	39
2.3 Microstructural characterization.....	40
2.3.1 Techniques based on X-ray diffraction .....	40
2.2.2 Theory of x-ray diffraction.....	40
2.2.3 Specular diffraction measurements with laboratory sources .....	42
2.2.4 X-ray diffraction with synchrotron radiation.....	43
<b>Chapter 3 Effect of molecular weight on microstructure and charge carrier transport in a semicrystalline poly(thieno)thiophene .....</b>	<b>45</b>

3.1	Introduction .....	45
3.2	Results and discussion .....	46
3.2.1	Synthesis and molecular weight fractionation .....	46
3.2.2	Effect of molecular weight on the charge carrier mobility.....	48
3.2.3	Thin film morphology.....	51
3.2.4	Thermal characterization.....	55
3.2.5	Charge transport across grain boundaries in PBTTT .....	57
3.2.3	Thin films microstructure determination.....	59
3.3	Conclusions .....	63
<b>Chapter 4</b>	<b>Effect of molecular weight on microstructure and charge carrier transport in diketopyrrolopyrrole based copolymers .....</b>	<b>65</b>
4.1	Introduction .....	65
4.2	Results and discussion .....	66
4.2.1	Synthesis and molecular weight fractionation .....	66
4.2.2	Effect of molecular weight on the charge carrier mobility.....	69
4.2.3	Thin film morphology.....	71
4.2.4	Thin films microstructure determination.....	72
4.2.5	Charge transport across grain boundaries in DPP-based copolymer.....	74
4.3	Conclusions .....	75
<b>Chapter 5</b>	<b>Controlling conjugated polymer morphology and charge carrier transport with a flexible linker approach.....</b>	<b>77</b>
5.1	Introduction .....	77
5.2	Results and discussion .....	78
5.2.1	Synthesis and purification.....	78
5.2.2	Thermal properties .....	80
5.2.3	Topological and microstructural characterization .....	82
5.2.4	Charge carrier transport in flexibly linked polymers .....	86
5.3	Conclusions .....	89

<b>Chapter 6</b>	<b>Enhancing thermal stability of solution-processed small molecule semiconductors thin films using a flexible linker approach.....</b>	<b>91</b>
6.1	Introduction .....	91
6.2	Results and discussion .....	92
6.2.1	Synthesis and purification .....	92
6.2.2	Thermal and optical properties of DPP(TBFu) <sub>2</sub> as an additive.....	93
6.2.3	Effect of flexible linker additive as a nucleation promoter in thin films.....	95
6.2.4	Effect of flexible linker additive in Bulk Heterojunction Solar Cells.....	99
6.2.5	Surface composition characterization by Nanomechanical indentation.....	104
6.3	Conclusions .....	104
<b>Chapter 7</b>	<b>Synthesis and characterization of alternated multiblock copolymers .....</b>	<b>107</b>
7.1	Introduction.....	107
7.2	Results and discussion.....	108
7.2.1	Synthesis and characterization.....	108
7.2.2	Block copolymer optical properties .....	114
7.2.3	Charge transport in MBC thin films.....	115
7.2.4	Topological and microstructural characterization.....	116
7.3	Conclusions .....	118
<b>Chapter 8</b>	<b>Conclusions.....</b>	<b>121</b>
8.1	Conclusions .....	121
8.2	Outlook.....	123
<b>Chapter 9</b>	<b>References.....</b>	<b>125</b>
9.1	References .....	125
<b>Chapter 10</b>	<b>Appendix.....</b>	<b>133</b>
10.1	Characterization techniques.....	134
10.2	Synthetic experimental procedure and characterization .....	135
10.3	Curriculum Vitae .....	165

## List of abbreviations

1D	One-dimensional
2D	Two-dimensional
Å	Angstrom
AFM	Atomic force microscopy
μA	Micro ampere
Anal.	Analysis
APPI	Atomic Pressure Photoionization
°C	Degree celsius
Calcd.	calculated
cm	Centimeter
δ	Chemical shift (NMR)
d	Duplet
DCM	Dicloromethane
DP	Degree of polyerization
DSC	Differential scanning calorimetry
ε	Extinction coefficient
Equiv.	Equivalent
ESI-TOF	Electrospray ionization-time of flight
Φ	Azimuthal angle 8XRD)
f <sub>0</sub>	Resonance Frequency Cantilever
g	Gram
GPC	Gel Permation Chromatography
h	Hours
h	Plank constant
HRMS	High Resolution Mass Spectrometry
Hz	Hertz
I <sub>d</sub>	Drain Current
ITO	Indium tin oxide
I-V	Current-Voltage
IR	Infrared

J	Coupling constant
K	Kelvin
k	Force Constant of cantilever
keV	Kiloelectron volts
kHz	Kilohertz
kV	Kilovolt
kW	Kilowatt
L	Liter
L	Channel length
$\mu$	Charge carrier mobility
m	Multiplet
m	Meter
M	Molar
mA	Milliampere
mbar	Millibar
MHz	Megahertz
ml	Milliliter
mm	Millimeter
$\mu$ L	Microliter
$\mu$ m	Micrometer
MALDI-TOF	Matrix Assisted Laser Desorption
MeOH	Methanol
Min	Minute
Mn	Number average molecular weight
Mw	Weight average molecular weight
M/z	Mass to charge ratio
N	Newton
Na	Sodium
PDI	Perylene diimide
NIR	Near Infrared
nm	Nanometer
NMR	Nuclear Magnetic Resonance
OFET	Organic Field Effect Transistor
OLED	Organic Light Emitting Diode

OSC	Organic Solar Cells
PEDOT:PSS	poly(3,4-ethylenedioxythiophene) polystyrene sulfonate
PBTTT	poly-(2,5-bis(3-alkylthiophen-2-yl)thienothiophene)
PDI	Polydispersity
ppm	Part per milion
$R_s$	Contact resistance
RMS	Roote mean square
$q_s$	Scattering vector
SAXS	Small angle x-ray scattering
SEC	Size exclusion chromatography
$\theta$	Scattering angle
T	Temperature
TEM	Scanning electron microscopy
THF	Tetrahydrofuran
UV-vis	Ultraviolet/visible
$V_d$	Drain voltage
$V_g$	Gate voltage
$V_{th}$	Threshold voltage
W	Channel width
WAXS	Wide angle x-ray scattering
wt%	Weight percentage
XRD	X-ray diffraction







# Chapter 1

## Introduction

Organic semiconductors (OSs) constitute a class of materials envisaged as active components in electronic devices such as organic solar cells (OSC) for direct conversion of sunlight into electrical power, organic light emitting diodes (OLED) for solid-state lighting in displays and organic field effect transistors (OFET) for large-area flexible circuitries and sensing technologies.<sup>[1]</sup> While organic electronics are not envisioned to replace traditional electronics, they possess many attractive aspects that may complement to existing technology in specific applications.<sup>[2]</sup> Indeed, differently from silicon-based analog devices that require high energy intensive batch manufacturing techniques, organic semiconductors can be dissolved into common solvents and processed through well-established solution-based printing techniques which could potentially reduce the production cost. Additionally, the prospect of low-temperature processing offered by solution-processed organic semiconductors enables deposition onto plastic and flexible substrates, expanding the versatility and applicability of the related devices.<sup>[3]</sup> Despite their promise solution-processed organic semiconductors are still in a stage of development. At present a commonly held view agrees that the performance, uniformity and operational stability achievable with organic semiconductors lags behind their traditional inorganic counterparts. In order to maximize the potential of organic semiconductors fundamental research and development is required to bring performance metrics to commercially-viable levels. A particular area of complexity and interest in the field of solution-processable organic semiconductor development is their intrinsic semi-crystalline nature, which brings challenges to the preparation of well-ordered, consistent, and high-performance thin film devices. Indeed, generally organic semiconductors consist of carbon-based molecular or polymeric materials with  $\pi$ -conjugated and various other functionalities that exhibit complex noncovalent interactions, i.e.  $\pi$ - $\pi$  stacking, H-bonding, and Van der Waals forces from which the optoelectronic properties (e.g. charge transport) originate. In solid state, macroscale devices based on organic semiconductors, the optoelectronic properties are known to be particularly sensitive to the microstructural arrangement/ordering/self-assembly of the semiconducting functionalities. For this reason, a large amount of effort has been put forth to control the orientation, size and distribution of ordered regions (among more disordered ones) across macroscale thin film devices. Despite the improved physical understanding of optoelectronic properties and of the factors that govern the formation of thin film morphology, organic

semiconductors still show 1-2 of magnitude poorer electronic properties (e.g. in terms of charge carrier mobility,  $\mu$ ) from the values predicted theoretically.<sup>[4]</sup> Charge carrier mobility in ideal single crystals of organic polymers is usually modelled in the context of the acoustic deformation potential scattering theory which is based on the assumption that relevant parameters are those only calculated in the  $\pi$ - $\pi$  stacking direction, as transport along the backbone is considered as much faster and therefore not limiting. However, significant divergences have been found when comparing charge carrier mobility values for a semicrystalline polymer like region-regular poly(3-hexylthiophene) (rr-P3HT) calculated using different models. Particularly, over one order of magnitude deviation was reported between the theoretical hole mobility calculated in a perfect rr-P3HT crystal ( $31 \text{ cm}^2\text{V}^{-1}\text{s}^{-1}$ ) vs device modeling ( $1 \text{ cm}^2\text{V}^{-1}\text{s}^{-1}$ ).

Despite this organic semiconductors do have a clear advantage over traditional inorganic semiconductors: the use of organic synthesis is a powerful tool to rationally design and chemically tune their optoelectronic properties. Currently, organic synthesis is extensively employed to precisely adjust the electronic structure of organic semiconductors through fine modifications of the chemical structure.<sup>[5]</sup> However, the power of organic chemistry to tune the unpredictable solid-state morphology of solution-processed organic semiconductors is limited by our understanding of the precise effect that chemical structure has on the self-assembly, crystal packing, domain size and ultimately the optoelectronic properties in the solid state. Given the paramount importance to control and understand the self-assembly processes in solid-state organic semiconductors and the existing limitations in our current understanding, the development of novel synthetic approaches to enable more effective control and optimization of the solid-state morphology of organic semiconductors over a wider set of length scales is needed.

In this context, the current thesis project aims to elucidate the relationship that links fundamental molecular structure (e.g. polymers' chain length or molecular weight, and covalent connectivity) to the self-assembly motifs, charge transport mechanisms, and crystalline domain microstructures of different classes of state-of-the-art conjugated organic semiconductors in solution-processed thin films. It will be demonstrated that subtle modifications of molecular structure can strongly influence overall properties like charge carrier mobility and macroscopic arrangements as a result of the highly complex nature of the interactions occurring in organic semiconductor thin-films. Moreover, the effectiveness of a newly developed synthetic strategy—the flexible linker approach—to tailor crystalline domain orientation and size while gaining insight into the charge transport dynamics in organic semiconductor devices will be presented. Ultimately, the synthetic approach developed herein is further employed to synthesize a new class of fully-conjugated alternating multi-block copolymers. Overall in this work, combined morphological and microstructural investigations, together with optoelectronic device testing are used to gain

deep insight into the operation of solution-processable organic semiconductors. In the following sections, brief reviews of the state-of-the-art organic semiconducting materials that have successfully led to improved physical understanding of transport, structure-property relationships and source of morphological instability in organic field effect transistors (OFET) and organic solar cells (OSC) are presented and will allow us to put the concepts presented in the course of this thesis into perspective.

## 1.1 Molecular engineering and charge transport in organic semiconductors

Organic materials can adopt a semiconducting behavior when the  $sp^2$  hybridization of carbon p-orbitals in a double bond leaves a  $p_z$  orbital free for  $\pi$ -bonding. Electrons in a single  $\pi$ -bond can become delocalized through conjugation with surrounding  $\pi$ -bonds, hence allowing charge carriers to delocalize over the extent of orbital overlap.<sup>[6]</sup> Molecular orbital (MO) splitting of each single conjugated molecule constitutes already a quantifiable energy difference (band gap) between the highest occupied molecular orbital (HOMO) playing the role of a valence band edge and the lowest unoccupied molecular orbital (LUMO) as the bottom of the conduction band. Theoretically, when isolated conjugated molecules are condensed from the gas phase into crystal, molecular levels split and give rise to electronic bands with energy dispersion on the order of few hundred millielectronvolts.<sup>[7]</sup> Experimental evidence of band transport in high purity organic single crystals, such as pentacene and rubrene (generally known as arenes), has been largely validated, but the practical application of single crystal organic semiconductors (OSs) still remains disadvantageous over inorganic materials. Not only is the electrical performance (as quantified by the charge carrier mobility,  $\mu$ , see Chapter 2) of these single crystals ( $1\text{-}20\text{ cm}^2\text{ V}^{-1}\text{ s}^{-1}$ )<sup>[8]</sup> 3 orders of magnitude lower than crystalline silicon (the benchmark inorganic semiconductor), but single crystal unfunctionalized arenes are also known to be very insoluble in common solvents—thus not offering solution processability. Moreover, because of their relatively high lying LUMO energy level, they are also highly unstable in the presence of light and oxygen; they easily undergo photochemical degradation which deteriorates their performance.<sup>[9]</sup> In contrast to single crystals, solution-processed OS materials in the thin film format necessarily have defects. Conjugated polymers in particular have been widely adopted in the field of OS research as they have superior processing characters. However conjugated polymers, especially, are semicrystalline in nature leading to a complex character of overall charge transport.<sup>[10]</sup> Room temperature thermal vibration, structural defects (i.e. bond planarity distortions) or mis-orientations prohibit coherent propagation of charges and lead to localization into electronic traps.<sup>[11]</sup> In real materials, MO energies follow a Gaussian distribution with a characteristic breadth proportional of the amount of disorder.<sup>[12]</sup> Charge transport is generally understood in this class of materials as hopping mechanism between individual localized states, meaning that charge carriers

occupy a single site at a time and are thermally excited to higher energy states from which, via drift or diffusion, are again trapped in another localized state. Although the occurrence of defect-limited charge transport may be an extrinsic effect (e.g. processing or purification related), there may also be important molecular design rules that influence the propensity of certain molecular structures towards the formation of defects. The most successful and widely explored design motifs for high mobility conjugated polymers have traditionally favored the formation of semicrystalline lamellar microstructures with edge-on polymer orientation (Figure 1-1) similar to that found in regioregular poly(3-hexylthiophene) (rr-P3HT, Figure 1-1a).<sup>[13]</sup> The characterization of the semicrystalline lamellar microstructures in a conjugated polymer thin film is typically accomplished by grazing-incidence X-ray diffraction, the results of which are shown in Figure 1-1, and will be explained in Chapter 2. The most successful realization of long range order in conjugated polymers was reported in poly-(2,5-bis(3-alkylthiophen-2-yl)thienothiophene) (PBTTT, Figure 1-1b)<sup>[14]</sup> where efficient charge transport is facilitated by the formation of alternating layers of conjugated backbones separated by layers of interdigitating flexible side chains parallel to the substrate plane and a charge carrier mobility as high as  $1 \text{ cm}^2 \text{ V}^{-1} \text{ s}^{-1}$  have been observed.<sup>[15]</sup>

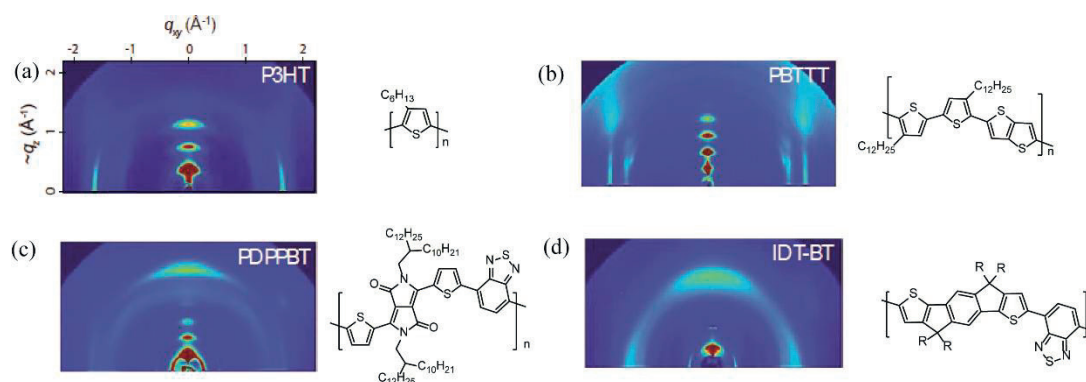


**Figure 1-1.** Wide angle x-ray scattering images of different high-mobility conjugated polymers. Adapted from reference (12).

In recent years, however significant attention have been focused on understanding the charge mechanism occurring in a class of high mobility donor-acceptor (D-A) type polymers.<sup>[16]</sup> These are usually regular copolymers with alternating electron deficient and electron rich units along the polymer backbone and exhibit a relatively low band gap which makes them ideal for solar cell applications (see chemical structure in Figure 1-2a). Examples of D-A polymers that have received most attention to date

are low-bandgap polymers based on electron deficient units of diketopyrrolopyrrole (PDPPBT, Figure 1-1c)<sup>[17]</sup> and cyclopentadithiophene (IDT-BT, Figure 1-1d)<sup>[18]</sup>. The exceptionally high mobilities in these materials cannot be rationalized as an extension of the design guideline inspired by the high degree of order found in semicrystalline polymers like *rr*-P3HT and PBTTT. Indeed, X-ray diffraction analysis images in Figure 1-1 of the highest mobility materials show that this class of more disordered materials appears nearly amorphous<sup>[19]</sup> as evidenced by the low diffraction intensity in either the alkyl or  $\pi$ -stacking directions (Figure 1-1c and Figure 1-1d). However, a clear understanding of the origin of high mobility in disordered polymer is still under debate,<sup>[20]</sup> but some molecular design requirements that appear necessary to achieve high mobility have been outlined.

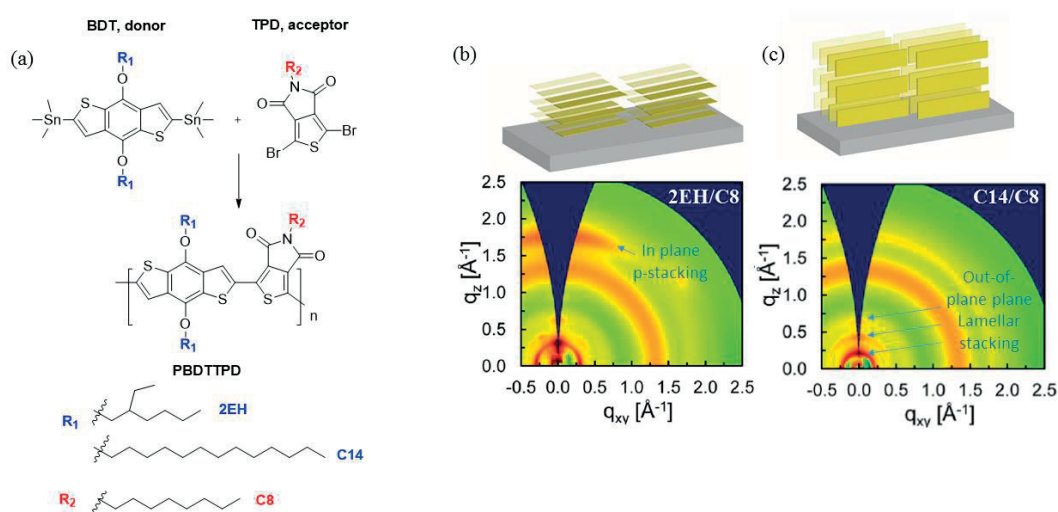


**Figure 1-2.** a) Synthesis of PBDTTPD polymer. b) 2D-GIXD images of the face-on orientation with branched chains in PBDTTPD c) 2D-GIXD images of the edge-on orientation with linear chains in PBDTTPD. Adapted from reference (23).

Evidence of the advantage of coplanar backbone conformation with minimum backbone torsion in this class of polymers over more ordered microstructures (PBTTT) has been highlighted in a recent work by DeLongchamp et al.<sup>[19]</sup> by showing that a weakly scattering indacenodithiophene-benzothiadiazole copolymer (see structure Figure 1-1-d) could achieve record charge carrier mobility (as high as 3.6 cm<sup>2</sup> V<sup>-1</sup> s<sup>-1</sup>). Charge transport in seemingly disordered films of this polymer has been depicted as almost unidimensional and occurring along the rigid backbone with occasional intermolecular hopping through small  $\pi$ -stacking regions (Figure 1-1f). Furthermore, a planar backbone conformation and the larger

conjugated cores present in DA copolymers are thought to enable chains to pack closely with small  $\pi$ - $\pi$  stacking distances while reducing structural disorder caused by variation in backbone conformation.<sup>[21]</sup> As recently shown by Beaujuge et al.<sup>[22]</sup> an important aspect of the molecular design of high mobility D-A copolymer relates to the choice of the solubilizing side chains. As shown in Figure 1-2, alkyl chain length and chemical structure can largely dictate the self-organization of the polymer during solution processing, by exerting an effect on the interchain packing and backbone conformation as much as  $\pi$ - $\pi$  stacking does with conjugated units.<sup>[23]</sup> Indeed, the striking difference in backbone orientation with respect to the substrate have been found to profoundly affect the charge transport mechanism in organic solar cells.<sup>[24]</sup> It is in fact questioned if whether a preferential face-on (see sketch Figure 1-2b) or edge on (Figure 1-2c) is preferred in order to optimize transport pathways in devices where charge migration occurs either horizontal (OFET) or normal (OSC) to the plane (see Chapter 2 for device working principles). Ultimately, additional complexity in understanding disorder and charge transport in conjugated polymers is introduced by the fact that nearly all polymer samples are polydisperse and contain a distribution of chain lengths.<sup>[25]</sup> Molecular weight (MW) is very well known to have a strong influence in rr-P3HT thin films but receives little or no quantitative attention in all the other polymers.<sup>[26]</sup> <sup>[27]</sup> The current knowledge on the effect of MW is quite speculative and it is usually understood with the charge transport along the chain backbone being far faster than intermolecular hopping. In rr-P3HT it has been shown that very low-MW fractions form crystalline aggregates (fibrils) that are poorly connected due to the presence of grain boundaries which in turn inhibit charge hopping between crystalline regions<sup>[28]</sup>. In high MW instead, less crystalline aggregates are bridged between them resulting in high mobilities. Thus, the complexity of the microstructure, the ambiguous charge transport mechanism and the effect of different molecular weights affect significantly the electronic properties and arise as major challenges in the field. <sup>[12]</sup> Novel and rational designing guidelines to address this issues would pave the way for the next generation of devices, more reproducible and efficient.

## 1.2 Morphological stability of electronic devices

Beyond the desired high mobility, the long-term stability, in particular, is essential for commercial application of OS-based devices. Only recently some attention has been devoted to the development of environmentally stable organic semiconductors with constant charge carrier mobility over long-term operating conditions and under applied thermal and mechanical stress. In this respect, mechanical properties of organic semiconductors are attractive features for roll-to-roll large area manufacturing of electronic devices onto flexible substrates where a high degree of mechanical compliance, together with



electronic behavior, is required. Indeed, depending on the molecular structure and thin films' microstructure most conjugated polymers are intrinsically more mechanically compliant than inorganic crystalline materials. Some highly crystalline small molecule semiconductors show very little tolerance to strain while some polymers can extensively deform. Due to its relatively high degree of crystallinity PBTTT thin films exhibit cracks at strains as low as 3%<sup>[29]</sup>, while a similar poly-thiophene, P3HT, owing to its 2D semi-crystalline domains nature can be bent and even stretched as high as 150% while maintaining good electrical performance.<sup>[30]</sup> Despite the significant need for bottom-up device fabrication strategies and the impressive number of already-reported conjugated polymers, only a handful of strategies have been reported to improve plasticity of semiconducting materials. Synthesis of statistical and block copolymers of rr-P3HT in which compliant domains of rr-P3OT (C8) are tethered by rigid domains of rr-P3HT (C6) was showed by Lipomi and coworkers<sup>[31]</sup> as an effective strategy to decrease the tensile modulus of the overall film. Physical blending of the pure P3HT and P3OT chains as well, confirmed how overall film's mechanical properties appear to be dominated by the more compliant P3OT. While P3HT will almost certainly have a role in the future of organic electronics, they are not anymore the highest-performing materials in the literature in terms of charge-carrier mobility in field effect transistor. Moreover, the alkyl chain blending strategy proposed for P3HT is not directly transferrable to other conjugated polymers. In this respect, a more general approach that can be extended to state of the art high-mobility polymers is needed to concretely stabilize intermolecular  $\pi$ -stacking charge transport network while polymer chains undergo mechanical stress.<sup>[32]</sup>

An established method to evaluate the stability of organic materials in devices like OFETs<sup>[33]</sup> and OSC<sup>[34]</sup> is based on the monitoring of the evolution of their performance (e.g. charge carrier mobility or power conversion efficiency) both under repeated cycles of plastic deformation or over a consistent period of time (hours or days) at a given temperature in order to accelerate degradation processes ( $T_{\text{ann}} = 80^{\circ}\text{C} - 120^{\circ}\text{C}$ ). Changes in the crystal structure arising from expansion of crystal lattices under thermal stress have shown to have also a primary role in the degradation mechanism.<sup>[35]</sup> In this respect, it is well known that, owing to the weak interaction forces, organic semiconductors are likely to change crystalline phase, a behavior that is described as polymorphism.<sup>[36]</sup> Most small molecule semiconductors can therefore crystallize in a variety of polymorphs that can yield different crystal orientation and subsequently affect device performances.<sup>[37]</sup> For example, the effect of temperature on the long-term stability of a diF-TES-ADT based thin film OFET was showed by Jurchescu et al.<sup>[38]</sup> This work elucidated the influence of polymorphism on the long-term performance of the device. An order of magnitude increase in charge carrier mobility was found by promoting the formation of a different polymorph at higher temperature, in contrast to the phase normally present at high temperature. More recently, Mc

Neill et al.<sup>[35]</sup> identified a strong correlation between the measured in-plane thermal expansion coefficient and the mobility of crystalline small molecule that had been annealed and then rapidly quenched. Higher mobility was achieved mostly by favoring polymorphs with higher out of plane thermal expansion and smaller in plane spacing between adjacent molecules. Ultimately, the intrinsic stability of the semiconducting layer can also be improved by inhibiting degrading chemical dynamics occurring at the semiconductor/dielectric interface like electron trapping and oxygen-induced degradation reaction.<sup>[33]</sup>

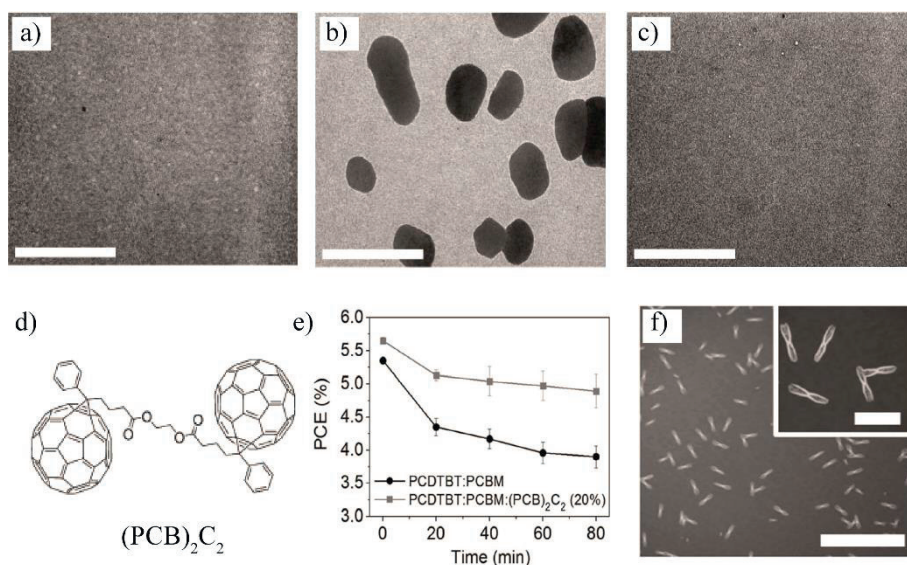


**Figure 1-3.** Solar cells morphological stability a) rr-P3HT:PCBM blend prior to annealing, b) annealing for 1h at 140°C c) annealing for 1h at 140°C with 17% of polymeric compatibilizer d) chemical structure of PBCM dimer e) degradation of solar cell efficiency as a function of annealing time at 85°C in nitrogen atmosphere f) PCBM crystals formed after annealing at 140°C for 1h. The scale bar is set is 2 μm. Adapted from references (6) and (44).

In particular, the need to control the thin film morphology under thermal stress is especially important for application in bulk heterojunction (donor-acceptor) blends (see Section 2-2 for solar cell working principle) present in solar cells where the domain size between the electron donating and electron accepting phases must be precisely controlled to achieve high power conversion efficiency. Bulk heterojunction (BHJ) solar cells have indeed a more pronounced morphological instability compared to OFET originating from the non-equilibrium state of the blend (a mixture of two typically immiscible components). The formation of the bulk heterojunction is kinetically driven by the phase segregation of both

components as well as their crystallization. The morphology can be controlled during device fabrication by employing solvent mixtures,<sup>[39]</sup> adding preferential solvents or post-deposition treatments<sup>[40]</sup> like thermal annealing<sup>[41]</sup>. However, once the desired morphology is obtained, in order to maintain high power conversion efficiency and to avoid device degradation over time it is necessary to “lock in” the ideal microstructure (Figure 1-3a).<sup>[42]</sup> During long operational periods the bi-component blend reaches a thermodynamically stable state characterized by full phase separation of the constituting components into well separated macroscopic domains with minimal interfacial area as shown in Figure 1-3b. In particular, the commonly-used C<sub>60</sub> fullerene-based electron acceptor species coded PCBM forms micron-scale crystallites<sup>[43]</sup> that are expelled from the blend and that inhibit charge transport to the electrodes (Figure 1-3f). For polymeric solar cells, one of the most used approaches to inhibit fullerene phase separation is to chemically crosslink fullerenes<sup>[44]</sup> or fullerene and conjugated polymer<sup>[6b]</sup> together in the BHJ after deposition. In most cases cross linking the active layer caused a significant performance decrease. Recently reported approaches proposed instead the use of PBCM derivatives<sup>[45]</sup> in the form of dimeric additives that were used as additives.<sup>[46]</sup> Durrant and coworkers<sup>[47]</sup> showed how a direct addition of covalently linked PCBM dimers (see chemical structure Figure 1-3d) in solution with the active components prior to deposition was able to provide a more structurally controlled and robust route to inhibit PBCM aggregation and stabilize the overall performance of solar cells under thermal stress as shown by the stabilization of device performance with the additive present (Figure 1-3e).

Comparable device performance to the polymer-based systems has now been achieved in bulk heterojunctions prepared with molecular semiconductors together with small molecule fullerene derivatives. In contrast to conjugated polymer semiconductors, molecular semiconductors have a much stronger tendency to self-assemble into highly crystalline domains with unpredictable domain size and higher densities of grain boundaries in a thin film. In a particular system with a small molecule donor coded DPP(TBFu)<sub>2</sub> Nguyen et al.<sup>[48]</sup> showed that the phase separation of a blend (with PCBM) is exclusively driven by the crystallization of the donor phase which suggests its primary role in the formation of the initially ideal morphology. However, despite the increase interest in using molecular semiconductors in BHJ solar cells and the primary role of the donor phase in the control of the phase separation (in comparison to PCBM acceptor) no strategies have been developed to improve the long-term stability of strongly phase segregating molecular semiconductors and, more importantly, the direct control over the dynamics of molecular donor crystallization has been overlooked.

## 1.4 Scope of the thesis

From the examples presented in the previous introduction sections it is evident that our understanding of structure-property relationships between rational molecular design and device performance in semicrystalline organic semiconductors is still highly empirical and challenged by the resulting microstructural complexity. We believe that the fine tuning currently used to adjust the electronic and structural properties of conjugated polymers often insufficient to optimize the overall device performance. Instead, obtaining new fundamental insights through a macromolecular synthetic approach operated on model organic semiconductors may lead to the design of new classes of compounds with unprecedented features and ultimately bring more concrete contributions on device characteristics. Since the early stage of this research, the intrinsic complexity of polymeric systems in terms of MW dependent charge carrier mobility, transport mechanism and resulting morphology has been considered as a limiting factor in understanding fundamental dynamics occurring in high performance devices. However, the preparation of polymers with low chain length distributions is still not achievable and the synthesis of new polymeric materials with well-controlled microstructural properties is subject to the established synthetic pathways.<sup>[49]</sup> In the present thesis, we therefore aim to shed some light into these general limitations related to the design and function of organic electronic materials. Herein, we develop synthetic strategies at macromolecular level to tailor the active layer's morphology while analyzing film formation properties and charge transport in OFET and OSC. The main aspects that will be addressed in the course of this thesis are:

1. Reducing microstructure complexity in semicrystalline and low-bandgap polymers by selecting precise chain length and understanding the relationship that links molecular weight, charge carrier transport mechanisms and morphology in the resulting thin-films. Understanding the role of chain length distribution (polydispersity, PDI) and providing new strategies to overcome grain boundaries in crystalline thin films (Chapter 3 and Chapter 4).
2. Understanding the role of intramolecular and intermolecular charge transport in thin films prepared with a semicrystalline polymer through the use of a synthetic model polymer where conjugation segment length and length of the entire chain can be independently controlled (Chapter 5). Enhancing film plasticity against mechanical and thermal stress, while maintaining constant charge transport is the key to ultimately improve long-term stability of organic electronic devices (Chapter 6).
3. Developing new synthetic approaches at the macromolecular level towards new materials with enhanced structural control for future generation of opto-electronic devices (Chapter 7).

# Chapter 2

## Experimental methods

### 2.1 Field effect transistors

In the introductory chapter, the strong dependence of the final device performance on the morphology of solution-processed small molecule and conjugated polymer based organic semiconductors was introduced. These effects are commonly investigated in thin-film transistors (TFTs) which are of great technological interest since they are one of the elementary component of thin film electronic while being a straightforward method to calculate the charge carrier mobility of a semiconductor. Organic field effect transistors (OFETs) allow the study of charge carrier transport in materials with great control over the processing conditions, thin film morphology, and charge densities while allowing in-situ physical characterization. OFETs are typically p-type (holes transporting devices) that are composed of a source and a drain electrode both in contact with the organic semiconductor (Figure 2-1 for a device schematic and basic operating principles). A dielectric layer insulates the organic layer and the electrodes from a gate electrode. Modulation of the negative voltage applied to the gate electrode ( $V_g$ ) controls the amount of charges (holes) created in the organic semiconductor. The holes migrate to the accumulation layer at the interface between the semiconductors and dielectric, and are swept out of the device upon application of a voltage ( $V_{ds}$ ) between the sources and drain electrode. Gate voltage modulation switches the device ON or OFF with the ON current ( $I_{on}$ ), the voltage required to turn the device ON ( $V_{th}$ ) and the charge carrier mobility ( $\mu_{FET}$ , explained below) being figures of merit for the electrical performance of the semiconducting material and the final device. High performance organic semiconductors are designed to maximize both charge injection and charge transport. Firstly, organic semiconductors electronic structure has to be suitable for holes/electron injection/ at moderate applied electric fields. The active layer should be free from impurities that can act as charge traps and uniformly cover the whole channel length. The crystal structure of the semiconducting material must provide extended orbital overlap, i.e. through  $\pi$ - $\pi$  stacking, to allow efficient charge percolation between adjacent molecules over long distances. On the other hand, because charge transport occurs along the first layers of materials, it is extraordinarily sensitive to the properties of the buried semiconductor/dielectric interface.

### 2.1.1 Transistors Fabrication

In the present thesis, bottom gate-bottom contact configuration field effect transistors were fabricated by spin coating under inert atmosphere onto n-doped silicon microchips with 230 nm SiO<sub>2</sub> gate dielectric ( $C = 18 \text{ nF/cm}^2$ ) and interdigitated 30 nm gold source and drain contacts (Generation 4 devices from Fraunhofer-Gesellschaft). Substrates were cleaned through a cycle of sonication in acetone, water and isopropanol and dried with a filtered air gun. Prior to film deposition, the cleaned surfaces were subjected to a UV Ozone treatment. Substrates surface was functionalized with octadecyltrichlorosilane (OTS-18) under inert atmosphere by immersing them in 10 mM solutions in toluene for 15 min at 60°C and then rinsed with fresh toluene solution before being dried with argon. The resulting surface hydrophobicity was assessed by contact angle measurements, resulting in an angle  $> 105^\circ$  with H<sub>2</sub>O. Polymer solutions were prepared under inert atmosphere with the dried polymers powders dissolved in the dried solvents (AcroSeal). Typical solution concentration were ranging from 5-10 mg/ml for conjugated polymers and 10-20 mg/ml for small molecule thin films. The totality of the TFTs prepared here were processed by spin coating onto the prepared substrates. Spin rate was set between 500 and 1000 rpm for polymer TFT and from 1500-2000 rpm for small molecules TFT. The total spin time was time was approximately 1 minute.

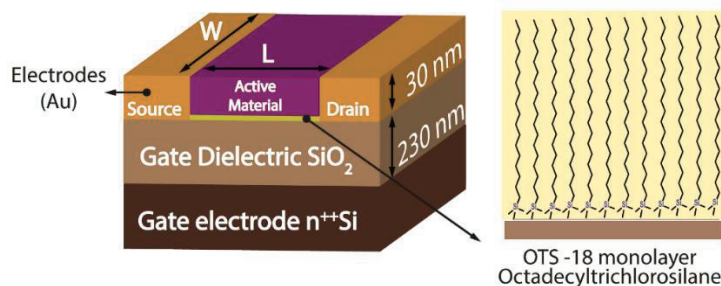


**Figure 2-1.** Geometry of a bottom gate-bottom contact organic thin film transistor, with ITS surface treatment. Typical device characteristic are defined as transistor width (W) and length (L).

### 2.1.2 Measuring device characteristics.

Electrical characterization was performed with a dual channel Keithley 2611 sourcemeter controlled through a custom Labview software. During extrapolation of the charge carrier mobility, a gradual channel approximation is assumed. At low gate voltages, the extracted current are proportional to the applied drain voltages, thus the transistor operates in linear regime. The measured source-drain current

is dependent on the device geometry with  $W$  being the channel width,  $L$  channel length,  $C_i$  the capacitance of the dielectric layer, the gate voltage  $V_g$ , the threshold voltage  $V_{th}$ , the drain voltage  $V_{ds}$  and the intrinsic mobility of charge carrier  $\mu_{FET}$ , in the material under investigation, as shown in Equation (2-1):

$$I_{ds} = \mu \frac{W}{L} C_i (V_g - V_{th}) V_{ds} \quad (\text{Eq. 2-1})$$

At higher source-drain voltages ( $V_{ds} > V_g - V_{th}$ ) the current is no longer dependent on the drain voltage, as shown in Equation (2-2) and the transistor enters in the saturation regime:

$$I_{ds} = \mu \frac{W}{2L} C_i (V_g - V_{th})^2 \quad (\text{Eq. 2-2})$$

Typical output characteristics ( $I_{ds}$  vs  $V_{ds}$ ) and transfer characteristics ( $I_{ds}$  vs  $V_g$ ) are shown in Figure 2-2. To characterize the devices, transfer characteristics were collected under nitrogen atmosphere and mobilities in the linear regime were determined according to the relationship given in Equation 2.3:

$$\mu_{lin} = \frac{m_{lin} \times L}{W \times C_i \times V_d} \quad (\text{Eq. 2-3})$$

where  $m_{lin}$  is the slope of the transfer curve at high  $V_g$ , with a  $V_d$  of -10V, as shown by the dotted line. Mobilities in the saturation regime instead were determined according to Equation (2.4).

$$\mu_{sat} = \frac{m_{sat}^2 \times 2L}{W \times C_i} \quad (\text{Eq. 2-4})$$

where  $m_{sat}$  represents the slope of  $I_{ds}^{(1/2)}$  vs  $V_g$  at high  $V_g$ , marked by the dotted lines in Figure 8c. Comparable mobilities calculated in the linear and saturation regimes assure that the applied models are consistent with device operation. The threshold voltage ( $V_{th}$ ) is estimated from the transfer curve in the saturation regime and the x-intercept (B) of the extrapolated linear fit of the curve at high  $V_g$  as derived from equation (2-5).

$$V_{th} = B - \frac{V_d}{2} \quad (\text{Eq. 2-5})$$

The  $I_{on}/I_{off}$  ratio is best estimated from a transfer curve in the saturation regime on a logarithmic scale. The value for  $I_{on}$  is defined as the value where the curve begins to flatten and the value for  $I_{off}$  is defined as the lowest current measured. Leakage currents are measured in the subthreshold region.

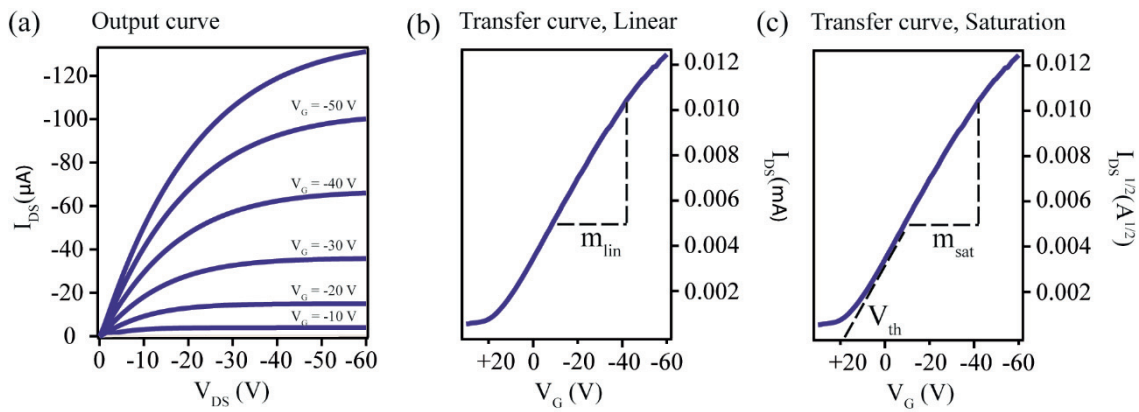


**Figure 2-2.** Example transistor characteristic for an OFET device a) Output characteristic for  $0 \text{ V} < V_g < -60 \text{ V}$ . b) Transfer characteristics in the linear regime ( $V_{ds} = -10 \text{ V}$ ) c) Transfer characteristic in saturation regime ( $V_d = -60 \text{ V}$ ), shown on in a linear scale.

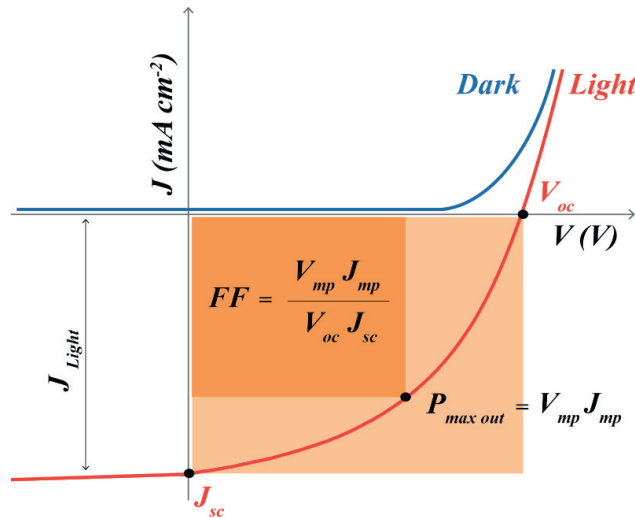
## 2.2 Bulk Heterojunction solar cells

### 2.2.1 Parameters of a Solar cell.

The overall performance of a solar cell is measured from its J-V curve (Figure 2-3), with  $J$  being the current per unit area of the cell, i.e., the current density. Typical parameters like the short-circuit current density ( $J_{sc}$ ), the open circuit voltage ( $V_{oc}$ ), and the fill factor (FF) can then be extracted from the J-V curve. The  $J_{sc}$  is representative of the amount of charge carriers extracted from the cell at short circuit, i.e. when both electrodes are put in direct contact without any load resistance. It is generally argued that  $J_{sc}$  can be increased with improved light absorption, charge separation and extraction. The  $V_{oc}$  instead represents the potential energy of the charges at open circuit. In organic solar cells (OSC), the  $V_{oc}$  is found to be related to the energy difference between the lowest occupied molecular orbital (LUMO) of the acceptor component and the highest occupied molecular orbital (HOMO) of the donor minus a -0.3



V correction factor. The FF represent instead the ratio of the maximum power of the cell over the ‘ideal power’ that correspond to the product  $J_{sc} \times V_{oc}$ . Ideal cells are characterized by  $FF = 1$  and the J-V curve is rectilinear. The maximum efficiency of the device at converting sunlight into electricity is called power conversion efficiency (PCE) and it is normally calculated from Eq. (2-6), and corresponds to the ratio between the maximum power produced in the device ( $P_{max\ out}$ ) and the incident power ( $P_{inc}$ ).



$$PCE (\%) = \frac{P_{max\ out}}{P_{inc}} = \frac{V_{mp} \times J_{mp}}{P_{inc}} = \frac{FF \times V_{oc} \times J_{sc}}{P_{inc}} \quad (\text{Eq. 2-6})$$

**Figure 2-3** Typical J-V curve of a solar cell in the dark and under illumination

### 2.2.2 Charge generation in solar cells.

The absorber layer of a state-of-the-art organic solar cell is made of so-called electron donor and acceptor molecules. A schematic diagram of the energy levels a typical donor-acceptor system is shown in Figure 2-4. It is generally accepted that in organic semiconducting materials bound neutral electron-hole pair (excitons) are generated upon photon absorption. Given the low dielectric constants of organic materials ( $\epsilon_r = 3-4$ ), Coulombic interactions between charged species are stronger in carbon based materials. Excitons in organic materials have binding energy up to 1 eV, which is far higher than the thermal energy at ambient temperature (25 meV). For this reason a dissociation of the exciton into free charges that can originate electrical current inside the device is very unlikely under ambient conditions. Hence, the most used strategy to facilitate exciton separation into free-charges is to combine a donor

with an acceptor material. The position of the energy LUMO levels (Figure 2-4b) and the electron affinities of the two components identify the donor and acceptor materials and creates the driving force for the rapid transfer of an electron from the donor to the acceptor. It is commonly accepted that the general mechanism for energy conversion in organic photovoltaics can be divided into 5 steps (Figure 2-4a): (i) light absorption in the donor and acceptor phase produces an exciton; (ii) the neutral exciton diffuses through the material; (iii) at the donor-acceptor interface the exciton can form a charge transfer (CT) state, i.e. an electron is in the acceptor phase and the hole remain in the donor phase; (iv) the CT state splits into free charge carriers; (v) the charges travel through the respective phases and collected at the electrodes.

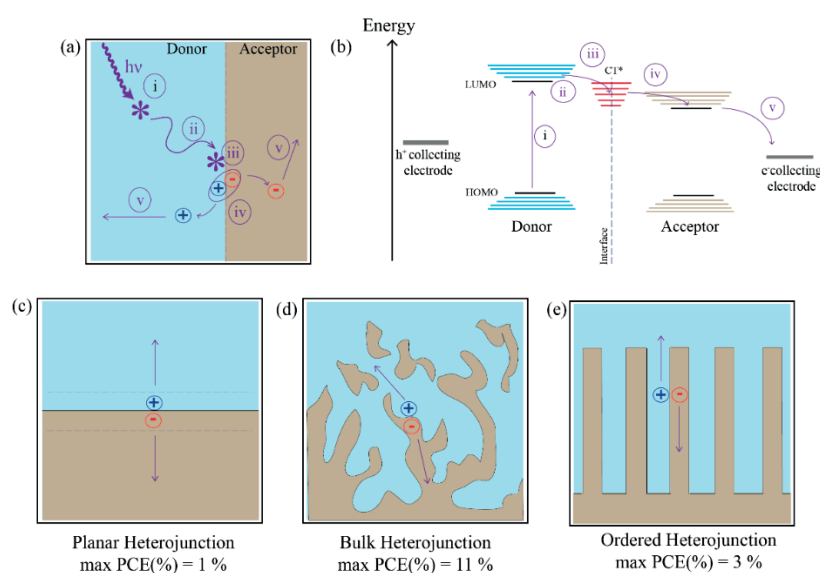


**Figure 2-4.** Mechanism of charge generation in organic photovoltaics depicted in a) the active layer and b) the corresponding energy diagram. Five steps have been emphasized: (i) light absorption, (ii) exciton diffusion to the interface, (iii) exciton splitting occurring in the charge transfer state (CT), (iv) free charges state formation and (v) charge transport to the electrodes.

All the aforementioned processes have been shown to be highly dependent from the morphology produced during film formation at the microscopical level. As illustrated in Figure 2-4c the first reported device composed of a p-type and an n-type organic semiconductors was characterized by a planar heterojunction where excitons were formed in the whole thickness of the active layer but only a small

fraction was split at the interface.<sup>[50]</sup> The interplay between the exciton diffusion length and the absorption coefficient limited the power conversion efficiency (~ 1% PCE). A breakthrough in the field was brought by Heeger et al. with the introduction of the bulk heterojunction in which randomly interpenetrating donor-acceptor phases were homogeneously distributed within the active layer the active layer.<sup>[51]</sup> In this generation of solar cells (Figure 2-4d), the active layer morphology was characterized by increased interfacial area and reduced domain sized. Moreover, the probability for the exciton to reach the interface was remarkably improved and PCE approaching 11% have been reported nowadays.<sup>[52]</sup> However, charge transport in bulk heterojunction solar cells still remains unoptimized and highly unpredictable due to the presence of grain boundaries and a large distribution in domain size. For this reason an “ordered heterojunction”, like in Figure 2-4e, characterized by a large interfacial area and ordered charge percolation pathways to the electrodes has been envisaged as a potential strategy to improve devices’ energy conversion.

### **2.2.3 Bulk Heterojunction solar cells Fabrication.**

Solar cells were fabricated with a 35-nm layer of PEDOT:PSS (Ossilla M 121 Al 4083) deposited and annealed (130°C) for 30 minutes on a plasma-treated glass substrate patterned with 300 nm of ITO. The BHJ active layer was spin-cast at 3000 rpm from a solution of DPP(TBFu)<sub>2</sub> and PC<sub>61</sub>BM in chloroform at a total solids concentration of 20-30 mg mL<sup>-1</sup>. The active layers were determined to be approximately 90-nm thick using a Bruker Dektak XT profilometer. An 80-nm-thick aluminum cathode was deposited (area 16 mm<sup>2</sup>) by thermal evaporation (Kurt J. Lesker Mini-SPECTROS). Solar cells were left overnight under vacuum to eliminate solvent traces and subsequently annealed on a temperature controlled hot plate under nitrogen atmosphere and quickly quenched onto a cold surface.

### **2.2.4 Measuring device characteristics.**

Electronic characterization was performed under simulated AM1.5G irradiation from a 300W Xe arc lamp set to 100 mW cm<sup>2</sup> with a calibrated Si photodiode (ThorLabs). Current-voltage curves were obtained with a Keithley 2400 source measure unit through a custom Labview interface. Testing was performed in a nitrogen filled glovebox.

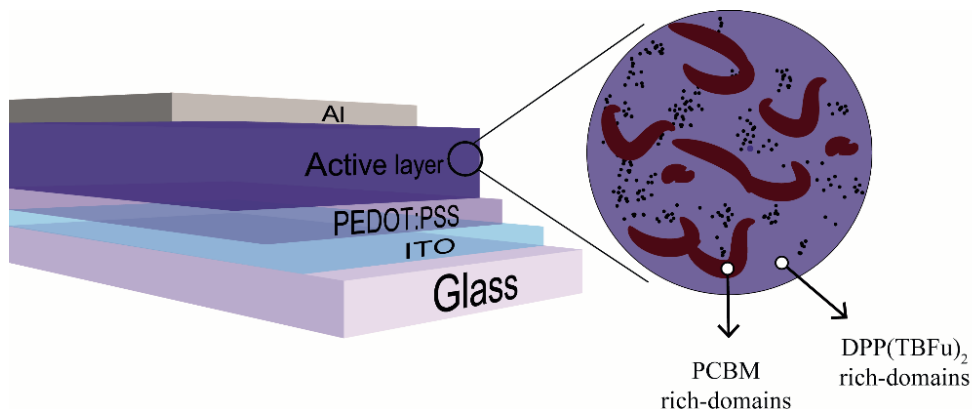


**Figure 2-5.** Architecture of a standard bulk heterojunction solar cell.

## 2.3 Microstructural characterization

### 2.3.1 Techniques based on X-ray diffraction.

X-ray scattering measurements are extensively used to provide detailed information about the molecular packing structure, crystallinity, orientation and size of crystalline domains throughout the whole film. Additionally, because of the non-destructive nature of this technique, there is significant interest in performing in-situ measurements on working devices and directly link crystalline texture with electronic properties. X-ray scattering experiments are usually performed on thin films in small angle x-ray scattering regime (SAXS) or wide angle x-ray scattering regime (WAXS). Wide angle experiments are typically used to probe molecular dimensions (0.1-10 nm) and provides information exclusively on the short range order like  $\pi$ - $\pi$  or lamellar stacking. SAXS instead probes long correlation length (typically  $> 10$  nm) and can be performed also on non-crystalline samples that still have different domains chemical composition. X-ray scattering from thin films of polymers is weak due to the low scattering strength of carbon atoms and the disordered nature of the films. For this reason Synchrotron facilities provide enough intensity to produce significant scattering signal over reasonable experimental times. Here the very basics of X-ray diffraction are discussed, but the reader is referred to other texts for a more detailed explanation.<sup>[53]</sup>

### 2.3.2 Theory of x-ray diffraction.

The physics behind X-ray diffraction is based on the coherent scattering of outgoing radiation beams from well-ordered lattice planes as described by a derivation of Bragg's law on constructive interference of reflected waves. As shown in Figure 12 the two waves are reflected off adjacent atomic planes. Constructive interference occurs when the outgoing waves have the same phase. For incoming radiation with wavelength  $\lambda$ , incident angle  $\theta$ , and interplanar spacing  $d$ , it follows that:

$$n2\pi = \frac{2\pi}{\lambda} * 2d\sin(\theta_B) \quad (\text{Eq. 2-7})$$

$$n\lambda = 2d\sin(\theta_B) \quad \text{Bragg's law}$$

with  $\theta_B$  being the incident angle for which Bragg condition is satisfied and is called the Bragg angle.

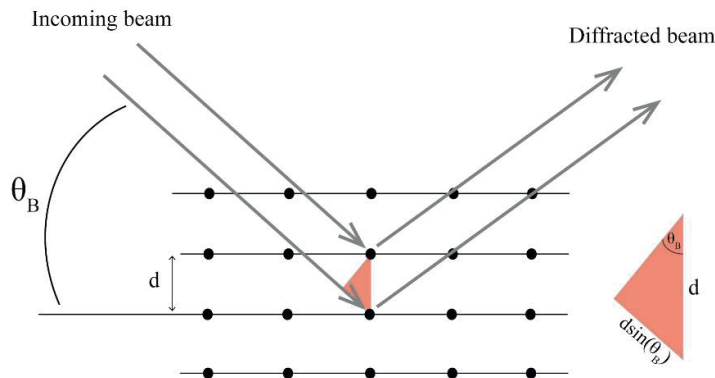


**Figure 2-6.** Derivation of Bragg's law in real space based on the requirement for constructive interference of incoming beams.

A conventional way to think about diffraction is by thinking in reciprocal space. In brief, all crystal lattices in real space have a corresponding lattice in reciprocal space which is described as a set of all vectors  $G_m$  that satisfy the identity for all lattice point position of the Bravais lattice vector  $R$  in real space.

$$G_m \cdot R_n = 2\pi N \quad (\text{Eq. 2-8})$$

For an infinite three dimensional lattice, defined by its primitive vectors ( $a_1, a_2, a_3$ ), its reciprocal lattice can be determined by generating its three reciprocal primitive vectors as described below:

$$G_m = m_1 \cdot b_1 + m_2 \cdot b_2 + m_3 \cdot b_3 \quad (\text{Eq. 2-9})$$

Where

$$b_1 = \frac{a_2 \times a_3}{a_1 \cdot (a_2 \times a_3)}$$

$$b_2 = \frac{a_3 \times a_1}{a_2 \cdot (a_3 \times a_1)}$$

$$b_3 = \frac{a_1 \times a_2}{a_3 \cdot (a_1 \times a_2)}$$

The general reciprocal lattice vector is defined as follows:

$$G_{hkl} = hb_1 + kb_2 + lb_3 \quad (\text{Eq. 2-10})$$

Where h, k and l are the Miller indices used to designate planes within a crystal. The integral value of  $G_{hkl}$  has a reciprocal relationship with the interplanar spacing ( $d_{hkl}$ ). Diffraction data throughout this thesis will be presented in reciprocal space, so it is necessary to define the scattering vector,  $q$ , as shown in Figure 2-7.

Bragg condition is satisfied when the scattering vector  $q$ , intersects the reciprocal lattice point, whose position is defined by the general reciprocal lattice vector  $G_{hkl}$  as defined as follows:

$$q_B = \frac{4\pi}{\lambda} \sin(\theta_B) = 2\pi |G_{hkl}| \quad (\text{Eq. 2-11})$$

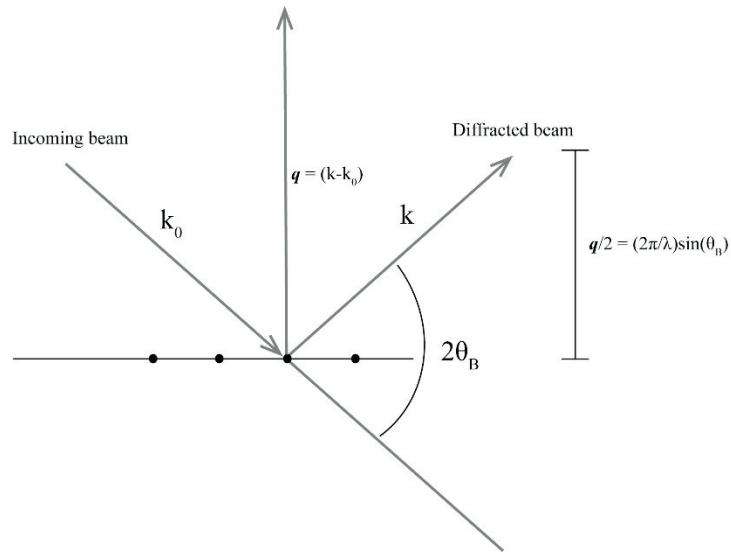


**Figure 2-7.** Relationship between incoming vector  $k_0$ , outgoing vector  $k$  and scattering vector  $q$ .

Accordingly, an alternative representation of Bragg's law is given in Equation and has been used to calculate the characteristic lamellar spacing between polymer chains.

$$q_B = \frac{2\pi}{d_{hkl}} \quad (\text{Eq. 2-12})$$

Much of the work presented in this thesis is dedicated to compare thin microstructural features in reciprocal space as a function of chain length, thermal treatments and molecular design.

### 2.3.3 Specular diffraction measurements with laboratory sources.

These measurements are used to investigate periodicity existing out-of-plane of the substrate. Specular X-ray scattering is performed with a standard Cu-K $\alpha$  x-ray source (0.15418 nm) on a Bruker D8 Advanced goniometer using grazing incidence conditions with an incidence angle of 0.2°, a scan speed of 0.05 degrees min<sup>-1</sup> and a Lynx Eye linear detector. The beam defining slits between the incoming beam and the sample,  $v_0$ -gap and  $h_0$ -gap, are both set as V5. A "Detector scan mode" is used to obtain high resolution peak position and peak shape analysis, but due to the low volume of crystalline material investigated (within  $qz = 0.03^\circ$  of the surface normal) it does not give complete information about the whole film microstructure. The detailed geometry of a specular diffraction setup is shown below.

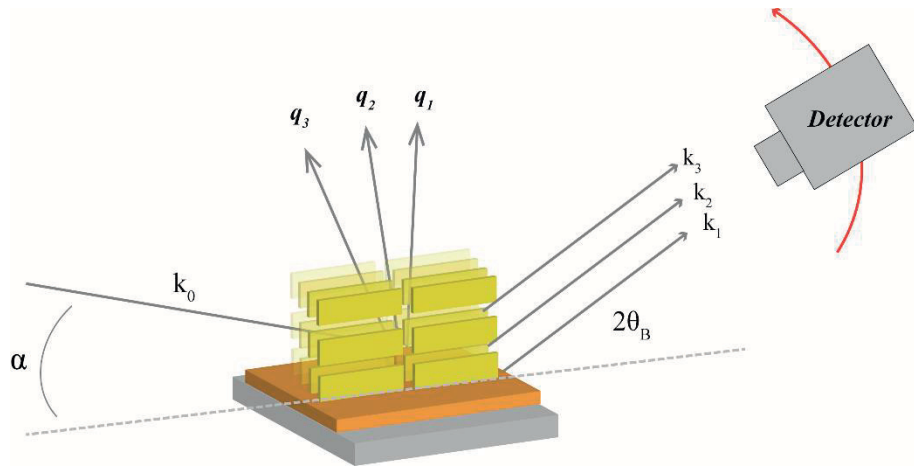


**Figure 2-8.** Grazing incidence X-ray diffraction geometry operated with a laboratory source. The incoming beam lies nearly in the plane of the substrate ( incidence angle  $\alpha = 0.2^\circ$ ) and  $q$  is the scattering vector, oriented perpendicular to the substrate for out of plane diffraction. Only beams diffracted from crystallites with  $0.03^\circ$  of orientational distribution are collected by the detector. Multiple orders ( $q_n$ ) can be detected.

### 2.3.4 X-ray diffraction with synchrotron radiation.

Measurements of two dimensional X-ray scattering were carried out at the European Synchrotron Radiation Facility on beam line BM02 and at ANKA Lightsource at KIT on beam line PDIFF. All the materials were prepared in our lab and processed in films ( $< 100$  nm) through spin-coating procedure from solution. Films are typically spin-coated on Si wafers with surface treated native oxide as in real transistor devices in order to have a high quality and appropriate surface of reference.



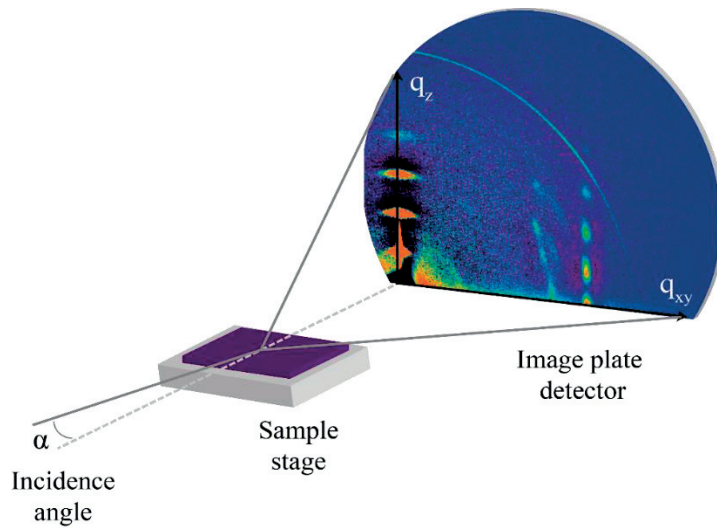


**Figure 2-9.** Geometry of grazing incidence with a two-dimensional image plate detector.<sup>[15]</sup>

The grazing incidence angle is optimized to maximize diffracted intensity from the film. Wide angle grazing incidence of in-plane and out-of-plane diffraction was carried with a  $0.15^\circ$  incidence angle (above the critical angle of polymer samples  $a = 0.08^\circ$ ) and an incident energy beam at 12.7 keV, corresponding to a photon wavelength of 0.0978 nm with the 2D detector and point detector. The sample was placed at a adjustable distance ranging from 18 mm to 30 mm form the 2D-detector with the exact distance calibrated using LaB6 standard. The in-plane component of the scattering vector projected on the detector is  $q_{xy}$ , and the vertical component is  $q_z$ . The 2D patterns displays a large but not accurate view of the reciprocal space due to distortion and the low resolution of the 2D detector, so there diffraction patterns are not ideal for quantitative measurements. The detailed geometry of a 2D grazing incidence X-ray diffraction is shown in Figure 2-8.



# Chapter 3

## Effects of molecular weight on microstructure and carrier transport in a semicrystalline poly(thieno)thiophene

### 3.1 Introduction

A prototype semicrystalline polymer that has emerged as promising candidate for application in solution-processed organic field-effect transistors (OFETs) is poly-(2,5-bis(3-alkylthiophen-2-yl)thienothiophene) (PBTTT).<sup>[14a]</sup> The dodecyl (C<sub>12</sub>), tetradecyl (C<sub>14</sub>) and hexadecyl (C<sub>16</sub>) versions of PBTTT have demonstrated p-type field-effect charge carrier mobility,  $\mu_{FET}$ , up to ca. 1 cm<sup>2</sup> V<sup>-1</sup> s<sup>-1</sup>.<sup>[15, 54]</sup> While this represents a leading performance for this class of materials, it remains in contrast to the expected value for p-type charge carrier (hole) mobility in perfectly crystalline PBTTT, which has been estimated to be at least an order of magnitude greater (up to 20 cm<sup>2</sup> V<sup>-1</sup> s<sup>-1</sup>).<sup>[4]</sup> Understanding and controlling the charge transport in conjugated polymer semiconductor thin-films remains a challenging fundamental goal that is complicated by the coexistence of crystalline and amorphous domains, crystallite size, and grain boundaries. One potential strategy to reduce microstructure complexity in semiconducting polymer thin-films is to separate the contributions to morphology and charge transport resulting from different polymer molecular weights (MW). Indeed, typical conjugated polymers prepared by step-growth methods have polydispersity indices (PDI = weight average molecular weight/ number average molecular weight, or  $M_w/M_n$ ) around 2 indicating that chain lengths of significant disparity are present. However, despite a few examples,<sup>[26, 55]</sup> examining the molecular weight dependence on the microstructure and charge carrier mobility has been mostly overlooked. In this work we investigate MW effects on the microstructure and electronic properties of PBTTT-C<sub>12</sub>-based thin-film transistors (TFTs) using samples with narrow PDIs and a broad range of different MWs. Also, in an effort to improve the performance of devices prepared with low MW PBTTT and to gain further insight into MW dependent charge transport mechanisms, we investigate a strategy based on blending highly crystalline low-MW fractions

with small percentages of high-MW fractions. This results in a facile route to increase both processability and charge transport of easily-prepared low MW polymers. The further combination of charge transport studies in TFTs and *in-situ* morphological characterization by AFM and out-of-plane XRD allow us to correlate the effects of micro-structural variation with the mobility, thereby providing valuable means to compare structure-property relationships among single MW fractions.

## 3.2 Result and discussion

### 3.2.1 Synthesis and MW fractionation

Since the Stille coupling-based step-growth polymerizations employed to obtain PBTTT-C<sub>12</sub> typically produce batches with M<sub>n</sub> below 30 kDa and broad PDI around 2,<sup>[14a]</sup> it is necessary to employ alternative strategies to access samples with M<sub>n</sub> > 30 kDa and low PDI. Our approach relies on preparatory size exclusion chromatography (prep-SEC), which affords separation of polymer chains lengths based on their characteristic hydrodynamic volume in solution. Starting from an initial crude batch (M<sub>n</sub> of ca. 20 kDa, PDI = 1.8) it was possible to collect fractions with M<sub>n</sub> ranging from 5.8 – 151 kDa and narrow PDI (typically 1.1–1.4) as is shown in the analytical SEC traces in Figure 3-1 and reported in Table 1. To avoid any issues with the poorer solubility of longer polymer chains, the prep-SEC system was maintained at a relatively high temperature (80°C), and low concentration of polymer was used in the mobile phase (chlorobenzene). It should be noted that the molecular weights reported in this work (similar to other reports) are calculated based on poly(styrene) standards. Due to the difference in molecular conformation in solution of a rigid conjugated polymer like PBTTT and coiled poly(styrene), SEC is known to overestimate molecular weights by a factor of 1.2–2.3.<sup>[56]</sup> Indeed, our comparison of the SEC results to NMR peak areas suggests that this number is 1.5 for low molecular weight fractions up to about 10 kDa. The calculation of this factor for higher molecular weights is more difficult due to limitations in resolving the end groups, but has recently been shown to increase slightly with increasing MW for rr-P3HT.<sup>[57]</sup> In addition, given the regiosymmetric nature of PBTTT, prep-SEC is expected to give more accurate separation by chain length compared to asymmetric polymers like rr-P3HT where regio-irregularities can cause changes in hydrodynamic volume independent of chain length.<sup>[58]</sup> Thus while it is challenging to report the true chain length of our PBTTT samples, we can be confident that our prepared

fractions do indeed include only chains of similar length. Slight variations observed in PDIs are attributed to dispersion effects in the column during elution and the elution volume collected for each fraction to obtain sufficient amounts for device fabrication.

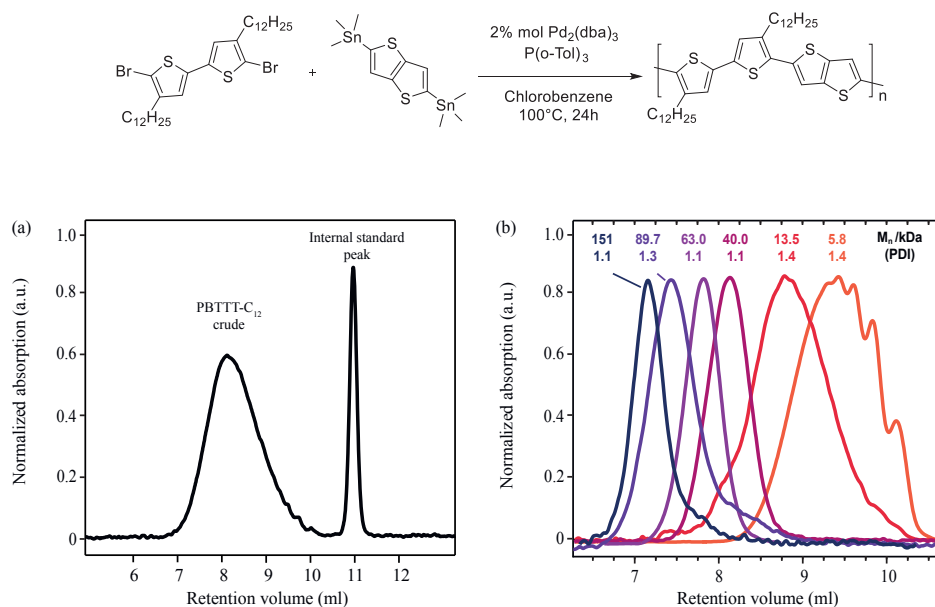


**Figure 3-1.** The analytical size exclusion chromatograms of the crude (a) and of the selected PBTTT fractions (b) separated by prep-SEC are shown as the normalized detector response versus elution volume of the mobile phase. The reported M<sub>n</sub> and PDI values for each fraction are versus polystyrene standards. For clarity, not all fractions employed in subsequent analysis are shown here.

Of particular note from the analytical SEC traces in Figure 3-1b is the presence of shoulders on the chromatograph of the 5.8 kDa sample corresponding to oligomers of BTTT. As we had concern that these could affect the electronic properties, we prepared an additional batch of PBTTT and separated a fraction with M<sub>n</sub> = 8.8 kDa and a PDI = 1.1. This fraction did not exhibit significant shoulder peaks from oligomers in the analytical SEC trace. The UV-vis absorption in solution (Figure 3-2a) show little dependence on molecular weight. The slight red-shift in absorption at high MW can be attribute to the presence of interacting aggregates in solution. As expected for semicrystalline polymers like PBTTT a drastic red-shift in absorption is found in the solid state (Figure 3-2 b). Interestingly, thin films made of

different MW show a larger shift of the absorption offset in low MW (710 nm) in comparison to medium and high MW (690 nm).

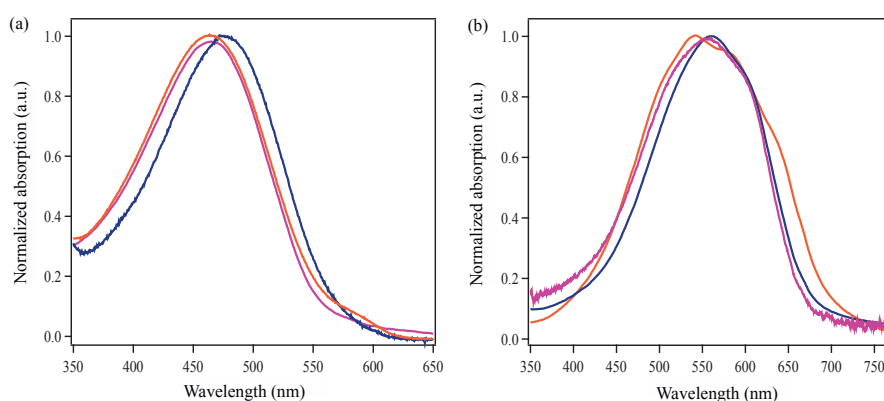


**Figure 3-2.** Normalized UV-Vis absorption spectra in solution (a) and in thin films (b) of 13.5 kDa (orange line), 31.7 kDa (purple line) and 89.7 kDa (blue line).

### 3.2.2 Effect of MW on the charge carrier mobility

To evaluate the charge transport characteristics of each fraction, TFTs were then prepared in the coplanar bottom-contact configuration with an octadecyltrichlorosilane (OTS) functionalized SiO<sub>2</sub> dielectric by spin coating from 1,2-dichlorobenzene. We note that concentrations of the solutions used for the depositions were varied so as to keep the film thickness for each device equivalent, and making sure to also use sufficiently thick films to avoid confinement effects.<sup>[59]</sup> Uniform semiconductor film formation of about 60 nm was observed for all MWs, except for the 5.8 kDa fraction where as-cast films were characterized by extremely rough and discontinuous films.

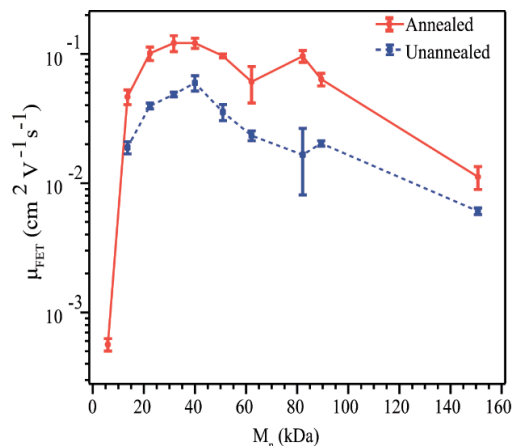


**Figure 3-3.** Average extracted (saturation regime) field-effect charge carrier mobility,  $\mu_{FET}$ , of annealed (180 °C, 10 min) PBTTT fractions as a function of number average molecular weight,  $M_n$ . Error bars corresponding to one standard deviation on multiple devices are also shown.

This was presumably a result of a poor substrate-solution interaction and rapid crystallization-aggregation of the material during the drying of the film. As the films were not continuous, we were unable to measure a field-effect with these as-cast devices, however after a thermal treatment, a field-effect was observed. After spin coating, all devices were subsequently examined at room temperature under a nitrogen atmosphere in the as-cast state and after a thermal annealing treatment (180 °C, 20 min, slow cooling), and the p-type  $\mu_{FET}$  was extracted from the current-voltage data and corresponding transfer curves. In order to compare charge carrier mobilities with previous reports<sup>[14a]</sup>, the annealing temperature was chosen accordingly within the alkyl chain melting temperature which in the specific case of PBTTT is identified with the formation of a liquid crystalline phase. As it will be discussed in section 3.2.4, low-MW fraction doesn't present a liquid crystalline phase, therefore annealing at 180°C induced a complete phase transition to the liquid phase and subsequent crystallization directly from the melt. In the linear regime of operation, the charge carrier mobility of our best performing (single device) annealed PBTTT TFTs was found to be  $0.17 \text{ cm}^2 \text{ V}^{-1} \text{ s}^{-1}$  (with the 31.7 kDa fraction), which is consistent with previous studies using this transistor geometry.<sup>[54b]</sup> In addition, we recorded consistent performance between repeat devices. Standard deviations on multiple samples are given with the tabulated results from all PBTTT fractions in Table 1, and the results are shown graphically in a semi-log plot as a function of  $M_n$  in Figure 3-3. Similar to what has been observed with rr-P3HT,<sup>[60]</sup> charge carrier mobility is extremely sensitive to chain length variation in the low MW range. For PBTTT we observe that a doubling of the number average molecular weight from 5.8 kDa to 13.5 kDa is responsible for an

increase in hole mobility of two orders of magnitude from  $5.5 \times 10^{-4}$  to  $4.5 \times 10^{-2} \text{ cm}^2 \text{ V}^{-1} \text{ s}^{-1}$  in annealed films. This is in direct contrast to what has been noted previously with this range of MW PBTTT films<sup>[60]</sup> where only a factor of three increase was observed over a similar range of  $M_n$  (8.1–17.9 kDa, which was the full range studied previously). However in the fractions used in that previous report, the PDIs were much higher (up to 2.9) indicating that a significant amount of chains over 15 kDa were present in the 8.1 kDa sample. This suggests that the long molecular weight chains in a low  $M_n$  sample of PBTTT can have a large influence on the film forming properties of the polymer. Indeed, with our supplementary fraction of PBTTT exhibiting a low  $M_n$  and PDI (8.8 kDa and a 1.1, respectively) mentioned previously we were not able to measure a field-effect under identical TFT preparation conditions (due to non-continuous film formation). This observation suggests that we were able to observe a field-effect after annealing the 5.8 kDa fraction due to the presence of longer molecular weight chains that aided the formation of a continuous film in that sample. To support this suggestion we blended 10 wt% of a 13.5 kDa fraction with the 8.8 kDa fraction and indeed we observed the formation of a continuous film. Our observations suggest the existence of a threshold molecular weight for PBTTT-C<sub>12</sub> between ca. 9–13 kDa which is required for film formation and TFT operation. These aspects will be discussed in more detail below.

**Table 3-1.** Molecular weight information and the corresponding charge carrier mobility of the PBTTT fractions prepared by prep-SEC.

$M_n$ (kDa)	$M_w$ (kDa)	PDI	Unannealed $\mu_{\text{sat}}$ ( $\text{cm}^2 \text{ V}^{-1} \text{ s}^{-1}$ ) <sup>a</sup>	Annealed $\mu_{\text{sat}}$ ( $\text{cm}^2 \text{ V}^{-1} \text{ s}^{-1}$ ) <sup>b</sup>	$V_{\text{TH}}$	$R_s$
5.8	8.12	1.4	--	$0.00055 \pm$	+18 V	2.5
13.5	18.9	1.4	$0.018 \pm 0.002$	$0.046 \pm 0.006$	-7 V	40 k $\Omega$
22.3	29.0	1.3	$0.039 \pm 0.002$	$0.100 \pm 0.012$	-10 V	-
31.7	41.2	1.3	$0.048 \pm 0.002$	$0.121 \pm 0.017$	+15 V	-
40.0	44.0	1.1	$0.059 \pm 0.008$	$0.122 \pm 0.011$	+15 V	1 k $\Omega$
51.0	56.2	1.1	$0.035 \pm 0.005$	$0.096 \pm 0.0032$	+10 V	-
62.3	69.2	1.1	$0.023 \pm 0.002$	$0.0601 \pm 0.019$	+7 V	24 k $\Omega$
82.4	98.9	1.2	$0.016 \pm 0.009$	$0.095 \pm 0.01$	+7 V	19 k $\Omega$
89.7	117	1.3	$0.020 \pm 0.001$	$0.064 \pm 0.007$	-10 V	-
151	166	1.1	$0.0056 \pm 0.0004$	$0.011 \pm 0.0022$	-23 V	-

<sup>a</sup> as spun from hot 1,2-dichlorobenzene; <sup>b</sup> at 180°C for 20 min under argon



Overall, the transistors prepared with our low MW PBTTT (5.8 kDa to 13.5 kDa) are characterized by low current (saturating at about 20  $\mu\text{A}$  for a device  $W/L = 500$ ) compared to higher molecular weight (typically saturating at more than 1 mA  $W/L = 500$ ). This suggests a large resistance to charge transport in the film. Also, positive threshold voltages of +18 V and relatively poor  $I_{\text{on}}/I_{\text{off}}$  ratios of  $10^2$  (5.8 kDa) and  $10^4$  (13.5 kDa) are noted with low MW samples. Regardless of thermal treatment we found  $\mu_{\text{FET}}$  to increase with MW up to a maximum at about  $M_n = 40$  kDa. In comparison to rr-P3HT, Stingelin and co-workers recently summarized literature reports and show for the most part that  $\mu_{\text{FET}}$  is independent for  $M_n > 25$  kDa up to about 90 kDa.<sup>[25]</sup> In contrast to these reports with rr-P3HT, we observe seemingly more complex behavior with our PBTTT fractions in this work. While we do find a decrease in  $\mu_{\text{FET}}$  as chain length is increased from the optimum of around 40 kDa, this decrease first occurs relatively quickly with increasing  $M_n$ . The average  $\mu_{\text{FET}}$  exhibited by the TFT prepared with 51.0 kDa PBTTT show a 21% decrease from the average value of the 31.7 and 40.0 kDa fractions, and the 62.3 kDa fraction decreased by a factor of 2. In addition, we observed more variation in device performance at this molecular weight. As the  $M_n$  further increased from ca. 60 to ca. 90 kDa  $\mu_{\text{FET}}$  remained approximately constant with an increased statistical variation compared to the lower molecular weights. Interestingly, we measured  $\mu_{\text{FET}}$  up to  $0.14 \text{ cm}^2 \text{ V}^{-1} \text{ s}^{-1}$  for the best single device prepared with the 82.4 kDa fraction, while the average was just under  $0.1 \text{ cm}^2 \text{ V}^{-1} \text{ s}^{-1}$ . Finally, for the highest  $M_n$  fraction, a factor of 5 decrease in  $\mu_{\text{FET}}$  was observed. For unannealed films the trend observed in the annealed devices is roughly mirrored with  $\mu_{\text{FET}}$  consistently 2-3 times smaller before the annealing step for medium molecular weights. From ca. 60 to ca. 90 kDa the unannealed films showed comparatively lower  $\mu_{\text{FET}}$  and a higher variability was observed similar to the annealed condition.

### 3.2.3 Thin films morphology

In order to gain insight into how the morphology of the films correlates to the observed charge carrier mobility we next examined the topography of the transistor thin-films by atomic force microscopy (AFM). We note that while AFM only measures the surface morphology, and not the buried dielectric/polymer interface where the charge transport generally occurs, strong correlations between surface morphology and charge transport are routinely observed.<sup>[5b]</sup> In combination with other characterization techniques, AFM is undoubtedly a powerful tool to gain insights into thin film morphology. Overall we observed three distinct morphologies. For the low molecular weight fractions (5.8–13.5 kDa), tapping mode micrographs reveal the existence of well-defined fibril-like structures which are on the order of 1  $\mu\text{m}$  in length and anisotropically oriented onto the substrate (Figure 3-5a). Previous studies on rr-P3HT

and PBTTT suggest that polymer chains in this fibril-like structure are highly ordered along their growth direction through  $\pi$ - $\pi$  stacking.<sup>[28]</sup> Interestingly, we found that the diameter of the fibers was constant across the film and varied with  $M_n$ . For the 5.8 kDa fraction the peak-to-peak distance on the height trace was found to be roughly 35 nm while the 13.5 kDa fraction showed a distance of 50 nm. Given the reported<sup>[61]</sup> repeat unit length of 1.33 nm, this corresponds to polymer chains with degrees of polymerization,  $n = 26$  and  $38$  for the 5.8 kDa and 13.5 kDa samples, respectively, assuming a single polymer chain extends the full distance of the fiber diameter (as has been established by Brinkmann and Rannou for rr-P3HT)<sup>[27a]</sup>.

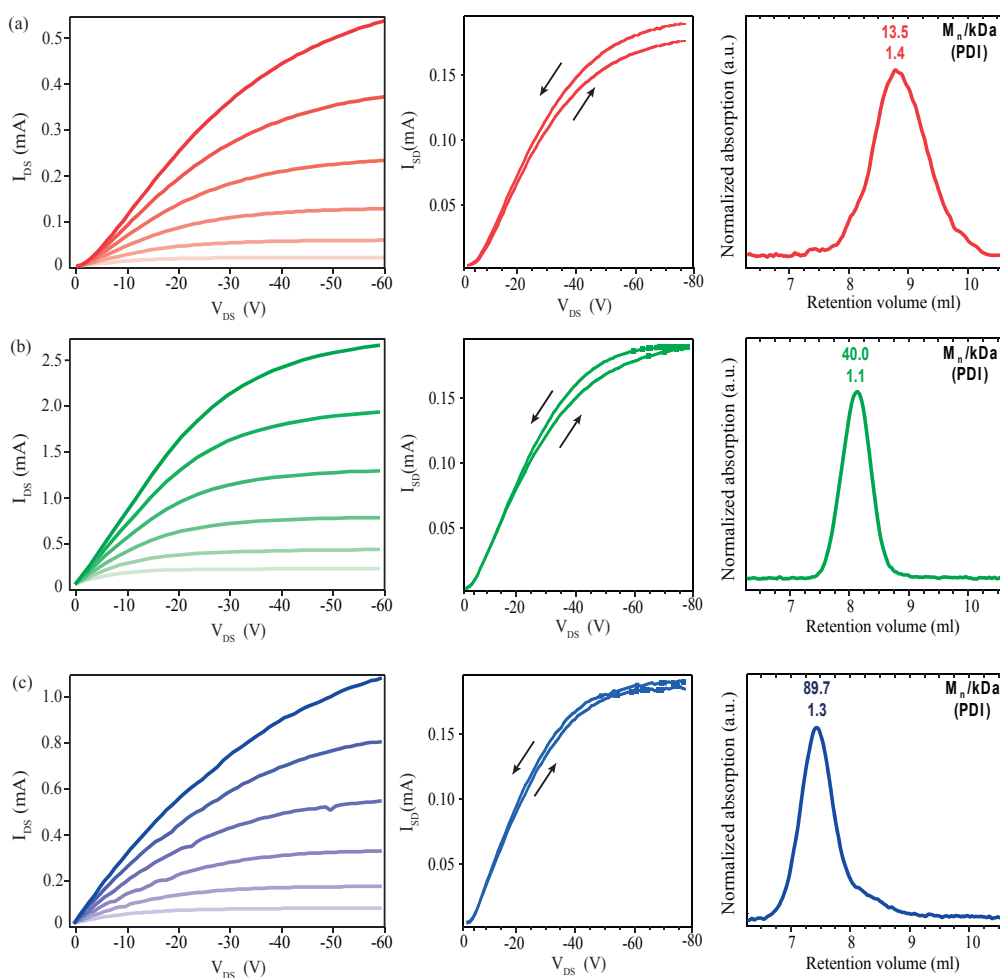


**Figure 3-4.** Typical output curves (left row) and hysteresis curves measured at  $V_g = -10$  V (central row) as a function of the molecular weight fractions reported in the GPC traces (right row).

However, the number average degree of polymerization based on the SEC data (with a correction factor of 1.5), is only 6 or 14, respectively, for the two samples. To rationalize this discrepancy, we suggest that the diameter could be strongly influenced by the longest polymer chains in each sample. Indeed, the 5.8 kDa fraction does include ca. 1% of polymer chains with a degree of polymerization of 26 or higher based on the SEC trace. These chains would have a length similar to the observed diameter. Our attempts to further support this claim with the 8.8 kDa, PDI 1.1 sample were unsuccessful as this sample had such a strong tendency to form large, discontinuous crystalline domains on the OTS-treated substrate, that neither AFM imaging nor  $\mu_{FET}$  measurement were possible. In addition we note that the area between fibers of this type may include some amorphous material that would cause an overestimation of the crystalline domain width. Nevertheless our observations of the different behavior of the 5.8kDa and the 8.8kDa samples does suggest that a small fraction of higher molecular weight polymer chains (>8.8 kDa) can drastically affect the film formation, morphology and TFT performance. However, despite the highly ordered appearance of the fiber morphology, and the indicated ability to control the fiber size by varying the molecular weight, this morphology is known to exhibit poor charge carrier mobility due to the high density of grain boundaries that hinder charge hopping between the fibrils. It is commonly conjectured that it is not until the chains are long enough to link crystal domains that the charge carrier mobility attains the best values. Indeed, as the chain length increases we observe the “terraced” morphology consistent with previous reports. Fractions with  $M_n$  of 20–50 kDa showed this morphology (Figure 3-5b) where the step height observed (2 nm) matches well the reported  $d_{100}$  spacing of 1.96 nm.<sup>[5b]</sup> Interestingly, the morphology of thin-films prepared with the 22.3 kDa fraction shows hints of fibers suggesting that this  $M_n$  represents a transitional length from fibers to terraces. As previously mentioned, the ability of PBTTT to form these highly ordered terraced structures has been considered to be the origin of the observed high charge carrier mobility.<sup>[4]</sup> Indeed the maximum  $\mu_{FET}$  we found was in these medium molecular weight fractions (30–40 kDa). We found that the terraced domain size is apparently not dependent on the length of polymer chain. This is expected considering that the size of the terraced domains is typically significantly larger than the length of a polymer chain (a 30 kDa PBTTT chain would be about 40 nm in length, fully extended assuming a SEC correction factor of 1.5). Nevertheless, the terraced domain size has been shown to be influenced by processing conditions.<sup>[14b]</sup> We found terraces to only exist for a narrow range of molecular weight (30–50  $M_n$ ), and at  $M_n$  equal to 60 kDa or greater we did not observe regular steps in the micrographs even in the annealed films. Rather a rough surface is found with a range of feature sizes of 10–100 nm that is similar to what has been observed for high molecular weight films of rr-P3HT. This is best seen in Figure 3-5c for the 89.7 kDa polymer. Smoother films (but still without terraces) were observed for the 62.3 kDa material,

again suggesting another transition point. Indeed, more variation in transistor performance at this molecular weight was observed.<sup>[14c]</sup>

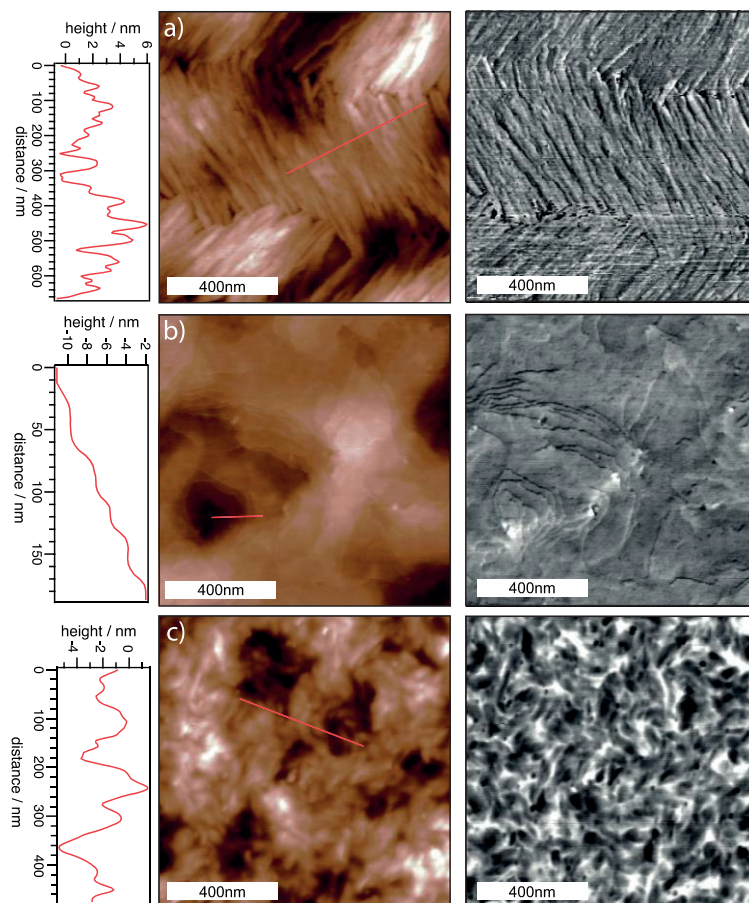


**Figure 3-5.** Atomic force microscopy height (left) and phase (right) images in tapping-mode of the surface morphology of spin-cast thin films of (a) 5.8 kDa, (b) 40.0 kDa and (c) 89.7 kDa. The respective cross sections provide information about a) the width of the fibrils b) the 2 nm step-height of single terraces and c) the disappearance of terrace-like structures at high MW.

Moreover, we note a good correlation of the disappearance of the terrace morphology and the decrease in  $\mu_{FET}$  from the highest average values around 40 kDa to values twice lower at 62 kDa. To differentiate between the intrinsic ability to form the terrace morphology and a possible kinetic constraint to lamellar organization, we increased the annealing time by a factor of 10 for the 89.7 kDa fraction and no increase

in  $\mu_{FET}$  or terrace formation was seen. Taken together these observations suggest that a film made from chains with molecular weight greater than 60 kDa (corresponding to a degree of polymerization of 60, or a polymer length of ca. 80 nm, assuming a SEC correction factor of 1.5) is sufficiently entangled to inhibit large-scale lamellar ordering. This molecular weight is more than the ca. 30–40 kDa entanglement molecular weight implied by results reported with rr-P3HT,<sup>[25]</sup> as expected given the increased rigidity of the chain.

### 3.2.4 Thermal characterization

In order to further support the claim that PBTTT samples above 60 kDa are inhibited from large-scale lamellar ordering by entanglement, and to gain further insight into the link between molecular weight and morphology, we performed a thermal analysis by differential scanning calorimetry (DSC) of polymer fractions from each of the three regions. The second heating and cooling curves are shown in Figure 3-6 for the 5.8 kDa, 13.5 kDa, 31.7 kDa and 89.7 kDa fractions.

**Table 3-2.** Transition temperatures and specific enthalpies of the critical points observed in the second cycle DSC scans. Subscripts “m” and “c” signify melting and crystallization, respectively.

$M_n$ (kDa)	$T_{1,m}$ (°C)	$\Delta$ $H_{1,m}$	$T_{2,m}$ (°C)	$\Delta H_{2,m}$ (J g <sup>-1</sup> )	$T_{1,c}$ (°C)	$\Delta H_{1,c}$ (J g <sup>-1</sup> )	$T_{2,c}$ (°C)	$\Delta H_{2,c}$ (J g <sup>-1</sup> )
5.8	153	1.	--	--	135	-2.1	--	--
13.5	184	5.	--	--	205	-12.1	126	-3.8
31.7	163	8.	247	11.0	120	-7.3	238	-8.8
89.7	167	4.	259	7.5	114	-3.7	240	-8.1

Thermal transitions for the alkyl side chain crystallization ( $T_1$ , around 120°C) and the conjugated backbone crystallization ( $T_2$ , around 240°C) can be clearly identified for the higher molecular weight fractions consistent with previous thermal observations of PBTTT.<sup>[5b, 54a]</sup> The temperatures and specific enthalpies for each transition are given in Table 2. In contrast to the high MW fractions, the low MW fractions exhibited variable behavior. Only one transition for the melting/crystallization of the backbone

was observed for the 5.8 kDa fraction and the 13.5 kDa fraction did not exhibit a clear separation between the two transitions. This suggests that the strength of the  $\pi$ - $\pi$  stacking interaction is strong in the 5.8 kDa polymer and that the backbone alone drive crystallization.

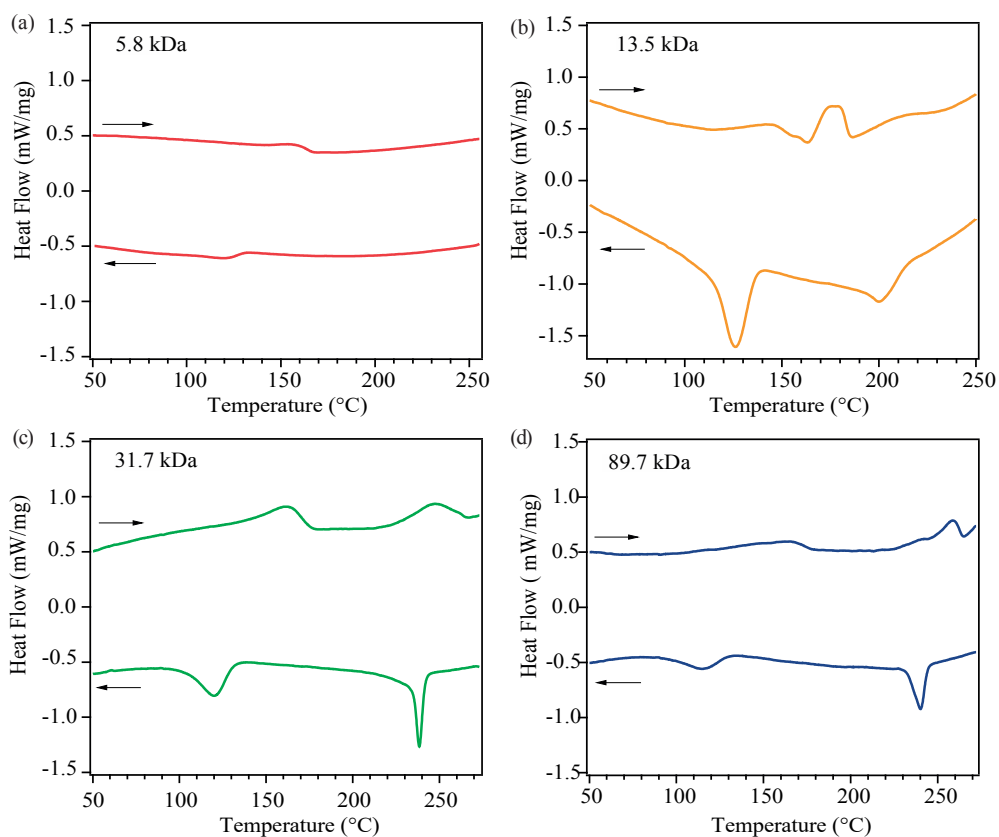


**Figure 3-6.** DSC second heating and cooling thermograms measured at 20 °C/min as a function of drop-cast PBTBT films as a function of MW. Scans have been baseline corrected and offset for clarity.

For the 13.5 kDa fraction, the backbone and side chain crystallizations are well-differentiated in the cooling curve but not the heating curve suggesting that the strength of the  $\pi$ - $\pi$  stacking interaction begins to become important at this chain length. At 31.7 kDa the polymer exhibits clear transitions between the backbone and side chain crystallizations in both the melting and cooling curves. We observed an increase in the melting backbone temperature,  $T_{2,m}$  and a large decrease in enthalpy of fusion of the side chains,  $\Delta H_{1,c}$ , with increasing  $M_n$  for these higher molecular weight fractions. This clearly shows that a

decreasingly smaller percentage polymer arranges in a crystalline phase as polymer chain length increases. Moreover, we note that the enthalpy of crystallization of the backbone,  $\Delta H_{2,c}$ , remains more similar for the 31.7 kDa and 89.7 kDa fractions as compared to  $\Delta H_{1,c}$ . This decrease in  $\Delta H_{1,c}$  while  $\Delta H_{2,c}$  remains relatively constant with increasing  $M_n$  suggests that after the backbone crystallizes in the 89.7 kDa polymer, the material is in a conformation that prevents side chain recrystallization to the degree that it is present in the 30.7 kDa polymer. As previously reported for rr-P3HT,<sup>[25]</sup> high MW fractions show both a higher backbone melting temperature and a larger supercooling  $\Delta T$  ( $T_m - T_c$ ) due to the increased driving force required to crystallize entangled chains from the melt. We found the supercooling  $\Delta T_2$  to be 9 °C and 19 °C for the 30.7 and 89.7 kDa fractions, respectively, for the backbone transition and  $\Delta T_1 = 43^\circ\text{C}$  and  $53^\circ\text{C}$  for the side chain transition. This large increase in the supercooling for both thermal transitions further suggests that PBTTT does indeed become entangled at a critical molecular weight lower than 89.7 kDa. While further testing of the mechanical properties, not possible with the amounts of materials obtained in this study, is needed to verify classical polymer entanglement, the morphological results combined with the thermal results are consistent with an increasing degree of entanglement starting at about 60 kDa for PBTTT.

### 3.2.5 Charge transport across grain boundaries in PBTTT

As it is of strong interest to better understand the nature of the formation of the terrace morphology, we proceeded next to test the hypothesis that a specific chain length (from 30–50 kDa) is needed to afford the terrace morphology. To accomplish this, we combined the low  $M_n$  sample (5.8 kDa), which gave the fiber morphology, with varying amounts of a good-performing high MW fraction that did not exhibit terraces (89.7 kDa). In this case one might expect that if terrace formation is driven by the presence of chains long enough to link localized ordered domains, terrace formation could be induced by adding a small number of long chains to a low molecular weight film as long as the fraction of high MW chains was sufficiently small to avoid entanglement. The field-effect charge carrier mobility as a function of the fraction of high  $M_n$  polymer is shown in Figure 3-7. Interestingly, a strong effect on  $\mu_{FET}$  was observed upon combining the 5.8 kDa and the 89.7 kDa fractions. While pure low-MW (5.8 kDa) exhibited mobility around  $5 \times 10^{-4} \text{ cm}^2 \text{ V}^{-1}\text{s}^{-1}$ , as soon as 5% of high molecular weight chains were introduced in the spin-coating solution, the charge carrier mobility increased 2 orders of magnitude (to as high as  $0.12 \text{ cm}^2 \text{ V}^{-1}\text{s}^{-1}$  for a single device). Further increase in the fraction of long chains showed no additional increase in charge carrier mobility. At a 1:1 ratio a slight decrease in average transistor mobility over the 5% case is noted. Overall the 5% blended thin film gave a higher average mobility than the 89.7

kDa polymer alone suggesting that a morphology better suited for charge transport exists at this condition. AFM analysis of the thin film topography (Figure 3-7) does not, however, indicate that terraced features are present. Rather a rough morphology is found that resembles more closely the morphology of the 89.7 kDa fraction. Upon close inspection of this morphology, we observe the suggestions of fibers of a similar diameter to the pure 5.8 kDa film that are randomly oriented and seem to be embedded in a matrix. While this faintly suggests a hybrid morphology that combines aspects of the two component polymers, a few more concrete conclusions can be stated based on these observations. The first important aspect of the blending procedure is the improvement of the processability of the film. The low molecular weight fractions were consistently affected by rapid aggregation responsible for making inhomogeneous films. However, adding only a small % of the high MW fraction it becomes possible to have a continuous and homogenous film suitable for long-range charge transport. Indeed, a device prepared with the 8.8 kDa + 5wt% 89.7 kDa showed an average  $\mu_{FET}$  of  $0.08 \text{ cm}^2 \text{ V}^{-1}\text{s}^{-1}$ . This is in contrast to the neat 8.8 kDa film which was not measurable. Moreover, we note that since the 5.8 kDa fraction includes a significant amount of oligomer chains, but still attains high  $\mu_{FET}$  when blended with a small amount of the high MW polymer, we can conclude that the presence of these oligomers does not fundamentally limit the charge transport. Because the low MW samples exhibit a better solubility, this blending strategy suggests that the environmentally unfavorable chlorinated aromatic solvents typically used to process PBTTT and similar materials can be reduced or even eliminated. Indeed, preliminary solution-processed devices spin cast out of THF:5% chlorobenzene and THF only exhibited hole mobilities respectively of  $0.055 \text{ cm}^2 \text{ V}^{-1}\text{s}^{-1}$  ( AFM image in Figure 3-7c) and  $0.016 \text{ cm}^2 \text{ V}^{-1}\text{s}^{-1}$  with the 8.8 kDa + 5wt% 89.7 kDa blend.

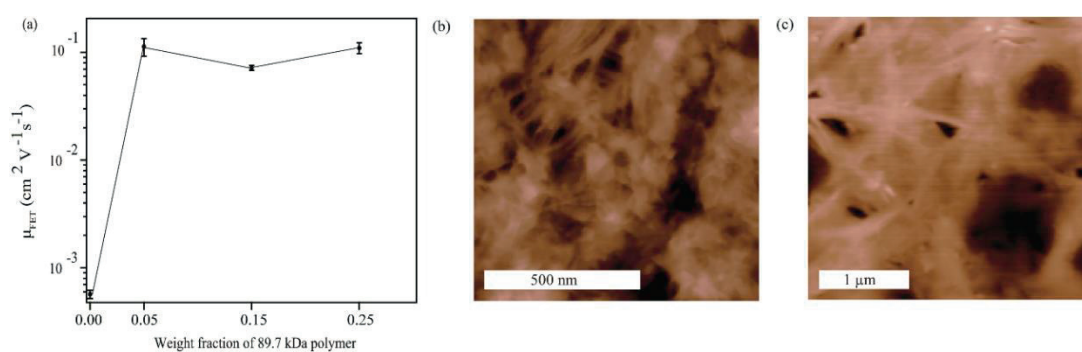


**Figure 3-7.** (a) Average extracted (saturation regime) field-effect charge carrier mobility,  $\mu_{FET}$ , of annealed (180 °C, 20 min) PBTTT fractions as a function of weight fraction of high MW polymer chains in the blend with 5.8 kDa. Error bars corresponding to one standard deviation on multiple devices are



also shown. (b) Tapping-mode atomic force microscopy of spin cast films of 5% high MW blend and (c) tapping-mode atomic force microscopy of spin cast films of 8.8 kDa with 5% high MW blend.

More importantly, the fact that only a small amount of the 89.7 kDa polymer needs to be added to the 5.8 kDa film to drastically improve the mobility strongly reinforces the notion that the charge carrier mobility of the low  $M_n$  films exhibiting the fiber morphology are indeed limited by grain boundaries. Finally, as reasonably high charge carrier mobility was obtained with the blending approach and no terraces were observed, it suggests that the planar orientation of the  $\pi$ - $\pi$  stacking afforded by the terraced morphology is not necessary to obtain state-of-the-art charge carrier mobility in PBTTT films. Indeed, this is strengthened by the fact that we observed (single device)  $\mu_{FET}$  up to  $0.14 \text{ cm}^2 \text{ V}^{-1}\text{s}^{-1}$  using the (non-terrace-forming) 82.4 kDa fraction. Only slightly higher champion mobility was observed in the best devices that exhibited a terraced morphology ( $0.17 \text{ cm}^2 \text{ V}^{-1}\text{s}^{-1}$ ).

### 3.2.6 Thin films microstructure determination

To further support the view that the planar orientation of the  $\pi$ - $\pi$  stacking is not critical to charge transport, we analyzed the out-of-plane x-ray reflections from thin-films in a grazing incidence geometry and by transmission electron diffraction. As shown in Figure 3-9 for the 2D grazing incidence XRD, all the MW fractions analyzed exhibit a measurable degree of out-of-plane scattering corresponding to lamellar packing (a axis, (h00) diffraction) with side chains preferentially oriented normal to the substrate whereas electron diffraction patterns (Figure 3-10) confirm the  $\pi$ - $\pi$  stacking (b axis, (0k0) diffraction) in the plane of the film. In specular 1D scans (Figure 3-8), the dominating (100) reflection was found at a value of the scattering vector,  $q$ , from  $3.26$ – $3.42 \text{ nm}^{-1}$  corresponding to a  $d$ -spacing of  $1.84$ – $1.93 \text{ nm}$ , which is similar to the value of  $1.92 \text{ nm}$  reported previously.<sup>[15]</sup> Interestingly we found this value to change significantly with MW as seen by the shift in the h00 reflections (Figure 3-8b, normalized curves). Fitting the positions of the 100, 200, and 300 reflections gives the  $d$ -spacing as  $1.87 \pm 0.01$ ,  $1.85 \pm 0.01$ ,  $1.89 \pm 0.02$ , and  $1.94 \pm 0.01$ , respectively for the 5.8, 13.5, 31.7, and 89.7 kDa fractions. While an increase in  $d$ -spacing has been previously reported with an increase of MW for rr-P3HT,<sup>[13a]</sup> it is surprising to observe this in PBTTT where the interdigitation of the alkyl side chains strongly determines the size of the a-axis lattice constant. For the current case of PBTTT, we observe a statically significant change in the  $d$ -spacing only for the 89.7 kDa fraction where entanglement influences the morphology. We suggest that the increased amount of chain stress caused by the bends and folds implied in an entangled morphology prevents the lattice from reaching its minimum energy in the a-axis direction. This is well supported by the decrease in  $\Delta H_{1,c}$  for the 89.7 kDa fraction as compared to the 31.7 kDa polymer.

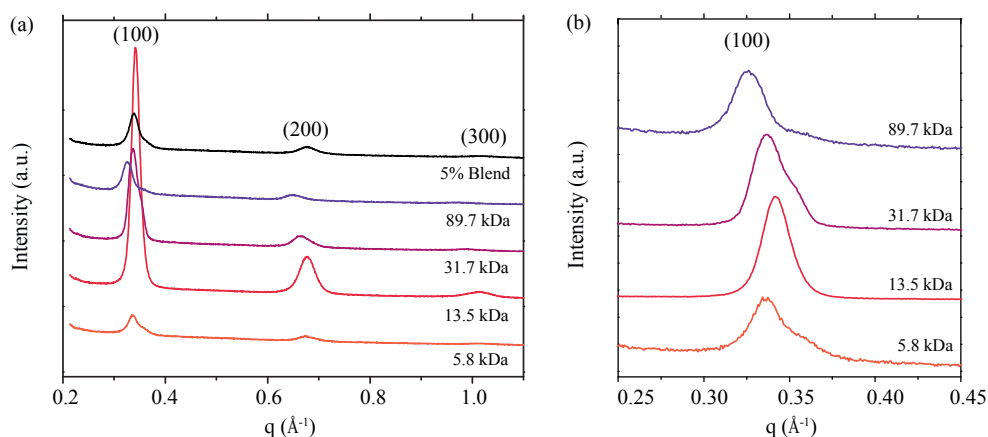


**Figure 3-8.** (a) Out of plane grazing-incidence x-ray diffractograms are shown as a function of the scattering vector,  $q$ , for different molecular weight PBTBT and the 5wt% blend of 89.7 kDa chains in 5.8 kDa. (b) Normalized 100 reflections overlaid to compare the peak positions.

While this may not have a great effect on the  $\mu_{FET}$  as the backbone crystallization appears less affected according to the DSC results and charges are not preferred to transport in this direction, the measurement of the  $d$ -spacing may be a suitable method for identifying the presence of an entangled morphology. In addition, given the uniform film thickness employed between samples, the intensities of the  $h00$  reflections, together with the DSC results can give additional insight into the relative orientation of crystalline domains in the thin-films. In the specular scans (Figure 3-8), an overall decrease in the out-of-plane reflection intensity for the (100) reflection is observed from 13.5 kDa to 89.7 kDa and is attributed to the loss of registration in lamellar structures that are observed both in fiber-like and terrace-like morphologies, and is consistent with the changing magnitude of  $\Delta H_{1,c}$ . The comparatively low intensity peak registered for the 5.8 kDa fraction is consistent with the DSC results as well, however the poor overall crystallinity of this fraction is surprising, and cannot be attributed to impurities, given the results of the blending experiment. More interestingly, the 13.5 kDa polymer gave the most intense reflection even though the  $\mu_{FET}$  exhibited by this fraction was 3 times less than terrace-forming fractions. This accords with the DSC results, which show the largest  $\Delta H_{1,c}$  for this fraction, and further reinforces the notion that a high degree of  $\pi$ - $\pi$  stacking in the direction of charge transport is not the only requirement for attaining the best charge carrier mobility.<sup>[62]</sup> Indeed, the terrace-forming 31.7 kDa fraction has a weaker (100) reflection but a showed a higher  $\mu_{FET}$ . The origin of the shoulder observed most strongly

on this fraction is not known, but asymmetric reflections have been observed before to a lesser extent.<sup>[14b, 15]</sup> Since this shoulder clearly occurs for other fractions, it cannot solely be attributed to the terraced morphology.

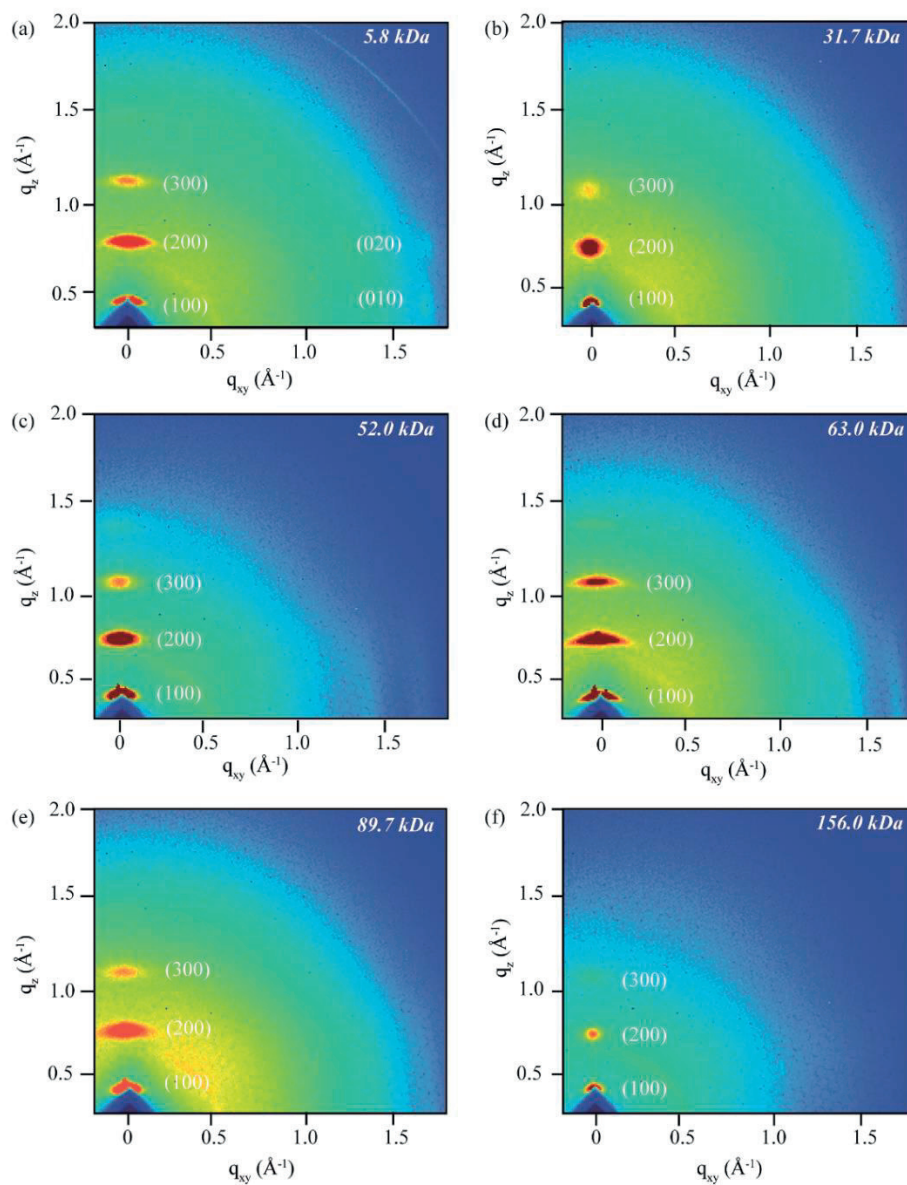


**Figure 3-9.** 2D-detector images of grazing-incidence x-ray diffraction of (a) 5.8 kDa, (b) 40.0 kDa, (c) 52.0 kDa, (d) 63.0 kDa, (e) 89.7 kDa and (f) 156 kDa films. Out of plane diffractions are displayed as a function of the scattering vector,  $q_z$ , and in plane diffractions in  $q_{xy}$ . In plane reflections resulted to be too weak to allow quantitative evaluation of molecular order along the  $\pi$ - $\pi$  stacking direction.

The fraction exhibiting an entangled morphology, shows a further decrease in the (100) reflection, similar to what has been shown by McGehee and coworkers for rr-P3HT,<sup>[14b]</sup> and only a slight increase is observed over the 5.8 kDa + 5wt% 89.7 kDa blend film suggesting that no drastic changes in ordering occurs upon the blending of these two disparate fractions. 2D-GIXD images (Figure 3-9a and Figure 3-9b) show in low MW thin films hints of in-plane diffraction that are attributed in PBTTT to  $\pi$ - $\pi$  stacking motif. However, the low intensity of (0k0) diffractions makes possible quantitative estimations difficult. Instead, the intensity of the 010 reflections as measured by the electron diffraction (Figure 3-10) corresponding to backbone  $\pi$ -stacking support the conclusions drawn by the XRD as they are strongly dependent upon MW. Both 13.5 kDa and 31.7 kDa showed narrow and intense isotropic scattering rings which confirm that both fibrils and terraced structures exhibit strong  $\pi$ - $\pi$  stacking. The weak scattering rings observed for the 89.7 kDa film clearly indicate the lower amount of in-plane  $\pi$ - $\pi$  stacking present in the entangled film. This observation, combined with the fact that the 89.7 kDa and 31.7 kDa fractions showed a similar  $\Delta H_{2,c}$  (suggesting the overall amount of  $\pi$ - $\pi$  stacking present is similar) further suggests that while the entanglement does prevent terrace formation, and the general alignment of polymer domains, it does not change greatly the amount of  $\pi$ - $\pi$  stacking. The electron diffraction pattern for 5.8 kDa PBTTT shows a clear anisotropy in the 010 reflection which is in agreement with the high degree of alignment that the fibers showed in the AFM images. This degree of anisotropy is lost in the 5% blend with high MW polymer chains while a slightly higher intensity of the reflections is observed as in the case of the out of plane peaks. The relatively small amount of in-plane  $\pi$ - $\pi$  stacking observed in the 89.7 kDa film but the reasonable charge carrier mobility observed at this MW together with the results from blending the 5.8 kDa fraction with the high MW suggest that terrace formation and in-plane alignment are not as important as the interconnectivity afforded by the use of long polymer chains in obtaining high performance transistors of PBTTT.

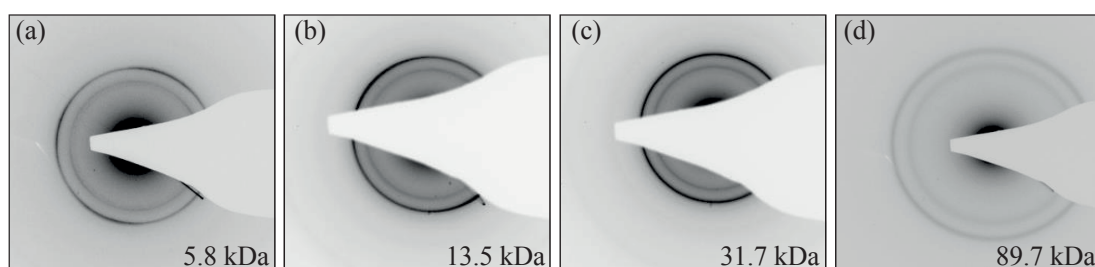


**Figure 3-10.** Transmission electron microscopy diffraction patterns of PBTTT thin films as a function of molecular weight.

Overall our results give important insight into the terrace morphology observed in PBTTT. The formation of the terraced morphology can be viewed as a subtle interplay between the backbone and side chain crystallizations. The weak  $\pi$ - $\pi$  stacking interactions in fiber-forming PBTTT cause the chains to enter a liquid-crystalline state and rearrange to a nematic state when annealing the polymer at 180°C. However, in terrace-forming PBTTT, annealing at 180°C is not sufficient to melt the backbone and the polymer morphology is driven by  $\pi$ - $\pi$  stacking interactions and large terraces can form through the interconnection of local domains. The influence of the substrate,<sup>[63]</sup> and the ability of the polymer chains to retain sufficient physical mobility are most likely factors that also need to be taken into consideration in this kind of studies. While it is known that long-range ordering of the  $\pi$ - $\pi$  stacking domains is not present in this morphology, charge transport can still be facilitated by the fact that the backbones are all in the same plane. In contrast, at  $M_n$  greater than 60 kDa, entanglement restricts polymer movement during the annealing preventing in-plane ordering and increases the a-axis packing distance. However, this does not drastically affect the overall  $\mu_{FET}$  as the amount of  $\pi$ - $\pi$  remains similar and interconnectivity between domains remains high. Indeed this final observation provides a plausible explanation for the complex behavior of  $\mu_{FET}$  for PBTTT with  $M_n$  from 40-150 kDa: as the MW increases and terrace formation is no longer accessible due to polymer entanglement,  $\mu_{FET}$  decreases due to a decrease in in-plane alignment and a decreased density of crystal packing. However as the polymer chain length increases after terrace formation disappears, an increase in  $\mu_{FET}$  could be expected as the connectivity between crystalline domains improves due to the presence of longer chains. Finally, at increasingly high molecular weight, processing becomes a difficulty as solubility (even in hot dichlorobenzene) becomes the limiting factor. Indeed we found the 151 kDa fraction to crash out of solution only seconds after heating was removed from the vial containing the mixture. This caused poor film formation with the inclusion of aggregates which most likely were formed as the solution cooled during the early stages of the spin coating.<sup>[14c]</sup>

### 3.3 Conclusions

Overall this study shows that precisely varying the molecular weight of a rigid-backbone conjugated polymer with interdigitating side chains has a large effect on the material characteristics and allows the control over the morphology adopted by the polymer in a thin film. Thin film transistor performance data were combined with microstructure and morphological characterization to give insight on the evolution of the charge carrier transport mechanism in high-mobility polymeric semiconductors as a function of molecular weight. Three distinct regions were observed. For medium  $M_n$  material around 30–40

kDa the most reproducibly high  $\mu_{FET}$  was observed, corresponding to clear long-range ordering in the thin films by way of terrace-like structures as observed by AFM. For smaller  $M_n$ , an increased crystallinity of the polymer in the thin film was observed, corresponding to a fiber morphology as seen by AFM. However, the  $\mu_{FET}$  was lower in these fractions presumably due to poor interconnectivity of the crystalline domains. In contrast, MW higher than the optimum range showed significantly less side-chain crystallinity and no terrace formation most likely due to polymer chain entanglement. A  $M_n$  of around 60 kDa was identified as the critical MW for entanglement. Despite this, reasonably high  $\mu_{FET}$  was observed in fractions of ca. 80 kDa suggesting that a balance between domain connectivity and polymer processability is a crucial issue. This strongly supports the view that the interconnectivity of polymer domains is the most important factor for high charge carrier mobility in polymer transistors. With this we can conclude that while the self-assembly observed in the terrace formation clearly promotes good long-range carrier transport for medium  $M_n$  PBTTT (30–40 kDa), the terrace formation itself is not critical for obtaining good transistor performance as long as good interconnectivity is obtained. In addition, the drastic increase in  $\mu_{FET}$  observed by blending 5% of a high MW polymer into a low MW fraction was found to further support our aforementioned conclusions and suggests a novel route to easily increase the processability and transistor performance of low MW conjugated polymeric or oligomeric semiconductors. As the synthesis and solubility of MW weight conjugated materials is an important factor limiting the application of these materials, the strategy of using only a small amount of long chains to facilitate the interconnectivity of crystalline domains will likely be a viable route to increase the applicability of these materials. Ultimately, blending different MW fractions could potentially be a new strategy to affect mechanical properties of the overall films, as discussed in the introductory chapter, while preserving transport properties.

# Chapter 4

## The effect of MW on morphology and charge carrier mobility in diketopyrrolo-pyrrole based polymer

### 4.1 Introduction

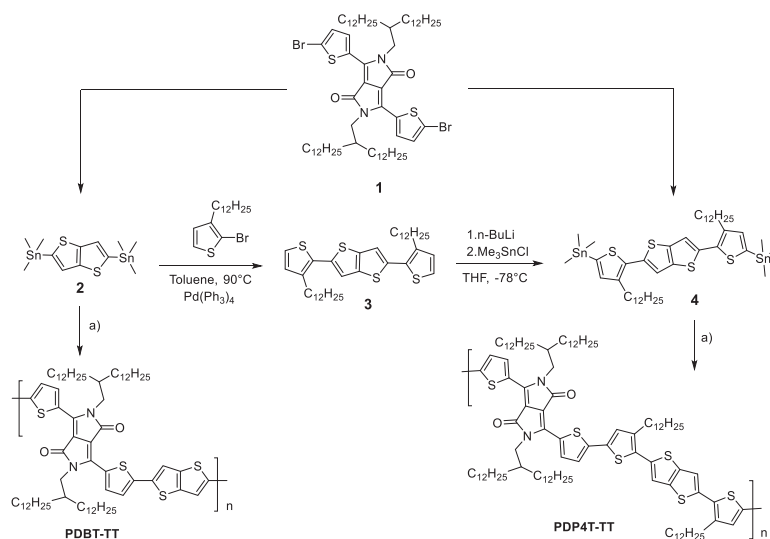
In the introductory chapter, the family of donor-acceptor alternating copolymers has been briefly presented in merit to their outstanding performance in organic field-effect transistors (OFETs) and organic photovoltaics (OPV). In a this new generation of semiconducting polymers often lacks the significant long-range solid-state crystallinity (based on  $\pi$ -stacking interactions) reported in poly-bithiophene-thienothiophene (coded PBTTT)<sup>[14a]</sup> in Chapter 3. In previous reports, an increased backbone rigidity has been identified as a reasonable explanation for superior semiconducting performance despite the lack of crystallinity.<sup>[19]</sup> Indeed, recent studies on this new class of polymers suggest that in absence of extended  $\pi$ -stacking motifs in the solid state, charge transport occurs mostly uni-dimensionally along the highly rigid conjugated backbone with occasional intermolecular hopping through sparse  $\pi$ -linkages present in stacked aggregates.<sup>[19, 64]</sup> This charge transport mechanism implies a significant importance of the effect of polymer chain length (as characterized by the polymer chain molecular weight) on the semiconducting performance. However, the study of the effect of the polymer molecular weight and molecular weight distribution (polydispersity index, PDI) is confounded by the step-growth polymerization used, which leads to variable MWs and PDIs often over 2 implying a wide variation of chain lengths in a single polymer sample. Indeed while much is now known regarding the effects of MW and PDI on PBTTT,<sup>[14c, 65]</sup> much less is known about the new class of push-pull polymers. A few studies have shown a vague relationship between MW and semiconductor performance which suggests that higher MW leads to leads to increased charge carrier mobility and performance in photovoltaic devices.<sup>[55, 66]</sup> However, the high PDIs and relatively low range of MWs investigated (Typically up to a number average molecular weight,  $M_n$ , of about 50 to 80 kDa) renders possible considerations on MW weaker due to the considerable overlap among each MW distributions. Moreover it is not known whether the effects of chain entanglement<sup>[14c, 67]</sup> are important for the highest molecular weight chains. In this respect, systematic studies like reported for rr-P3HT and PBTTT, are needed to better elucidate

the effects of MW and PDI on the semiconducting properties of this new class of polymers. In this chapter, we employ standard Stille coupling polymerizations and subsequent MW fractionation by preparative gel permeation chromatography to precisely characterize the effect of MW on the properties of two rigid backbone diketopyrrolopyrrole–thienothiophene copolymers, coded PDBT-TT and PDPP4T-TT. We isolate fractions ranging from  $M_n$  of 6 kDa to 160 kDa with extremely low polydispersity (PDI < 1.3) and characterize the fractions optoelectronic properties, thin film molecular packing behavior, and charge carrier mobility.

## 4.2 Results and discussion

### 4.2.1 Synthesis and MW fractionation

Scheme 4-1 shows the chemical structures and the synthetic route to the studied polymers. Long and branched alkyl chains (1-bromo-2-decyltetradecane) were used to insure high solubility and high MW. The corresponding stannylated thienothiophene **2** was coupled by Stille coupling with 2-bromo, 3-dodecyl thiophene to obtain **3** with a 50% yield. Subsequent stannylation of **3** with trimethyl tin chloride yields **4** as a yellow solid. PDBT-TT was obtained by Stille coupling based polymerization of **1** and **2** using  $\text{Pd}_2(\text{dba})_3$  as catalyst while PDP4T-TT was obtained under the same reaction conditions using **1** and **4**.



**Scheme 4-1.** Synthesis of PDBT-TT and PDP4T-TT polymers and related monomers. a)  $\text{Pd}_2(\text{dba})_3$ , chlorobenzene, 100°C, 24h.



As shown in the analytical GPC traces in Figure 4-1 (grey line), initial crude batches of PDBT-TT and PDPP4T-TT with number-average molecular weights of respectively  $M_n = 65.6$  kDa (PDI= 1.9) and  $M_n = 25.5$  kDa (PDI = 2.4) were obtained. The Stille coupling based step-growth polymerization used to obtain these polymers produced batches with extremely high polydispersity indexes as expected. To access a range of samples with variable  $M_n$  and a low PDI we employed preparatory size exclusion chromatography (Prep-SEC) which affords the separation of polymer chains based on their characteristic hydrodynamic volume in solution. To avoid aggregation and precipitation of longer polymer chains inside the column, the prep-SEC system was maintained at a relatively high temperature (80 °C), and low concentration of polymer was used in the mobile phase (chlorobenzene). As common practice the molecular weights are calculated through a calibration curve based on poly(styrene) standards. Starting from initial crude batches with PDI of about 2.0 it was possible to isolate fractions in quantities in the milligram range with  $M_n$  ranging from 9 to 160 kDa and a narrow PDI (typically 1.1–1.3) as shown in representative analytical SEC traces (Figure 4-1). Due to the lower crude MW obtainable in the polymerization of PDPP4T-TT, the highest MW fraction isolated was 70 kDa, while in contrast higher  $M_n$  fractions were accessible for PDBT-TT (up to 160 kDa).

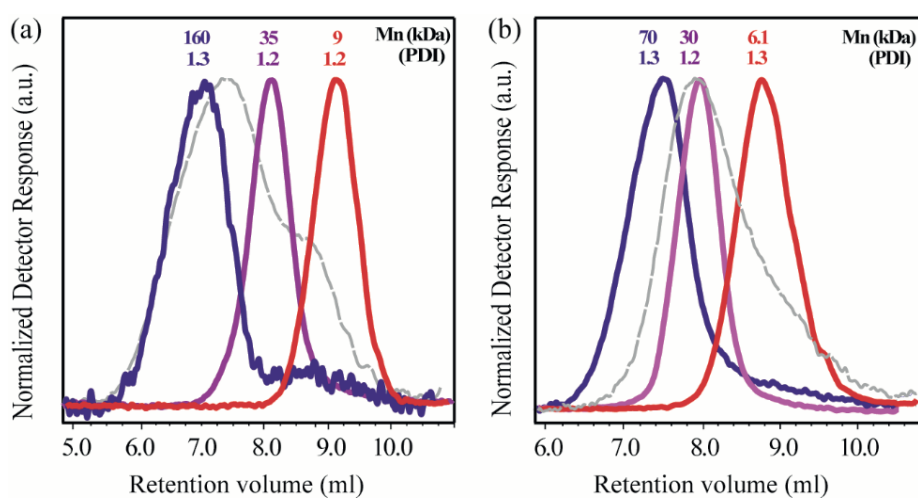


**Figure 4-1.** Analytical size exclusion chromatograms of selected a) PDBT-TT and b) PDPP4T-TT fractions separated by prep-SEC are shown as the normalized detector response versus elution volume of the mobile phase. The grey line represents the crude polymerization chromatograph. The reported  $M_n$  and PDI values for each fraction are versus polystyrene standards. For clarity, not all fractions employed in subsequent analysis are shown here.

The optical absorption spectra of low and high MW fractions of PDBT-TT and PDPP4T-TT in dilute chloroform solution (0.1 mg/ml) and in solid state thin-films (on OTS-functionalized glass) are shown in Figure 4-2. Both polymers show absorption profiles to be dependent on the MW. In particular, low MW PDBT-TT presents two peaks at wavelengths of 690 and 750 nm in the solid state. These peaks are red-shifted to 760 and 820 nm in the high MW fraction and the lower energy peak strengthens in relative intensity. This increase in lower energy absorption is usually attributed to the increase in exciton delocation distance due to physical aggregation of the chains.<sup>[68]</sup> Indeed, this trend is already seen in dilute solution. Whereas the low MW fraction does not show a clear low energy absorption peak in solution (suggesting the absence of aggregation) the low energy peak dominates in the high MW fraction suggesting that 160kDa PDBT-TT forms aggregates in solution which are then carried over into the spin-cast film. At least, the difference in absorption profile between low and high MW PDBT-TT suggest that MW has a drastic influence on the thin film formation and microstructure. In stark contrast, PDPP4T-TT shows only a marginal dependence of its optical properties on MW. More precisely, similar profiles are observed for both low and high MW and only a weak red-shift in the UV-vis absorption spectrum is observed from solution to thin film. However, the appearance of a low-energy peak in the absorption profile in the solid state represents a clear indication of interchain interaction in the thin films.

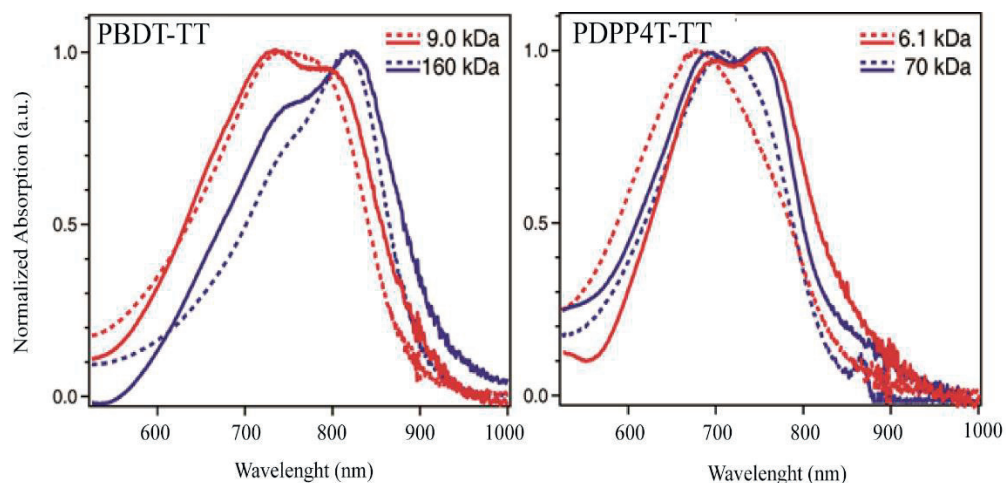


**Figure 4-2.** Normalized UV-vis absorption spectra for PDBT-TT and PDPP4T-TT in chloroform solution (broken lines) in thin film (solid lines) format. The molecular weight of each fraction is indicated.

## 4.2.2 Effect of MW on the charge carrier mobility

To evaluate the charge transport properties in the thin film format as a function of MW, field effect transistors were prepared in the coplanar bottom-contact configuration with an octadecyltrichlorosilane (OTS)-functionalized SiO<sub>2</sub> dielectric by spin coating the polymer solution in chloroform into films with thickness ranging from 50 to 60 nm. After spin-coating, all devices were subsequently examined at room temperature under a nitrogen atmosphere in the as-cast state and after a thermal annealing treatment (180 °C, 20 min, slow cooling). The p-type field effect charge carrier mobility,  $\mu_{\text{FET}}$ , was extracted from the current–voltage data (i.e. the corresponding transfer curves) in the saturation regime. The average measured  $\mu_{\text{FET}}$  (over at least 5 transistors) as a function of  $M_n$  for PDBT-TT and PDPP4T-TT is shown in Figure 4-3 for the thermally annealed films. The charge carrier mobility of our best performing annealed TFTs of PDBT-TT and PDPP4T-TT were found respectively to be up to 0.3 cm<sup>2</sup> V<sup>-1</sup> s<sup>-1</sup> and 0.03 cm<sup>2</sup> V<sup>-1</sup> s<sup>-1</sup>, which is consistent with previous studies and with comparable number-average molecular weights.<sup>[64]</sup> For both polymers we observe a particularly low mobility at extremely low  $M_n$  on the order of 3×10<sup>-4</sup> cm<sup>2</sup> V<sup>-1</sup> s<sup>-1</sup>.

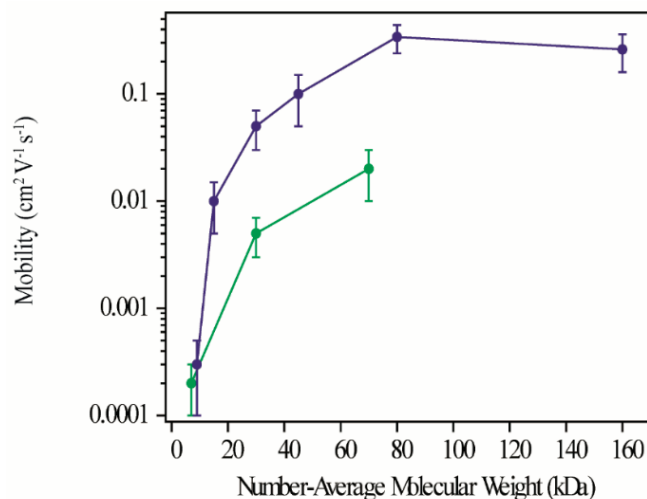


**Figure 4-3.** Average extracted (saturation regime) field-effect charge carrier mobility,  $\mu_{\text{FET}}$ , of annealed (180 °C, 20 min) PDBT-TT (blue continuous line) and PDPP4T-TT (green continuous line) fractions as a function of number-average molecular weight,  $M_n$ . Error bars corresponding to one standard deviation on multiple devices are also shown.

Although charge carrier mobility-molecular weight plots are routinely reported to directly relate electronic behavior with the overall polymeric mass, these plots are not anymore accurate when comparing polymers constituted of extremely different repeating units' molecular mass. In this respect, the overall conjugation length, as a product of degree of polymerization and the length of the conjugated repeating unit, is a more suitable metric, in place of MW, to relate the effective rigid and conjugated chain length with the corresponding charge carrier mobility. The accurate estimation of the true length by GPC is however still problematic due to the ubiquitous use of polystyrene standard as mean for MW calculations.<sup>[57]</sup> In the specific case of the polymers under investigation in this chapter, both the similar rigid nature and hole mobility-MW trend shown in Figure 4-3 still allow a quantitative comparison between PDBT-TT and PDPP4T-TT. An increase in  $M_n$  from 9 kDa to 30 kDa brings an increase in  $\mu_{\text{FET}}$  of two orders of magnitude in PDBT-TT and only one in PDPP4T-TT. The maximum  $\mu_{\text{FET}}$  for PDBT-TT was achieved with the 80 kDa fraction, and further increase of the  $M_n$  did not produce a statistically significant decrease in  $\mu_{\text{FET}}$ , and the charge transport properties can be considered to be essentially constant between 80 and 160 kDa based on our results. PDPP4T-TT generally follows the same trend as PDBT-TT however, the unavailability of fractions with  $M_n$  greater than 70 kDa prevents the observation of any saturation of  $\mu_{\text{FET}}$ . With respect to the thermal annealing (not shown in Figure 4-3) we note a systematic but small increase of  $\mu_{\text{FET}}$  for both polymers. For the 70 kDa PDBT-TT an increase from 0.1 to 0.2  $\text{cm}^2\text{V}^{-1}\text{s}^{-1}$  was observed from the as-cast film after 180°C for 20 min while the PDPP4T-TT increased from 0.01 to 0.03  $\text{cm}^2\text{V}^{-1}\text{s}^{-1}$ . In addition we performed a preliminary investigation of the effects of the PDI. As previously mentioned, similar polymers reported in the literature typically possess much larger polydispersity ( $\text{PDI} > 2$ ), and due to the challenges in directly controlling PDI, the effect of this aspect on the charge carrier mobility is usually overlooked.<sup>[69]</sup> In order to assess the effect of the PDI on the electronic performance compared to the narrow PDI fractions investigated herein, MW fractions with PDI larger than two were produced by combining different MW fractions. Thin film transistors prepared with assembled sample of PDPPBT-TT ( $M_n = 18$  kDa,  $\text{PDI} = 2.2$ ) and PDPP4T-TT ( $M_n = 14$  kDa,  $\text{PDI} = 2.1$ ) were found to exhibit average  $\mu_{\text{FET}}$  of  $6.0 \times 10^{-4} (\pm 3.4 \times 10^{-5})$  and  $2.7 \times 10^{-4} (\pm 2.1 \times 10^{-5}) \text{cm}^2\text{V}^{-1}\text{s}^{-1}$ , respectively.

### 4.2.3 Thin films morphology

In order to gain insight about the relationship between charge carrier mobility and morphology, we examined the topography of the transistor thin films by atomic force microscopy (AFM). Height images for the different MW for PDBT-TT and PDPP4T-TT are shown in Figure 4-4. It worth stating that while

AFM only measures the surface morphology, and not the buried dielectric/polymer interface where the charge transport is known to occur, inferences relating the charge transport to the topography are valuable and commonly drawn in bottom contact transistors. Indeed, similar to the extracted  $\mu_{\text{FET}}$  for the polymers presented here, the thin film morphology is affected by the MW. In contrast to low-MW (< 20 kDa) rr-P3HT and PBTTT, which form well-defined fibrils, the topography of low MW fractions of both DPP-based polymers under investigation here suggest randomly oriented spherical and poorly interconnected aggregates (ca. 200 nm in size, See Figure 4-4a and 4-4d) which give rise to a high surface roughness of the film (RMS roughness of about 5 nm for both films). As the chain length of PDBT-TT increases to 45 kDa (Figure 4-4b), the surface morphology shows hints of fibril formation on the order of 100 nm in length and randomly oriented on the substrate. A decrease in surface roughness from 4.9 nm (for the 12 kDa fraction) to 0.8 nm (45 kDa fraction) is also noted. Further increase in the MW up to 82 kDa (Figure 4-4c), suggests an enhancement in length and width of PDBT-TT fibers (reaching 500 nm in length). Previous studies on rr-P3HT and PBTTT suggest that the polymer chains in similar types of structures are highly ordered driven by  $\pi$ - $\pi$  stacking, and the chain length. The width of the fibers were found to be consistent with the polymer chain length, suggesting chains are fully extended and aligned perpendicular to the fiber axis.<sup>[70]</sup>

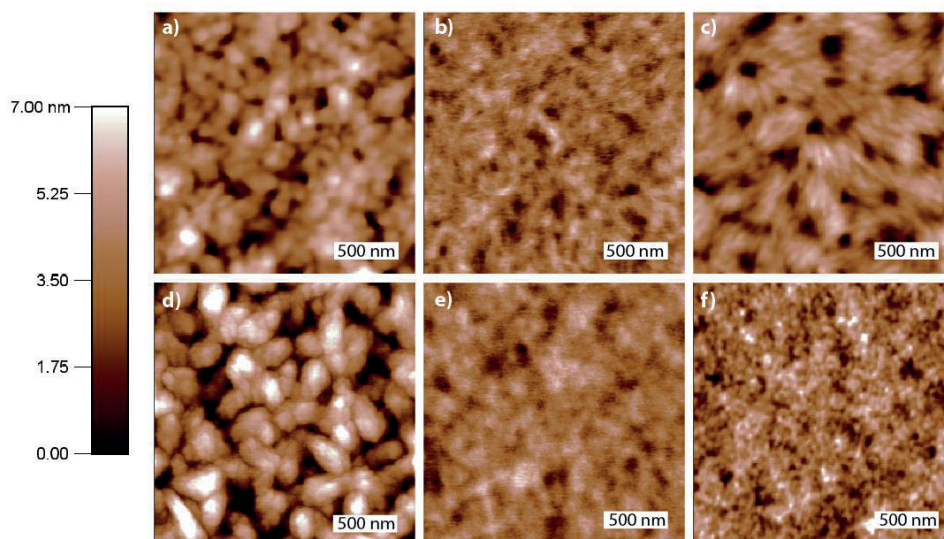


**Figure 4-4.** Tapping-mode atomic force microscopy images of the surface morphology of spin-cast thin films of PDBT-TT of a) 12 kDa b) 45 kDa c) 82 kDa and PDPP4T-TT of d) 6.5 kDa e) 72 kDa

Similarly, the diameter of the PDBT-TT fibers shown in Figure 4-4 is constant across each film but notably varies with  $M_n$ . For the 45 kDa fraction the peak-to-peak distance in the topography data was found to be 35 nm while the 82 kDa fraction showed a distance of 100 nm. The corresponding degree of polymerization of PDBT-TT at 32 kDa and 85 kDa is, respectively,  $n = 27$  and  $n = 72$ . Assuming that a single polymer chain extends the full length of the fiber with a repeating unit of 1.60 nm, it should have a length of 43 nm at 35 kDa and 115 nm at 82 kDa. The discrepancy (10%) between the measured fiber length and the predicted lies within the experimental error in GPC-based calculation of  $M_n$  and AFM tip deconvolution in resolving fine features, and strongly suggests a similar type of self-assembly of the medium and high  $M_n$  PDBT-TT.

#### 4.2.4 Thin films microstructure determination

In contrast to the well-defined features of PDBT-TT, at comparable high  $M_n$  (72 kDa) the PDPP4T-TT polymer reveals no hints of macromolecular organization in the surface morphology (Figure 4-4e). However, since the UV-vis data indicate that ordering over some length scale is reasonably occurring in the PDPP4T-TT, we sought to further characterize the microscopic organization of the polymer films. We analyzed out-of-plane X-ray reflections from thin films in a grazing incidence geometry for both the PDBT-TT and the PDPP4T-TT as a function of  $M_n$ . Interestingly, all PDPP4T-TT fractions and even the low MW fraction of PDBT-TT (9.0 kDa) show no clear scattering in the 2D-GIXD images in the out-of-plane direction (see Figure 4-6), suggesting only weak self-assembly.

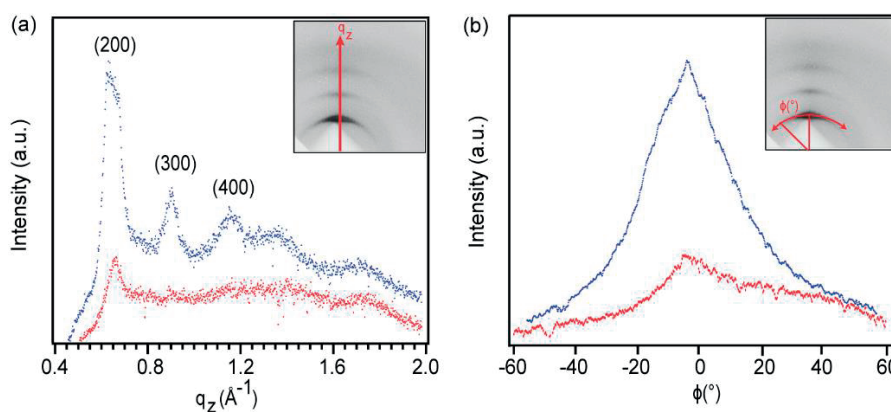


**Figure 4-5.** (a) Specular profiles grazing incidence x-ray diffractograms are shown as a function of the scattering vector  $q_z$ , for PDBT-TT of 30 kDa (red line) and 80 kDa (blue line). (b) Grazing incidence peak arching analysis (Azimuthal cut data) for the (200) peak for PDBT-TT of 30 kDa (red line) and 80 kDa (blue line).

However, clear diffraction was noted for the medium and high  $M_n$  PDBT-TT films. Figure 4-5a reports the out-of-plane scattering for PDBT-TT corresponding to lamellar packing (h00) with side chains preferentially oriented normal to the substrate. The (200) peak was found at a value of the scattering vector,  $q_z$ , of  $0.63 \text{ \AA}^{-1}$  corresponding to a  $d$ -spacing of  $20 \text{ \AA}$ , which is in good agreement with the value previously found by Zhang et al<sup>[71]</sup>. Interestingly, the high MW fraction has a higher degree of crystallinity compared to the medium weight fraction as shown by the strong intensities of (h00) diffractions along the  $q_z$ . Given the non-interdigitating nature of the long branched solubilizing chains, we found no effect of MW on the  $d$ -spacing of as previously reported for PBTTT. In addition we note that the crystal domains in the high MW fraction were better oriented to the substrate compared to the medium MW fraction as suggested by the arc shape of the (200) in the 2D-GIWAX images (see Figure 4-5b for the Azimuthal cut data)

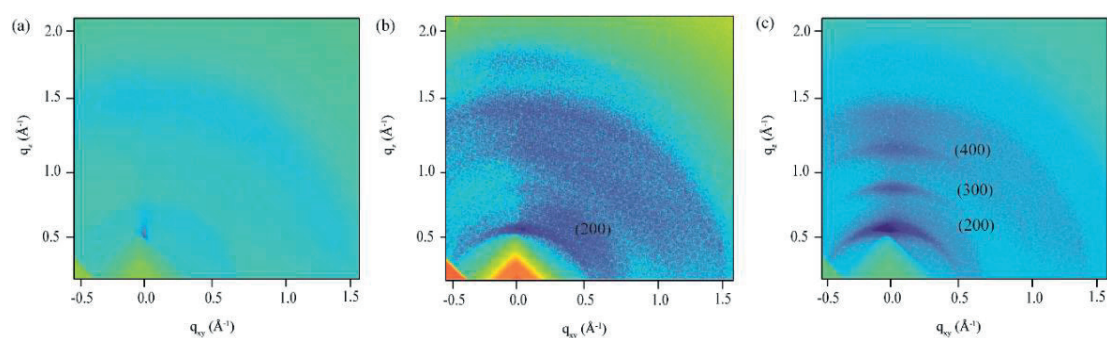


**Figure 4-6.** 2D-GIXD images of PDBT-TT polymer at (a) 9 kDa (b) 35 kDa and (c) 85 kDa.

### 3.2.5 Charge transport across grain boundaries in DPP-based copolymers

Further insight into the role of the different chain lengths on the overall transport properties can be gained by combining low-MW fractions of  $M_n = 9 \text{ kDa}$  and  $M_n = 6.1 \text{ kDa}$  for PDBT-TT and PDPP4T-TT respectively with varying amounts of a high mobility high-MW fraction (70-80 kDa) of the respective polymer. In transistor devices prepared identically to those discussed above, the field-effect charge carrier mobility as a function of the fraction of high- $M_n$  polymer was extracted from the saturation regime, and is shown in Figure 4-7. Interestingly, for both the semicrystalline PDBT-TT and the (presumably) amorphous o PDPP4T-TT an increase of  $\mu_{\text{FET}}$  was observed upon combining the low and high molecular weight in a weight ratio ranging from 5% to 25%. While pure low-MW fractions exhibited

mobility ranging from  $2 \times 10^{-4}$  to  $9 \times 10^{-4}$   $\text{cm}^2\text{V}^{-1}\text{s}^{-1}$ , increasing the amount of high-molecular-weight chains increased  $\mu_{\text{FET}}$  until  $0.07 \text{ cm}^2\text{V}^{-1}\text{s}^{-1}$  for PDBT-TT and until  $0.02 \text{ cm}^2\text{V}^{-1}\text{s}^{-1}$  for PDPP4T-TT. Further increase in the fraction of long chains showed no additional increase in charge carrier mobility. The morphology of the 25 % high MW 75% low MW mixture for PDBT-TT is shown in the inset of Figure 4-6 and suggests features more similar to the pure high MW fraction indicating that the long chains are dominating the morphology of the film. In comparison with our previous work on blending PBTTT low MW (5.8 kDa) with high MW in which a sharp increase in mobility was recorded just upon the addition of 5% weight ratio, for PDBT-TT and PDPP4T-TT a much higher weight ratio of high-MW was required in order to attain a substantial improvement in the charge carrier mobility. In contrast we note that in work by Salleo and coworkers on rr-P3HT a different behavior was observed where the addition of a small amount of long chains had little effect on the overall charge carrier mobility.<sup>[69]</sup> The difference in these behaviors are a point of interest which will be addressed in the discussion section.

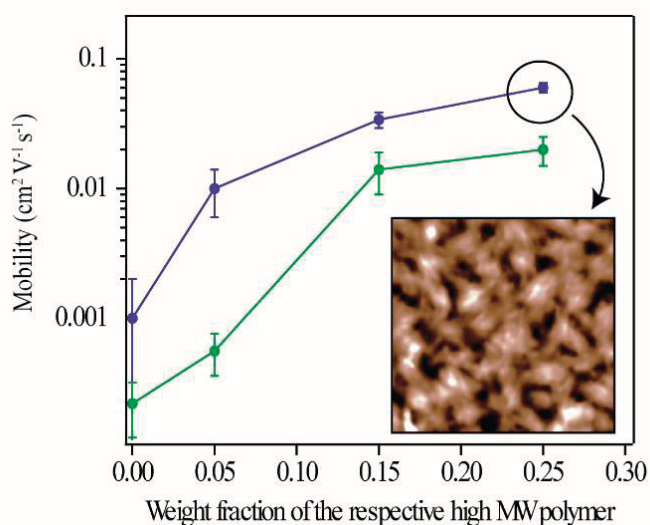


**Figure 4-7.** Average extracted (saturation regime) field-effect charge carrier mobility,  $\mu_{\text{FET}}$ , of annealed (180 °C, 20 min) PDBT- TT and PDPP4T-TT fractions as a function of weight fraction of high-MW polymer chains in the blend with 6.1 kDa for PDPP4T-TT and 9 kDa for PDBT-TT. The inset shows tapping-mode atomic force microscopy of spin cast film of 25% high MW blend. The image represents and film area of  $2 \mu\text{m} \times 2 \mu\text{m}$ .



## 4.3 Conclusions

All the analysis presented so far point to a general conclusion that in the DPP-based polymers investigated here, the charge carrier mobility is extremely sensitive to chain length variation especially in the low-medium MW range. Low MW fractions of DPP-based polymers are characterized by disordered aggregates that have poor charge transport properties due to low degree of crystalline organization. Similarly, low MW fractions of semicrystalline polymers like PBTTT are known to be characterized by comparable low charge carrier mobility due to the presence of high grain boundaries density at fiber-like aggregate interface but highly crystallinity in the in-plane (010)  $\pi$ - $\pi$  stacking direction and out-of-plane interdigitated lamellar stacking direction (100). In the DPP-based polymers investigated herein, the increase in charge carrier mobility at higher MW suggests that the threshold MW from which film formation and inter-chain connectivity is achieved is much less defined as compared to PBTTT films. Previous studies on a rigid quadriquinone-based semiconducting polymer, unexpectedly showed constant hole mobility through the whole range of MW investigated (12 kDa – 46 kDa, PDI > 2) in spite of a switch from no preferential lamellae orientation in edge-on direction at low-MW to an higher density of out-of-plane lamellae at high MW.<sup>[72]</sup> Instead both DPP-polymers, investigated here, showed an increase in hole mobility of one (in PDPP4T-TT) and two orders of magnitudes (in PDBT-TT) in the range from 9 kDa to 30 kDa, without major increase in chain organization. This behavior is however in stark contrast to comparable MWs in polythiophenes, which are instead characterized by considerable change in surface morphology in the aforementioned MW range. Owing to the higher backbone rigidity, both high MW fractions of the DPP-based polymers show some indication of aggregating behavior even in dilute solution, which is likely preserved (or enhanced) in the thin film during spin casting. For PDBT-TT, this manifests into the formation of detectable crystalline domains in the solid state. These observations are well supported from the UV-Vis absorption spectrum in the solid state. Indeed, the slight red-shift observed from solution to the solid state for low and high MW suggests that PDPP4T-TT does not both  $\pi$ -stack either improve chains organization, hence is expected to form highly amorphous films. Interestingly, in a completely amorphous PDPP4T-TT, relatively high hole mobilities ( $\mu_{\text{FET}} = 0.03 \text{ cm}^2 \text{ V}^{-1} \text{ s}^{-1}$ ) have been found in spite of the absence of self-assembled features and crystalline domains (Figure 4-4f). Overall our data point to the conclusion that the highest charge carrier mobility in thin films can be achieved only when the interconnectivity of the rigid chains is greatly improved as a result of the presence of sufficiently long chains ( $M_n$  of ca. 70 kDa). As shown by PDBT-TT, achieving self-assembly of long chains, even if disoriented, is however highly desirable since do-

mains can be largely connected by long-tie molecules still present in the fraction. In contrast, semicrystalline polymer like rr-P3HT and PBTTT show respectively a flattening and gradual decrease in charge carrier mobility at ultra-high MW. In this regime, the lower transport of an interdigitating polymer like PBTTT is normally explained in terms of chain entanglement that hinders both intrachain carrier transport by increasing the density of backbone twist and folds, while also impeding interchain hopping by decreasing  $\pi$ -overlap among surrounding chains.

In summary, we showed how chemically similar DPP-polymers can have different microstructures as a function of MW while presenting the same trend in terms of charge carrier mobilities. In this class of less ordered polymers, the highest charge carrier mobilities are exclusively obtained exploiting the efficient intrachain transport occurring across long and rigid chains. The results presented here seem to suggest that the presence of poorly crystalline low-medium MW chains is only detrimental for the overall hole mobility in crude batches. Therefore avoiding massive presence of disordered low MW chains and selecting the highest possible  $M_n$  (i.e.  $M > 80$  kDa) is necessary in order to optimize charge carrier mobility in poorly ordered films. In this view, achieving (or if not possible, fractionating by prep-SEC) the highest possible MW may be a viable strategy to optimize the performance or improving specific properties polymeric devices like in TFTs.

# Chapter 5

## Controlling conjugated polymer morphology and charge carrier transport with a flexible-linker approach

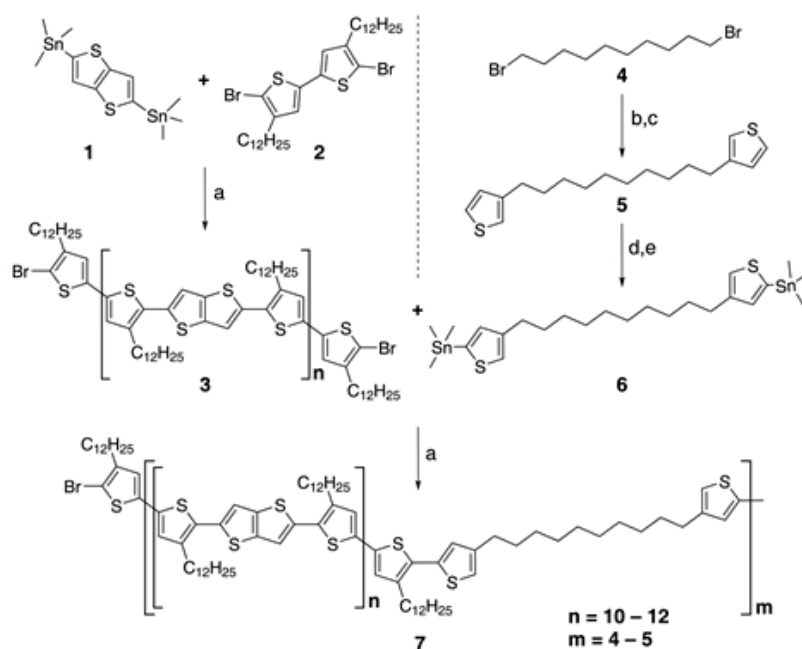
### 5.1 Introduction

In the previous chapters, we have shown how polymer molecular weight (MW) and conjugated backbone rigidity have been established as fundamental structural factors that affect the morphology and accordingly the charge carrier mobility,  $\mu_h$  in field-effect transistors (FETs). While short, stiff chains exhibit advantageous self-assembly and high crystallinity driven by  $\pi$ - $\pi$  stacking, the presence of a two-phase morphology where  $\pi$ -stacked crystalline moieties are interconnected by (long) flexible macromolecules has been identified as being a requirement for high  $\mu_h$ .<sup>[62], [25, 28]</sup> In contrast, studies using long and stiff polymer chains suggest that only occasional  $\pi$ -stacking is required while quasi-1D intramolecular transport is the most important factor.<sup>[19]</sup> A comprehensive understanding of these factors is complicated by the fact that the aspects of chain length and chain stiffness are intimately linked in any given polymer through the intrinsic chain rigidity, which is defined by the polymer repeating unit.<sup>[73]</sup> Because of this limitation it is not possible to separately tune the polymer chain length and overall chain stiffness. However, this ability would undoubtedly advance the capability to rationally control chain self-assembly and thin-film morphology while also affording fundamental insights into the factors that link structure, morphology and performance of polymer semiconductors.<sup>[74]</sup> In order to illustrate this concept we sought to design a novel class of semiconducting polymers where the conjugated segment length and the polymer chain length can be independently controlled. Herein we describe the preparation and purification of a prototype polymer of this class by covalently linking low MW rigid conjugated segments with flexible aliphatic linkers. To demonstrate this new type of polymer we chose poly(2,5-bis(3-dodecylthiophen-2-yl)thieno(3,2-b)thiophene) (PBTTT-C<sub>12</sub>) as a model system given its demonstrated high charge carrier mobility, which is known to be strongly influenced by the thin film morphology and molecular weight of the polymer chains.<sup>[4, 14c, 63]</sup>

## 5.1 Results and discussion

### 5.2.1 Synthesis and product purification

Scheme 4-1 details the synthetic route employed, which began with the preparation of short rigid segments of PBTTT-C<sub>12</sub> via the standard Stille-coupling based polycondensation.<sup>[14a]</sup> A reaction feed ratio of *ca.* 1.7:1 between the brominated bithiophene (**1**) and the stannylated thienothiophene (**2**) was employed to control the molecular weight and favour bromine end groups. The crude polymer was purified with preparatory size exclusion chromatography (prep-SEC) to yield (**3**) with a number average molecular weight,  $M_n$ , of 11.7 kDa and a low polydispersity index, PDI, of 1.19 relative to polystyrene (PS) standards. A correction factor<sup>[14c]</sup> of 1.5 on GPC-calculated MW implies an actual degree of polymerization of  $n = 10-12$ , and MALDI-TOF MS confirmed that more than 90% of (**3**) was terminated by two bromine end groups, while a small amount of H/Br end groups (less than 10% were detected, Figure 5-1a and Figure 5-1b).



**Scheme 4-1.** Synthetic route towards the flexibly-linked PBTTT (**7**). Reaction conditions: a) Pd<sub>2</sub>(dba)<sub>3</sub>, P(o-Tol)<sub>3</sub>, 24h, CB, 100°C, b) Mg in THF, 0°C to RT, c) 3-bromothiophene, Ni(dppp)Cl<sub>2</sub>, -30°C to RT, d) n-BuLi/TMED, THF, -78°C to RT and e) Me<sub>3</sub>SnCl, THF, -78°C to RT.

The remaining Br/Br functionality on the short PBTTT polymer **3** allowed the coupling with the non-conjugated linker (**6**) again under standard conditions.<sup>[75]</sup> Given the difficulty to obtain high conversions with large molecular weight substrates in Stille-coupling reactions, and the small amount of H/Br end groups present, a fraction of the starting polymer (**3**) was expected to remain after the coupling. However, analytical size exclusion chromatography (Figure 5-1c) of the crude coupling reaction (broken trace) confirmed the success of the coupling as the  $M_n$  of the product increased substantially compared to the starting material (grey trace). (Figure 5-1c) of the crude coupling reaction (broken trace) confirmed the success of the coupling as the  $M_n$  of the product increased substantially compared to the starting material (grey trace).

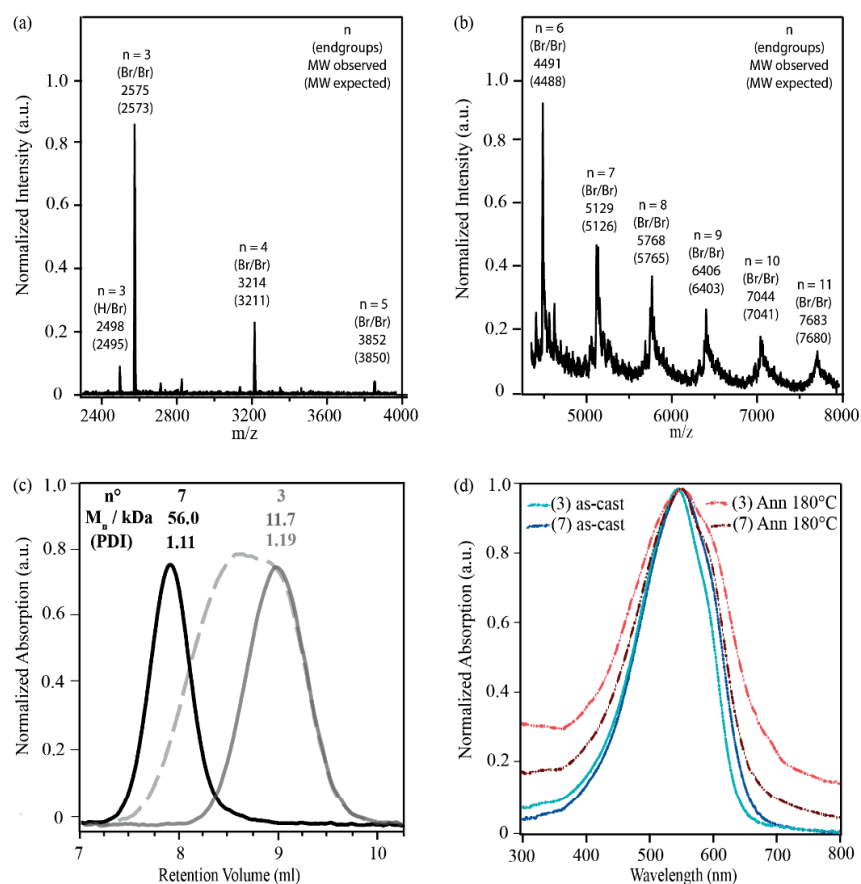


**Figure 5-1.** a) MALDI-TOF spectrum of compound **3** in reflection mode (left) and linear mode (right) using *trans*-2-(3-(4-*tert*-Butylphenyl)-2-methyl-2-propenylidene) malononitrile as matrix b) Analytical size exclusion chromatographs of PBTTT starting material (**3**) (grey line), after polymerization with a flexible linker (dashed line) and the purified FL-PBTTT (**7**) (black line). The reported  $M_n$  values and polydispersities are calculated versus PS standards. (c) UV-Vis Absorption spectra of thin films of low MW-PBTTT **3** and the flexible linker polymer **7** in the "as cast state" and after thermal annealing at 180°C.

After purification by prep-SEC, it was possible to isolate a high molecular weight fraction of (7) in milligram quantities while also minimizing any contamination from residual starting polymer (3). Based on the analytical SEC characterization of the purified flexibly-linked polymer, FL-PBTTT (7), (Figure 5-1c, solid black trace,  $M_n = 56.0$  kDa), the secondary degree of polymerization,  $m$ , was estimated to be 4–5.

## 5.2.2 Thermal properties

Analysis by differential scanning calorimetry (DSC, Figure 5-2b) revealed unique thermal properties of the FL-PBTTT (7) compared to the starting polymer (Figure 5-2a). Previous reports have shown that PBTTT with  $M_n > ca.$  30 kDa exhibits two endothermic transitions at *ca.* 120°C and 230°C corresponding to the side-chain and conjugated backbone melting, respectively.<sup>[5b, 76]</sup> The presence of a mesophase between these two transitions has been attributed to the formation of a thermotropic liquid crystalline phase that is critical to achieve the self-assembly observed in the best performing thin films.<sup>[54a]</sup> In contrast, PBTTT with  $M_n < ca.$  12 kDa typically shows only one transition at *ca.* 170°C,<sup>[5b]</sup> consistent with a lowered backbone melting temperature expected with a shorter chain length and the absence of the side chain transition. This behaviour is presumably caused by the dominating crystallization of the conjugated backbone during cooling, which limits organization of the side chains.<sup>[25]</sup>

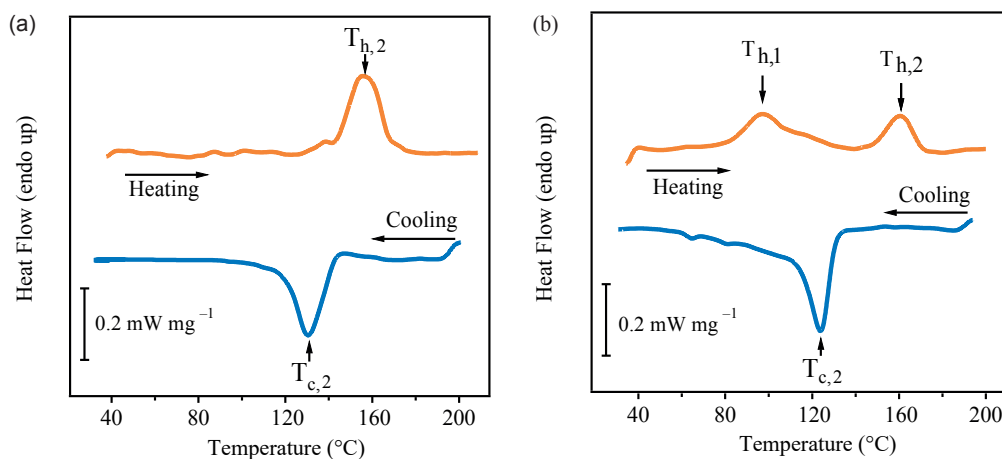


**Figure 5-2.** Second heating/cooling thermographs (baseline corrected) from differential scanning calorimetric analysis of (a) polymer 3 and (b) FL-PBTTT 7. The heating and cooling rates were 20°C/min.

For our starting polymer (**3**) the second heating and cooling curves, shown in Figure 5-2a, exhibit the thermal behaviour anticipated for the low MW PBTTT with one endothermic transition during heating at 170°C. Our newly-synthesized FL-PBTTT (**7**) exhibits an endothermic transition at the same temperature, however an additional distinct endothermic transition at 95°C is also observed (Figure 5-2b). We note that this behaviour is similar to that of high MW PBTTT albeit transitions occurred at lower temperatures. In addition, both polymers **3** and **7** showed similar enthalpies of crystallization upon cooling ( $\Delta H_c = 9.8$  and  $8.6 \text{ J g}^{-1}$ , respectively), suggesting that our linking strategy did not affect the ability of  $\pi$ -conjugated segments in the FL-PBTTT to crystallize. This is supported by solid-state UV-Vis spectra (Figure 5-1d) which confirm similar absorption properties between polymers **3** and **7** including the presence of a shoulder at 600 nm, commonly ascribed to vibronic coupling induced by  $\pi$ - $\pi$  stacking, this further indicates that the conjugation length has not been significantly altered by our linking approach.

### 5.2.3 Topological and microstructure characterization

In addition to thermal behaviour, the microstructural properties of solution-cast PBTTT thin films have been considered to be critical for the electronic performance.<sup>[4, 77]</sup> PBTTT with  $M_n$  between 20 and 60 kDa typically exhibits large-area terrace structures when cast onto alkyl-functionalized  $\text{SiO}_2$  substrates and thermally annealed in the mesophase between the two melting temperatures.<sup>[14c]</sup> This characteristic morphology can be observed by atomic force microscopy (AFM, Figure 5-3e) and by grazing incidence x-ray diffraction (GIXD, Figure 5-4b). In this characteristic morphology, polymer chains self-assemble with their alkyl groups extending in a direction perpendicular to the substrate while the conjugated backbone forms  $\pi$ -stacked lamellae parallel to the substrate.<sup>[15]</sup> The topographical profile along the indicated diagonal line in each case is shown below. Alternatively, low MW PBTTT ( $10 < M_n < 20 \text{ kDa}$ ) exhibits a characteristic fibril or haystack type morphology as reported in Figure 5-3d.<sup>[5b, 14c]</sup> In this case the morphology is dominated by the strong organization in the  $\pi$ -stacking direction, and individual chains are unlikely to extend to adjacent crystal domains. This results in a relatively higher concentration of grain boundaries and poorer alignment with the substrate compared to the terrace-forming case. In order to gain insight into how the unique assembly of the FL-PBTTT affects its microstructural properties, we next spin-casted films from *o*-dichlorobenzene onto octyldecyltrichlorosilane (OTS)-functionalized  $\text{SiO}_2$  substrates to yield films that were *ca.* 60 nm thick (avoiding confinement effects<sup>[63]</sup>).

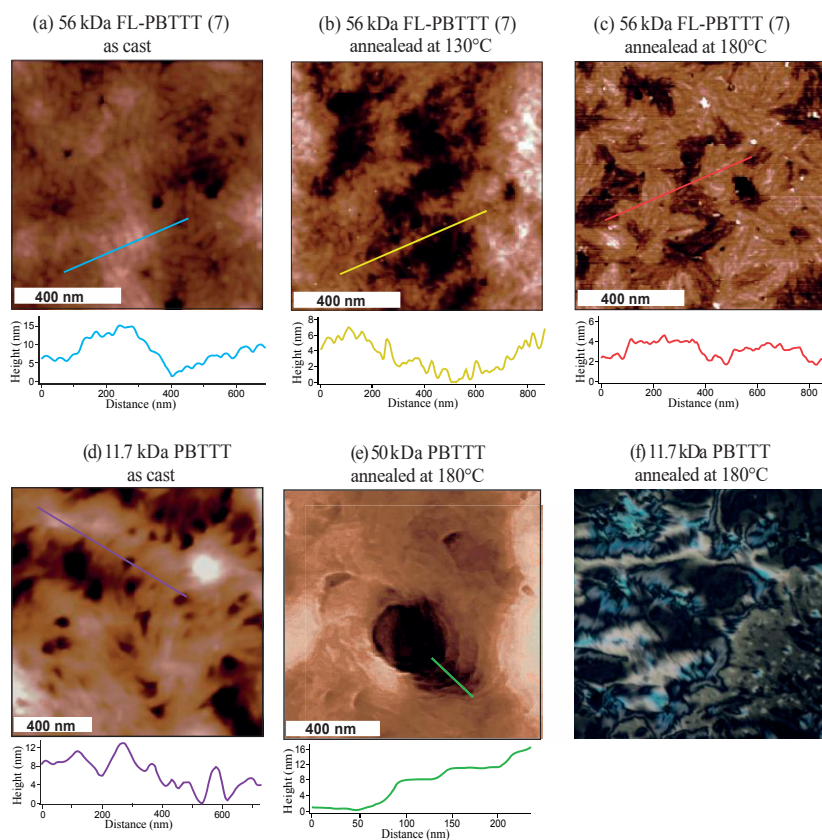


**Figure 5-3.** Tapping mode AFM topography of a) FL-PBT TT as cast from *o*-dichlorobenzene 20 mg mL<sup>-1</sup>, b) FL-PBT TT after annealing at 130°C, c) after annealing at 180°C d) starting polymer **3** and e) 50 kDa PBT TT (fully conjugated) annealed at 180°C. f) Polarized optical microscopy (epi-illumination) of the starting polymer **3** after annealing at 180°C on OTS-treated SiO<sub>2</sub> substrates.

The as-cast topography of a thin film of **3** (Figure 5-3d) exhibits a root mean square (RMS) roughness of 6.1 nm and clearly shows the expected fibril-like structures, which are of the order of 1 μm in length and isotropically oriented on the surface. GIXD patterns show strong out-of-plane reflections corresponding to the *d*-spacing (*h*00) peaks (between the π-stacked lamellae). The arched shape of the peaks suggests that the starting polymer crystallizes with the lamellae poorly aligned with the substrate. [15] AFM topography of the as-cast films of FL-PBT TT (Figure 5-3a) establishes a comparable presence of spatially confined fibrils of 30 nm in width and *ca.* 300 nm in length as previously seen for low MW of PBT TT. This confirms the results from the DSC and UV-Vis data in that our flexible linker approach does not impede the π-π stacking



between conjugated segments. AFM image (Figure 5-3a) also suggests an improved fibril interconnectivity compared to polymer **3** as supported by the lower measured surface roughness value of 3.5 nm. The apparent improvement in microstructural organization was confirmed by the considerably more elliptical (less arching) shape of the (h00) peaks observed by 2D-GIXD (see also peak shape analysis Table 5-1) suggesting an unexpected alignment of  $\pi$ -stacked lamellae parallel to the substrate after spin-casting the film. We note that the intensity of the (h00) peaks are less than those observed in the film of polymer **3** suggesting a kinetic limitation for crystallization during spin-casting induced by the flexible linker. This observation is consistent with a higher degree of entanglement of the polymer chains in the FL-PBTTT.

The effect of thermal annealing the FL-PBTTT on the thin film morphology was next investigated. After treatment at 130°C (between the two thermal transitions) and cooling to room temperature, the RMS roughness of the FL-PBTTT film decreases slightly to 2.2 nm (Figure 5-3b). While the 30 nm fibre thickness remains preserved, the length of the fibres appears qualitatively shorter. GIXD plots of the film after annealing reveals a considerably higher intensity of (h00) peaks suggesting thermally induced self-assembly of the  $\pi$ -stacked lamellae.

However, a clear increase in arching of the (100) peak indicates that the crystalline domains lose orientation with respect to the substrate. After annealing at 180°C (above  $T_{h,2}$ ) the FL-PBTTT film remains continuous and AFM (Figure 5-3c) reveals considerably smoother films (RMS roughness of 0.8 nm) and crystalline domains on the order of a few hundred nanometers in size. Surprisingly, terrace-like features appear with lateral dimensions on the order of hundreds of nanometers and step heights of 2 nm (consistent with the  $d$ -spacing in PBTTT-C<sub>12</sub><sup>[14b]</sup>). In contrast to the smooth terrace structure observed in 20–50 kDa PBTTT (Figure 5-3f), an embedded fibre substructure is observed with the FL-PBTTT, suggesting a hierarchical organization of the conjugated segments which are presumably  $\pi$ - $\pi$  stacked in fibres and forming lamellae aligned with the substrate. This model is supported by the GIXD which clearly shows a reversal from the peak arching (observed after annealing at 130°C) to sharp and elliptical (h00) peaks confirming the return of the film to a domain orientation more coherent with the substrate.

We note that the intensity of the (h00) peaks decreases slightly from the 130°C case, and is considerably less than observed with 50 kDa PBTTT processed at the same conditions (Figure 5-3e), but remains higher than the as-cast state (See Figure 5-4e). The observed transformations of the thin-film morphology of the FL-PBTTT by thermal annealing are in stark contrast to the behaviour of standard (fully conjugated) PBTTT for all MWs.

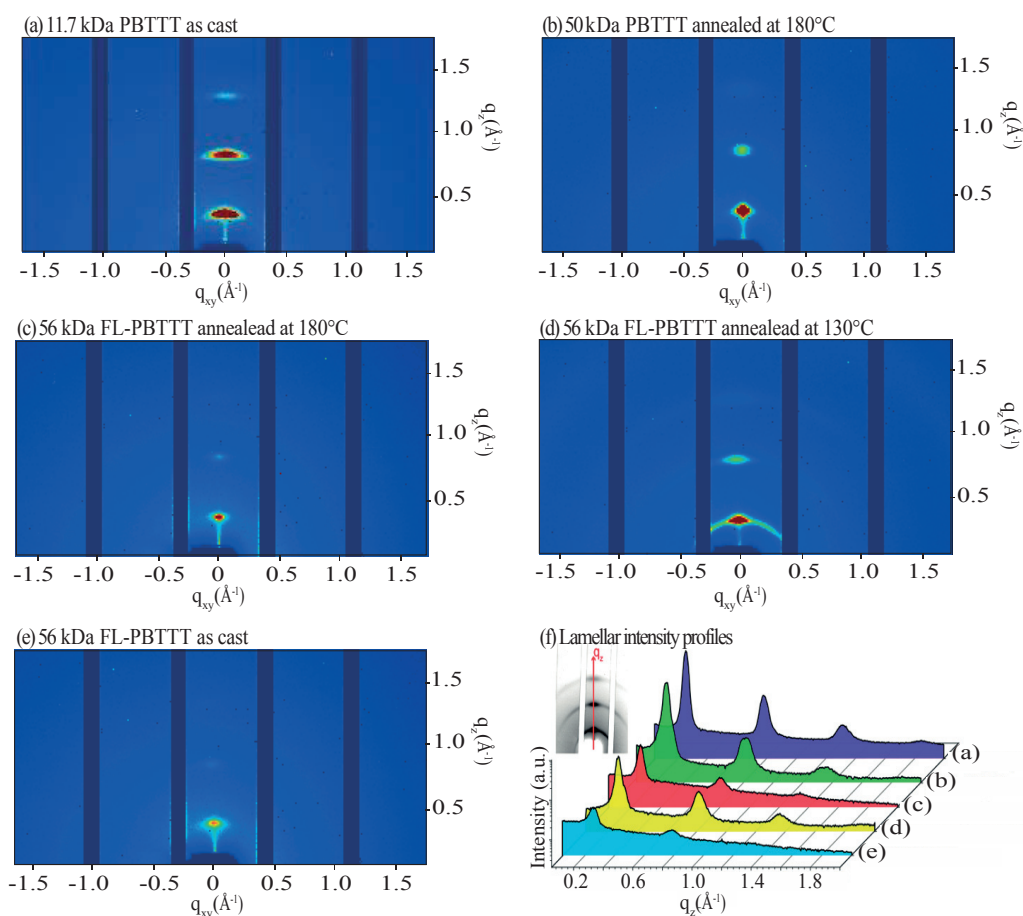


**Figure 5-4.** In situ 2D GIXD plots of the same films with the vertical direction corresponding to the out-of-plane scattering vector,  $q_z$ , and the horizontal direction corresponding to  $q_{xy}$ . Red areas represent the highest scattering intensity while blue represent the lowest. (f)  $q_z$  cuts of the GIXD profiles extracted from the 2D images. The data represent the scattering intensity in the out of plane direction (i.e.  $q_{xy}=0$ ).

When the starting polymer **3** was annealed, no change in morphology was observed until the temperature surpasses 180°C, in accordance with the DSC results. Annealing at this temperature causes the films to partially segregate from the substrate and micrometer sized domains visible by eye and in polarized optical micrographs (Figure 5-3f) are formed. In addition, we note that de-wetting also occurs in films of higher MW, terrace-forming PBTBT on OTS treated SiO<sub>2</sub> when annealed past the second thermal transition,<sup>[76]</sup> whereas PBTBT with  $M_n > 60$  kDa does not form terraces after annealing, presumably due to chain entanglement.<sup>[14c]</sup> The differences

clearly evidence that the flexible linker approach offer a unique level of control over the polymer chain self-assembly and thin film microstructure. In addition, our results suggest that the ability to form the ordered terrace-like structure is not defined by the conjugated segment length, but rather the overall length of the polymer chain..

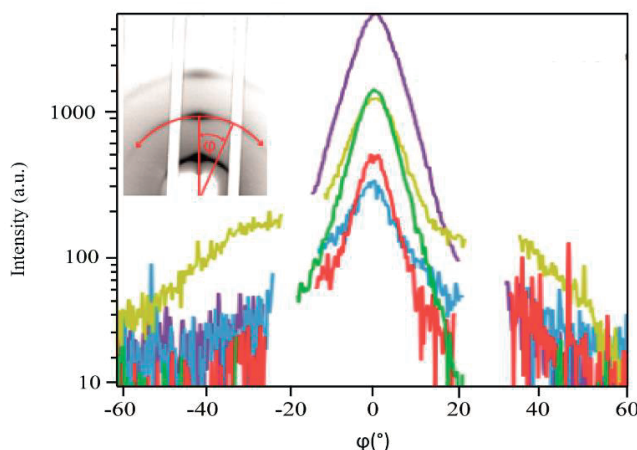


**Figure 5-5** Grazing incidence peak arching analysis for the (200) peak. The Full Width at Half Maximum (FWHM) of the Azimuthal cut data from Figure 5-4 are compared to quantify the shape of the peak. FWHM values were obtained via fitting the peaks with Voigt functions. Higher values of the FWHM ratio indicate more arched shape while lower values represent more cylindrically symmetric peaks. Lines colour is in accordance with the conditions use in Figure 5-4f.

**Table 5-1.** Grazing incidence peak arching analysis for the (200) peak. The FWHM of the Azimuthal cut data and the  $q_z$  cut data (Figure 5-5) are compared to quantify the shape of the peak. FWHM values were obtained via fitting the peaks with Voigt functions. Higher values of the FWHM ratio indicate more arched shape while lower values represent more cylindrically symmetric peaks.

Material	Film condition	2D GIXD Figure location	FWHM Azimuthal cut ( $^{\circ}$ )	FWHM $q_z$ cut ( $\text{\AA}^{-1}$ )	FWHM ratio ( $^{\circ}\text{\AA}^{-1}$ )
Polymer 3	as cast	Figure 5-4a	9.7	0.031	313
FL-PBTTT 7	as cast	Figure 5-4e	9.7	0.052	187
	annealed 130 $^{\circ}$ C	Figure 5-4d	10.5	0.041	256
	annealed 180 $^{\circ}$ C	Figure 5-4c	7.6	0.040	190
56 kDa PBTTT	annealed 180 $^{\circ}$ C	Figure 5-4b	8.5	0.053	160

## 5.2.4 Charge carrier transport in flexible linker polymers

Electronic investigations using bottom-contact / bottom gate field effect transistors were next performed on the same thin-films (on OTS treated SiO<sub>2</sub>). Well-formed output curves were observed for all conditions. Typical examples of the output I<sub>sd</sub> vs V<sub>d</sub> data and the resulting transfer curves are shown in Figure 5-6. The values for μ<sub>h</sub>, extracted from the saturation region, are shown in Table 5-2 as an average of at least three devices for each condition, along with the extrapolated threshold voltage, V<sub>th</sub> and contact resistance, R<sub>c</sub>. Regardless, the observed performance of polymer **3** was found to perform similar to previously reports of PBTTT with M<sub>n</sub> < 12 kDa and PDI = 1.1.<sup>[14c]</sup> The partial de-wetting of the film after the annealing caused a drastic rise in R<sub>c</sub> and a decrease in the measured μ<sub>h</sub> by almost 2 orders of magnitude. The relatively large standard deviation indicates the variability of the device performance after annealing. Compared to the starting polymer, the FL-PBTTT exhibited a similar as-cast μ<sub>h</sub>, but both V<sub>t</sub> and R<sub>c</sub> were found to be lower. This can be attributed to the formation of a more continuous film afforded by our flexible linker strategy. Interestingly, despite the substantial increase in crystallinity after annealing at 130°C the electronic parameters of **7** remained approximately constant. This can be rationalized in light of the topography, which suggests no improvement in domain connectivity and implies that the transport is mostly limited by grain boundaries.

**Table 5-2.** Average electronic parameters of the transistors fabricated in this work

Material	Film condition	μ <sub>h</sub> (cm <sup>2</sup> V <sup>-1</sup> s <sup>-1</sup> )	V <sub>t</sub> (V)	R <sub>c</sub> (kΩ)
Polymer <b>3</b>	as cast	0.01 ± 0.002	+22 ± 3	77 ± 6
	annealed 180°C	0.01 ± 0.002	+18 ± 2	4300 ± 300
FL-PBTTT <b>7</b>	as cast	0.01 ± 0.001	+6 ± 2	45 ± 5
	annealed 130°C	0.015 ± 0.004	+6 ± 2	40 ± 5
	annealed 180°C	0.04 ± 0.003	+8 ± 4	12 ± 3
56 kDa PBTTT	As cast	0.03	-	-
	annealed 180°C	0.08	-	-

However, annealing at 180°C afforded FET devices with substantially higher saturation currents (see Figure 5-6a), a decreased  $R_c$  and an increase in  $\mu_h$  by a factor of 4 compared to the as-cast film. This drastic increase is in contrast to the observed decrease in overall crystallinity compared to the 130°C annealed but correlates precisely with the improved alignment of the  $\pi$ - $\pi$  stacking lamellae in the direction of charge transport. Taken together, our observations give further insight into the effect of morphology on charge transport. Since the FL-PBTTT material enables the evolution from a highly crystalline fibril-type morphology to a (less crystalline but aligned) terraced-type morphology without altering the chain length and accordingly the charge transport within individual chains (as supported by the unchanging UV-vis spectra), we can attribute the 4-fold higher in the mobility to the improved intermolecular alignment afforded by the terrace morphology. This is in contrast to the recent conjecture that the relatively high  $\mu_h$  observed in lamellar-stacked (terrace-forming) PBTTT is not due to the 2D charge-transport network afforded by self-assembly, but rather to the coincident enhancement of backbone coplanarity that improves the intramolecular transport.<sup>[19]</sup> Indeed our results suggest that disrupting conjugation along the backbone does not destroy charge transport in the overall film as long as conjugated segments are able support long-range percolation through a 2D  $\pi$ -stacking network. While a large increase in the mobility can be achieved solely through the development of an aligned intermolecular charge transport network, we note that a sample of terrace-forming, fully conjugated PBTTT with the same  $M_n$  as the FL-PBTTT (56 kDa) and a PDI of 1.1 yields a  $\mu_h$  of *ca.* 0.08 cm<sup>2</sup> V<sup>-1</sup> s<sup>-1</sup> using the same device geometry and annealing conditions, and the maximum  $\mu_h$  was found to be 0.12 cm<sup>2</sup> V<sup>-1</sup> s<sup>-1</sup> using 30-40 kDa PBTTT.<sup>[14c]</sup>

While it is difficult to compare the performance of these polymers to the FL-PBTTT given the presence of the flexible linker, it is remarkable that the difference is only a factor of 2-3 between the FL-PBTTT and fully conjugated polymer. This highlights that both intermolecular alignment and transport within individual chains are important. Since the most recently reported polymers with state-of-the-art  $\mu_h$  are comprised of rigid chains with extended backbone alignment for up to hundreds of nanometers (giving favourable intramolecular transport) but fewer  $\pi$ -stacking domains (limiting intermolecular transport),<sup>[19]</sup> our results suggest that further improvement can be gained through optimization of intermolecular transport in the film as presented here. Future optimization of the conjugated segment length, rigidity and the number of joined segments is expected to give further insights into the respective roles of intra-, and inter-molecular charge carrier transport as well as afford more precise control over chain self-assembly in conjugated polymer electronic devices.

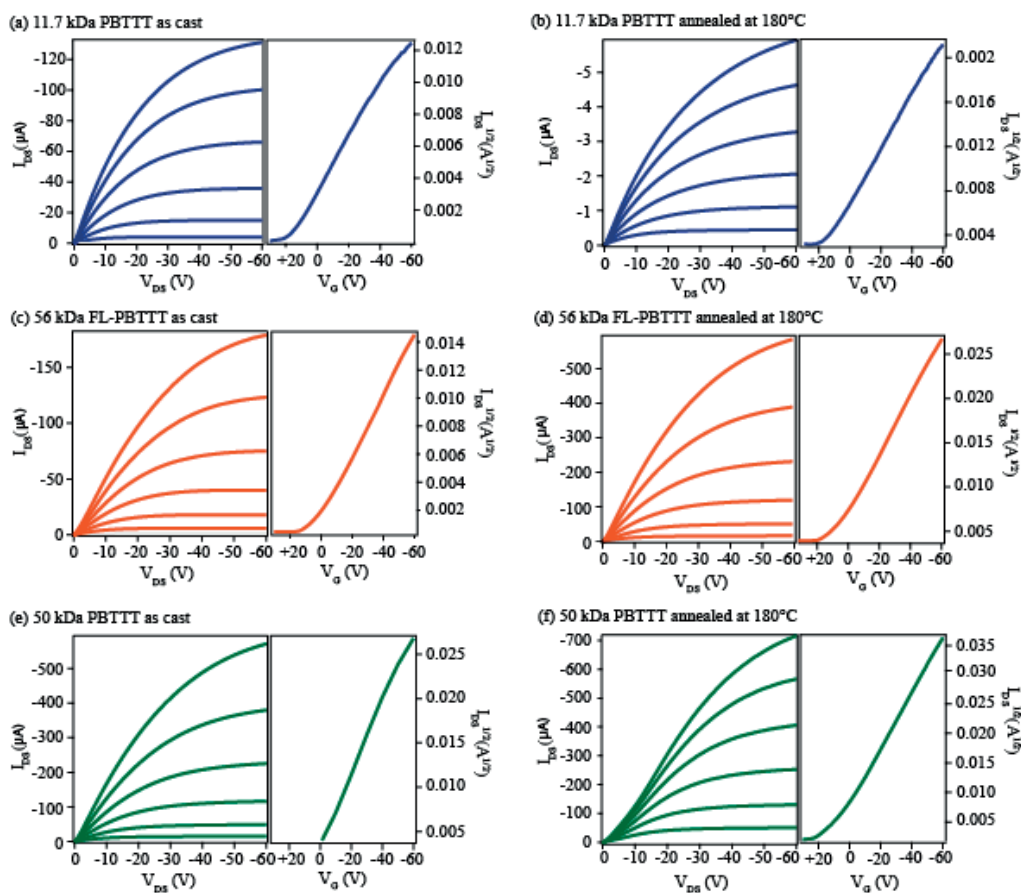


**Figure 5-6.** Transistor output curves (left) and the resulting transfer curves (right) for all the conditions tested. Devices channel length and width were of 20  $\mu\text{m}$  and 10 mm.

## 5.3 Conclusions

In this chapter, we have shown the successful preparation and purification of a prototype in a class of semiconducting polymer that allows independent control over the conjugated segment length and overall chain length by covalently linking low-MW conjugated segments with flexible aliphatic linkers. Our FL-PBTBT material exhibited improved thin-film formation compared to the low-MW starting polymer and unique thermal properties. Importantly, our linking strategy had a clear effect on the chain self-assembly and allowed control between distinct thin film morphologies without altering the chain length. This ability allowed us to gain insight into the important factors that direct the self-assembly between (highly crystalline) fibril-type structures

to (less crystalline) aligned terrace-type morphologies. The subsequent electronic characterization of the thin films remarkably showed that including the non-conjugated linker did not drastically reduce the charge transport. Rather the performance of the different films compared to their respective morphologies revealed the key role of a 2D  $\pi$ -stacking network aligned in the charge transport direction over films with high crystallinity and poorer alignment. Moreover our FL-PBTTT served as a model to understand the performance of fully-conjugated PBTTT by indicating that its relatively high performance is not solely due to improved intramolecular transport but that the 2D charge-transport network afforded by self-assembly contributes significantly to the high charge carrier mobility. These results support the view that the optimization of the intermolecular transport by chain self-assembly in aligned domains is a principle objective for improving charge transport in semiconducting polymer based devices. In addition, we expect that the success of our flexible linker approach at obtaining a unique level of control over the polymer chain self-assembly and thin film microstructure will find suitable application in the optimization of morphology in bulk heterojunction photovoltaics, sensors, OLEDs and other devices employing polymer semiconductors.





# Chapter 6

## Enhancing thermal stability of solution-processed small molecule semiconductor thin films using a flexible linker approach.

### 6.1 Introduction

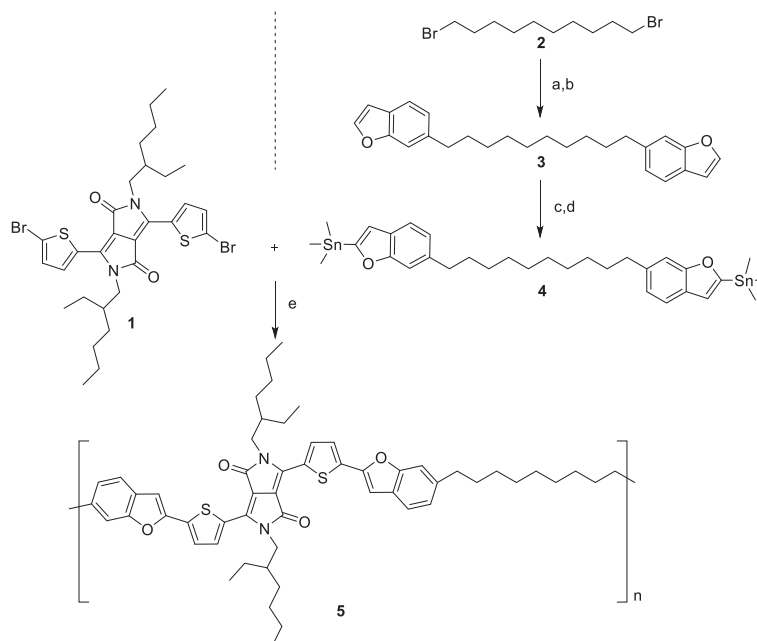
Preparative-SEC was shown so far to be a power tool to purify polymeric batches and reduce their microstructure complexity by obtaining samples with desirable low polydispersities to gain insights into charge transport mechanisms in conjugated polymers. However, Prep-SEC is still a too expensive and not scalable technique for industrial applications, thus in a large scale scenario, conjugated polymers would continue to present batch-to-batch inhomogeneities and purification issues from catalyst residues and unreacted species. In this respect, the design of systems that overcome typical polymers' purification problem is thus of high interest. Molecular semiconductors instead offer direct purification, higher structural precision and batch-to-batch consistency to an extent more suitable for concrete industrial applications.<sup>[48]</sup> However, the strong tendency of conjugated molecular organic semiconductors to self-assemble into crystalline domains results in drawbacks like dewetting, poor thin film formation due to low solution viscosity, unpredictable crystalline domain sizes, and grain boundaries and that confound the morphological control and charge transport in devices fabricated from these materials. In particular, the need to control the thin film morphology is especially important for application in bulk heterojunction (BHJ) photovoltaics where the domain size between the electron donating and electron accepting phases must be precisely controlled to afford high power conversion efficiency.<sup>[78]</sup> For BHJ devices prepared with molecular semiconductor donors and the common small-molecule fullerene derivative, phenyl-C<sub>61</sub>-butyric acid methyl ester (PC<sub>61</sub>BM) as the acceptor, the crystallization of the donor phase has been recently shown to be the driving force for blend separation.<sup>[79]</sup> Thus developing strategies to afford control over donor crystallization is of paramount importance. While volatile additives like diiodooctane<sup>[80]</sup> and more recently non-volatile nucleation promoters<sup>[81]</sup> or insulating polymers<sup>[82]</sup> have been employed to offer control over the thin-film formation and crystalline domain size, these approaches do

not nominally act on the donor phase nor do they address the intrinsic stability of the thin film morphology. Indeed, enhancing the long-term morphological stability of BHJ photovoltaics is one of the major remaining challenges in the field.<sup>[45, 47]</sup> Specifically, the inherent thermodynamic immiscibility of the donor and acceptor phases drives phase separation and eventually decreases device performance, even at normal operating temperatures.<sup>[83]</sup> Given the drawbacks of molecular organic semiconductors, the enhanced thin film thermal stability that has been achieved by using a “flexible linker approach<sup>[23]</sup> could reasonably provide a route to control over molecular donor crystallization and improve morphological stability in thin film devices. This strategy employed well-defined conjugated segments that are covalently linked with flexible aliphatic chains into polymeric materials. Herein, we extend the flexible-linker strategy to molecular organic semiconductors using a common small molecule donor, 3,6-Bis(5-(benzofuran-2-yl)thiophen-2-yl)-2,5-bis (2-ethylhexyl)pyrrolo (3,4-c) pyrrole 1,4 (2H ,5H )-dione, coded as DPP(TBFu)<sub>2</sub>.<sup>[48]</sup> When the flexibly-linked material is employed as an additive in thin films, a unique level of control is observed over the morphology and the thermal stability of pure donor films in transistor devices and in blends with PC<sub>61</sub>BM for BHJ photovoltaics.

## 6.2 Results and discussion

### 6.2.1 Synthesis and purification

The synthesis of the flexibly-linked DPP(TBFu)<sub>2</sub> derivative (coded FL-DPP(TBFu)<sub>2</sub>) is shown schematically in Scheme 6-1. In a first step, the Stille-coupling polycondensation between the brominated diketopyrrolopyrrole (1) core and the stannylated benzofuran dimer (4), followed by standard purification yielded a broad PDI batch of FL- DPP(TBFu)<sub>2</sub>. Subsequent, preparatory size exclusion chromatography of the crude polymerization batch yielded the targeted Flexibly Linked polymer (5) FL-DPP(TBFu)<sub>2</sub> with a number average molecular weight, M<sub>n</sub>, of 10 kDa and a PDI of 1.4 (n ≈ 11-15) in the hundred-milligram scale (Figure 6-1a).



**Scheme 6-1.** Synthetic route towards the flexibly-linked FL-DPP(TBFu)<sub>2</sub> polymer (5). Reaction conditions, a) Mg in THF, 0°C to RT, b) 3-bromothiophene, Ni(dppp)Cl<sub>2</sub>, -30°C to RT, c) n-BuLi/TMED, THF, -78°C to RT and d) Me<sub>3</sub>SnCl, THF, -78°C to RT, e) Pd<sub>2</sub>(dba)<sub>3</sub>, P(o-Tol)<sub>3</sub>, 24h, CB, 100°C.

## 6.2.2 Thermal and optical properties of DPP(TBFu)<sub>2</sub> as an additive.

To gain a first insight into the crystallization behavior of the FL-DPP(TBFu)<sub>2</sub> polymer, we performed differential scanning calorimetry (DSC). The neat material did not exhibit a detectable glass transition nor enthalpic transitions associated with melting/crystallization in the temperature range of 50-240°C. However, when combined with the parent DPP(TBFu)<sub>2</sub> small molecule, a significant change in the crystallization occurred. Cooling curves obtained after melting blends of the FL-additive (at a weight fraction,  $f_{FL}$ ) and the small molecule are shown in Figure 6-1b. A strong dependency on the DPP(TBFu)<sub>2</sub> crystallization temperature,  $T_c$ , upon addition of the FL-additive is clearly observed. With  $f_{FL}$  at only 1 wt%, a pronounced shift of the exothermic crystallization to higher temperatures is noted compared to the neat small molecule ( $f_{FL} = 0$ ). This observation is consistent with the behavior of a nucleation promoter,<sup>[45, 81]</sup> suggesting the FL-additive acts to reduce the driving force needed to nucleate stable nuclei of DPP(TBFu)<sub>2</sub>. The maximum shift of the crystallization onset was found to be  $\Delta T_c = 10$  °C with  $f_{FL} = 5$  wt%, which is consistent in magnitude with recent reports of small molecule, non-conjugated nucleation promoters.<sup>[45]</sup>

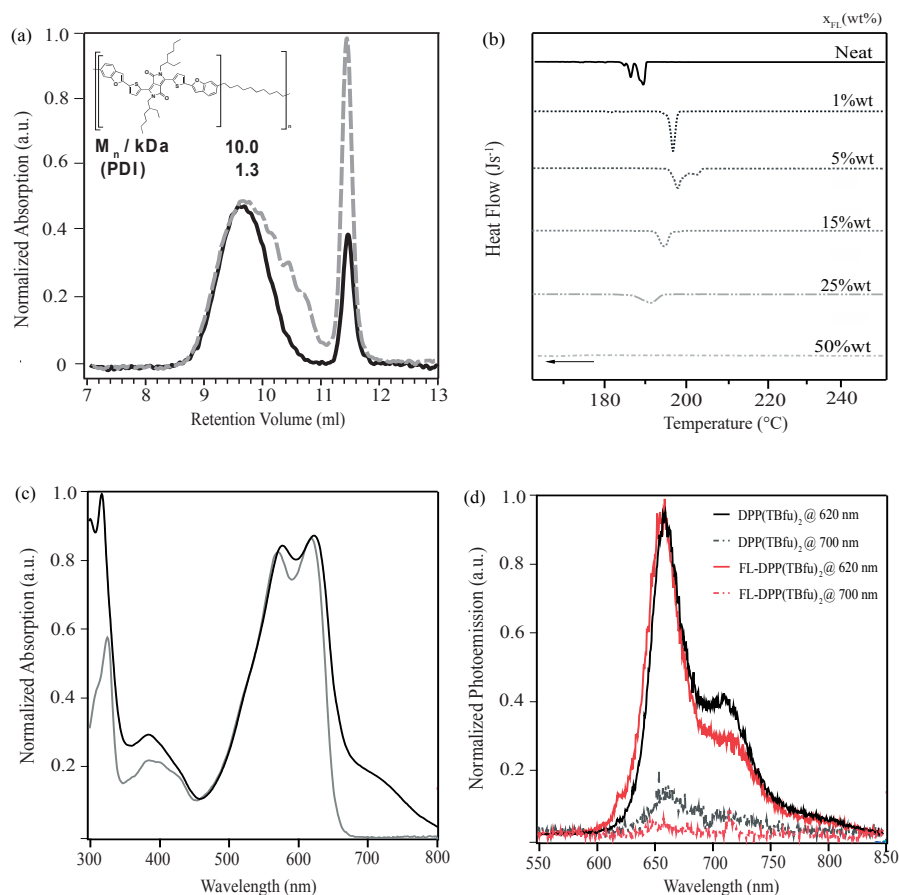


**Figure 6-1.** a) Analytical size exclusion chromatographs of the crude polymerization (grey continuous line), after fractionation by SEC (black continuous line). The reported  $M_n$  values and polydispersities are calculated versus PS standards. (b) Differential scanning calorimetry cooling curves for different amounts of FL-DPP(TBFu)<sub>2</sub> in DPP(TBFu)<sub>2</sub>. c) Uv-Vis absorption spectra in solution of DPP(TBFu)<sub>2</sub> small molecule ( grey line) and FL-DPP(TBFu)<sub>2</sub> polymer (black line). d) Fluorescence spectra of DPP(TBFu)<sub>2</sub> in solution with excitation at 620 nm (black solid line) and 700 nm (black dashed line) and of FL-DPP(TBFu)<sub>2</sub> with excitation at 620 nm (red solid line) and 700 nm (red dashed line).

For higher  $f_{FL}$  the onset of crystallization returns to lower temperatures and the enthalpy of the crystallization decreases, meaning the complete disruption of the ability of the blend to crystallize. We note that for  $f_{FL} = 1$  and 5 wt%, comparable enthalpies of crystallization are observed ( $\Delta H_c = 34.7$  and  $30.1 \text{ J g}^{-1}$ , respectively) with respect to the neat material ( $39.9 \text{ J g}^{-1}$ ) suggesting that the overall degree of crystallinity is not strongly reduced despite the addition of the amorphous FL-DPP(TBFu)<sub>2</sub>. Given the insulating nature of the aliphatic linker, the polymerization is not expected to further extend the conjugation length over several repeating units like in conjugated polymers. FL-DPP(TBFu)<sub>2</sub> is thus expected

to retain the same bandgap and absorption profile of the conjugated molecule DPP(TBFu)<sub>2</sub>. The UV-Vis spectra in solution (Figure 6-1c) shows very similar absorption profiles between the single small molecule and the corresponding flexible linker polymer synthesized here. However, in the case of FL-DPP(TBFu)<sub>2</sub> an absorption shoulder is observed extending further above 700 nm. In order to reveal the nature of this unexpected feature and to confirm the purity of the synthetic route used here, we performed fluorescence measurements on the small molecule and on the newly synthesized FL-DPP(TBFu)<sub>2</sub> (Figure 6-1d). Interestingly, excitation at 700 nm doesn't produce any emission in either materials, suggesting that the tail observed in FL-DPP(TBFu)<sub>2</sub> absorption is probably caused by polymeric chain aggregation in solution.<sup>[68]</sup>

### 6.2.3 Effect of flexible linker additive as a nucleation promoter in thin films

The effect of our FL strategy on the on the charge transport properties of solution-cast thin films was next investigated in bottom-contact/bottom-gate field-effect transistors. Devices prepared with the neat FL material showed no field-effect mobility ( $\mu_{\text{FET}}$ ) confirming that the absence of crystalline ordering (as indicated by the DSC results) prevents long-range charge carrier transport. However, as-cast films of the FL material blended with DPP(TBFu)<sub>2</sub> gave measurable  $\mu_{\text{FET}}$  for a wide range of  $f_{\text{FL}}$ , and for  $f_{\text{FL}}$  up to 5 wt%, the values were comparable with the neat DPP(TBFu)<sub>2</sub> film with  $\mu_{\text{FET}} \approx 1-2 \times 10^{-5} \text{ cm}^2 \text{ V}^{-1} \text{ s}^{-1}$  (Figure 6-2). We note that the values of the as-cast  $\mu_{\text{FET}}$  are similar to previous reports of the as-synthesized small molecule (which contains a mixture of stereoisomers). AFM images in Figure 6-1 show a slight increase in fiber diameter in films where FL-DPP(TBFu)<sub>2</sub> was used as an additive. As annealing is typically performed to increase the crystalline ordering and to better charge carrier transport,<sup>[84]</sup> we next investigated the effect of the annealing temperature on transistors prepared with neat DPP(TBFu)<sub>2</sub> ( $f_{\text{FL}} = 0$ ) and for  $f_{\text{FL}} = 1$  and 5 wt%. The results are shown in Figure 6-3. Annealing at 50°C for 30 min improved  $\mu_{\text{FET}}$  in all cases, however, subsequent annealing at higher temperatures caused a decrease in  $\mu_{\text{FET}}$  for neat DPP(TBFu)<sub>2</sub> devices. In contrast, the observed temperature dependence is quite different in the presence of the FL additive. The measured  $\mu_{\text{FET}}$  increases slightly as a function of temperature until 150°C for the 1 wt% devices, while the 5 wt% devices remain fairly constant from 70°C - 150°C, suggesting that a more robust charge carrier transport network is created when adding the FL-DPP(TBFu)<sub>2</sub>.

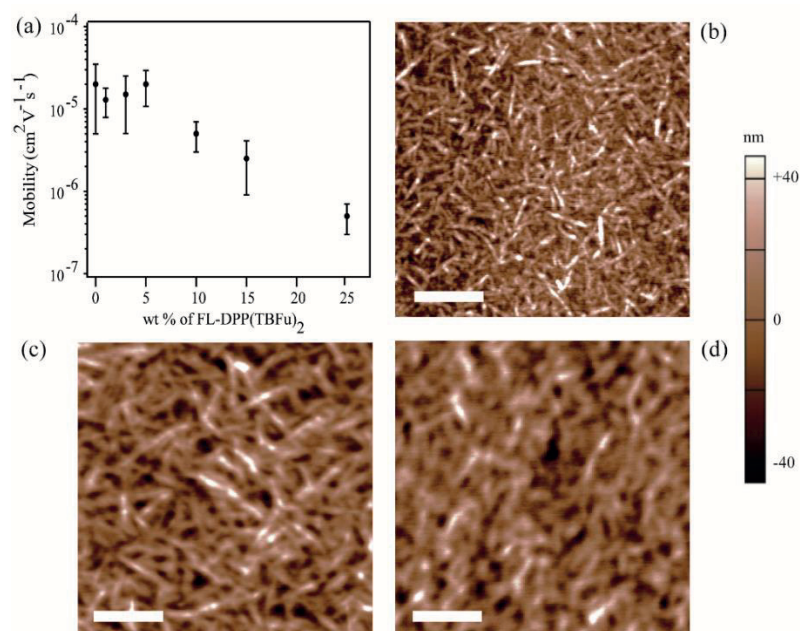


**Figure 6-2.** (a) Average extracted field effect mobility as a function of FL-DPP(TBFu)<sub>2</sub> weight percentage. Atomic force micrographs of as cast films with with b) 0 wt% c) 1 wt% and d) 5wt% of FL-DPP(TBFu)<sub>2</sub>. Scale bar is 1  $\mu\text{m}$ .

To better establish the thermal stability of the active layer, a set of devices, prepared by annealing at 100°C so that they have similar initial performance, were further subjected to a long-term thermal stress, with periodic quenching to 30°C for testing. The measured  $\mu_{\text{FET}}$  is reported against the annealing time at 100°C in Figure 6-4. While  $\mu_{\text{FET}}$  drops an order of magnitude for  $f_{\text{FL}} = 0$ , a considerably smaller decrease is observed when  $f_{\text{FL}} = 1$  wt%, and notably at 5 wt% the performance remains constant. Visualizing the active layer morphology with atomic force microscopy (AFM) gives further insight into the origin of the improved thermal performance of the transistors with the added FL-DPP(TBFu)<sub>2</sub>. As-cast films with 0-5 wt% of the FL additive all exhibit a similar fibril-type morphology, but with a slightly larger feature size when the additive was present. After the extended thermal stress test at 100°C for a total of 3 hours, a drastic difference is observed between the topology of the films as shown in Figure 6-4. The neat (0 wt%) device exhibits small circular domains (ca. 100-200 nm) and a few longer shards. The disappearance here of the initial fibril type morphology may be due to a dewetting from the substrate or possibly caused by the formation of defects during the rapid quenching process at the semiconductor dielectric interface,<sup>[85]</sup> which propagate and alter the domain morphology. Indeed, the thermal

annealing of solution-processed molecular semiconductor films has recently been shown to induce the formation of trap states, likely at grain boundaries, that reduce charge carrier transport.<sup>[35]</sup>

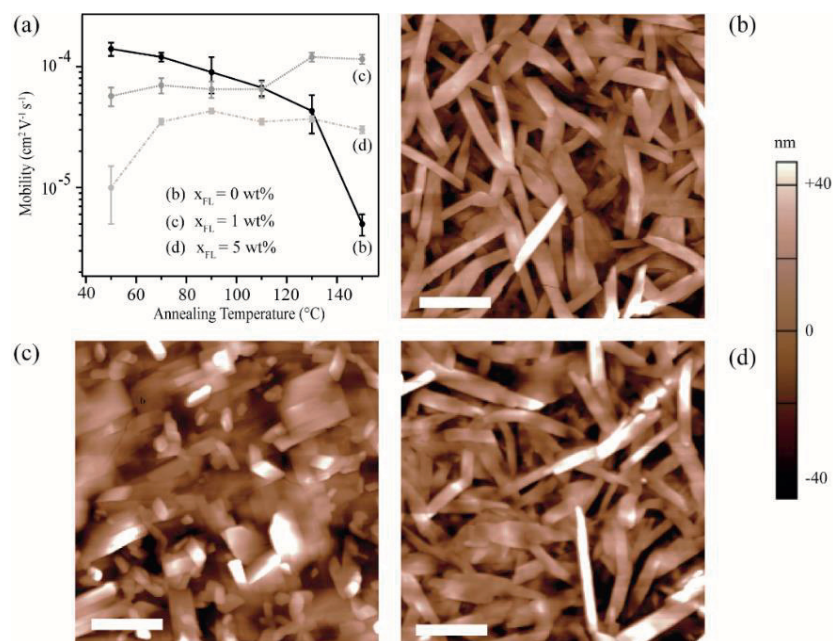


**Figure 6-3.** (a) Average extracted field effect mobility as a function of thin film annealing temperature. Atomic force micrographs (b-d) show the topology of the thin film transistor active layer after annealing at 190°C with b) 0 wt% c) 1 wt% and d) 5wt% of FL-DPP(TBFu)<sub>2</sub>. The scale bar is set at 2.5 μm.

In stark contrast to the neat DPP(TBFu)<sub>2</sub> devices, when  $f_{FL} = 1$  or 5 wt%, films exhibit large banded features that are 200-500 nm in width and more than a micron in length after the extended annealing test. In addition, the roughness of the film decreases considerably with  $f_{FL} = 5$  wt%. The transistor device thermal stability data, together with the evolution of the morphology, demonstrate that the FL-DPP(TBFu)<sub>2</sub> actively participates in the stabilization of the thin-film charge transport network. In contrast to the typical behavior of a nucleation promotor, which increases the number of nucleation events thus leading to a smaller crystalline domain size,<sup>[81b]</sup> the FL additive also apparently promotes larger crystalline domains. Given the relatively short length of the FL polymer chain (ca. 40 nm) compared to the observed domain size, and the amount of FL additive employed, this explanation would be possible if the FL-additive is positioned at the crystal grain boundaries and a polymer chain bridged two adjacent domains.

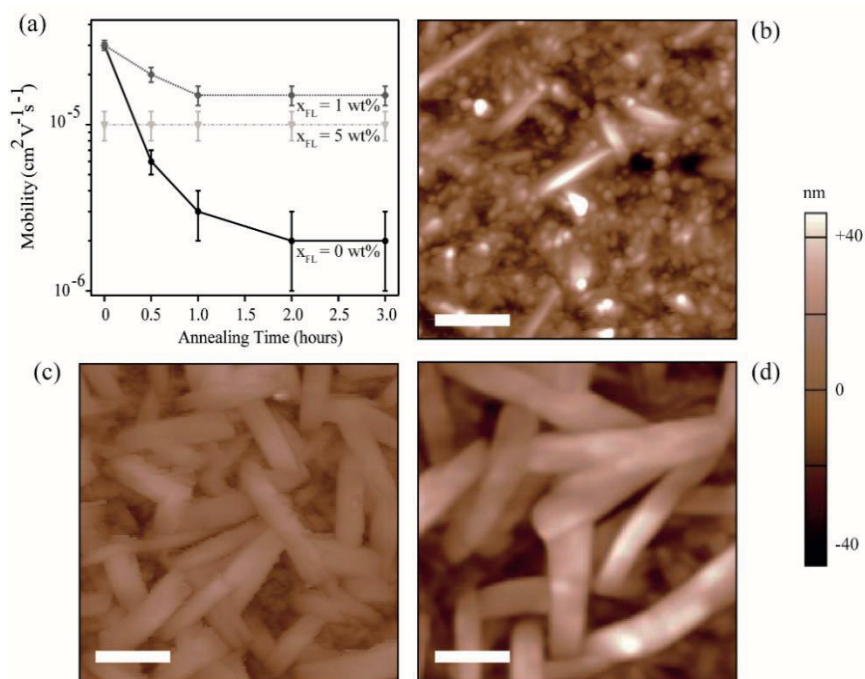


**Figure 6-4.** (a) Field effect mobility as a function of annealing time at 100°C. Atomic force micrographs (b-d) show the topology of the thin film transistor active layer after 3.0 hours at 100°C with b) 0 wt% c) 1 wt% and d) 5wt% of FL-DPP(TBFu)<sub>2</sub>. Scale bar is 500 nm.

This is reasonable as the FL-additive is likely positioned at the grain boundary due to its action as a nucleation promotor. However, we do not suspect that the FL-additive can act as a traditional tie-molecule, which typically would link many crystallite domains. Another aspect that may affect the formation of a more stable charge transport network is the nucleation of a different crystal form of the DPP(TBFu)<sub>2</sub> via the FL additive. Indeed polymorph formation has been observed with stereoisomers of DPP(TBFu)<sub>2</sub> and are known to have an effect on the charge transport.<sup>[86]</sup> Analysis of thick films (deposited on SiO<sub>2</sub> and annealed at a high temperature of 190 °C, yet below the melting point, to maximize crystallinity) by grazing incidence wide angle X-ray scattering (GIWAX, Figure 6-5) supports the notion that a change in crystal formation could play a role. While at  $f_{\text{FL}} = 0$  the diffraction peaks match previously reported films annealed at low temperature (80°C),<sup>[81a]</sup> distinctive Bragg rods are observed when  $f_{\text{FL}} = 1 \text{ wt}\%$ , suggesting a thin film polymorphism. Analysis of the films annealed at 190°C by AFM supports this by indicating a clear change from fiber-like features (500 nm in width) observed in the neat film



(Figure 6-5a) to wide platelets observed with  $f_{FL} = 1$  wt% (Figure 6-5b). While the complete understanding of the complex role of the FL- DPP(TBFu)<sub>2</sub> on the thin film crystallinity is undoubtedly beyond the scope of this initial demonstration of the flexible linker concept, the strong effect of the FL additive on the morphology and performance of donor-only films is clear.

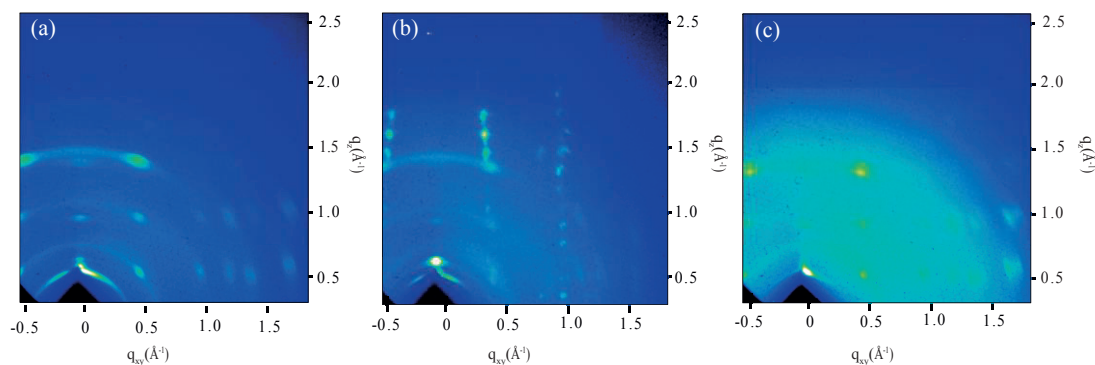


**Figure 6-5.** 2D GIWAXS images of (a) neat DPP(TBFu)<sub>2</sub> thin films (b) thin films with 1 wt % of FL-DPP(TBFu)<sub>2</sub> and (c) thin films with 5 wt % of FL-DPP(TBFu)<sub>2</sub> annealed at 190 °C.

#### 6.2.4 Effect of flexible linker additive in Bulk heterojunction solar cells

Given the common use of DPP(TBFu)<sub>2</sub> as an electron donor small molecule blended in bulk heterojunction (BHJ) photovoltaic cells with fullerene-based electron acceptors, we next probed the effect of the inclusion of the FL additive in DPP(TBFu)<sub>2</sub>:PC<sub>61</sub>BM solar cells. Standard ITO/PEDOT:PSS/BHJ/Al devices were fabricated by standard procedures as described in the experimental section. We compared the performance of devices with  $f_{FL} = 0 - 5$  wt% (based on the total mass of the active layer in DPP(TBFu)<sub>2</sub>:PC<sub>61</sub>BM blends at a ratio of 3:2) and found for devices tested without annealing, the photovoltaic figures of merit,  $J_{sc}$ ,  $V_{oc}$  and FF were not affected by the presence of the FL additive (Figure 6-6a) and were consistent with previous reports with “as-cast” active layers. The invariance of  $V_{oc}$  supports the notion that the presence of the additive does not change the HOMO level of the donor phase, which is reasonable considering the nature of the conjugated segment is unchanged. The unchanging  $J_{sc}$  and FF values of the as-cast devices with  $f_{FL} = 0 - 5$  wt% suggest that the FL-additive does not have a significant effect on the BHJ morphology during the initial film formation (spin casting from chlorobenzene), despite its established activity as a nucleation promotor for the donor phase.

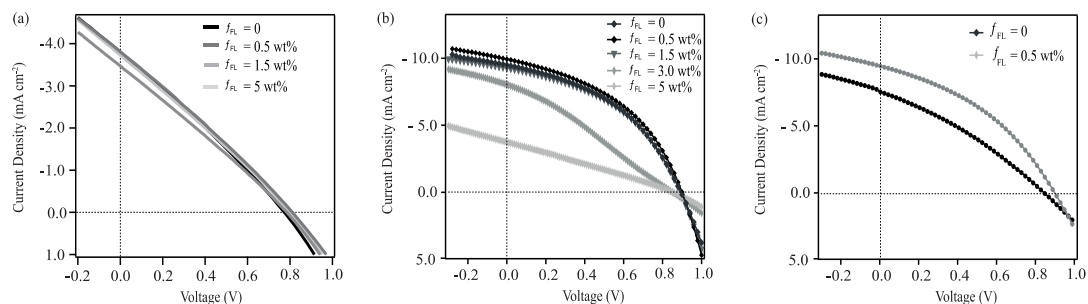


**Figure 6-6.** Upper Panel. J-V curves for as-cast BHJ photovoltaic devices (a) not annealed (b) annealed at 110°C of 90 nm thick active layer (c) and annealed 140 nm thick active layer with 3:2 DPP(TBFu)<sub>2</sub>:PC<sub>61</sub>BM and a loading of FL- DPP(TBFu)<sub>2</sub> as indicated.

Annealing devices with  $f_{FL} = 0$  at 100°C for 10 min gave an average device PCE of  $3.4 \pm 0.3\%$ . We note that this value is slightly lower than state-of-the-art values obtained when using PC<sub>71</sub>BM due to an expected lower  $J_{sc}$  with the use of PC<sub>61</sub>BM here. Devices with  $f_{FL} = 0.5$  and 1.5 wt% exhibited equivalent performance when the annealing time was optimized to one hour, instead of 10 min in the  $f_{FL} = 0$  case. Optimized “best-case” J-V curves for  $f_{FL} = 0 - 5$  wt% are shown in Figure 6-6b and the average PCE as a function of the annealing time at 100°C is shown for  $f_{FL} = 0$  and 0.5 wt% in Figure 6-8a. When  $f_{FL} = 3$  or 5 wt%, the best-case J-V performance (Figure 6-6b) is significantly decreased, exhibiting lower FF and  $J_{sc}$ , which indicates increased recombination and poorer charge carrier transport. Remarkably, the thermal stability of the device performance was found to be significantly different between the  $f_{FL} = 0$  and 0.5 wt%.

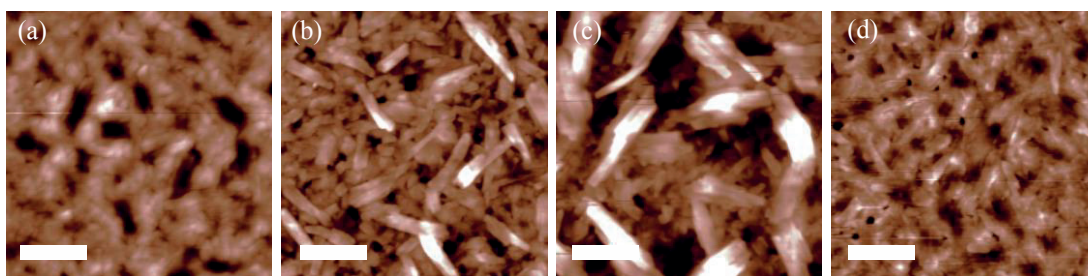


**Figure 6-7** Atomic force microscopy images of as-cast DPP(TBFu)<sub>2</sub>:PCBM blends with a) 0 wt% b) 1.5 wt% c) 3 wt% and d) 5 wt% of FL-DPP(TBFu)<sub>2</sub>. The scale bar is 500 nm.

After only 3 hours of thermal stress at 100°C, a decrease in the PCE from 3.4% to 2.3% is observed when  $f_{FL} = 0$ . This observed trend, common for many systems employing PC<sub>61</sub>BM, is primarily attributed to a decrease in FF and  $J_{sc}$  due to the phase segregation of the PC<sub>61</sub>BM from the donor phase. In contrast, device performance remains stable at 3.2% with  $f_{FL} = 0.5$  wt%, even after 22 hours of annealing at 100°C. This suggests a different evolution of the microstructure of the BHJ during the thermal stress test. However, supposing that the longer rod-shaped donor domains observed in stabilized BHJ blends with the FL-additive could afford improved charge carrier transport over longer distance, we hypothesized that a greater difference in device performance (with and without the FL-additive) would be observed if thicker active layers were employed.

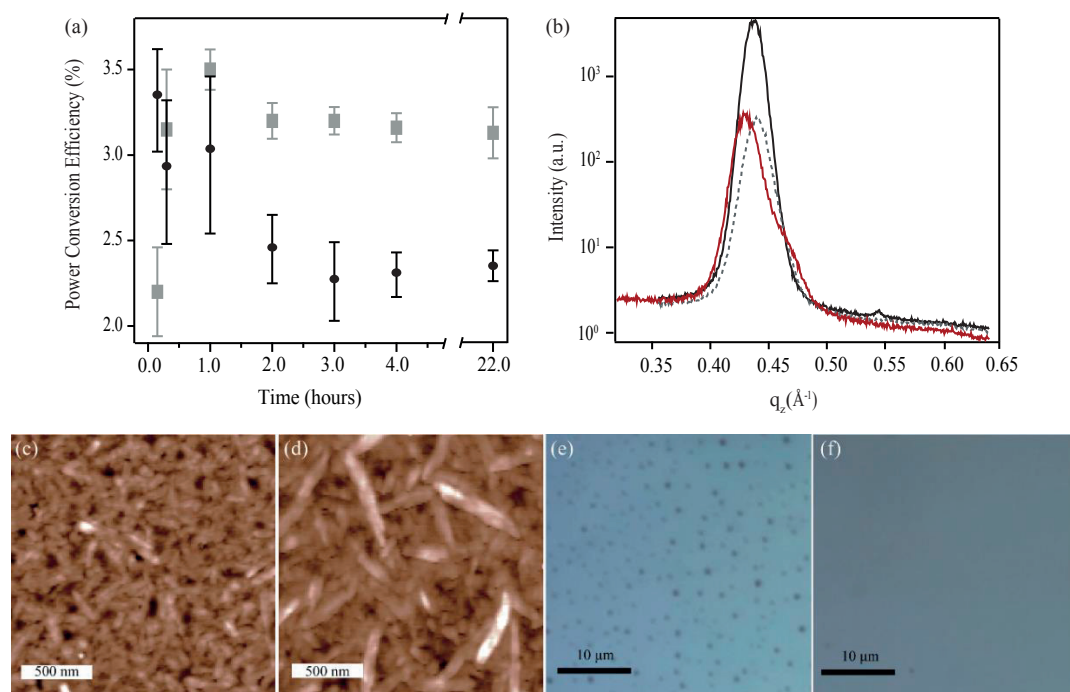


**Figure 6-8.** (a) Average power conversion efficiency as a function of the annealing time at 100°C for neat film (black dots) and with 0.5% of FL- DPP(TBFu)<sub>2</sub> ( grey dots) (b) Out-of-plane x-ray diffraction (radiation / wavelength: Cu K-alpha 1, 0.154 nm) around the (020) peak of neat DPP(TBFu)<sub>2</sub> : PC<sub>61</sub>BM thin films (red line) before and after (black line) 22 hours annealing and (grey dashed line) with the addition of 1.5 wt% of FL-DPP(TBFu)<sub>2</sub>. Films thickness of all samples were measured to be 150 ± 5 nm. Atomic force microscopy images of DPP(TBFu)<sub>2</sub>:PCBM blends after annealing at 100°C for 22h with c) 0 wt% d) 0.5 wt% of FL-DPP(TBFu)<sub>2</sub>. The scale bar is 500 nm. Optical microscopy of the same film (e) shows an overview of the film and the many PCBM regions. In contrast the optical image of the film with 1.5 wt% of the FL-additive after annealing at 100°C for 22 hours (f) shows few large phase segregated regions.

To provide preliminary evidence to support this notion, we increased the thickness of the active layer by 50% (i.e. from 90 nm to 140 nm). After optimized annealing at 100°C, devices with  $f_{\text{FL}} = 0$  gave a 40% lower PCE compared to devices with  $f_{\text{FL}} = 0.5$  wt% (Figure 6-6c). As expected, the difference was due to a drop in FF and  $J_{\text{sc}}$  which are found to be, respectively, 0.34 and 7.5 mA cm<sup>2</sup> (for  $f_{\text{FL}} = 0$ ), compared to 0.45 and 9.9 mA cm<sup>2</sup> (for  $f_{\text{FL}} = 0.5$  wt%). Even though significant PCE improvement was not observed over the thinner cells, this result suggests that in thicker BHJ films—where increased crystallinity is required to afford efficient charge extraction—the FL-additive can support a more intimate mixing of the donor and acceptor, while still providing suitable crystallinity for charge transport. Moreover, we note that out-of-plane XRD measurements in BHJ indicate that the donor has similar crystallinity in the blend film without the FL-additive after 10 min annealing compared to the  $f_{\text{FL}} = 0.5$  wt% blend film when annealing for 1 hour (Figure 6-8b), therefore no increased overall crystallinity of the donor phase is observed using the FL-additive, consistent with the DSC results which suggest a slight decrease in donor crystallinity.

### 6.2.5 Surface composition characterization by Nanomechanical indentation

Insight into the origin of the improved thermal stability of the donor:acceptor blends with the FL-additive was next sought by examining the morphology of the active layer with AFM and nanomechanical mapping<sup>[87]</sup> to identify donor-rich and acceptor-rich domains. Indeed, as the Young's modulus (YM) of neat PC<sub>61</sub>BM (ca. 17 GPa) and neat DPP(TBFu)<sub>2</sub> (ca. 3 GPa) are significantly different (Figure 6-9), YM mapping can give information on the domain composition. Combined topographical and YM map results are shown in Figure 6-10. The active layer topography after annealing at 100°C for 10 min (unconfined by the Al top electrode) is shown in Figure 6-10a (left panel), and exhibits rod-shaped domains 100-200 nm in size when  $f_{\text{FL}} = 0$  (similar to previous reports<sup>[48]</sup>). We note that the topography of as-cast BHJ films when  $f_{\text{FL}} = 0 - 5$  wt% are similar, except with slightly larger rod-shaped domains for  $f_{\text{FL}} = 0.5$  and 1.5 wt% (Figure 6-7a and Figure 6-7b). The YM maps are displayed to the right of their corresponding topography images in Figure 6-10. Here domains of low YM, corresponding roughly to the rod-shaped domains, are distinguishable from areas of higher modulus, confirming that these rod domains are donor-rich and further suggesting that the donor and acceptor are mixed at a length scale of ca. 100 nm. For films with no FL-additive ( $f_{\text{FL}} = 0$ ) that have been annealed for 22 hours at 100°C, the topology (Figure 6-8c) shows the absence of rod-shaped domains and the presence of circular domains, similar to the donor only film shown in Figure 6-7a. The corresponding YM map gives values < 6 GPa suggesting that the surface of the film is composed primarily of DPP(TBFu)<sub>2</sub> (i.e. no PC<sub>61</sub>BM-rich domains

are present). Indeed, micron-sized PC<sub>61</sub>BM-rich domains are observed by AFM, YM mapping, (Figure 6-9c and Figure 6-9d) and by optical microscopy (Figure 6-8e) suggesting that the PC<sub>61</sub>BM has segregated from the DPP(TBFu)<sub>2</sub> on a length scale too-large for BHJ operation.

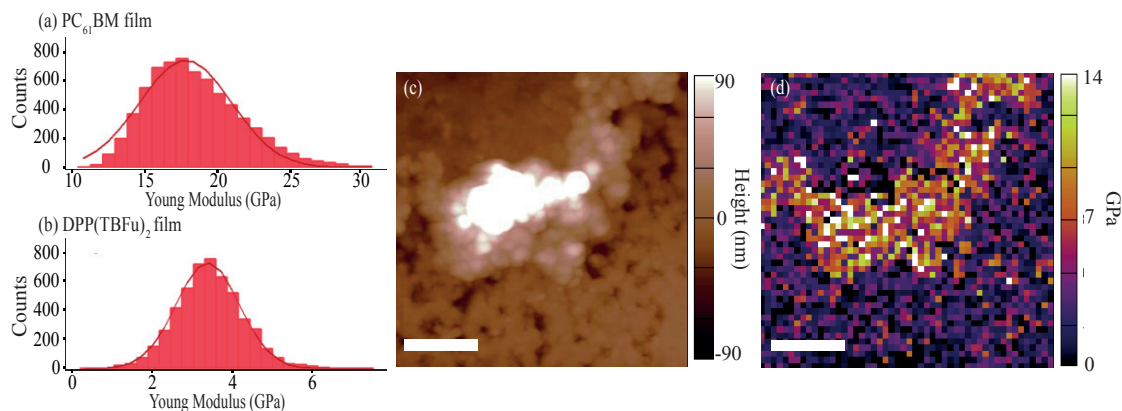


**Figure 6-9.** Distribution of calculated Young's Modulus on films a) PC<sub>61</sub>BM and b) DPP(TBFu)<sub>2</sub>. The data come from measuring neat films after annealing at 100°C for 10 min. note the different scales on the x-axis. YM maps and optical microscopy of thin films. (c) shows the topography a DPP(TBFu)<sub>2</sub>:PCBM without the FL-additive and annealed for 22 hours at 100°C. Here a section of the film with a large phase segregated region is shown. The Corresponding YM map (d) shows that the large phase segregate region is of high YM consistent with PCBM.

We note that the performance of the corresponding photovoltaic device ( $f_{FL} = 0$ ) after annealing for 22 hours likely stabilizes at a non-zero value due to the effect of the morphological confinement brought by the Al top contact.<sup>[88]</sup> With the FL-additive present in the BHJ, a considerably different morphology is observed after thermal annealing for 22 hours (Figure 6-8d). In this case the topography shows a comparatively rougher film with longer rod-shaped domains similar to those observed in the neat films (Figure 6-8c). The YM map indicates that these rod-shaped regions exhibit a lower modulus consistent with the DPP(TBFu)<sub>2</sub>. Moreover, we note that Young's moduli higher than 10 GPa are also measured in high proximity to the rod-shaped domains, indicating that small PC<sub>61</sub>BM-rich domains remain present in the film with the FL-additive present after thermal treatment for 22 hours. This considerable difference in behavior of the morphology is indeed consistent with the observed difference in device performance and suggests that the FL-additive strategy is effective at extending the morphological stability

of BHJ molecular solar cells. In addition, we note that our morphological observations suggest an apparent increase in donor domain size when the FL-additive is present in blends with PC<sub>61</sub>BM and optimized thermal annealing is performed.

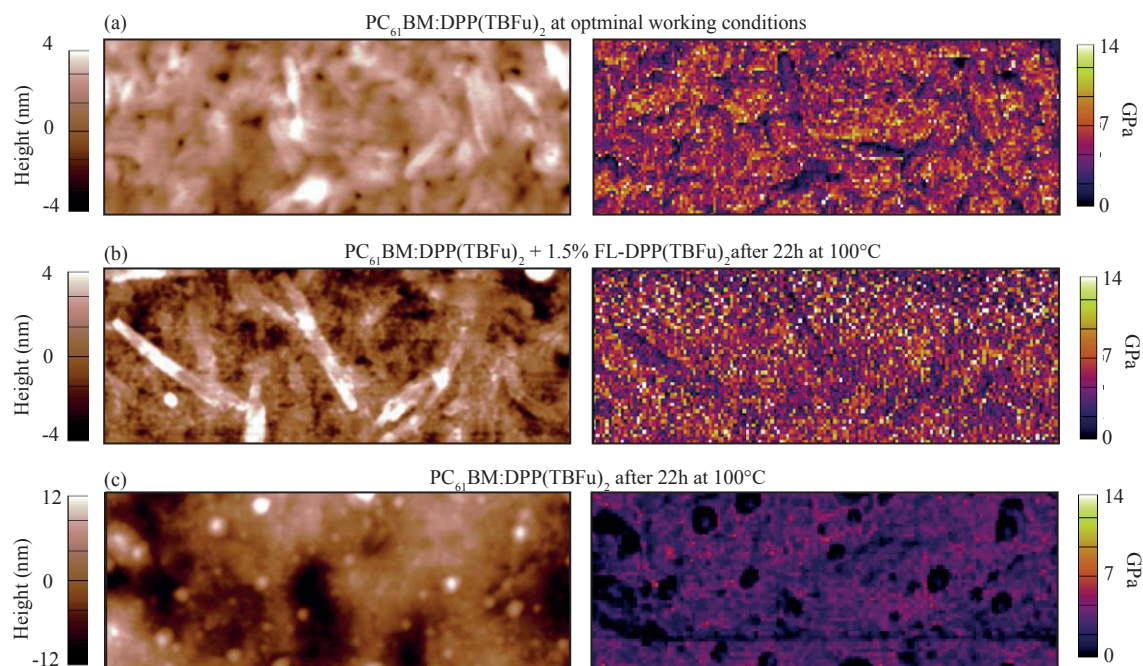


**Figure 6-9.** Bulk heterojunction topography (left panels) and Young's modulus mapping (right panels) of the corresponding area. The scale bars is 500 nm.

## 6.3 Conclusions

The improved BHJ thermal stability and lower comparative donor crystallinity can be rationalized again by the ability of the FL-additive to promote the nucleation of the donor phase. The presence of the amorphous FL-additive at the grain boundaries of the donor crystallites can maintain a stable donor transport network while also providing amorphous regions for PCBM, thereby limiting PCBM exclusion. This combination of beneficial characteristics is unique among additives to bulk heterojunctions. We cannot, however, exclude the possibility of donor polymorph formation playing a role in the BHJ stability. Indeed, we would not expect a difference in the XRD analysis as polymorphs reported for DPP(TBFu)<sub>2</sub> exhibit similar scattering vectors for the main peak.<sup>[86]</sup> Further analysis of the BHJ crys-

tallinity is a point of interest given these initial results. Importantly, we note that the FL-additive strategy presented here is significantly different than recently-reported approaches to reactively cross-link the donor and acceptor after BHJ formation. While these crosslinking approaches have been shown to improve the thermal stability of BHJs when polymer donor phases are used, as a drawback, they rely on the uncontrolled reaction of functional groups that likely add electronic defects to the film. In addition, we emphasize that the observed behavior of the FL-additive is also distinct from simply blending in insulating (inert) polymer additives, in molecular bulk heterojunctions.<sup>[82]</sup> While this approach offers some control over the thin film formation, since the inert polymer segregates from the BHJ, it does not improve thermal stability. Overall the device results and morphological investigations presented here demonstrate that the strategy of linking molecular semiconductors with flexible aliphatic chains to polymers that possess defined conjugated segments, but extended covalent connectivity, is a viable way to control the crystalline behavior of solution-processed molecular semiconductor thin films.





# Chapter 7

## Synthesis and characterization of alternated multiblock copolymers

### 7.1 Introduction

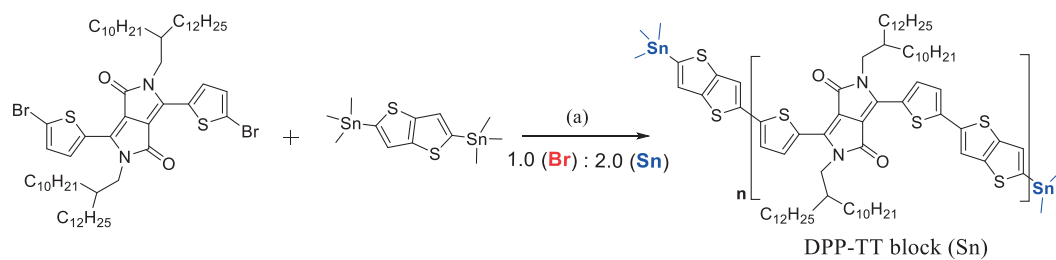
As introduced in Section 2-2, in an ideal BHJ, high interfacial area between pure donor and acceptor phases is required to efficiently separate the generated excitons into free charges. However, the domain interconnectivity must also be retained to afford continuous percolating pathways for charge collection at the electrodes. Among many strategies to control the BHJ morphology, post-deposition thermal annealing and the use of high boiling solvent additives have been used most recently exploited to tune nanoscale domain size by promoting partial phase separation of the donor and acceptor, thus leading to enhancement mainly in short circuit photocurrent.<sup>[89]</sup> Despite the control over the thin film formation and crystalline domain size that these approaches offer, they do not specifically impact intrinsic stability of the active layer morphology. Indeed, the thermodynamic immiscibility of the chemically dissimilar components induces macroscopic phase segregation in the active layer and inevitably decreases device performance during standard operational conditions.<sup>[6b]</sup> It is thus of great interest to develop a single material that can self-assemble into a thermodynamically stable morphology of hole and electron conducting domains at the nanoscale level. The use of conjugated block copolymers (BCP), consisting of covalently joined conjugated segments (usually a donor and an acceptor block) have been envisaged as active materials in OPV given their unique structural control through micro-phase separation and desirable retention of optoelectronic properties of both constituent polymeric blocks.<sup>[90]</sup> Despite recent advances in the PCE in solar cells using a donor-acceptor di-block copolymer coded, P3HT-b-PFTBT, only a very limited number of fully conjugated donor-acceptor block copolymers have been reported.<sup>[91]</sup> In fact, the lack of widely applicable synthetic strategies for conjugated block copolymer synthesis limits the comprehensive screening necessary to optimize and improve charge carrier properties and self-assembly in high performance devices. The most successful strategies involve the step growth polycondensation of AB type monomers onto mono functionalized rr-P3HT.<sup>[92]</sup> However, this widely used method results in a substantial mixture of homo-polymers and block copolymers due to the low yielding reaction mechanism. Hawker et al. recently developed a modular strategy to improve the yield in step

growth reactions by employing Stille coupling polymerization of AA + BB monomers along end-functionalized rr-P3HT chains.<sup>[49a]</sup> The higher MW achieved in a P3HT-b-DPP di-block copolymers showed unprecedented phase separation of the donor and acceptor crystalline domains and paved the way for low-band gap polymer incorporation in block copolymers for OPV. Albeit high yielding chemistries were developed, the not trivial replacement of rr-P3HT in block copolymer step growth polymerization and the restricted number of molecular architectures accessible (i.e. diblock and triblock) remain still considerable limitations for applications of block copolymers in optoelectronics. To address this challenge and open new directions in block copolymer design, the development of synthetic methods that can afford access to an unlimited portfolio of nanostructured morphologies with expanded physical properties is required.<sup>[93]</sup> Herein, we present a new synthetic strategy to synthesize the first of a class of fully conjugated and alternating multi-block copolymer (MBC) composed of electron donating poly-(2,5-bis(3-alkylthiophen-2-yl)thienothiophene) (PBTTT) and two electro-accepting blocks based diketopyrrolopyrrole - thienothiophene copolymer (DPP-TT) and perylenediimide-thiophene (PDI-T) block. Furthermore, the facile nature of the synthetic procedure reported herein enables high degree of polymerization and offers the possibility to replace the use of rr-P3HT as both donor material and initiator in previously reported step growth reactions. Ultimately, when the alternating multi-block copolymers are solution processed in to thin films, a relatively high degree of self-assembly and micro-domain phase separation is observed.

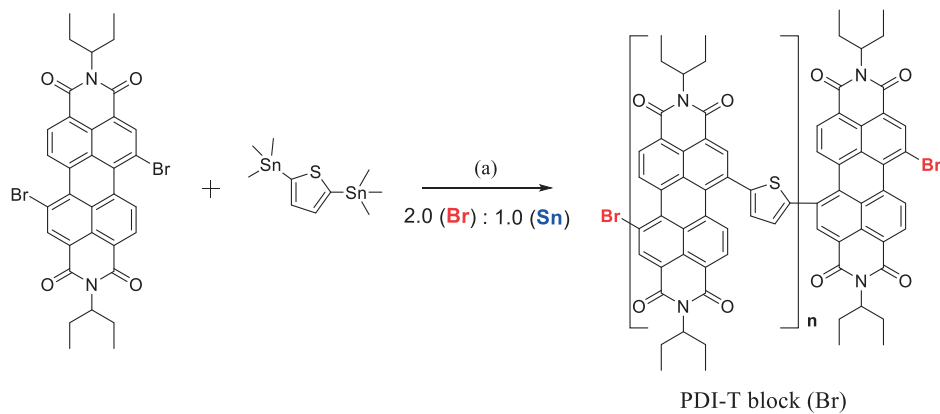
## 7.2 Results and discussion

### 7.2.1 Synthesis and characterization

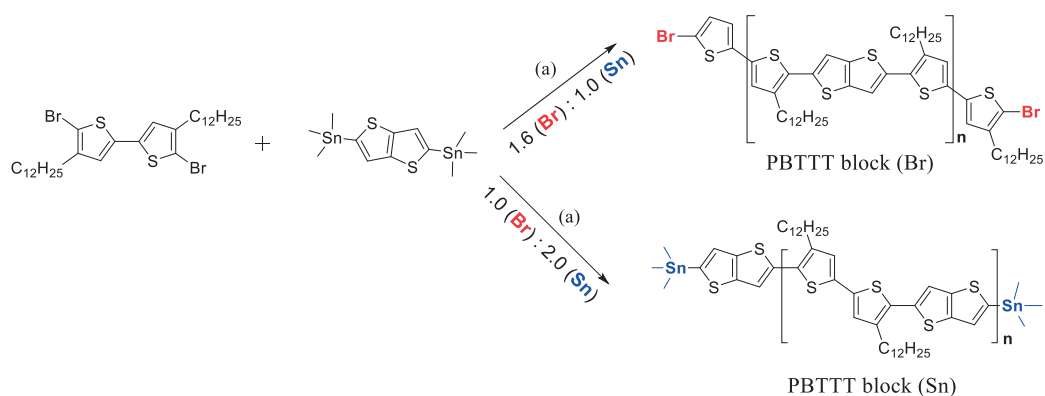
The synthesis of two alternating multiblock copolymers, coded **MBC1** and **MBC2** is shown schematically in Scheme 7-4 and Scheme 7-5. As recently developed by our group<sup>[23]</sup>, bromine di-functionalized conjugated blocks can be produced by classical Stille-coupling through an imbalanced stoichiometry of AA (brominated) vs. BB (trimethyl-stannylated) type monomers in PBTTT (Scheme 7-3). Here we extended this strategy to low-band gap polymers like DPP-TT (Scheme 7-1) and PDI-T (Scheme 7-2). Accordingly, the block length was tuned between 5 kDa and 14 kDa with polydispersity of 1.2-1.3 for all three polymeric “macromonomer” synthesized. As shown in the NMR and MALDI-TOF-MS spectra (see Appendix chapter) the functionalization method developed for di-brominated macromonomer also proved to be successful to directly functionalize polymeric macromonomers with trimethyl-stannyl end groups.



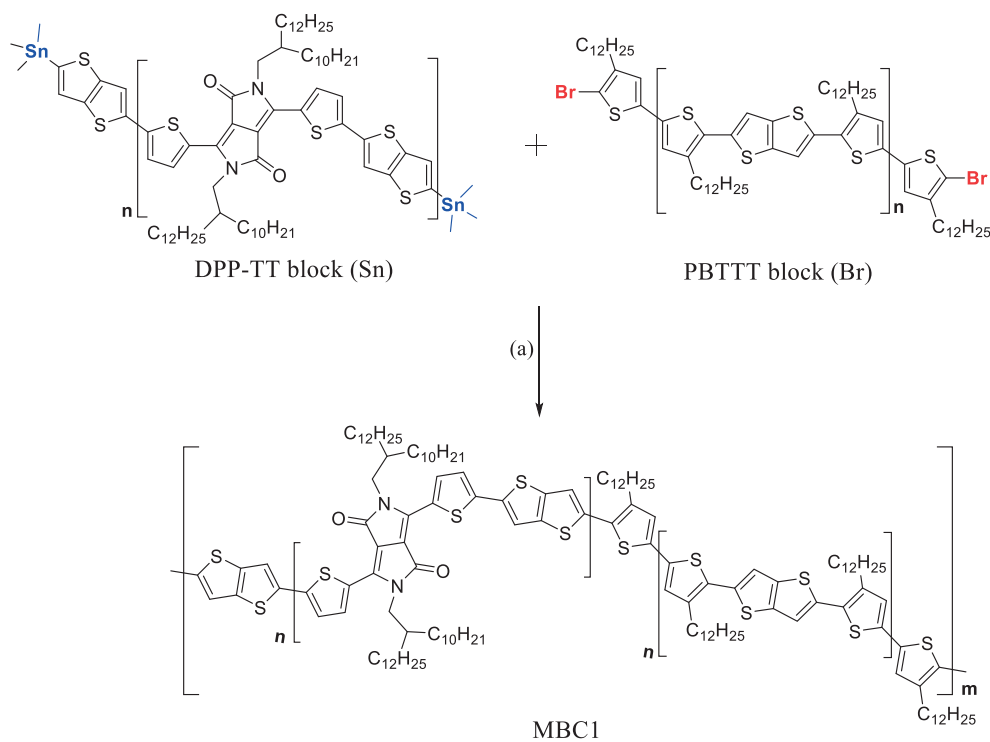
**Scheme 7-1.** Synthetic path for the synthesis of the di-stannylated DPP-TT block ( $M_n = 5$  kDa, PDI 1.2). Typical values of  $n = 3$ -6 repeating units. Polymerization condition a)  $\text{Pd}_2(\text{dba})_3$ ,  $\text{P}(\text{o-Tol})_3$  in chlorobenzene for 2h at 60 °C.



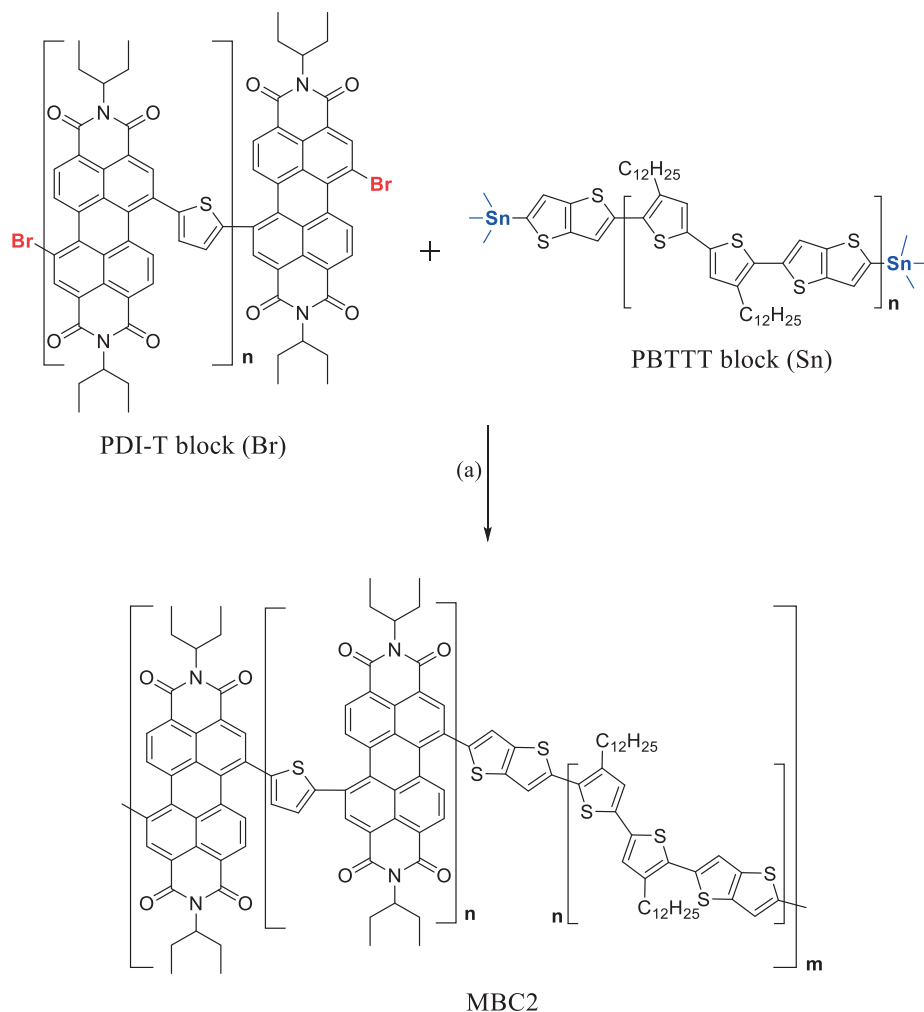
**Scheme 7-2.** Synthetic path for the synthesis of the di-brominated PDI-T block ( $M_n = 7$  kDa, PDI 1.3). Typical values of  $n = 6$ -10 repeating units. Polymerization condition a)  $\text{Pd}_2(\text{dba})_3$ ,  $\text{P}(\text{o-Tol})_3$  in chlorobenzene for 2h at 100 °C.



**Scheme 7-3.** Synthetic path for the synthesis of the di-brominated PBTTT block ( $M_n = 10$  kDa, PDI 1.2) and di-stannylated PBTTT block ( $M_n = 14$  kDa, PDI 1.2). Typical values of  $n = 10$ -15 repeating units. Polymerization condition a)  $\text{Pd}_2(\text{dba})_3$ ,  $\text{P}(\text{o-Tol})_3$  in chlorobenzene for 2h at  $60^\circ\text{C}$ .



**Scheme 7-4.** Synthetic path for the synthesis of the alternated multi block copolymer MBC1 ( $M_n = 51$  kDa, PDI 1.2) after purification by prep-SEC. Typical values of  $m = 5$ -7 repeating units. Polymerization condition a)  $\text{Pd}_2(\text{dba})_3$ ,  $\text{P}(\text{o-Tol})_3$  in chlorobenzene for 1h at  $100^\circ\text{C}$ .



**Scheme 7-5.** Synthetic path for the synthesis of the alternated multi block copolymer MBC2 ( $M_n = 65\text{kDa}$ , PDI 1.2) after purification by prep-SEC. Typical values of  $m = 6-8$  repeating units. Polymerization condition a)  $\text{Pd}_2(\text{dba})_3$ ,  $\text{P}(\text{o-Tol})_3$  in chlorobenzene for 1h at  $100^\circ\text{C}$ .

In fact, MALDI-TOF-MS confirms an almost quantitative functionalization of terminal groups in di-brominated and di-stannylated blocks. **MBC1** (Scheme 7-4) was synthesized by Stille coupling polycondensation between the di-brominated PBT TT macromonomer (6,  $M_n = 10\text{ kDa}$ ) and the di-stannylated DPP-TT macromonomer (8,  $M_n = 5\text{ kDa}$ ). **MBC2** (Scheme 7-5) was synthesized following the same procedure for **MBC1** but the coupling reactions included di-stannylated PBT TT macromonomer

( $M_n = 14$  kDa) and di-brominated PDI-T macromonomer ( $M_n = 7$  kDa). We note also that for macromonomer copolymerization, a precise 1:1 ratio between AA + BB segments was empirically determined to be necessary to afford macromonomer polymerization. In this view, achieving low polydispersity of the starting blocks is advantageous for accurately determining the number of end-groups, and for verifying the successful progression of the MBC polymerization. As shown by the analytical size exclusion chromatography (SEC) data in Figure 7-1, the Stille cross-coupling polymerization successfully increased the molecular weight, but potentially left some portion of unreacted macromonomers. The subsequent purification of the MBC polymerization by preparatory-SEC afforded fractions of high-MW multiblock copolymers with a number average molecular weight of 50 kDa for **MBC1** and 60 kDa for **MBC2** with polydispersity of 1.2-1.3 ( $n = 6-8$ ). From the analytical GPC trace it is reasonable to conclude that the purified fractions are almost homopolymer free (less than 5% overlap).

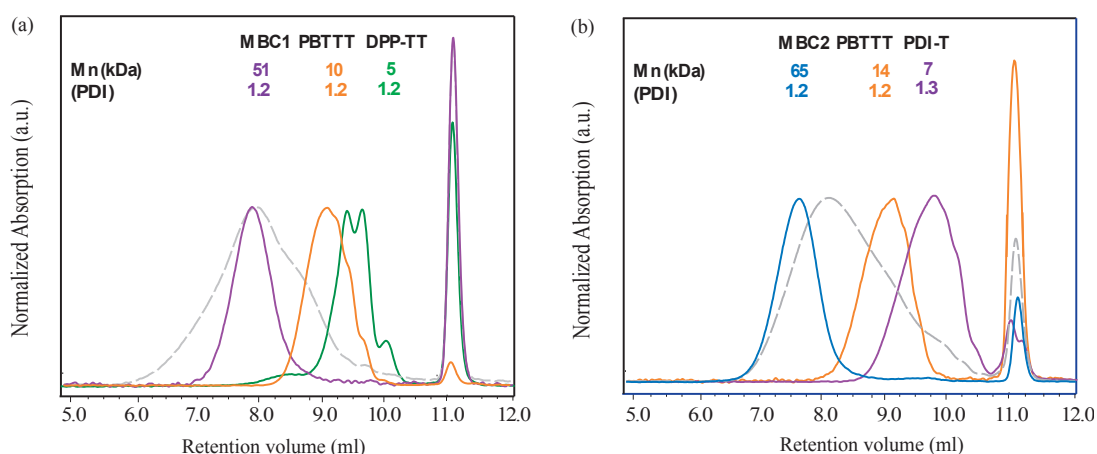


**Figure 7-1.** GPC traces for MBC1 (a) and MBC2 (b) and corresponding starting blocks. The grey broken lines show the crude polymerization.

Due to the nature of the condensation reaction occurring during block polymerization, it is critical to fully characterize the reaction products and to provide evidence of the incorporation of both blocks in the final multiblock copolymer. In the  $^1\text{H-NMR}$  spectrum of **MBC2**, two peaks corresponding to the alkyl chains of PDIT and PBT TT segments are observed at  $\delta = 5.11$  and 2.84 ppm and for aromatic ring at 8.74 and 7.11 ppm respectively (see Figure S10-18 in Appendix). These results clearly indicate that the incorporation of PBT TT segments and PDIT segments was successful and yielded the desired block

copolymers. We note that the observed area of the aliphatic chain and aromatic ring peaks indicate a ratio between the blocks of 1:2, that consistent the presence of shorter PDIT ( $M_n = 7$  kDa) chains compared to the PBTTT ( $M_n = 14$  kDa) segment. The expected unbalance in the NMR peak integration seems also to suggest that an equal number of PDIT and PBTTT blocks are presence on average along the same chain. The electronic configuration (HOMO/LUMO levels) of the multi-block polymers in the solid state thin film configuration was then investigated by cyclic voltammetry (CV) to further support the incorporation of both macromonomer moieties. All the multiblock copolymers and the parent homopolymers show a single reversible reduction wave. Figure 7-2 illustrates the oxidation peak of **MBC1**, which is in good correspondence with the oxidation of PBTTT at 0.2 V vs Ag/Ag<sup>+</sup> (HOMO = -4.65 eV) and a reduction peak belonging to DPPTT at -1.25 V vs Ag/Ag<sup>+</sup> (LUMO = -3.65 eV). As already reported, PDI based copolymers typically show two reversible reduction waves commonly assigned to the formation of a PDI polymer anion and dianion.<sup>[94]</sup> Accordingly, **MBC2** shows a weak reduction peak at -1.05 V vs Ag/Ag<sup>+</sup> and visible reduction at -1.25 V vs Ag/Ag<sup>+</sup> as for PDIT block (LUMO = -3.15 eV). The first oxidation peak instead is found at 0.25 V vs Ag/Ag<sup>+</sup> (HOMO = -4.7 eV) which correspond to the PBTTT oxidation potential and a second one at 0.8 V vs Ag/Ag<sup>+</sup> as shown for PDIT.

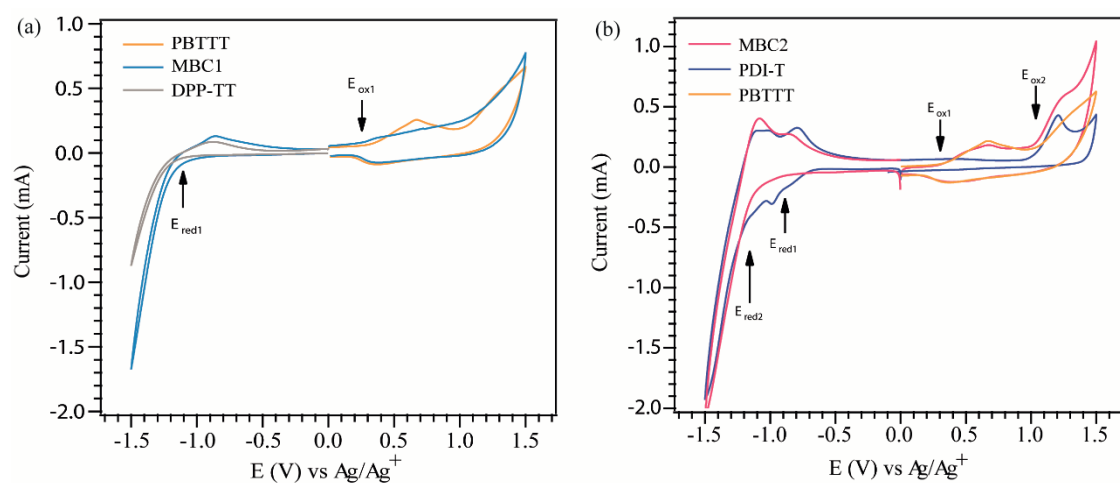


**Figure 7-2.** CV profiles of (a) MBC1 and (b) MBC2. The measurements were recorded at a scan rate of 50 mV/s with 50 mM solution of TBAP as electrolyte in acetonitrile.

## 7.2.2 Block copolymers optical properties

Solution and solid state UV-Vis absorption of **MBC1** (Figure 7-3a, purple line) showed two characteristic absorption peaks resulting from the PBTTT (yellow line) and DPP-TT block (green line) at 480 nm and 700 nm, respectively.<sup>[95]</sup> The thin film absorption spectrum (Figure 7-3a, red line) is significantly red-shifted as compared to the spectrum in solution, suggesting that conjugation length or pi-pi stacking are enhanced during casting. In the solid state, the red-shift of the PBTTT segment is more pronounced and intense compared to the DPPTT block. This observation already suggests that during film formation, the PBTTT rigid block attains a higher degree of order compared to the DPP-TT block. A striking difference is in contrast seen for **MBC2** (Figure 7-3b) where the absorption spectra shows and unbalanced weighted-composition between the PBTTT and PDIT block compared to the NMR data.<sup>[96]</sup> In solution, **MBC2** (Figure 7-3b, black line) shows a clear red-shift from neat PBTTT (yellow line) and an extension of absorption in the region of absorption of PDIT (red line). In thin film (Figure 7-3b, purple line), the lack of a red-shifted absorption shoulder in correspondence of PDIT is attributed to the high percentage (35% from NMR) of highly amorphous PDIT which reasonably induces more random conformations in the high MW fractions of **MBC2** due to the more bulky conformations of the PDIT compared to linear polythiophene chains in PBTTT. Indeed, despite the verified presence of PBTTT, the absence of a vibronic peak and a bathochromic shift in the solid state UV-Vis (normally attributed to effective chain stacking) in **MBC2**, is consistent with this view. The UV-vis spectra suggest also that the precise block selection has a crucial influence on the optical properties of the multiblock copolymer in solution and in particularly in thin films.

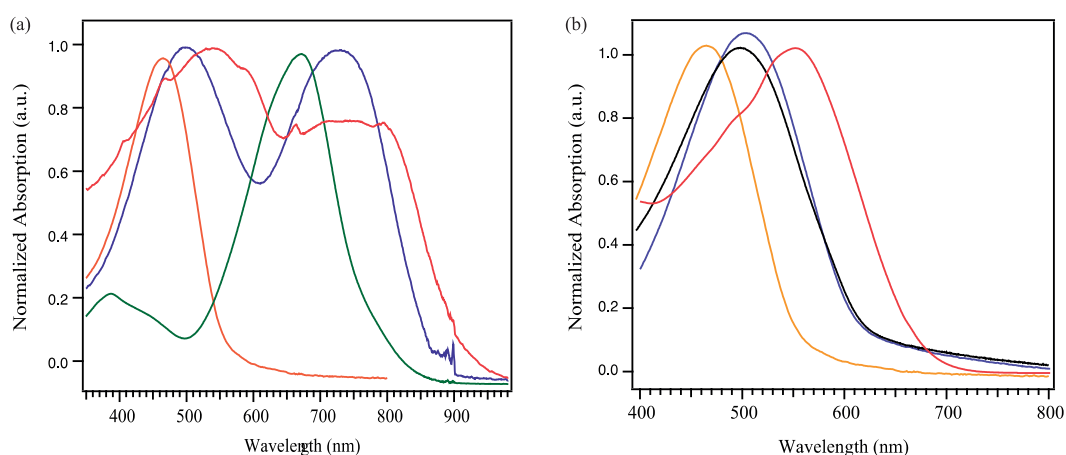


**Figure 7-3.** Absorption spectra in solution and thin films of MBC1 (a) and MBC2 (b).



### 7.2.3 Charge transport in MBC thin films

Given the unexpected difference in absorption spectra between **MBC1** and **MBC2** we were interested to investigate the effect that covalent attachment of the macromonomer blocks has on the field effect charge carrier mobility in this new class of fully conjugated block copolymers. The charge transport properties of **MBC1** and **MBC2** were accordingly investigated in bottom contact/bottom-gate field effect transistors (FETs). Devices were prepared by spin coating from solution at a concentration of 10 mg/ml in o-DCB. Interestingly, as-cast devices processed from **MBC1** gave a hole mobility of  $0.05 \text{ cm}^2 \text{ V}^{-1} \text{ s}^{-1}$ , which is comparable with hole mobility of non-annealed PBTTT of same MW.<sup>[14c]</sup> FETs made from 60 kDa fraction of **MBC2** exhibited a drastic decrease in hole mobility below  $0.000045 \text{ cm}^2 \text{ V}^{-1} \text{ s}^{-1}$  despite the presence of PBTTT segments along the chain like in **MBC1**. Thermal annealing is routinely performed to increase crystalline packing in PBTTT by heating the film above the first LC transition ( $180^\circ\text{C} - 200^\circ\text{C}$ ).<sup>[14a]</sup> In both MBC films annealing resulted in an overall increase in hole mobility, in particular **MBC1** showed a slightly increased in  $\mu_{\text{FET}}$  to  $0.08 \pm 0.01 \text{ cm}^2 \text{ V}^{-1} \text{ s}^{-1}$ . Also in **MBC2**, the measured  $\mu_{\text{FET}}$  double to  $0.0002 \pm 0.0001 \text{ cm}^2 \text{ V}^{-1} \text{ s}^{-1}$  upon annealing at  $200^\circ\text{C}$  while remaining fairly constant up to  $250^\circ\text{C}$ . A similar trend as a function of annealing temperature is observed also for the FET threshold voltage: we found that it decreases from more than +7V in as cast films of **MBC1** to 0V after annealing at  $200^\circ\text{C}$ . Further annealing at higher temperatures reverses the effect back to as-cast values of around +6V. In **MBC2** based FET devices, thermal annealing has no effect on threshold voltage which remained constant at +15V. Overall, the high mobility of **MBC1** compared to the poorer mobility of **MBC2** shows that, by varying the constituent blocks is it possible to maintain stable charge transport properties of PBTTT (or severely reduce it) while adding a second functionality, i.e. high light absorption properties of DPP-TT block. Indeed, low MW blocks of PBTTT show one order of magnitude higher mobility when included in an alternated sequence with DPP-TT in **MBC1** ( $\mu_{\text{FET}} = 0.08 \pm 0.01 \text{ cm}^2 \text{ V}^{-1} \text{ s}^{-1}$ ) than when directly cast in field effect transistors ( $\mu_{\text{FET}} = 0.009 \pm 0.001 \text{ cm}^2 \text{ V}^{-1} \text{ s}^{-1}$ ).<sup>[14c]</sup>

### 7.2.4 Topological and microstructural characterization

It has been extensively shown that microstructural properties of solution processed conjugated polymer thin films are critical to the optoelectronic performance. Hence, the surface morphology of the annealed TFTs were analyzed by AFM and height and phase images are shown in Figure 7-4. Despite the high MW and the multiblock nature, annealed films of **MBC1** showed a well-defined and distinct domains that can be attributed to nanoscale phase assembly of PBTTT and DPP-TT segments. Additionally, our

synthetic strategy appears to not impede pi-pi stacking between conjugated segments as shown by the unexpected (presumed) alignment of pi-stacked lamellae parallel to the substrate. The size of fibrillary nanodomains shown in Figure 7-4 are characterized by typical width of 30 nm which is in good accordance with reported fibrils made of 10 kDa chains. Indeed, we have already shown that low MW PBTTT can form rod-like fibers thanks to its highly rigid backbone. In comparison, albeit the comparable rod-like nature of DPP-TT backbone, low MW fractions are known to form highly disordered and poorly connected aggregates. Rod-containing block copolymers are known to have a more complex phase diagram since, above the Flory-Huggins segregation strength parameter ( $\chi N$ ), there is an additional driving force to the micro-phase separation that originates from the strong tendency of the rod-block to crystallize in the form of nanowires or fibrils.<sup>[97]</sup> By additionally confirming the importance that covalent attachment of semi-crystalline blocks has on the formation of well-defined nanostructures, our results represent the first example of self-assembly in fully conjugated multi-block copolymers.

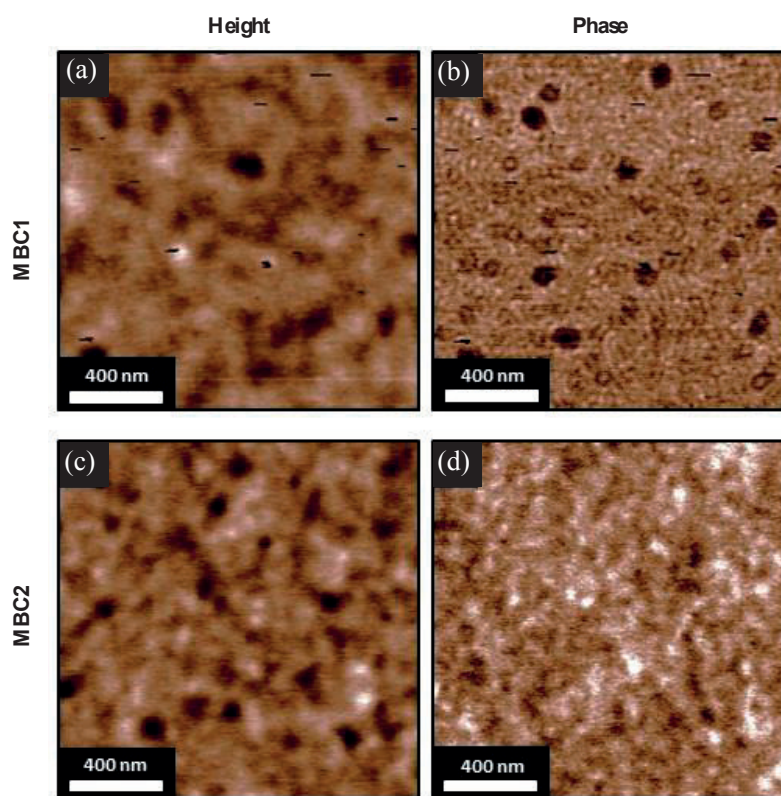


**Figure 7-4.** AFM height and phase images of MBC1 (a-b) and MBC2 (c-d) after annealing at 200°C.

In the annealed film of **MBC2**, phase images showed increased fibrils width (50 nm) which is in line with the high MW of PBTTT (14 kDa) used in synthesis of **MBC2**. Despite the presence of PBTTT rigid block **MBC2** films showed a much less observable phase separation compared to **MBC1** which is consistent with its lower observed charge carrier mobility. Despite the different hole transport and self-assembly capabilities, both **MBC1** and **MBC2** exhibit domain sizes on the scale of 20-60 nm, which correlate well with the  $\sim 10$  nm diffusion length of photogenerated excitons typically found in these materials. By enabling incorporation of polymers that with previous synthetic methods were not amenable to be included in block copolymers, we found that optoelectronic properties of multi-block copolymers are extremely sensitive to either block co-crystallization into conducting self-assembled nanodomains. However, AFM reveals the presence of surface nanoscale domains but it doesn't provide information about the effective crystalline structure of the film. In organic electronic devices, nanostructures orientation throughout the whole thickness of the active layer plays a crucial role in device performance and therefore we investigated in-situ the morphologies of previously prepared TFTs by grazing incidence x-ray scattering. **MBC1** showed three out-of-plane diffractions that indicate the formation of highly crystalline interdigitated lamellae as typically seen for PBTTT. We have showed that MW has an effect on lamellar  $d$ -spacing in PBTTT due to alkyl chain interdigitation occurring in the solid state. In this respect we found that **MBC1** presents a slightly larger  $d$ -spacing of 22.4 Å when compared to fully conjugated 50 kDa PBTTT ( $d = 21$  Å). We believe that the increase distance in the interdigitated lamellae is caused by the presence of longer and branched alkyl chains on the DPP-TT block that expands the lamellae slightly. It worth noting that our strategy of linking along the same chain multiple conjugated blocks does not influence PBTTT crystallization motifs in highly ordered out of plane lamellae. We hypothesize that in the out-of-plane XRD scan of **MBC2** films, the suppressed lamellae formation is caused by inclusion of bulky perylenes units along the chain which avoids effective PBTTT alkyl chain interdigitation. However, a  $d$ -spacing comparable with **MBC1** is found and can be attributed to isolated regions of PBTTT that are could be situated in the terminating parts of the chains where chain movement and crystallization is less constrained. Kline et al. demonstrated that alkyl chain interdigitation on thiophene based polymer like PBTTT control backbone orientation and 2D p-p stacking in plane network formation. This interdigitation model reasonably explains why self-assembled **MBC1** has superior charge transport in respect to **MBC2** where the absence of side chain interdigitation prevents registry between adjacent lamella and leave the backbone highly tilted. Hence, we believe the high structural incompatibility between the PBTTT and PDIT blocks remains the major contributor for the still detectable micro-phase separation in highly disordered **MBC2** films (Figure 7d). As already reported for weakly interdigitating neat PBTTT analogs, the interdigitated regions and the backbone are

separated by a presumably underdense, noninterdigitated regions. In other words, in **MBC2** only a restricted percentage of chains interdigitate, whereas in **MBC1** the degree of interdigitation is comparable to standard fully conjugated PBTTT meaning that DPPTT block does not affect the degree of alkyl chains packing but only the d-spacing. Differently from previous results on P3HT-b-DPP di-block copolymer where the crystallization of both blocks participates in the formation of these domains, the absence of contribution from highly disordered DPP TT and PDIT blocks (at MW < 30 kDa) suggests that the strong self-assembly of PBTTT is sufficient to form ordered nano-domains.

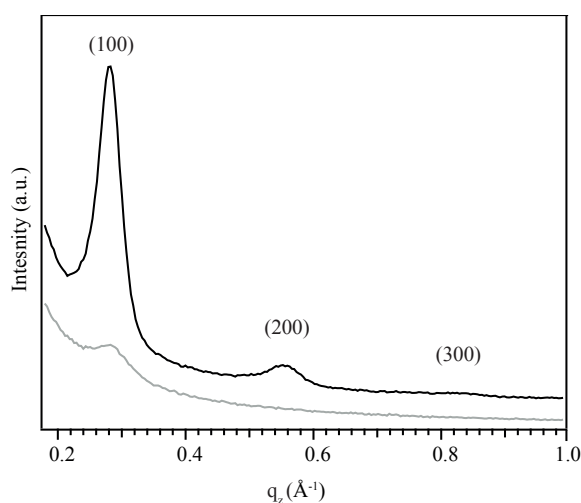


**Figure 7-5.** Specular X-ray diffraction (h00) of MBC1 (black line) and MBC2 (grey line) thin film transistors.

### 7.3 Conclusions

In this chapter we showed how the extension of high yield Stille-coupling poly-condensations to couple di-functionalized conjugated polymeric block represents an effective strategy to synthesize alternated multi-block copolymers that can retain high charge carrier mobility and show long range order through the formation of highly oriented domains in thin films as shown by AFM phase images. The covalent linkage between chemically different blocks was shown to not decrease the charge transport ability of the constituent blocks if an adequate degree of self-assembly is achieved. This approach results thus highly promising for the further design of the next generation of semiconducting polymers with stable

electronic properties and with the possibility to combine multi-blocks (i.e. functionalities) along the same chain. Despite its early stage, the macromolecular approach shown here results to be a promising strategy to also concretely bring an higher level of control over morphologies and internal processes taking place at lengths scale relevant to fabricate ideal active layers in OPV and OLED. Ultimately, through the straightforward functionalization of the polymer blocks developed here, it seems now possible to access a much larger number of combinations between the constituting blocks for applications of block copolymers in optoelectronics. For this reason, further development is needed to optimize the overall structure of this class of polymers and some guidelines will be outlined in the outlook section.



# Chapter 8

## Conclusions and outlook

### 8.1 Conclusions

In the present thesis, combined electrical and morphological investigations of the role of molecular weight on the charge-transport and self-assembly properties in different families of conjugated polymer were performed. The outcome of these initial studies contributed to the development of novel design criteria for semiconducting polymers, i.e. the flexible linker concept and the alternated multi-block copolymer architecture. In particular, the flexibly linked approach demonstrated to be a viable strategy to address one of the long-standing challenges of the field of organic electronics, the enhancement of the thermal stability of organic thin films in transistor and solar cells. In Chapter 3, we present a comprehensive analysis of the effect of the MW on the material characteristics of a prototype rigid-backbone conjugated polymer with interdigitating side chains (e.g. PBTTT), demonstrating that the morphology can be easily tuned by fine selection of the MW. Three distinct regions with high charge carrier mobility ( $\mu_{FET}$ ) were observed. For medium  $M_n$  material around 30–40 kDa the most reproducible high  $\mu_{FET}$  was demonstrated, which correlates with clear long-range ordering in the thin films characterized by terrace-like structures as observed by AFM. For smaller  $M_n$ , an increased crystallinity of the polymer in the thin film was noticed, corresponding to a fiber morphology as seen by AFM. The  $\mu_{FET}$  was lower in these fractions presumably due to poor interconnectivity of the crystalline domains. Surprisingly, a drastic increase in  $\mu_{FET}$  was observed by blending 5% of a high MW polymer into a low MW fraction. This brought out a novel route that would potentially increase the processability and transistor performance of low MW conjugated polymeric or oligomeric semiconductors. In contrast, MW higher than the optimum range showed significantly less side-chain crystallinity and no terrace formation most likely due to polymer chain entanglement. Overall, while the self-assembly observed in the terrace formation clearly promotes good long-range carrier transport for medium  $M_n$  PBTTT (30–40 kDa), the terrace formation itself is not critical for obtaining good transistor performance as long as good interconnectivity is obtained. In less ordered polymers instead, the highest charge carrier mobilities are exclusively obtained exploiting the efficient intrachain transport occurring across long and rigid chains.

The results reported herein point out that the presence of poorly crystalline low-medium MW chains is in fact detrimental for the overall hole mobility in crude batches. This means that the chain length distribution (PDI) plays a crucial role as important as  $M_n$  in influencing the overall hole mobility of the crude sample. In summary, the achievement or if not possible, the selection of the highest possible MW as discussed here by means of preparatory size exclusion chromatography offers a doable strategy to optimize the performance or improving specific properties polymeric devices like in transistors and solar cells. In chapter 5, we describe the successful synthesis of a new class of semiconducting polymers where low-MW conjugated segments are covalently linked along the same polymeric chain with flexible aliphatic linkers. Our FL-PBTTT material exhibited improved thin-film formation compared to the low-MW starting polymer and unique thermal properties. Importantly our linking strategy demonstrated a clear effect on the chain self-assembly and allowed precise control between distinct thin film morphologies without altering the chain length. Moreover our FL-PBTTT served as a model to understand the performance of fully-conjugated PBTTT by indicating that its relatively high performance is not solely due to improved intramolecular transport but that the 2D charge-transport network afforded by self-assembly contributes significantly to the observed high charge carrier mobility. These results support the view that the optimization of the intermolecular transport by chain self-assembly in aligned domains is a principle objective for improving charge transport in semiconducting polymer based devices. In Chapter 6, further extension of the flexible linker concept to molecular semiconductors led to the development of polymers where rigid conjugated cores DPP(TBFu)<sub>2</sub> were linked with flexible aliphatic chains into polymers that possess defined conjugated segments and extended covalent connectivity. We have demonstrated that our new class of polymeric additive can promote donor nucleation in neat films and BHJ blends to improve thermal stability and long range charge transport. The suspected presence of the amorphous FL-additive at the grain boundaries of the donor crystallites could reasonably maintain a stable donor transport network while also providing amorphous regions for PCBM, thereby limiting its exclusion. This combination of beneficial characteristics was found to be unique among additives used in bulk heterojunctions. Ultimately, high yield Stille-coupling poly-condensations to couple di-functionalized conjugated polymeric block ( as developed in Chapter 5) represented an effective strategy to synthesize fully conjugated and alternated multi-block copolymers. As shown in Chapter 7 this new class of semiconducting materials can retain high charge carrier mobility and long-range order through the formation of highly oriented crystalline domains in thin films. Furthermore, the straightforward application of this strategy to the whole library of conjugated polymers currently available in organic electronics can now concretely bring a higher degree of control over morphologies and over the internal processes taking place at length scales relevant to fabricate ideal active layers in OPV and OLED and potentially improve device performance.



## 8.2 Outlook

Given the promising results presented in this thesis, resulting from a more macromolecular-driven approach in conjugated polymer design, rather from the routinely employed energy levels' and single atom's fine tuning, several routes have been opened for future works. It is certainly of great interest to continue carrying studies on the effect of molecular weight on the performance and crystalline texture of semiconducting polymers through chain length separation through size exclusion chromatography. Subjects for next studies could be the extremely high mobility polymers that have been more recently synthesized and that belongs to the less investigated family of disordered polymers like C<sub>16</sub>IDT-BT and the new synthesized block copolymers. Since the flexible linker approach is straightforward and can be applied to a wide variety of different conjugated small molecules, we believe that this strategy can have a much broader range of applications in controlling and stabilizing the active layer morphology not only in molecular BHJ PVs, but also in OLEDs, and TFTs. However, the real nature of the interactions occurring in the film when a precise amount of flexibly linked polymer or dimer is used in the active layer remains still in its infancy. Moreover, it is not clear how the flexible linker approach could potentially increase the thermal stability in other systems and increase also the overall performance of the resulting device. Due to the limited amount of information that can be extracted from a single molecule like DPP(TBFu)<sub>2</sub> it would be beneficial to apply these flexible linker concept into a wider class of high efficiency conjugated small molecules like the benzodithiophene (BDT) core family. Here, several molecules can be chosen as a function of a wide range of different structural parameter, crystallinity and behaviour when used in solar cells. Finally, in Chapter 7, we introduce a new approach to synthesize alternating block copolymers composed by low band-gap polymers which, so far, were inaccessible by traditional synthetic routes. This strategy opens a new doorway to screen a wide family of block copolymers evaluating the effect that a particular blocks have on the charge-carrier properties and overall performance in a device. Hence, we consider that this synthetic route could potentially contribute to the rational design of the next generation of solar cells constituted of a unique donor-acceptor materials with tunable chain orientation to the substrate. Furthermore, the introduction of multiple block functionalities (e.g. light absorption, chain rigidity or elasticity) along the same polymeric chain would offer incomparable opportunities for designing new nanostructured materials with enhanced functionality and properties. First, for application in solar cells, we can imagine the possibility of including a third block (exciton generating layer) in-between the donor and acceptor block in order to facilitate the exciton splitting and diminishing geminate recombination. Second, in the field of stretchable electronic devices the development of intrinsically stretchable semiconductors is highly desirable. One possible strategy to synthesize materials with combined elasticity and charge transport properties would be to develop

multi-block copolymers  $(AB)_n$  composed of a conjugated block (A) covalently linked to an elastomeric block (B) in an alternated fashion along the same polymeric chain. Achieving a relatively high degree of self-assembly is then needed to allow the expression of the two functionalities in the thin film. Overall, I believe that the results presented in this thesis clearly evidence that there are fundamental aspects of organic electronics such as the morphology control and the rational design of block-copolymers that remain poorly understood but hold the key to develop a new generation of devices more efficient and reliable.

# Chapter 9

## References

- [1] aP. M. Beaujuge, J. M. J. Fréchet, *Journal of the American Chemical Society* **2011**, *133*, 20009-20029; bM. L. Hammock, A. Chortos, B. C. K. Tee, J. B. H. Tok, Z. Bao, *Advanced Materials* **2013**, *25*, 5997-6038; cA. Chortos, Z. Bao, *Materials Today* **2014**, *17*, 321-331.
- [2] B. C.-K. Tee, A. Chortos, A. Berndt, A. K. Nguyen, A. Tom, A. McGuire, Z. C. Lin, K. Tien, W.-G. Bae, H. Wang, P. Mei, H.-H. Chou, B. Cui, K. Deisseroth, T. N. Ng, Z. Bao, *Science* **2015**, *350*, 313-316.
- [3] S. J. Benight, C. Wang, J. B. H. Tok, Z. Bao, *Progress in Polymer Science* **2013**, *38*, 1961-1977.
- [4] C. Wang, L. H. Jimison, L. Goris, I. McCulloch, M. Heeney, A. Ziegler, A. Salleo, *Adv. Mater.* **2010**, *22*, 697-701.
- [5] aL. G. Mercier, M. Leclerc, *Accounts of Chemical Research* **2013**, *46*, 1597-1605; bI. McCulloch, M. Heeney, M. L. Chabinyc, D. DeLongchamp, R. J. Kline, M. Cölle, W. Duffy, D. Fischer, D. Gundlach, B. Hamadani, R. Hamilton, L. Richter, A. Salleo, M. Shkunov, D. Sparrowe, S. Tierney, W. Zhang, *Adv. Mater.* **2009**, *21*, 1091-1109.
- [6] aD. A. da Silva Filho, E. G. Kim, J. L. Brédas, *Advanced Materials* **2005**, *17*, 1072-1076; bK. Sivula, Z. T. Ball, N. Watanabe, J. M. J. Fréchet, *Advanced Materials* **2006**, *18*, 206-210.
- [7] J.-L. Brédas, D. Beljonne, V. Coropceanu, J. Cornil, *Chemical Reviews* **2004**, *104*, 4971-5004.
- [8] T. W. Kelley, L. D. Boardman, T. D. Dunbar, D. V. Muires, M. J. Pellerite, T. P. Smith, *The Journal of Physical Chemistry B* **2003**, *107*, 5877-5881.
- [9] A. Maliakal, K. Raghavachari, H. Katz, E. Chandross, T. Siegrist, *Chemistry of Materials* **2004**, *16*, 4980-4986.
- [10] J. Rivnay, R. Noriega, R. J. Kline, A. Salleo, M. F. Toney, *Physical Review B* **2011**, *84*.
- [11] R. Noriega, A. Salleo, A. J. Spakowitz, *Proceedings of the National Academy of Sciences of the United States of America* **2013**, *110*, 16315-16320.
- [12] R. Noriega, J. Rivnay, K. Vandewal, F. P. V. Koch, N. Stingelin, P. Smith, M. F. Toney, A. Salleo, *Nat Mater* **2013**, *12*, 1038-1044.

- [13] aR. Joseph Kline, M. D. McGehee, M. F. Toney, *Nat. Mater.* **2006**, *5*, 222-228; bD. T. Duong, M. F. Toney, A. Salleo, *Physical Review B* **2012**, *86*.
- [14] aI. McCulloch, M. Heeney, C. Bailey, K. Genevicius, I. MacDonald, M. Shkunov, D. Sparrowe, S. Tierney, R. Wagner, W. Zhang, M. L. Chabinye, R. J. Kline, M. D. McGehee, M. F. Toney, *Nat Mater* **2006**, *5*, 328-333; bR. J. Kline, D. M. DeLongchamp, D. A. Fischer, E. K. Lin, L. J. Richter, M. L. Chabinye, M. F. Toney, M. Heeney, I. McCulloch, *Macromolecules* **2007**, *40*, 7960-7965; cA. Gasperini, K. Sivula, *Macromolecules* **2013**, *46*, 9349-9358.
- [15] M. L. Chabinye, M. F. Toney, R. J. Kline, I. McCulloch, M. Heeney, *Journal of the American Chemical Society* **2007**, *129*, 3226-3237.
- [16] Z.-G. Zhang, J. Wang, *J. Mater. Chem.* **2012**, *22*, 4178-4187.
- [17] aH. Chen, Y. Guo, G. Yu, Y. Zhao, J. Zhang, D. Gao, H. Liu, Y. Liu, *Advanced Materials* **2012**, *24*, 4618-4622; bH. Bronstein, Z. Chen, R. S. Ashraf, W. Zhang, J. Du, J. R. Durrant, P. Shakya Tuladhar, K. Song, S. E. Watkins, Y. Geerts, M. M. Wienk, R. A. J. Janssen, T. Anthopoulos, H. Sirringhaus, M. Heeney, I. McCulloch, *Journal of the American Chemical Society* **2011**, *133*, 3272-3275.
- [18] W. Zhang, J. Smith, S. E. Watkins, R. Gysel, M. McGehee, A. Salleo, J. Kirkpatrick, S. Ashraf, T. Anthopoulos, M. Heeney, I. McCulloch, *Journal of the American Chemical Society* **2010**, *132*, 11437-11439.
- [19] X. Zhang, H. Bronstein, A. J. Kronemeijer, J. Smith, Y. Kim, R. J. Kline, L. J. Richter, T. D. Anthopoulos, H. Sirringhaus, K. Song, M. Heeney, W. Zhang, I. McCulloch, D. M. DeLongchamp, *Nat Commun* **2013**, *4*.
- [20] H. Sirringhaus, *Adv. Mater.* **2014**, *26*, 1319-1335.
- [21] C. B. Nielsen, M. Turbiez, I. McCulloch, *Adv. Mater.* **2013**, *25*, 1859-1880.
- [22] C. Cabanetos, A. El Labban, J. A. Bartelt, J. D. Douglas, W. R. Mateker, J. M. J. Fréchet, M. D. McGehee, P. M. Beaujuge, *J. Am. Chem. Soc.* **2013**, *135*, 4656-4659.
- [23] A. Gasperini, S. Bivaud, K. Sivula, *Chemical Science* **2014**, *5*, 4922-4927.
- [24] X. Guo, N. Zhou, S. J. Lou, J. Smith, D. B. Tice, J. W. Hennek, R. P. Ortiz, J. T. L. Navarrete, S. Li, J. Strzalka, L. X. Chen, R. P. H. Chang, A. Facchetti, T. J. Marks, *Nat Photon* **2013**, *7*, 825-833.
- [25] F. P. V. Koch, J. Rivnay, S. Foster, C. Müller, J. M. Downing, E. Buchaca-Domingo, P. Westacott, L. Yu, M. Yuan, M. Baklar, Z. Fei, C. Luscombe, M. A. McLachlan, M. Heeney, G. Rumbles, C. Silva, A. Salleo, J. Nelson, P. Smith, N. Stingelin, *Prog. Polym. Sci.*

- [26] J.-F. Chang, J. Clark, N. Zhao, H. Sirringhaus, D. Breiby, J. Andreasen, M. Nielsen, M. Giles, M. Heeney, I. McCulloch, *Physical Review B* **2006**, *74*.
- [27] aM. Brinkmann, P. Rannou, *Adv. Funct. Mater.* **2007**, *17*, 101-108; bW. Ma, J. Y. Kim, K. Lee, A. J. Heeger, *Macromol. Rapid Commun.* **2007**, *28*, 1776-1780.
- [28] R. J. Kline, M. D. McGehee, E. N. Kadnikova, J. Liu, J. M. J. Fréchet, M. F. Toney, *Macromolecules* **2005**, *38*, 3312-3319.
- [29] B. O'Connor, R. J. Kline, B. R. Conrad, L. J. Richter, D. Gundlach, M. F. Toney, D. M. DeLongchamp, *Advanced Functional Materials* **2011**, *21*, 3697-3705.
- [30] S. Savagatrup, A. D. Printz, T. F. O'Connor, A. V. Zaretski, D. J. Lipomi, *Chemistry of Materials* **2014**, *26*, 3028-3041.
- [31] S. Savagatrup, A. D. Printz, D. Rodriquez, D. J. Lipomi, *Macromolecules* **2014**, *47*, 1981-1992.
- [32] A. D. Printz, S. Savagatrup, D. J. Burke, T. N. Purdy, D. J. Lipomi, *RSC Advances* **2014**, *4*, 13635-13643.
- [33] P. A. Bobbert, A. Sharma, S. G. J. Mathijssen, M. Kemerink, D. M. de Leeuw, *Adv. Mater.* **2012**, *24*, 1146-1158.
- [34] M. Jørgensen, K. Norrman, S. A. Gevorgyan, T. Tromholt, B. Andreasen, F. C. Krebs, *Advanced Materials* **2012**, *24*, 580-612.
- [35] E. Gann, X. Gao, C.-a. Di, C. R. McNeill, *Advanced Functional Materials* **2014**, *24*, 7211-7220.
- [36] G. Giri, R. Li, D.-M. Smilgies, E. Q. Li, Y. Diao, K. M. Lenn, M. Chiu, D. W. Lin, R. Allen, J. Reinspach, S. C. B. Mannsfeld, S. T. Thoroddsen, P. Clancy, Z. Bao, A. Amassian, *Nat Commun* **2014**, *5*.
- [37] M. Mas-Torrent, C. Rovira, *Chem. Rev. (Washington, DC, U. S.)* **2011**, *111*, 4833-4856.
- [38] O. D. Jurchescu, D. A. Mourey, S. Subramanian, S. R. Parkin, B. M. Vogel, J. E. Anthony, T. N. Jackson, D. J. Gundlach, *Physical Review B* **2009**, *80*, 085201.
- [39] A. K. K. Kyaw, D. H. Wang, C. Luo, Y. Cao, T.-Q. Nguyen, G. C. Bazan, A. J. Heeger, *Advanced Energy Materials* **2014**, *4*, n/a-n/a.
- [40] G. Li, Y. Yao, H. Yang, V. Shrotriya, G. Yang, Y. Yang, *Advanced Functional Materials* **2007**, *17*, 1636-1644.
- [41] R. C. Hiorns, R. de Bettignies, J. Leroy, S. Bailly, M. Firon, C. Sentein, A. Khoukh, H. Preud'homme, C. Dagron-Lartigau, *Adv. Funct. Mater.* **2006**, *16*, 2263-2273.
- [42] G. Li, R. Zhu, Y. Yang, *Nat Photon* **2012**, *6*, 153-161.

- [43] K. Sivula, C. K. Luscombe, B. C. Thompson, J. M. J. Fréchet, *Journal of the American Chemical Society* **2006**, *128*, 13988-13989.
- [44] B. J. Kim, Y. Miyamoto, B. Ma, J. M. J. Fréchet, *Advanced Functional Materials* **2009**, *19*, 2273-2281.
- [45] C. Lindqvist, J. Bergqvist, C.-C. Feng, S. Gustafsson, O. Bäcke, N. D. Treat, C. Bounioux, P. Henriksson, R. Kroon, E. Wang, A. Sanz-Velasco, P. M. Kristiansen, N. Stingelin, E. Olsson, O. Inganäs, M. R. Andersson, C. Müller, *Advanced Energy Materials* **2014**, *4*, n/a-n/a.
- [46] L. Derue, O. Dautel, A. Tournebize, M. Drees, H. Pan, S. Berthumeyrie, B. Pavageau, E. Cloutet, S. Chambon, L. Hirsch, A. Rivaton, P. Hudhomme, A. Facchetti, G. Wantz, *Advanced Materials* **2014**, *26*, 5831-5838.
- [47] B. C. Schroeder, Z. Li, M. A. Brady, G. C. Faria, R. S. Ashraf, C. J. Takacs, J. S. Cowart, D. T. Duong, K. H. Chiu, C.-H. Tan, J. T. Cabral, A. Salleo, M. L. Chabinyc, J. R. Durrant, I. McCulloch, *Angewandte Chemie International Edition* **2014**, *53*, 12870-12875.
- [48] B. Walker, A. B. Tamayo, X.-D. Dang, P. Zalar, J. H. Seo, A. Garcia, M. Tantiwiwat, T.-Q. Nguyen, *Advanced Functional Materials* **2009**, *19*, 3063-3069.
- [49] aS.-Y. Ku, M. A. Brady, N. D. Treat, J. E. Cochran, M. J. Robb, E. J. Kramer, M. L. Chabinyc, C. J. Hawker, *Journal of the American Chemical Society* **2012**, *134*, 16040-16046; bY. Matsuo, R. Konno, T. Ishizone, R. Goseki, A. Hirao, *Polymers* **2013**, *5*, 1012; cJ. Han, D. Zhu, C. Gao, *Polymer Chemistry* **2013**, *4*, 542-549.
- [50] C. W. Tang, *Applied Physics Letters* **1986**, *48*, 183-185.
- [51] G. Yu, J. Gao, J. C. Hummelen, F. Wudl, A. J. Heeger, *Science* **1995**, *270*, 1789-1791.
- [52] H. Hu, K. Jiang, G. Yang, J. Liu, Z. Li, H. Lin, Y. Liu, J. Zhao, J. Zhang, F. Huang, Y. Qu, W. Ma, H. Yan, *Journal of the American Chemical Society* **2015**, *137*, 14149-14157.
- [53] J. L. Baker, L. H. Jimison, S. Mannsfeld, S. Volkman, S. Yin, V. Subramanian, A. Salleo, A. P. Alivisatos, M. F. Toney, *Langmuir : the ACS journal of surfaces and colloids* **2010**, *26*, 9146-9151.
- [54] aD. M. DeLongchamp, R. J. Kline, Y. Jung, E. K. Lin, D. A. Fischer, D. J. Gundlach, S. K. Cotts, A. J. Moad, L. J. Richter, M. F. Toney, M. Heeney, I. McCulloch, *Macromolecules* **2008**, *41*, 5709-5715; bT. Umeda, D. Kumaki, S. Tokito, *J. Appl. Phys.* **2009**, *105*, 024516-024515.
- [55] M. Tong, S. Cho, J. T. Rogers, K. Schmidt, B. B. Y. Hsu, D. Moses, R. C. Coffin, E. J. Kramer, G. C. Bazan, A. J. Heeger, *Adv. Funct. Mater.* **2010**, *20*, 3959-3965.
- [56] J. Liu, R. S. Loewe, R. D. McCullough, *Macromolecules* **1999**, *32*, 5777-5785.

- [57] M. Wong, J. Hollinger, L. M. Kozycz, T. M. McCormick, Y. Lu, D. C. Burns, D. S. Seferos, *ACS Macro Lett.* **2012**, *1*, 1266-1269.
- [58] B. McCulloch, V. Ho, M. Hoarfrost, C. Stanley, C. Do, W. T. Heller, R. A. Segalman, *Macromolecules* **2013**, *46*, 1899-1907.
- [59] B. G. Kim, E. J. Jeong, J. W. Chung, S. Seo, B. Koo, J. Kim, *Nat. Mater.* **2013**, *12*, 659-664.
- [60] Z. Bao, R. Hamilton, C. Bailey, W. Duffy, M. Heeney, M. Shkunov, D. Sparrowe, S. Tierney, I. McCulloch, R. J. Kline, D. M. DeLongchamp, M. Chabiny, D. J. Gundlach, *Proc. of SPIE* **2006**, *6336*, 633611-633611-633616.
- [61] I. McCulloch, M. Heeney, C. Bailey, K. Genevicius, I. Macdonald, M. Shkunov, D. Sparrowe, S. Tierney, R. Wagner, W. Zhang, M. L. Chabiny, R. J. Kline, M. D. McGehee, M. F. Toney, *Nat. Mater.* **2006**, *5*, 328-333.
- [62] R. Noriega, J. Rivnay, K. Vandewal, F. P. V. Koch, N. Stingelin, P. Smith, M. F. Toney, A. Salleo, *Nature materials* **2013**, *advance online publication*.
- [63] S. Himmelberger, J. Dacuña, J. Rivnay, L. H. Jimison, T. McCarthy-Ward, M. Heeney, I. McCulloch, M. F. Toney, A. Salleo, *Adv. Funct. Mater.* **2013**, *23*, 2091-2098.
- [64] W. Li, W. S. C. Roelofs, M. M. Wienk, R. A. J. Janssen, *Journal of the American Chemical Society* **2012**, *134*, 13787-13795.
- [65] L. Wang, X. Zhang, J. Zhang, H. Tian, Y. Lu, Y. Geng, F. Wang, *Journal of Materials Chemistry C* **2014**, *2*, 9978-9986.
- [66] aH. N. Tsao, D. M. Cho, I. Park, M. R. Hansen, A. Mavrinskiy, D. Y. Yoon, R. Graf, W. Pisula, H. W. Spiess, K. Müllen, *Journal of the American Chemical Society* **2011**, *133*, 2605-2612; bJ. J. Intemann, K. Yao, H.-L. Yip, Y.-X. Xu, Y.-X. Li, P.-W. Liang, F.-Z. Ding, X. Li, A. K. Y. Jen, *Chemistry of Materials* **2013**, *25*, 3188-3195; cW. R. Mateker, J. D. Douglas, C. Cabanetos, I. T. Sachs-Quintana, J. A. Bartelt, E. T. Hoke, A. El Labban, P. M. Beaujuge, J. M. J. Frechet, M. D. McGehee, *Energy & Environmental Science* **2013**, *6*, 2529-2537; dZ. Huang, E. C. Fregoso, S. Dimitrov, P. S. Tuladhar, Y. W. Soon, H. Bronstein, I. Meager, W. Zhang, I. McCulloch, J. R. Durrant, *Journal of Materials Chemistry A* **2014**, *2*, 19282-19289; eT. Vangerven, P. Verstappen, J. Drijkoningen, W. Dierckx, S. Himmelberger, A. Salleo, D. Vanderzande, W. Maes, J. V. Manca, *Chemistry of Materials* **2015**, *27*, 3726-3732.
- [67] K. Zhao, H. U. Khan, R. Li, Y. Su, A. Amassian, *Advanced Functional Materials* **2013**, *23*, 6024-6035.
- [68] J. Clark, J.-F. Chang, F. C. Spano, R. H. Friend, C. Silva, *Applied Physics Letters* **2009**, *94*, 163306.

- [69] S. Himmelberger, K. Vandewal, Z. Fei, M. Heeney, A. Salleo, *Macromolecules* **2014**, *47*, 7151-7157.
- [70] M. Brinkmann, P. Rannou, *Macromolecules* **2009**, *42*, 1125-1130.
- [71] X. Zhang, L. J. Richter, D. M. DeLongchamp, R. J. Kline, M. R. Hammond, I. McCulloch, M. Heeney, R. S. Ashraf, J. N. Smith, T. D. Anthopoulos, B. Schroeder, Y. H. Geerts, D. A. Fischer, M. F. Toney, *Journal of the American Chemical Society* **2011**, *133*, 15073-15084.
- [72] I. Osaka, M. Akita, T. Koganezawa, K. Takimiya, *Chemistry of Materials* **2012**, *24*, 1235-1243.
- [73] M. Ballauff, *Angewandte Chemie International Edition in English* **1989**, *28*, 253-267.
- [74] aX. Zhu, M. C. Traub, D. A. Vanden Bout, K. N. Plunkett, *Macromolecules* **2012**, *45*, 5051-5057; bG. Bounos, S. Ghosh, A. K. Lee, K. N. Plunkett, K. H. DuBay, J. C. Bolinger, R. Zhang, R. A. Friesner, C. Nuckolls, D. R. Reichman, P. F. Barbara, *Journal of the American Chemical Society* **2011**, *133*, 10155-10160.
- [75] S. Saito, K. Nakakura, S. Yamaguchi, *Angewandte Chemie International Edition* **2012**, *51*, 714-717.
- [76] D. M. DeLongchamp, R. J. Kline, Y. Jung, D. S. Germack, E. K. Lin, A. J. Moad, L. J. Richter, M. F. Toney, M. Heeney, I. McCulloch, *ACS Nano* **2009**, *3*, 780-787.
- [77] T. Schuettfort, B. Watts, L. Thomsen, M. Lee, H. Sirringhaus, C. R. McNeill, *ACS Nano* **2012**, *6*, 1849-1864.
- [78] M. T. Dang, L. Hirsch, G. Wantz, J. D. Wuest, *Chemical Reviews* **2013**, *113*, 3734-3765.
- [79] A. Sharenko, M. Kuik, M. F. Toney, T.-Q. Nguyen, *Advanced Functional Materials* **2014**, *24*, 3543-3550.
- [80] aA. Viterisi, F. Gispert-Guirado, J. W. Ryan, E. Palomares, *Journal of Materials Chemistry* **2012**, *22*, 15175-15182; bY. Sun, G. C. Welch, W. L. Leong, C. J. Takacs, G. C. Bazan, A. J. Heeger, *Nat Mater* **2012**, *11*, 44-48; cL. A. Perez, J. T. Rogers, M. A. Brady, Y. Sun, G. C. Welch, K. Schmidt, M. F. Toney, H. Jinnai, A. J. Heeger, M. L. Chabinyc, G. C. Bazan, E. J. Kramer, *Chemistry of Materials* **2014**, *26*, 6531-6541.
- [81] aA. Sharenko, N. D. Treat, J. A. Love, M. F. Toney, N. Stingelin, T.-Q. Nguyen, *Journal of Materials Chemistry A* **2014**, *2*, 15717-15721; bN. D. Treat, J. A. Nekuda Malik, O. Reid, L. Yu, C. G. Shuttle, G. Rumbles, C. J. Hawker, M. L. Chabinyc, P. Smith, N. Stingelin, *Nat Mater* **2013**, *12*, 628-633.
- [82] Y. Huang, W. Wen, S. Mukherjee, H. Ade, E. J. Kramer, G. C. Bazan, *Advanced Materials* **2014**, *26*, 4168-4172.



- [83] I. Cardinaletti, J. Kesters, S. Bertho, B. Conings, F. Piersimoni, J. D'Haen, L. Lutsen, M. Nesladek, B. Van Mele, G. Van Assche, K. Vandewal, A. Salleo, D. Vanderzande, W. Maes, J. V. Manca, *PHOTOE* **2014**, *4*, 040997-040997.
- [84] Y. Liu, C.-C. Chen, Z. Hong, J. Gao, Y. Yang, H. Zhou, L. Dou, G. Li, Y. Yang, *Scientific Reports* **2013**, *3*, 3356.
- [85] Z. Li, X. Zhang, Y. Zhang, C. F. Woellner, M. Kuik, J. Liu, T.-Q. Nguyen, G. Lu, *The Journal of Physical Chemistry C* **2013**, *117*, 6730-6740.
- [86] W. J. Liu, H. L. Yang, Z. Wang, L. S. Dong, J. J. Liu, *Journal of Applied Polymer Science* **2002**, *86*, 2145-2152.
- [87] J. D. A. Lin, O. V. Mikhnenko, T. S. van der Poll, G. C. Bazan, T.-Q. Nguyen, *Advanced Materials* **2015**, *27*, 2528-2532.
- [88] D. Wang, T. P. Russell, T. Nishi, K. Nakajima, *ACS Macro Letters* **2013**, *2*, 757-760.
- [89] H. Choi, S.-J. Ko, T. Kim, P.-O. Morin, B. Walker, B. H. Lee, M. Leclerc, J. Y. Kim, A. J. Heeger, *Advanced Materials* **2015**, *27*, 3318-3324.
- [90] P. D. Topham, A. J. Parnell, R. C. Hiorns, *Journal of Polymer Science Part B: Polymer Physics* **2011**, *49*, 1131-1156.
- [91] C. Guo, Y.-H. Lin, M. D. Witman, K. A. Smith, C. Wang, A. Hexemer, J. Strzalka, E. D. Gomez, R. Verduzco, *Nano Letters* **2013**, *13*, 2957-2963.
- [92] Y.-H. Lin, K. G. Yager, B. Stewart, R. Verduzco, *Soft Matter* **2014**, *10*, 3817-3825.
- [93] F. S. Bates, M. A. Hillmyer, T. P. Lodge, C. M. Bates, K. T. Delaney, G. H. Fredrickson, *Science* **2012**, *336*, 434-440.
- [94] E. Zhou, J. Cong, Q. Wei, K. Tajima, C. Yang, K. Hashimoto, *Angewandte Chemie International Edition* **2011**, *50*, 2799-2803.
- [95] J. W. Mok, Y.-H. Lin, K. G. Yager, A. D. Mohite, W. Nie, S. B. Darling, Y. Lee, E. Gomez, D. Gosztola, R. D. Schaller, R. Verduzco, *Advanced Functional Materials* **2015**, *25*, 5578-5585.
- [96] K. Nakabayashi, H. Mori, *Macromolecules* **2012**, *45*, 9618-9625.
- [97] E. A. Minich, A. P. Nowak, T. J. Deming, D. J. Pochan, *Polymer* **2004**, *45*, 1951-1957.



# Chapter 10

## Appendix

### 10.1 Characterization Techniques

**Atomic Force Microscopy.** AFM characterization was performed with an Asylum Research Cypher in AC mode at room temperature in air. Cantilevers with a resonance frequency on average of  $f_0 = 70$  kHz and  $k = 2$  N/m were used (Asylum research AC240TS). Scan rates between 0.5 and 1 Hz were applied with images resolution varying according to features size from  $10\ \mu\text{m} \times 10\ \mu\text{m}$  to  $500\ \text{nm} \times 500\ \text{nm}$ .

**Peak force analysis.** Measurements were recorded in ambient conditions using a Cypher S AFM from Asylum Research. A silicon tip (AC160TS) with a theoretical spring constant of  $42\ \text{N m}^{-1}$  was used. The experimental spring constant was obtained using the GetReal™ automated probe calibration feature of Asylum Research software. Over all the scans, a peak force of 100 nN was kept constant for all the samples. The reduced Young's modulus was obtained by fitting the retraction curve with the Derjaguin, Muller, Toropov (DMT) model, which accounts for the adhesion between the tip and the sample surface.

**Differential Scanning Calorimetry.** Melting temperatures,  $T_m$ , and enthalpies of fusion,  $\Delta H_f$ , were measured with a PerkinElmer DSC8000 differential scanning calorimeter calibrated with indium and zinc, using a scanning rate of  $10^\circ\text{C}$  and  $20^\circ\text{C}/\text{min}$ .  $\Delta H_f$  were calculated from the surface area underneath both melting endotherms. The material was deposited by drop-casting, and once the solvent evaporated, it was directly annealed in the pan at  $180^\circ\text{C}$  for 10 min.

**UV/Vis Spectroscopy.** Solution phase UV/Vis spectra ( $c = 0.1$  mg/ml In CB) were recorded on a Shimadzu UV-3600 UV-Vis-NIR spectrophotometer using standard quartz cuvette with 10 mm path length.

**Size exclusion chromatography.** 100 mg of product are completely dissolved in 10 ml of chlorobenzene was injected in a Size exclusion preparative column (PSS SDV preparative linear M,  $40\text{mm} \times 250\text{mm}$ ) at  $80^\circ\text{C}$  using CB as mobile phase at a constant elution flow of  $10\ \text{mL}/\text{min}$ . Fractions collection was carried out every 20 seconds. Single fractions were analyzed through an analytical size

exclusion PSS SDV analytical linear M column (8mm×250mm, 80°C, CB mobile phase, 1mL/min). The CB was removed and the samples were stored in an Ar glovebox until further use.

**Mass spectrometry.** Mass spectra were recorded at the Mass spectrometry service of EPFL on a thermo Scientific LTQ FT-ICR MS for APPI. Matrix-assisted laser desorption/ionization time of flight mass spectrometry (MALDI-TOF-MS) was carried on a Axima-CFR™ plus using malononitrile as matrix and THF as solvent. Reflectron mode is routinely used to detect small molecules and end-functionalized low MW polymers. Linear mode instead is necessary to investigate end functionalization in higher MW fraction (5 kDa -10 kDa).

**NMR spectroscopy.** The (<sup>1</sup>H) and (<sup>13</sup>C) NMR spectra were recorded at room temperature using per-deuterated solvents as internal standards on a NMR Bruker Advance III-400 spectrometer (Bruker, Rheinstetten, Germany). Chemical shifts are given in parts per million (ppm) referenced to residual <sup>1</sup>H or <sup>13</sup>C signals in CDCl<sub>3</sub> (<sup>1</sup>H: 7.26, <sup>13</sup>C: 77.0) and o-dichlorobenzene-d<sub>4</sub> (<sup>1</sup>H: 6.94).

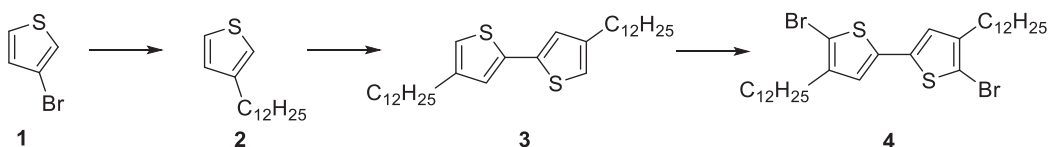
**Polarized Optical microscopy.** Polarized optical microscopy on thin films was carried out on an Nikon Eclipse LV 100 ND microscope with or without a polarizing filter.

**Transmission Electron Microscopy.** TEM sample preparation was performed with OTS treated glass slides onto which PBTTT was spin-coated and annealed. The thin films were then coated with amorphous carbon before polyacrylic acid (240 kDa) drops were deposited onto the carbon layer and let it dry for 2 hours. The solidified drops were delaminated off, floated on water to dissolve the polyacrylic acid, and deposited on TEM grids. Electron diffraction patterns were carried on a FEI CM12 Transmission Electron Microscope at 120 kV acceleration voltage at room temperature using low-dose operating conditions and at a spot size of 70 nm. Focusing and beam alignment were performed on sacrificial regions of the film. The electron beam was then blanked by a shutter and the area of analysis changed. Finally the beam shutter was opened for 2 s to acquire the ED pattern.

## 10.2 Synthesis procedures and analytical data for compounds

Reagents were purchased as reagent grade from commercial sources and used without further purification. THF, chloroform, chlorobenzene, dimethyl formaldehyde were purchased as technical grade and distilled once prior to use. Thin layer chromatography (TLC) analyses were performed on TLC plates from Merck; UV-vis (254 or 366 nm). Column chromatography was conducted on Silica gel SI &o from Merck (40-60  $\mu\text{m}$ ).

**Scheme 10-1.** Synthesis of 5,5'-Dibromo-4,4'-bis(dodecyl)-2,2'-bithiophene (**4**) following Mc Culloch et al. Liquid-crystalline semiconducting polymers with high charge-carrier mobility. *Nat Mater* **2006**, *5* (4), 328-333



**Dodecylthiophene-3-thiophene. (2)** To a solution of 1-bromododecane in deoxygenated and dried THF magnesium was added over a period of 1h. The resulting mixture was stirred at 50°C for 3h. Then, at -78°C 3-bromothiophene and the catalyst were added. The reaction mixture was stirred overnight at 50°C. Then, 2M aqueous sodium hydroxide was poured (slowly at the beginning). The aqueous layer was extracted with diethyl ether and the organic layer was washed with water twice, dried over  $\text{MgSO}_4$ , filtered and the solvent was removed. The product was chromatographed (hexane,  $\text{SiO}_2$ ) and distilled.  $B_p$  178-179°C (20mmHg),  $B_p$  bromothiophene 150°C (atm),  $B_p$  tetradecylthiophene 365°C (litt calc, 1 atm).

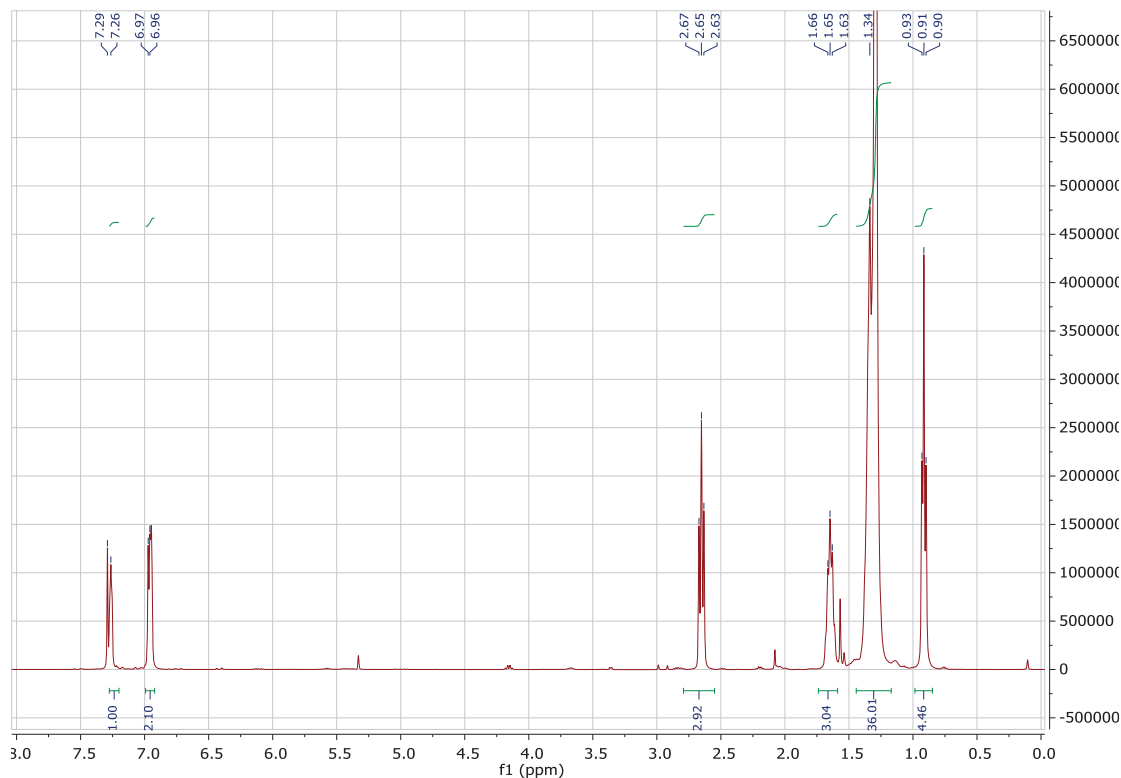


**Figure 10-1:** <sup>1</sup>H NMR spectrum in CHCl<sub>3</sub> of compound (2).

**4,4'-bis(dodecyl)-2,2'-bithiophene (3)** To a solution of TMEDA (7 ml) and dodecyl-3-thiophene (10 gr, 0.039 mol) in dried, n-BuLi (19 ml) was added drop wise at -78°C over a period of 30 min. After stirring for 30 min at this temperature, the mixture was stirred for 1 h more at rt. Then, anhydrous copper (II) chloride (6 gr, 0.04 mol) was added at -78°C in one portion. The mixture was allowed to warm to rt and stirred overnight. Then, some drop of water was added following by a 3M aqueous HCl (35 mL). The aqueous layer was extracted with diethyl ether (2\*50 mL). The combined organic layers were washed with a concentrated solution of sodium thiosulfate (10 mL), twice with water and one time with brine and dried over MgSO<sub>4</sub>. The mixture was passed through a plug of silica gel eluting with warm hexane (60°C). After evaporation of the solvent, the residue was recrystallized twice from hexane at -30°C.

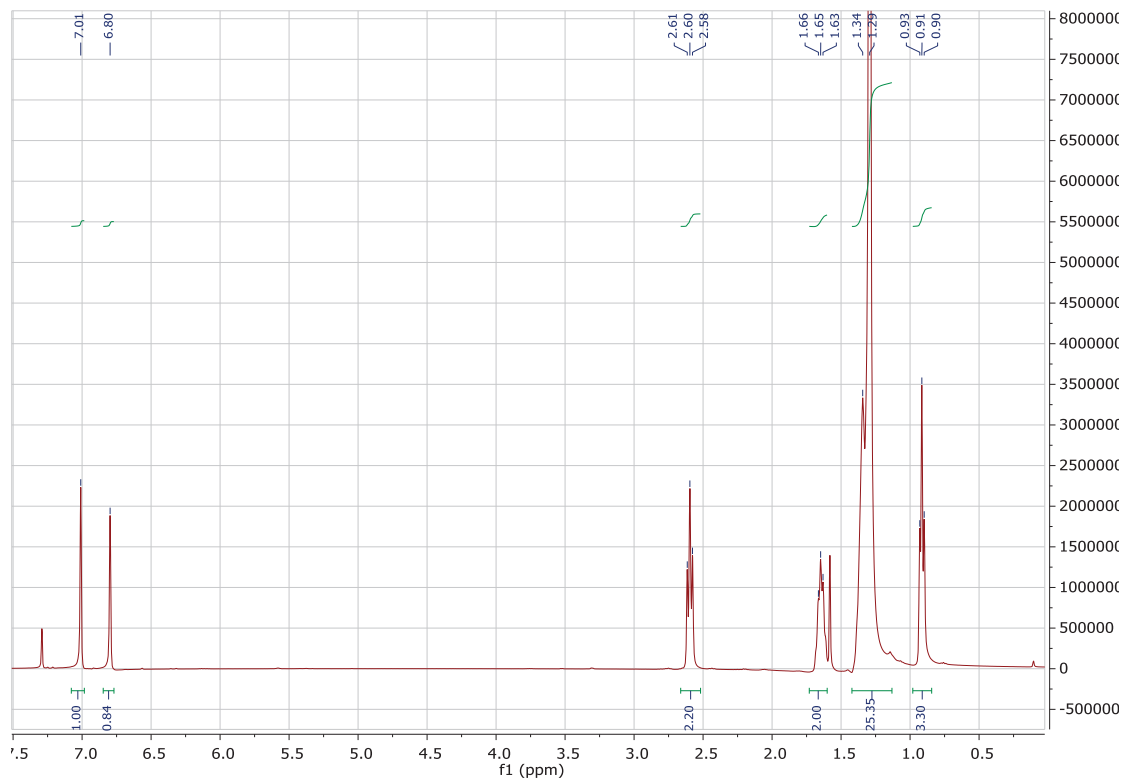


**Figure 10-2:** <sup>1</sup>H NMR spectrum in CDCl<sub>3</sub> of compound (3)

**5,5'-Dibromo-4,4'-bis(dodecyl)-2,2'-bithiophene (4)** To a solution of 4,4'-bis(dodecyl)-2,2'-bithiophene (0.51 g, 0.1 mmol) in 20 ml of chloroform and 5 ml of glacial acetic acid at RT in the dark was added N-bromosuccinimide (0.38g, 0.0025) portionwise over 1h . The resulting solution was stirred overnight. The solvent was removed under reduced pressure and the residue dissolved in a mixture of dichloromethane and water. The organic layer was separated and the aqueous layer extracted with dichloromethane. The combined organics were washed with sodium carbonate, water and brine, dried, filtered and concentrated under reduced pressure. The resulting crude was recrystallized twice from butanone and afforded the product (0.46g, 70% yield) as pale yellow crystals.

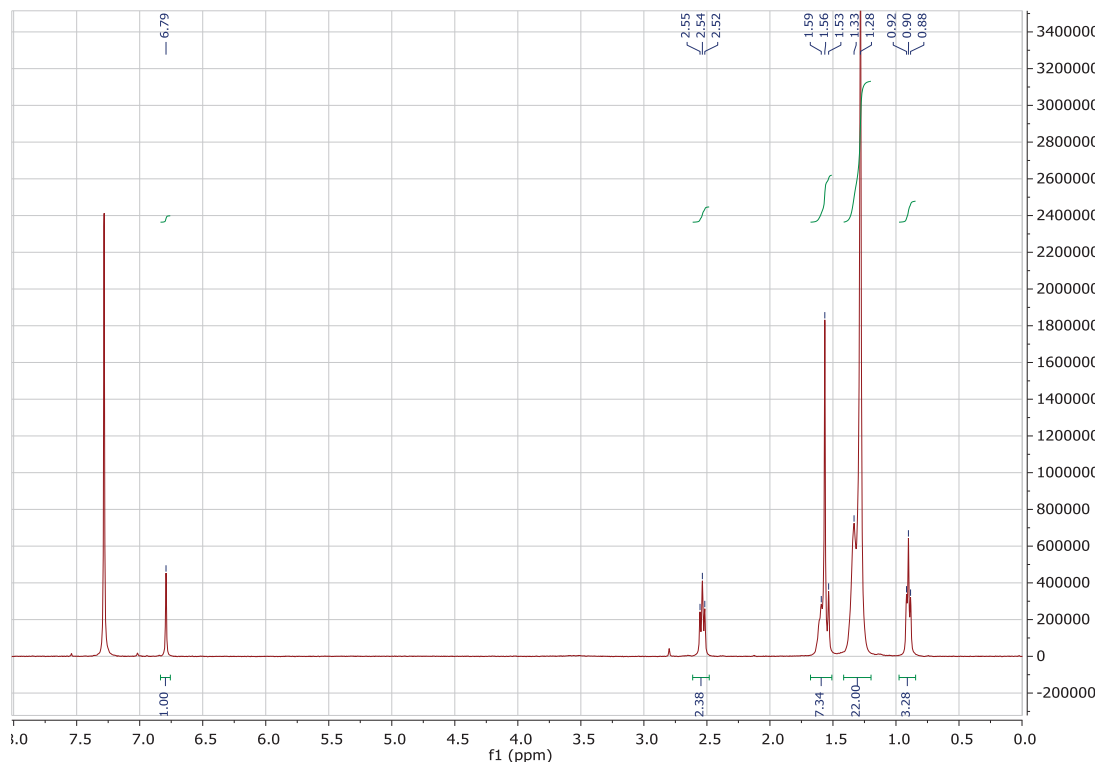
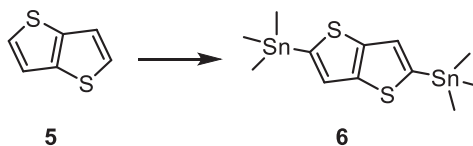


**Figure 10-3:**  $^1\text{H}$  NMR spectrum in  $\text{CDCl}_3$  of compound (4)

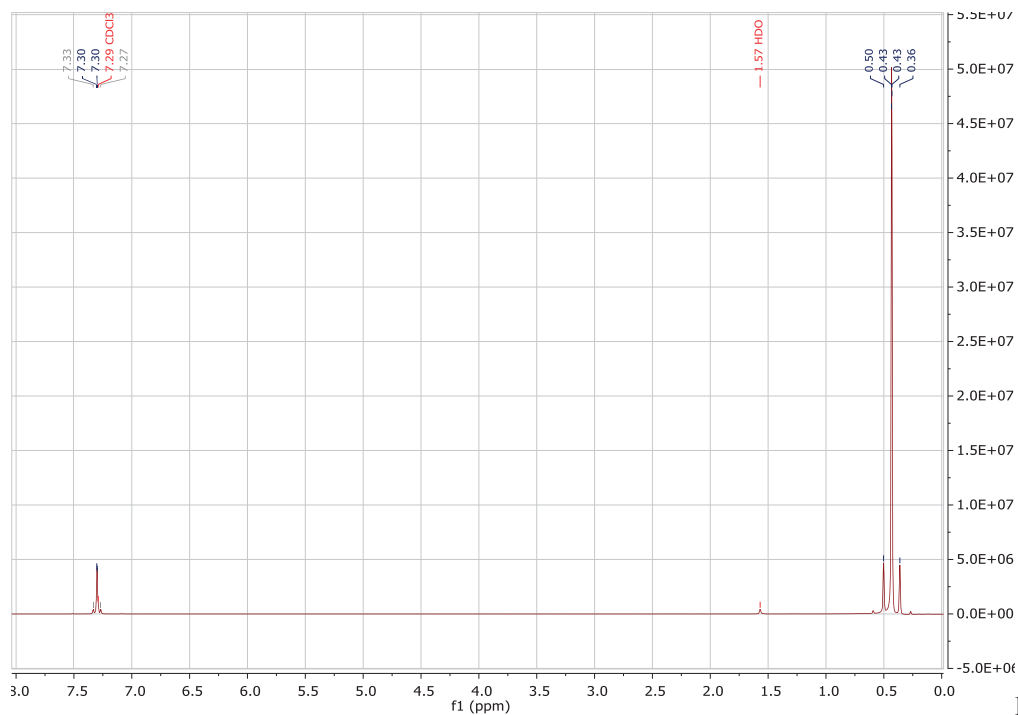
**Scheme 10-2.** Synthesis of 2,5-Bis-trimethylstannyl-thieno[3,2-b]thiophene (6)



**2,5-Bis-trimethylstannyl-thieno[3,2-b]thiophene.6** To a solution of thienothiophene (5g, 35.7 mmol) and TMEDA (13.3 ml, 89.25 mmol) in dried THF, a solution 2.5 M of  $n\text{BuLi}$  (31.4 ml, 78.6 mmol) was added dropwise at  $-78^\circ\text{C}$ . The solution was stirred for 2h at  $-78^\circ\text{C}$  and slowly warmed to rt and stirred for 1h more. After cooling to  $-78^\circ\text{C}$  a solution 1 M of trimethyltin chloride (71.4 ml, 71.4 mmol) was added in one portion. After stirring at  $-78^\circ\text{C}$  for 2 h, the solution was warmed to room temperature and stirred for overnight. The resulting mixture was poured into deionized water and 100 mL of  $\text{CHCl}_3$ .



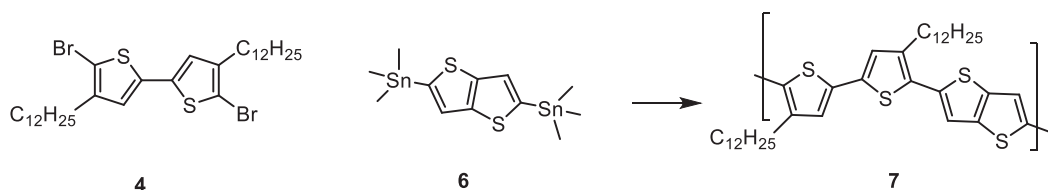
The organic layer was washed twice with 50 mL of water and dried over anhydrous Na<sub>2</sub>SO<sub>4</sub>. The organic layer was evaporated and dried over vacuum to afford a brown solid. The solid was then purified by two recrystallization from acetonitrile to afford the product as white crystals (9.8 gr, 60% yield)



Figure

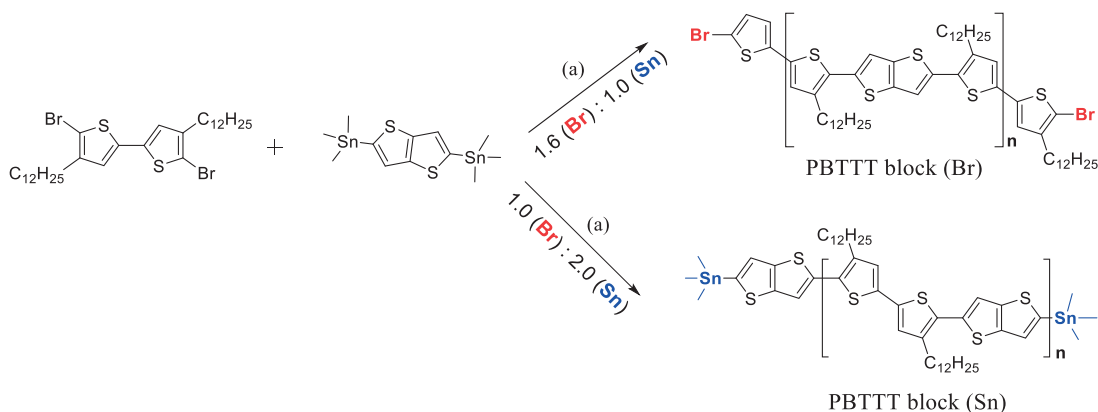
10-4: <sup>1</sup>H NMR spectrum of compound (6) in CDCl<sub>3</sub>.

**Scheme 10-3.** Synthesis of Poly(2,5-bis(3-dodecylthiophen-2-yl)thieno[3,2-b]thiophene) (C12)



**Poly(2,5-bis(3-dodecylthiophen-2-yl)thieno[3,2-b]thiophene) (C12) (7).** The polymer was synthesized by a Stille cross-coupling reaction of **4** (97.4 mg, 0.147 mmol) and **6** (68.7 mg, 0.147 mmol) at 100°C in chlorobenzene under inert atmosphere using 2% mol of tris(dibenzylideneacetone)dipalladium (2.7 mg) and excess of tri(*o*-tolyl)-phosphine (8 mg) as catalyst. At the end of the polymerization time (24 h) the catalyst was extracted by precipitation in methanol for 2 h. After purification by Soxhlet extractions, The polymer was collected by filtration and dried under vacuum to afford 85 mg of product (90%). The chlorobenzene polymer fraction was isolated and analyzed through an analytical size exclusion chromatography column (SEC) at 80°C using chlorobenzene as mobile phase at 1 mL min<sup>-1</sup>. Calculated mass  $M_n$  (27 kDa), PDI 1.8.

**Scheme 10-4.** Synthetic path for the synthesis of the di-brominated PBTTT block ( $M_n = 10$  kDa, PDI 1.2) and di-stannylated PBTTT block ( $M_n = 14$  kDa, PDI 1.2). Typical values of  $n = 10$ -15 repeating units. Polymerization condition a) Pd<sub>2</sub>(dba)<sub>3</sub>, P(*o*-Tol)<sub>3</sub> in chlorobenzene for 2h at 60°C.



**Poly(2,5-bis(3-dodecylthiophen-2-yl)thieno[3,2-b]thiophene) 7b. (Br terminated):** PBTTT polymerization conditions were optimized in order to preferentially synthesize short chains that exclusively resulted to be end-functionalized with bromine. A ratio of 1.6-1.8 to 1 of 2,5-dibromo-3-dodecylbithiophene to 5,5'-trimethyltin thieno[3,2b]thiophene was thus chosen. Typical number-average molecular weight ( $M_n$ ) of 5.5-7 kDa (PDI 1.4) against Polystyrene standards were calculated by analytical size exclusion chromatography using Chlorobenzene as eluent at 80°C. Successive fractionation by preparative SEC (in 80°C, chlorobenzene, 6 mL min<sup>-1</sup>, 40.0 x 250 mm column, linear M packing, Polymer Standards Service GmbH) allowed the selection of a narrow distribution of chains at 11.7 kDa with PDI 1.19. The sample solution in chlorobenzene was passed through a polytetrafluoroethylene filter (5 µm pore size) before injection.

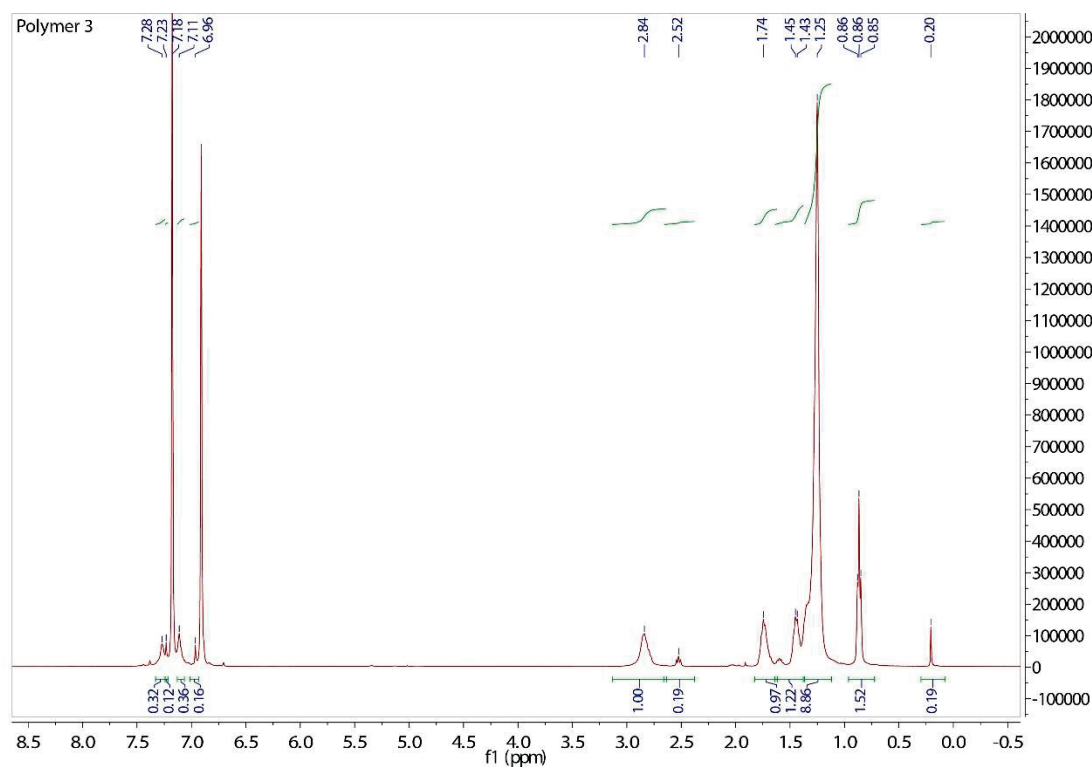


**Figure 10-5.** <sup>1</sup>H NMR spectrum of compound 3 the 11.7 kDa PBTTT with Br end-groups (in o-dichlorobenzene D<sub>4</sub>). NB: Integration of the aromatic region is complicated by solvent peaks.

**Poly(2,5-bis(3-dodecylthiophen-2-yl)thieno[3,2-b]thiophene) 7c.** (stannyl terminated): PBTTT polymerization conditions were optimized in order to preferentially synthesize short chains that exclusively resulted to be end-functionalized with trimethyl tin. A ratio of 1.8 to 1 of 5,5'-trimethyltin thieno[3,2b]thiophene (0.117 gr, 0.25 mmol) ( to 2,5-dibromo-3-tetradecylbithiophene (0.1 gr, 0.14 mmol) at 60°C in chlorobenzene(10 ml) under inert atmosphere using tris(dibenzylideneacetone)dipalladium (4 mg) and excess of tri(o-tolyl)-phosphine (15 mg) as catalyst. was thus chosen. Typical number-average molecular weight ( $M_n$ ) of 5.5-7 kDa (PDI 1.4) against Polystyrene standards were calculated by analytical size exclusion chromatography using Chlorobenzene as eluent at 80°C. Successive precipitation in hexane allowed the selection of a narrow distribution of chains at 10.7 kDa with PDI 1.2.

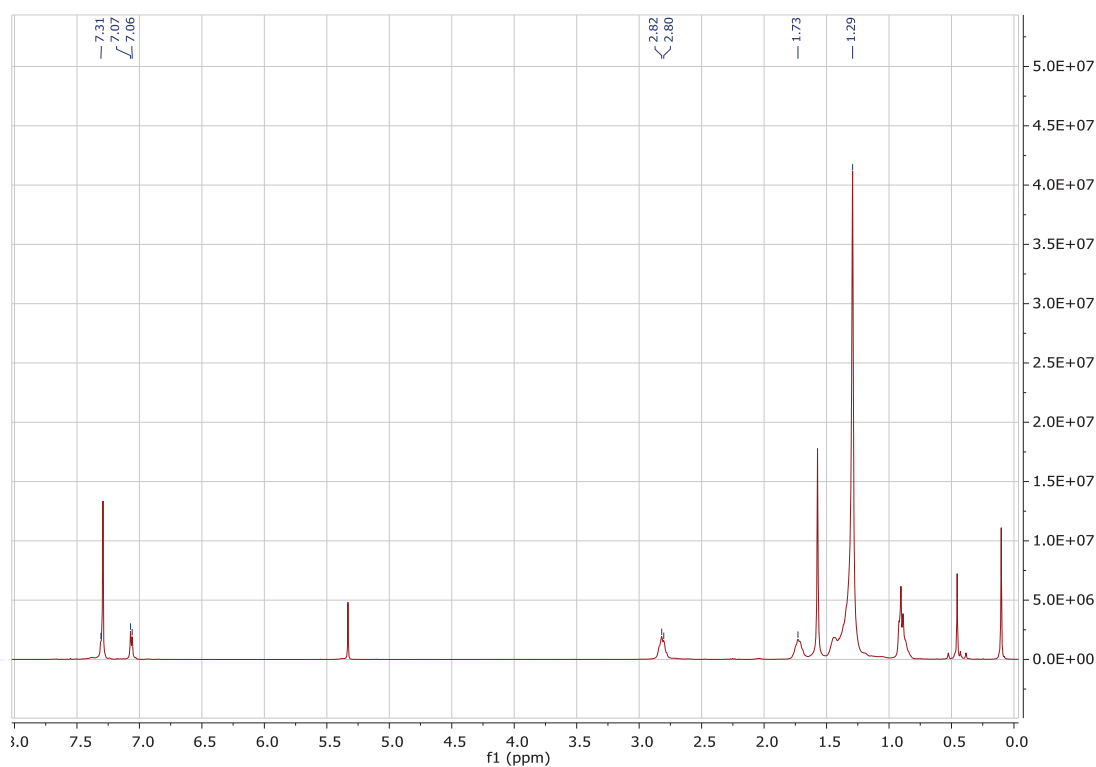


**Figure 10-6.**  $^1\text{H}$  NMR spectrum of compound 3 the 7kDa kDa PBTTT with Tin end-groups (in  $\text{CDCl}_3$ ). NB: Integration of the aromatic region is complicated by solvent peaks.

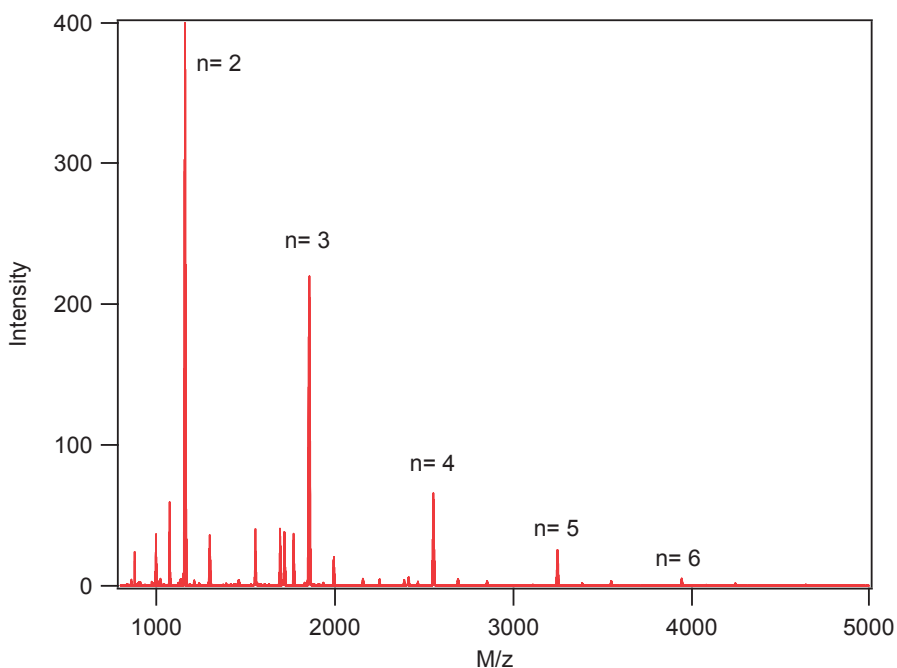
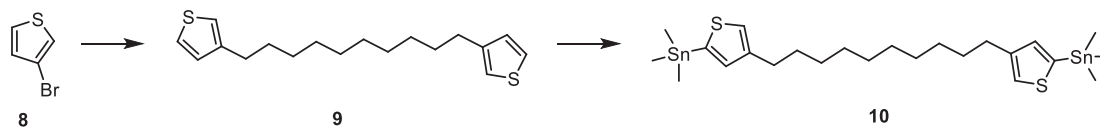


**Figure 10-6b** MALDI spectra of PBT TT-Tin functionalized in reflectron mode

**Scheme 10-5** Synthesis of 1,10-bis(5-(trimethylstannyl)thiophen-3-yl)decane (**10**)



**1,10-di(thiophen-3-yl)decane (9):** To a solution of 1,10-dibromodecane (9.14 g, 30.40 mmol) in dried tetrahydrofuran (80 mL), magnesium turnings (1.54 mg, 64.0 mmol) was added portion wised at 0°C in 1h under argon. The mixture was stirred for 4h at room temperature. Then, 3-bromothiophene (**8**, 10 g, 61.3 mmol) followed by dichloro[1,3-bis(diphenylphosphino)propane]nickel (670 mg, 1.23 mmol) were added quickly at -30°C under argon. The mixture was warmed to room temperature and stirred overnight. Afterward, a saturated solution of ammonium chloride was added (20 mL). The aqueous layer was extracted with diethyl ether (50 mL) and the organic layer was washed with brine (2 x 20 mL), dried over anhydrous magnesium sulfate, filtered and concentrated under vacuum. The residue

was subjected to silica gel chromatography using hexane as eluent or by distillation under vacuum ( $T_{\text{eb}} = 190^{\circ}\text{C}$  at 1.7 mbar) to afford 5.21 g (56%, 16.96 mmol) of a white solid.

Mp:  $43.5\text{--}46^{\circ}\text{C}$ ;  $^1\text{H NMR}$  (400 MHz,  $\text{CDCl}_3\text{-d}_3$ ):  $\delta=7.25$  (dd,  $^3J=4.9$  &  $^4J=3.0$  Hz, 2H), 6.95 (d,  $^3J=4.9$  Hz 2H), 6.93 (d,  $^4J=3.0$  Hz, 2H), 2.64 (t,  $^3J=7.7$  Hz, 4H), 1.67–1.59 (m, 4H), 1.36–1.29 (m, 12H);  $^{13}\text{C NMR}$  (101 MHz,  $\text{CDCl}_3\text{-d}_3$ ):  $\delta=143.31$  (2C), 128.38 (2C), 125.14 (2C), 119.87 (2C), 30.68 (2C), 30.41 (2C), 29.70 (2C), 29.58 (2C), 29.45 (2C); IR: 2918, 2845, 1466, 1431, 1078, 937, 864, 833, 791, 754, 727, 696, 679, 592 ; MS: 306 (EI): Calcd. [ $\text{C}_{18}\text{H}_{26}\text{S}_2$ ]: 306.15; Elmt. Anal. Calcd [ $\text{C}_{18}\text{H}_{26}\text{S}_2$ ]: C, 70.53; H, 8.55; Found : C, 70.72 ; H, 8.15

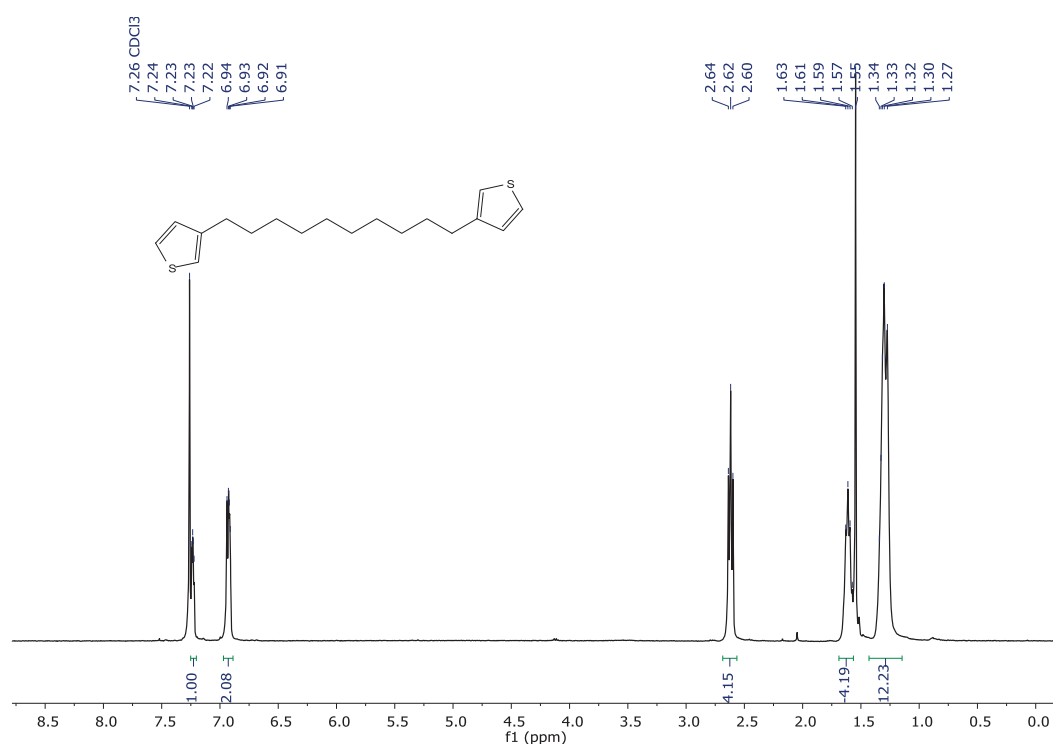


**Figure 10-7:**  $^1\text{H NMR}$  spectrum of compound (9) ( $\text{CDCl}_3$ ).

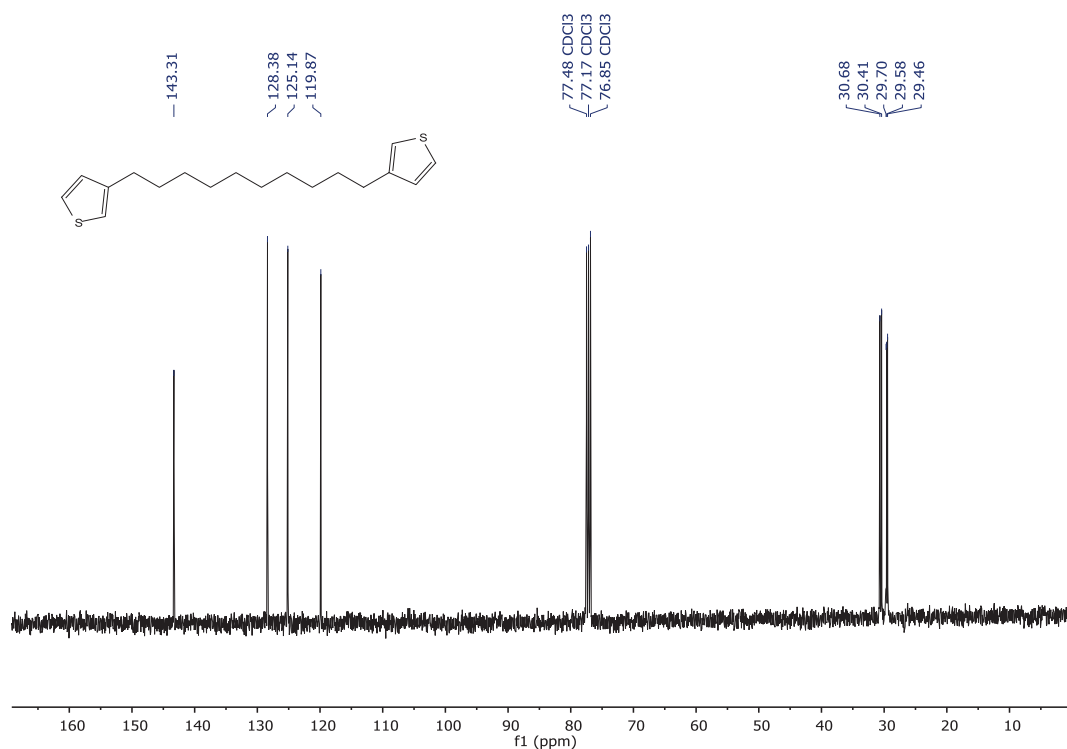


**Figure 10-8:**  $^{13}\text{C}$  NMR spectrum of compound **(9)** ( $\text{CDCl}_3$ ).

1,10-bis(5-(trimethylstannyl)thiophen-3-yl)decane (**10**) : To a solution of compound **9** (5.21 g, 16.99 mmol) in dried tetrahydrofuran (50 mL) and tetramethylethylenediamine (5.91 g, 7.62 mL, 50.88 mmol), a 2.5 M solution of n-butyllithium in hexane (14.25 mL, 35.62 mmol) was added dropwise at  $-78^\circ\text{C}$  under argon over a period of 15 min. Then the reaction mixture was stirred at  $-78^\circ\text{C}$  for 30 min and warmed to room temperature. After stirring for 1h30 at room temperature, trimethyltin chloride (7.10g, 35.62 mmol) in dried tetrahydrofuran (5 mL) was added at  $-78^\circ\text{C}$ . Then, the solution was stirred overnight at room temperature. Aqueous ammonium chloride (20 mL) and aqueous potassium fluoride (10 mL) were added. The aqueous layer was extracted with diethyl ether (30 mL) and the organic layer was washed twice with brine (20 mL), dried over anhydrous magnesium sulfate, filtered and concentrated under vacuum. The residue was subjected to reverse phase silica gel chromatography using hexane as eluent to afford a pale yellow oil. Finally, 7.2 g (67%, 11.39 mmol) of a white solid were obtained after recrystallization in isopropanol at  $-30^\circ\text{C}$ .

$^1\text{H}$  NMR (400 MHz,  $\text{CDCl}_3\text{-d}_3$ ):  $\delta$ =7.19 (s, 2H), 7.00 (s, 2H), 2.64 (t,  $^3J = 7.9$  Hz, 4H), 1.69-1.55 (m, 4H), 1.37-1.19 (m, 12H), 0.35 (s, 18H);  $^{13}\text{C}$  NMR (101 MHz,  $\text{CDCl}_3\text{-d}_3$ ):  $\delta$ =144.64 (2C), 137.28 (2C), 136.74 (2C), 125.79 (2C), 30.89 (2C), 30.12 (2C), 29.73 (2C), 29.62 (4C) -8.13 (6C); IR: 2922, 2899,

2847, 1464, 1177, 972, 912, 858, 833, 764, 741, 723, 534, 524, 511 ; MS: 634.07 (APPI): Calcd. [C<sub>24</sub>H<sub>42</sub>S<sub>2</sub>Sn<sub>2</sub>]: 634.08; Elmt. Anal. Calcd. [C<sub>24</sub>H<sub>42</sub>S<sub>2</sub>Sn<sub>2</sub>]: C, 45.60; H, 6.70; Found: C, 45.82; H, 6.09

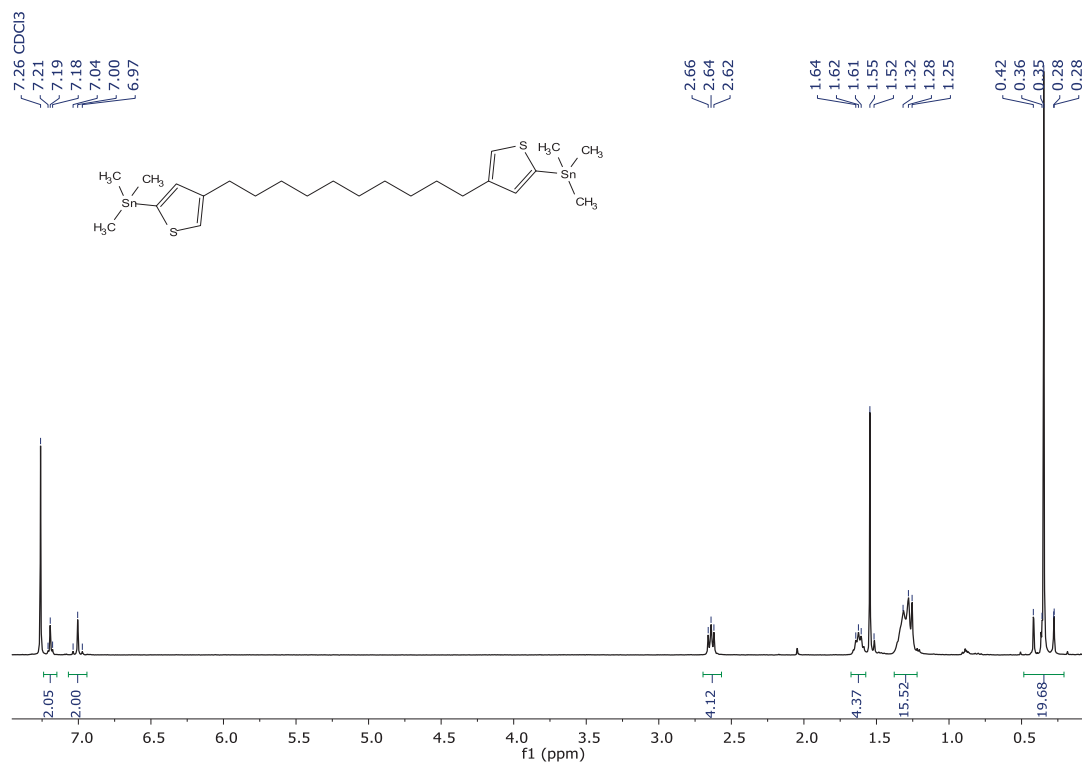


**Figure 10-9:** <sup>1</sup>H NMR spectrum of compound 10 (CDCl<sub>3</sub>).



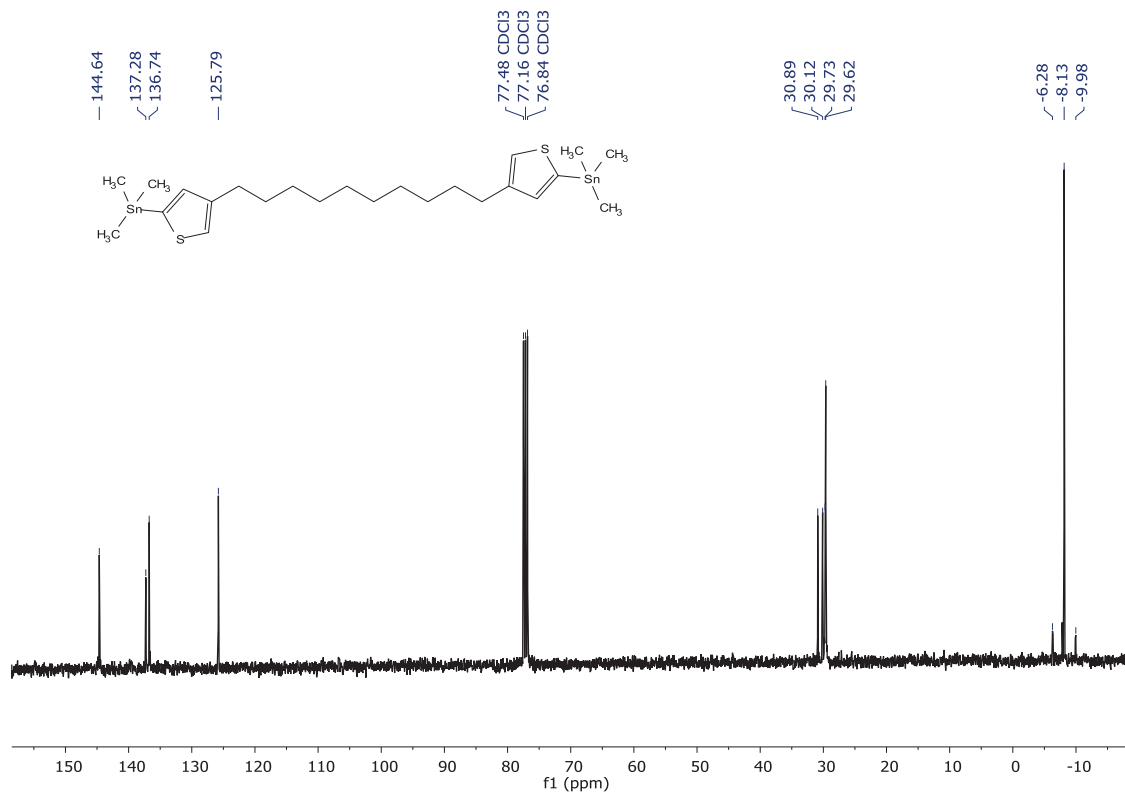
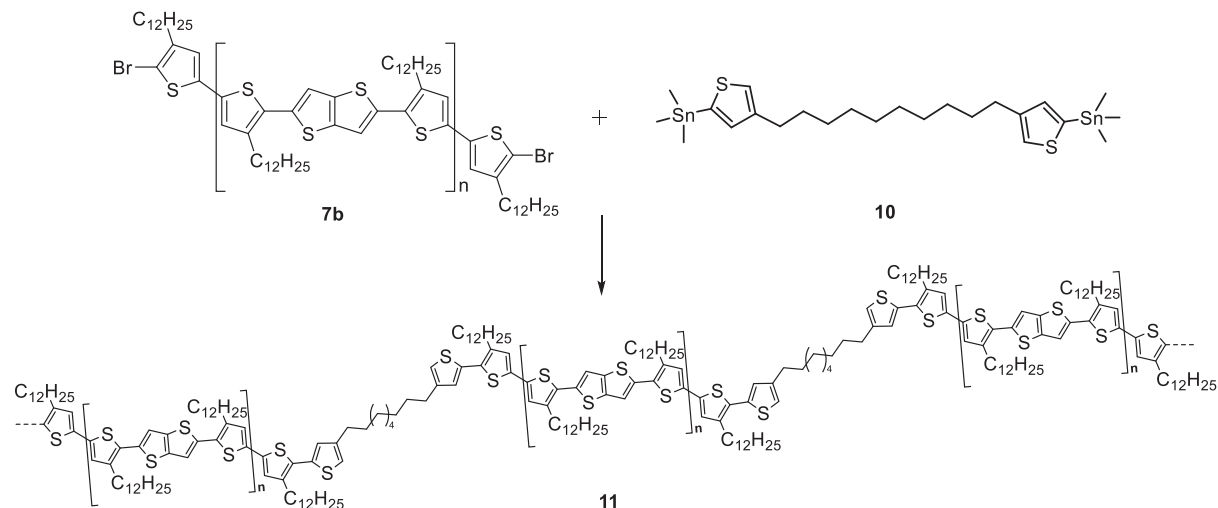


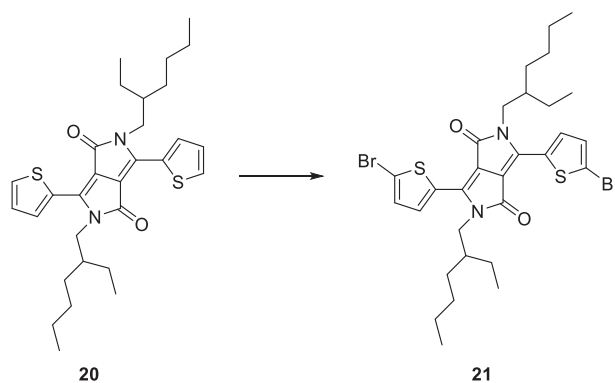
Figure 10-10:  $^{13}\text{C}$  NMR spectrum of compound 10 ( $\text{CDCl}_3$ ).

**Scheme 10-6:** Synthesis of Flexibly-link PBTTT Compound (11)



**Flexibly-link PBTTT Compound. 11;** In a 25ml round bottom flask 100 mg of compound 3 (8.4  $\mu\text{mol}$ ) and 6 (5.3 mg, 8.4  $\mu\text{mol}$ ) were added in 5 ml of anhydrous chlorobenzene under Argon atmosphere using 2% mol of tris(dibenzylideneacetone)dipalladium and tri(o-tolyl)-phosphine as a catalyst. At the end of the polymerization time (36 h) the polymer was isolated by precipitation in methanol for 2 h. The crude polymer fraction was analyzed through an analytical size exclusion chromatography column (SEC) at 80°C using chlorobenzene as mobile phase at 1 mL min<sup>-1</sup>. Successive fractionation by preparative SEC (in 80°C, chlorobenzene, 6 mL min<sup>-1</sup>, 40.0 x 250 mm column, linear M packing, Polymer Standards Service GmbH) afforded to selective isolate the high molecular weight fraction (black solid curve, Figure 1 main text) with a  $M_n$  of 56.0 kDa and a PDI of 1.1.

**Scheme 10-6** 3,6-di(2-bromothiophene-2-yl)-2,5-di(2-ethylhexyl)-pyrrolo[3,4c]pyrrole-1,4-dione (**22**)



3,6-Di(2-bromothiophene-5-yl)-2,5-di (2-ethylhexyl)-pyrrolo[3,4-c]pyrrole-1,4-dione. **22** In a 250 ml round bottom flask **21** (1 g, 1.9 mmol) was dissolved in 201/ ml of  $\text{CHCl}_3$  and in the dark was cooled down to  $0^\circ\text{C}$ . NBS (0.78 gr, 4.4 mmol) dissolved in  $\text{CHCl}_3$  was slowly dripped from a dropping funnel for 1h. The solution was stirred overnight. The organic layer was dried over  $\text{MgSO}_4$  and the solvent was evaporated under reduced pressure afforded the product (0.9 g , 70 % yield) as a solid dark purplish powder.

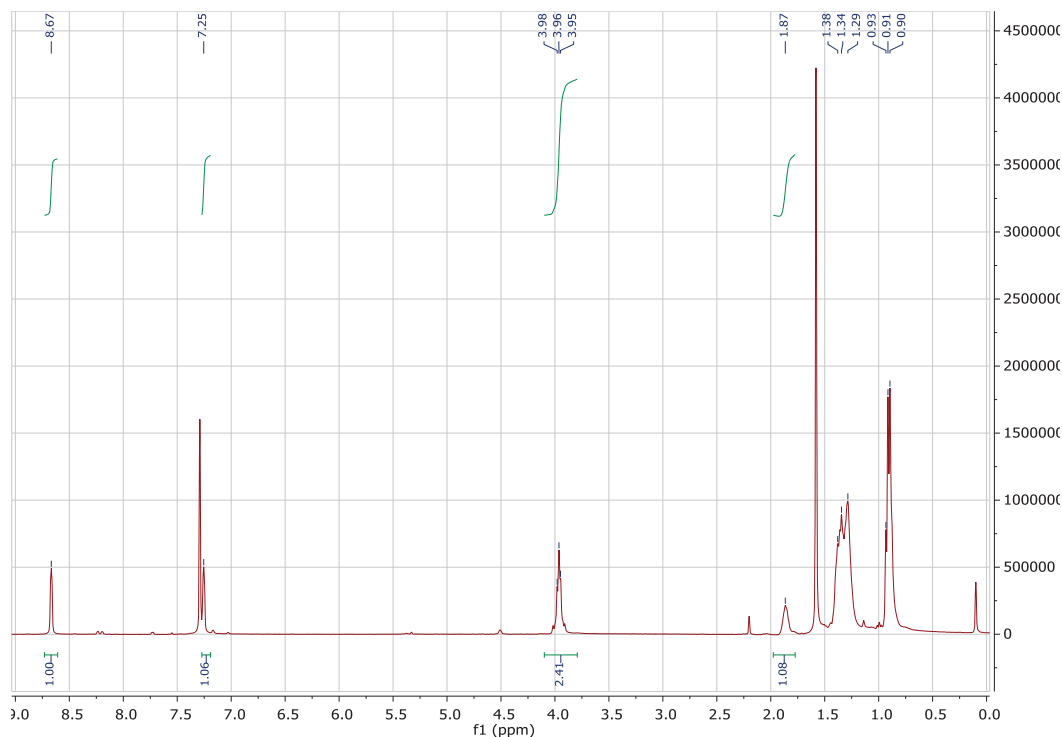
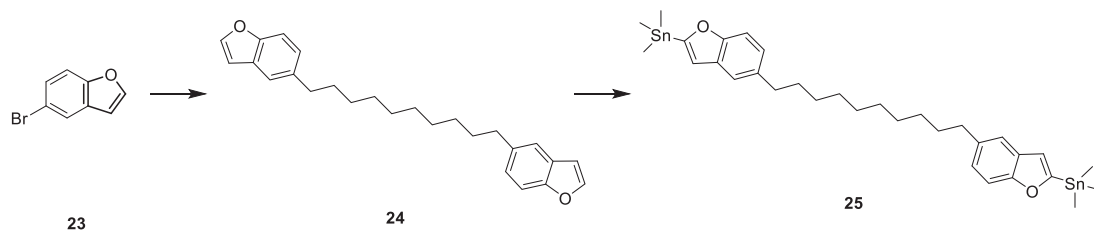


**Figure 10-11:**  $^{13}\text{C}$  NMR spectrum of compound 21 ( $\text{CDCl}_3$ ).

**Scheme 10-7 . 1,10-bis(5-(trimethylstannyl)benzofurane-3-yl)decane (**25**)**



**1,10-di(benzofurane-5-yl)decane (**24**):** To a solution of 1,10-dibromodecane (1.269 g, 2.1 mmol) in dry tetrahydrofuran (15 mL), magnesium turnings (0.22 g, 4.2 mmol) were added portion-wise at rt over 1h under argon. The mixture was stirred for 4h at room temperature. Then 5-bromobenzofuran (1 g, 5.1 mmol) followed by dichloro[1,3-bis(diphenylphosphino)propane]nickel (90 mg, 0.16 mmol) were added quickly at  $-78^\circ\text{C}$  under argon. The mixture was warmed to reflux and stirred overnight. Afterwards, a saturated solution of ammonium chloride was added (20 mL). The aqueous layer was extracted

with diethyl ether (50 mL) and the organic layer was washed with brine (2 x 20 mL), dried over anhydrous magnesium sulfate, filtered and concentrated under vacuum. The residue was subjected to silica gel chromatography using hexane as eluent to afford 0.41 g (42%, 1.1 mmol) of a white solid.

Mp: 43.5-46 °C;  $^1\text{H}$  NMR (400 MHz,  $\text{CDCl}_3\text{-d}_3$ ):  $\delta$ =7.25 (dd,  $^3J = 4.9$  &  $^4J = 3.0$  Hz, 2H), 6.95 (d,  $^3J = 4.9$  Hz 2H), 6.93 (d,  $^4J = 3.0$  Hz, 2H), 2.64 (t,  $^3J = 7.7$  Hz, 4H), 1.67-1.59 (m, 4H), 1.36-1.29 (m, 12H);  $^{13}\text{C}$  NMR (101 MHz,  $\text{CDCl}_3\text{-d}_3$ ):  $\delta$ =143.31 (2C), 128.38 (2C), 125.14 (2C), 119.87 (2C), 30.68 (2C), 30.41 (2C), 29.70 (2C), 29.58 (2C), 29.45 (2C); IR: 2918, 2845, 1466, 1431, 1078, 937, 864, 833, 791, 754, 727, 696, 679, 592 ; MS: 306 (EI): Calcd. [ $\text{C}_{18}\text{H}_{26}\text{S}_2$ ]: 306.15; Elmt. Anal. Calcd [ $\text{C}_{18}\text{H}_{26}\text{S}_2$ ]: C, 70.53; H, 8.55; Found : C, 70.72 ; H, 8.15

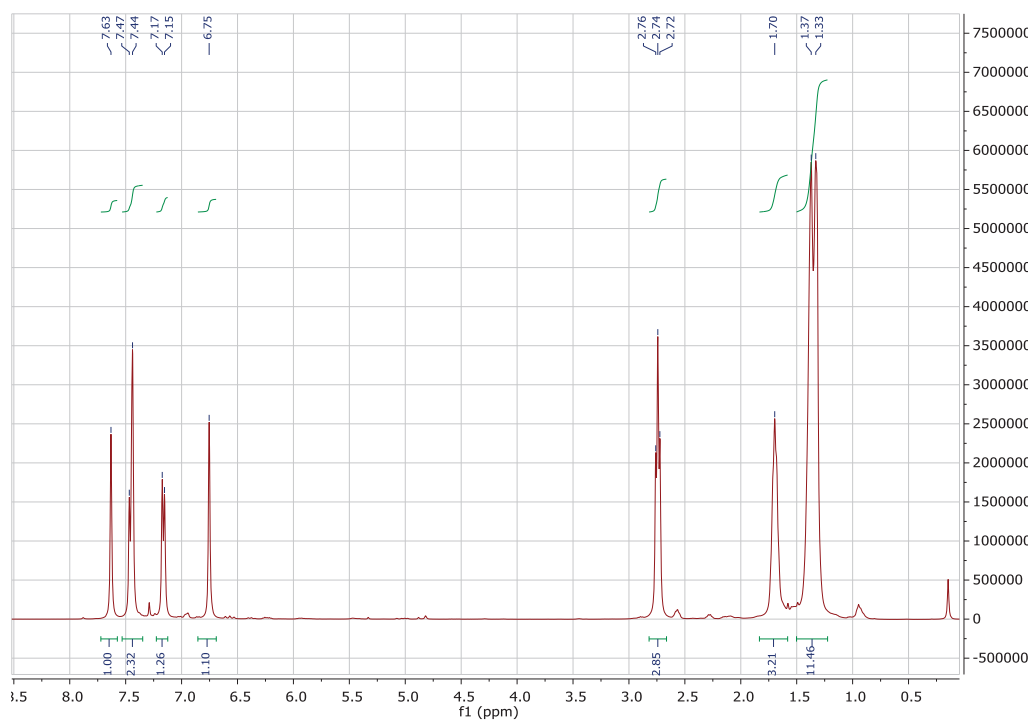


**Figure 10-12:**  $^1\text{H}$  NMR spectrum of compound **24** ( $\text{CDCl}_3$ ).

**1,10-bis(5-(trimethylstannyl)benzofurane-3-yl)decane (25)** : To a solution of compound **24** (0.18 g, 0.48 mmol) in dry tetrahydrofuran (15 mL) and tetramethylethylenediamine (0.5 g, 0.7 mL, 5 mmol), a 2.5 M solution of n-butyllithium in hexane (0.5 mL, 1.22 mmol) was added dropwise at  $-78^{\circ}\text{C}$  under argon over a period of 15 min. Then the reaction mixture was stirred at  $-78^{\circ}\text{C}$  for 30 min and warmed to room temperature. After stirring for 1h30 at room temperature, trimethyltin chloride crystals (0.24g, 1.2 mmol) were added at  $-78^{\circ}\text{C}$ . Then, the solution was stirred overnight at room temperature. Aqueous ammonium chloride (20 mL) and aqueous potassium fluoride (10 mL) were added. The aqueous layer was extracted with diethyl ether (30 mL) and the organic layer was washed twice with brine (20 mL), dried over anhydrous magnesium sulfate, filtered and concentrated under vacuum. The residue was subjected to reverse phase silica gel chromatography using hexane as eluent to afford a pale brown solid. Finally, 0.144 g (45%, 0.2 mmol) of a white solid were obtained after recrystallization in isopropanol at  $-30^{\circ}\text{C}$ .

$^1\text{H}$  NMR (400 MHz,  $\text{CDCl}_3\text{-d}_3$ ):  $\delta=7.19$  (s, 2H), 7.00 (s, 2H), 2.64 (t,  $^3J = 7.9$  Hz, 4H), 1.69-1.55 (m, 4H), 1.37-1.19 (m, 12H), 0.35 (s, 18H);  $^{13}\text{C}$  NMR (101 MHz,  $\text{CDCl}_3\text{-d}_3$ ):  $\delta=144.64$  (2C), 137.28 (2C), 136.74 (2C), 125.79 (2C), 30.89 (2C), 30.12 (2C), 29.73 (2C), 29.62 (4C) -8.13 (6C); IR: 2922, 2899, 2847, 1464, 1177, 972, 912, 858, 833, 764, 741, 723, 534, 524, 511 ; MS: 634.07 (APPI): Calcd. [ $\text{C}_{24}\text{H}_{42}\text{S}_2\text{Sn}_2$ ]: 634.08; Elmt. Anal. Calcd. [ $\text{C}_{24}\text{H}_{42}\text{S}_2\text{Sn}_2$ ]: C, 45.60; H, 6.70; Found: C, 45.82; H, 6.09.

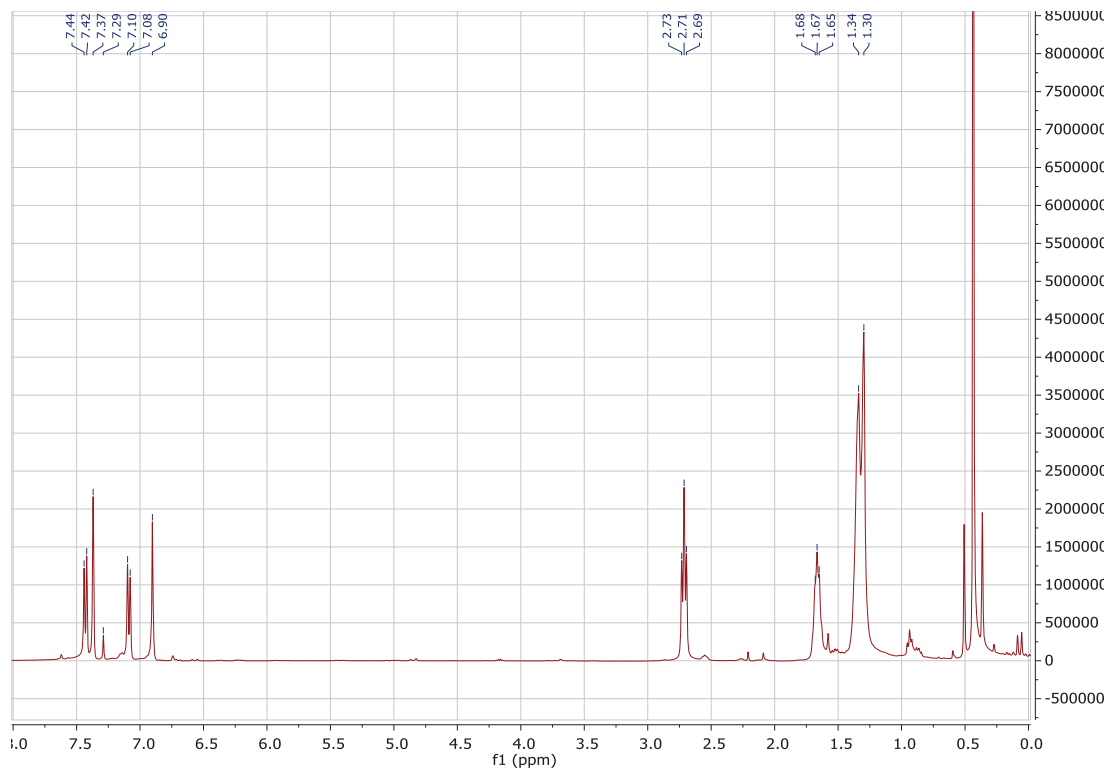
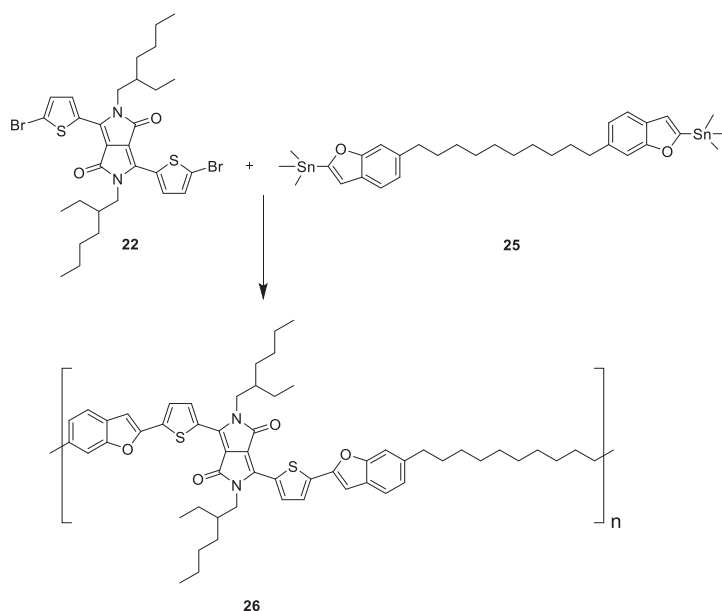


**Figure 10-13:** <sup>1</sup>H NMR spectrum of compound 25 (CDCl<sub>3</sub>).

**Scheme 10-8** Flexibly-linked DPP(TBFu)<sub>2</sub> (**26**)



**Flexibly-linked DPP(TBFu)<sub>2</sub> (26)** In a 50 ml round bottom flask 144 mg of compound **25** (0.25 mmol) and **22** (140 mg, 0.25 mmol) were added in 10 ml of anhydrous chlorobenzene under an Argon atmosphere using 2 mol% of tris(dibenzylidene-acetone)dipalladium and tri(*o*-tolyl)-phosphine as a catalyst. At the end of the polymerization (24 h) the polymer was isolated by precipitation in methanol for 2 h. The crude polymer fraction was analyzed through an analytical size exclusion chromatography column (SEC) at 80°C using chlorobenzene as mobile phase at 1 mL min<sup>-1</sup>. Successive fractionation by preparative SEC (in 80°C, chlorobenzene, 6 mL min<sup>-1</sup>, 40.0 x 250 mm column, linear M packing, Polymer Standards Service GmbH) afforded to selective isolate the high molecular weight fraction with a M<sub>n</sub> of 10.5 kDa and a PDI of 1.4 (vs. PS standards)



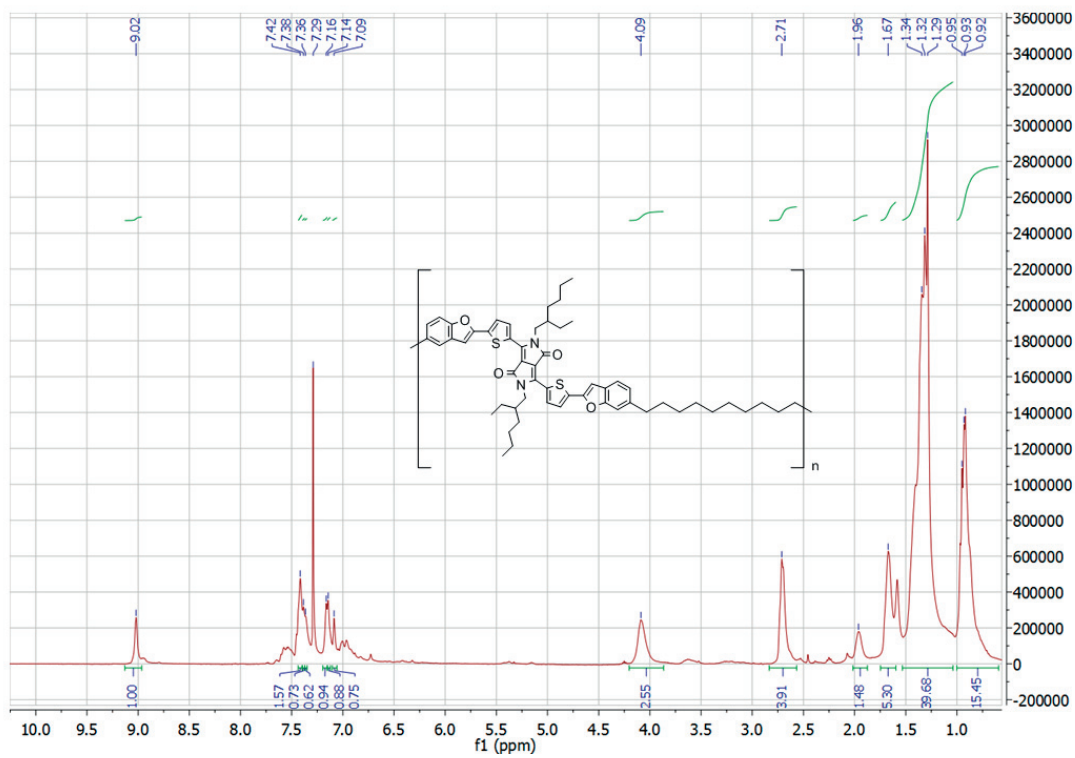
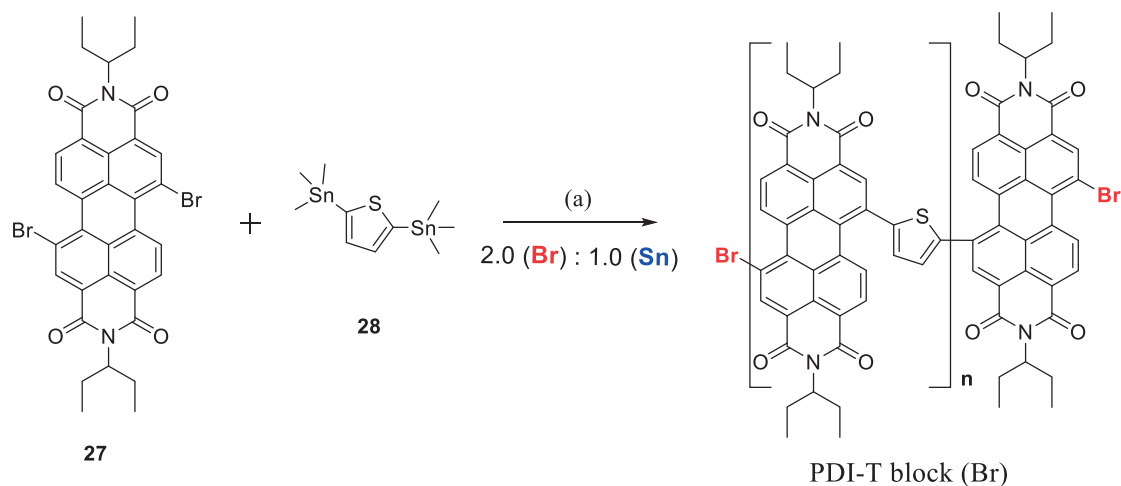


**Figure 10-14:** <sup>1</sup>H NMR spectrum in CDCl<sub>3</sub> of Flexibly-linked DPP(TBFu)<sub>2</sub> (26).

**Scheme 10-9** Flexibly-linked DPP(TBFu)<sub>2</sub> (26)



**Synthesis of 5,12-dibromo-2,9-bis(1-ethylpropyl)-Anthra[2,1,9-def:6,5,10-d'e'f']diisoquinoline-1,3,8,10(2H,9H)-tetrone.**

2,9-bis(1-ethylpropyl)-Anthra[2,1,9-def:6,5,10-d'e'f']diisoquinoline-1,3,8,10(2H,9H)-tetrone (1 gr mg, 0.1 mmol), was dissolved into 50 mL of CHCl<sub>3</sub>, to which 5.7 mL of bromine (60 equivalents) was dropwise added. The mixture was allowed to react under reflux for 2 days. The reaction was monitored by using TLC for 3 h. The excess of bromine was removed by flow of N<sub>2</sub>, and the solvent was removed under vacuum. It was purified by column chromatography on silica gel (DCM/hexanel, 5:1 v/v) to afford compound 27 (isomeric mixture) as a dark-red solid.

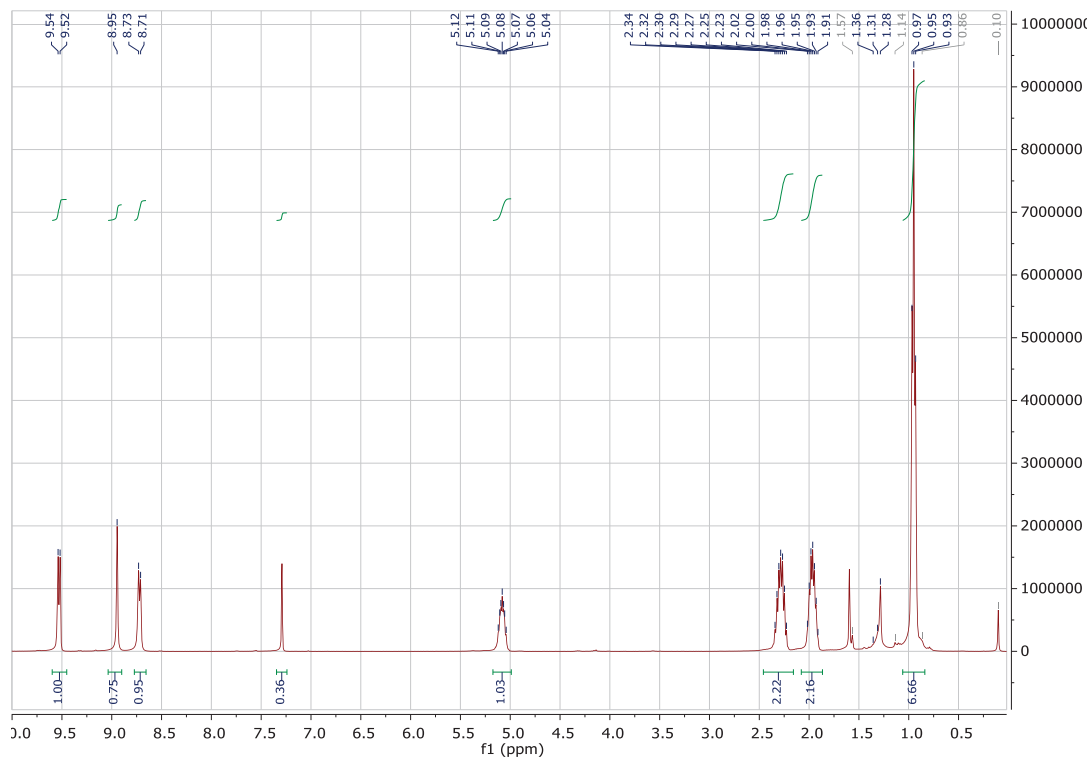


**Figure 10-15:**  $^1\text{H}$  NMR spectrum in  $\text{CDCl}_3$  of compound (27)

**1,1'-(2,5-thiophenediyl)bis[1,1,1-trimethyl-Stannane (28)** To a solution of 2,5 dibromothiophene (1g, 20 mmol) in dried THF, a solution 2.5 M of  $n\text{BuLi}$  ( 16 ml, 0.042 mol) was added dropwise at  $-78^\circ\text{C}$ . The solution was stirred for 2h at  $-78^\circ\text{C}$  and slowly warmed to rt and stirred for 1h more. After cooling to  $-78^\circ\text{C}$  a solution 1 M of trimethyltin chloride (40 ml, 0.042 mol) was added in one portion. After stirring at  $-78^\circ\text{C}$  for 2 h, the solution was warmed to room temperature and stirred for overnight. The resulting mixture was poured into deionized water and 100 mL of  $\text{CHCl}_3$ . The organic layer was washed twice with 50 mL of water and dried over anhydrous  $\text{Na}_2\text{SO}_4$ . The organic layer was evaporated and dried over vacuum to afford a brown solid. The solid was then purified by one recrystallization from ethanol to afford the product as white needles ( 6 gr, 73% yield).  $^1\text{H}$  NMR (400 MHz,  $\text{CDCl}_3$ ,  $\delta$ ) 7.37 (s, 2H), 0.36 (s, 18H).

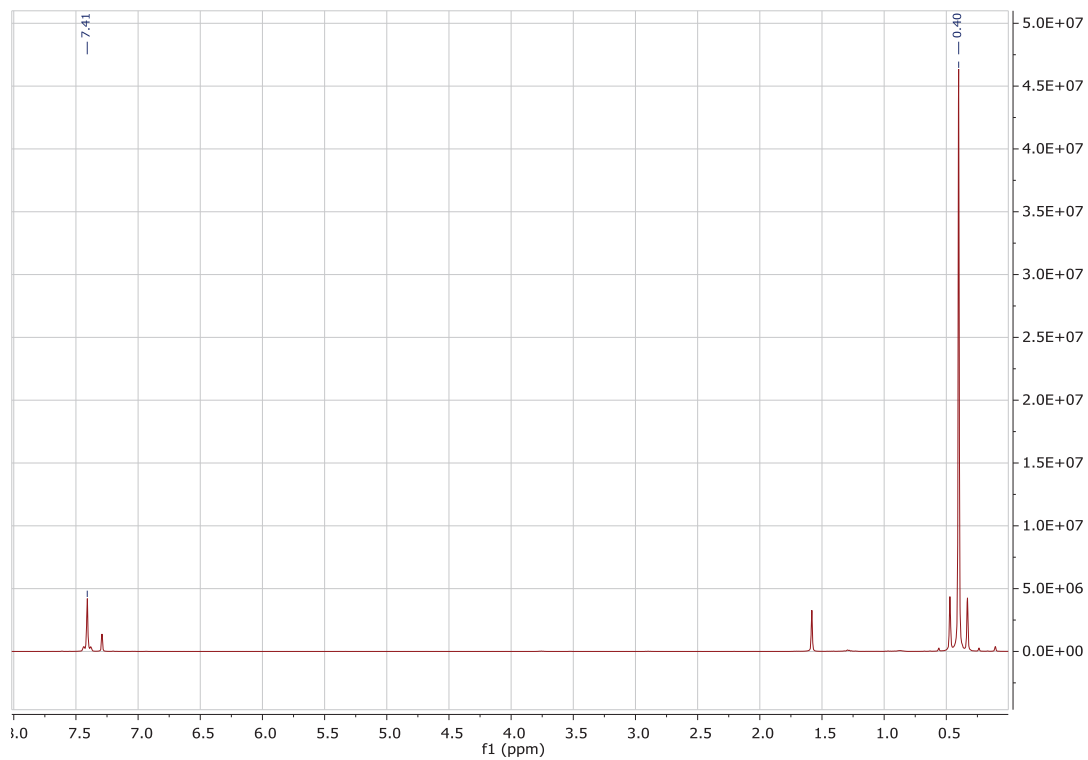
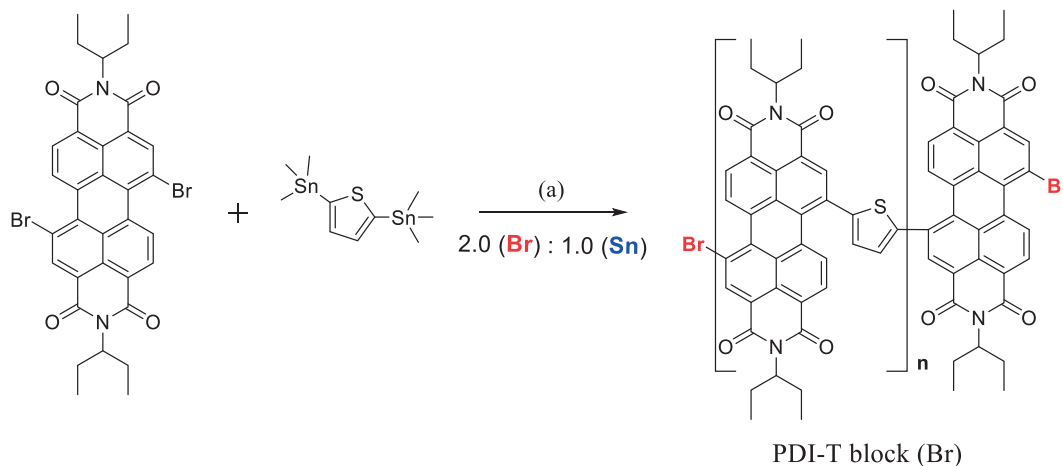


**Figure 10-16:**  $^1\text{H}$  NMR spectrum in  $\text{CDCl}_3$  of compound (28).

**Scheme 10-10** Synthetic path for the synthesis of the di-brominated PDI-T block ( $M_n = 7$  kDa, PDI 1.3). Typical values of  $n = 6-10$  repeating units.



**PDI-T (br terminated).** PBTTT polymerization conditions were optimized in order to preferentially synthesize short chains that exclusively resulted to be end-functionalized with bromine. A ratio of 2 to 1 of 2,9-bis(1-ethylpropyl)-Anthra[2,1,9-*def*:6,5,10-*d'e'*]diisoquinoline-1,3,8,10(2*H*,9*H*)-tetrone (0.1 gr, 0.145 mmol) to 1,1'-(2,5-thiophenediyl)bis(1,1,1-trimethyl-Stannane) (28) (0.03 gr, 0.07 mmol) at 100°C in chlorobenzene (5 ml) under inert atmosphere using tris(dibenzylideneacetone)dipalladium (3 mg) and excess of tri(*o*-tolyl)-phosphine (9 mg) as catalyst was thus chosen. The crude polymer fraction was analyzed through an analytical size exclusion chromatography column (SEC) at 80°C using chlorobenzene as mobile phase at 1 mL min<sup>-1</sup>. Successive fractionation by preparative SEC (in 80°C, chlorobenzene, 6 mL min<sup>-1</sup>, 40.0 x 250 mm column, linear M packing, Polymer Standards Service GmbH) afforded to selective isolate the high molecular weight fraction with a  $M_n$  of 7 kDa and a PDI of 1.3 (vs. PS standards).

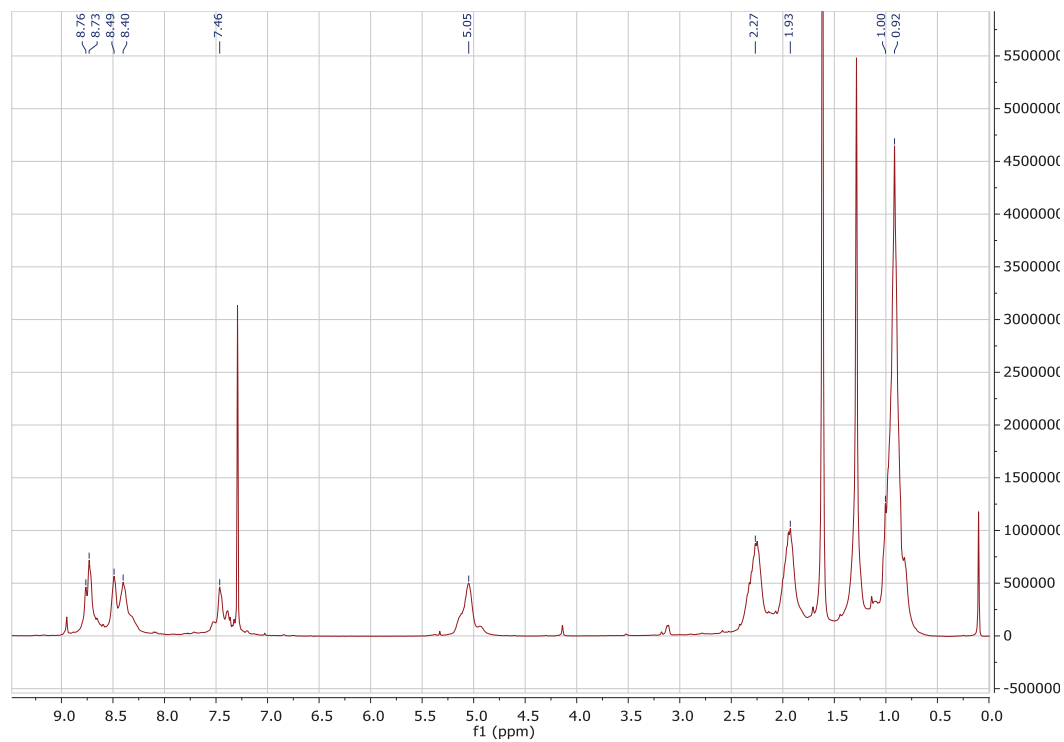
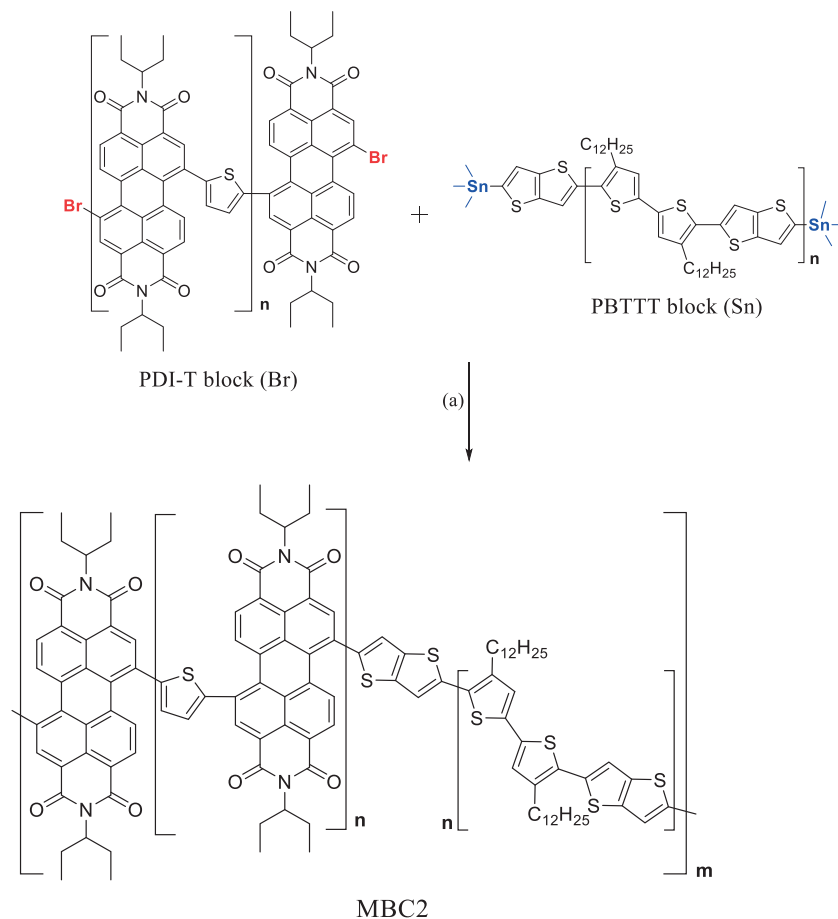


**Figure 10-17:** <sup>1</sup>H NMR spectrum in CDCl<sub>3</sub> of PDI-T block .

**Scheme 10-11.** Synthetic path for the synthesis of the alternated multi block copolymer MBC2 ( $M_n = 65\text{kDa}$ , PDI 1.2) after purification by prep-SEC. Typical values of  $m = 6-8$  repeating units.



**MBC2** A molar ratio of 1:1 of PDI-T (br) block (7 mg) and PBTTT-tin block (14 mg) was chosen. The reaction was run at  $100^\circ\text{C}$  in chlorobenzene (2 ml) under inert atmosphere using tris(dibenzylideneacetone)dipalladium (2 mg) and excess of tri(o-tolyl)-phosphine (6 mg) as catalyst for 1h. The crude polymer fraction was analyzed through an analytical size exclusion chromatography column (SEC) at  $80^\circ\text{C}$  using chlorobenzene as mobile phase at  $1\text{ mL min}^{-1}$ . Successive fractionation by preparative SEC (in  $80^\circ\text{C}$ , chlorobenzene,  $6\text{ mL min}^{-1}$ ,  $40.0 \times 250\text{ mm}$  column, linear M packing, Polymer Standards Service GmbH) afforded to selective isolate the high molecular weight fraction with a  $M_n$  of 65 kDa and a PDI of 1.2 (vs. PS standards)

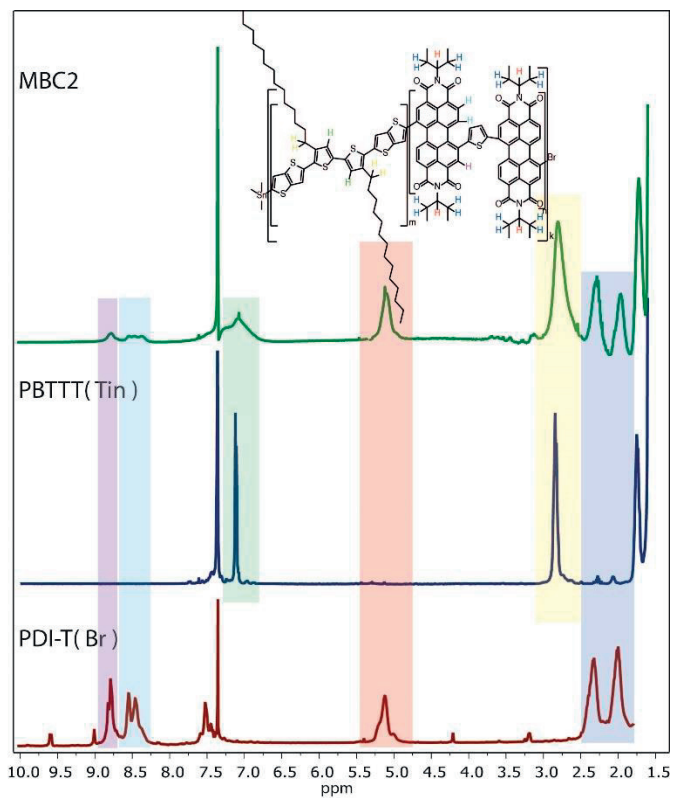
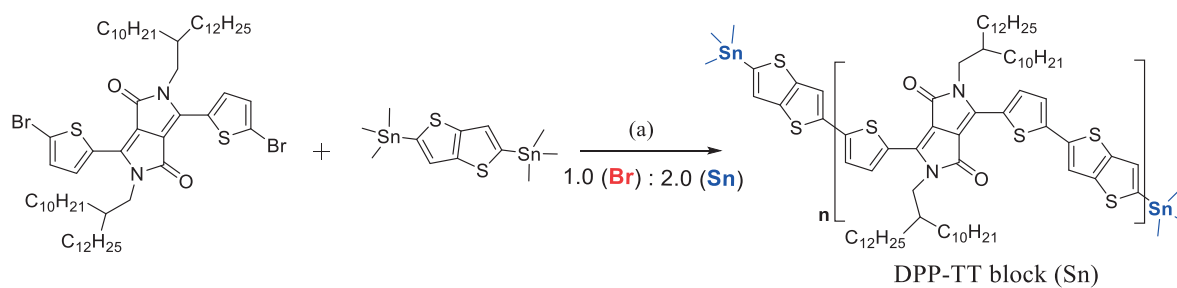


**Figure 10-18.** Combination of  $^1\text{H-NMR}$  (400 MHz) in  $\text{CDCl}_3$  of PDI-T, PBTTT-tin and MBC2 .

**Scheme 10-12.** Synthetic path for the synthesis of the di-stannylated DPP-TT block ( $M_n = 5$  kDa, PDI 1.2). Typical values of  $n = 3-6$  repeating units.





**DPP-TT. (stannyl terminated):** DPP-TT polymerization conditions were optimized in order to preferentially synthesize short chains that exclusively resulted to be end-functionalized with trimethyl tin. A ratio of 2 to 1 of 5,5'-trimethyltin thieno[3,2b]thiophene (0.1 gr, 0.21 mmol) to 3,6-bis(5-bromo-2-thienyl)-2,5-bis(2-decyltetradecyl)-2,5-dihydro- Pyrrolo[3,4-*c*]pyrrole-1,4-dione, (0.12 gr, 0.11 mmol) at 60°C in chlorobenzene (7 ml) under inert atmosphere using tris(dibenzylideneacetone)dipalladium (4 mg) and excess of tri(*o*-tolyl)-phosphine (15 mg) as catalyst was thus chosen. Precipitation in butanone afforded typical number-average molecular weight ( $M_n$ ) of 5.5-7 kDa (PDI 1.) against Polystyrene standards, calculated by analytical size exclusion chromatography using Chlorobenzene as eluent at 80°C.

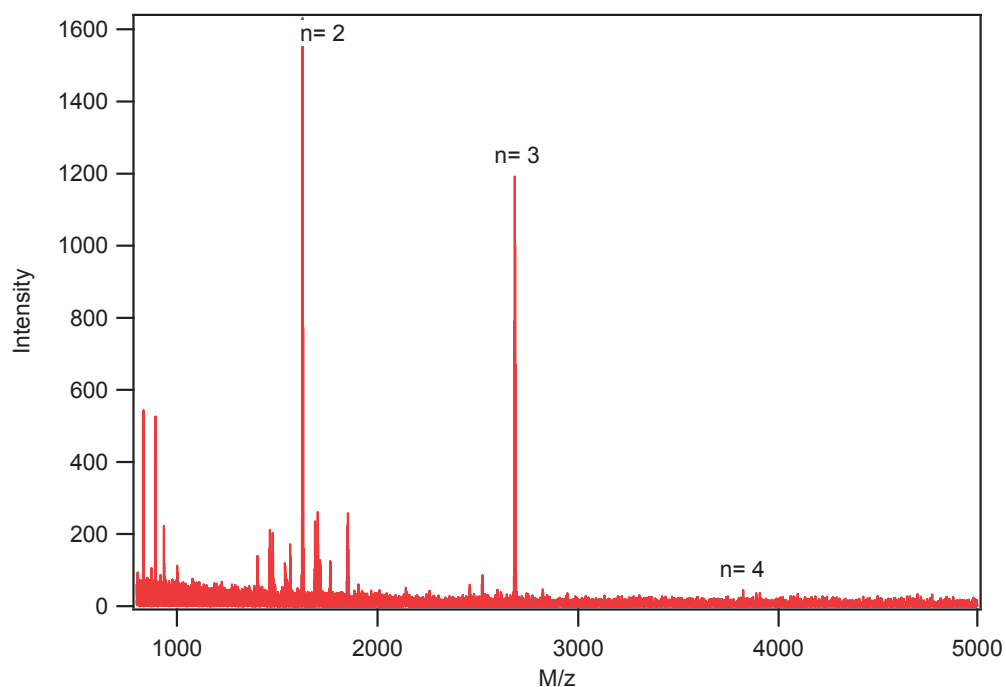
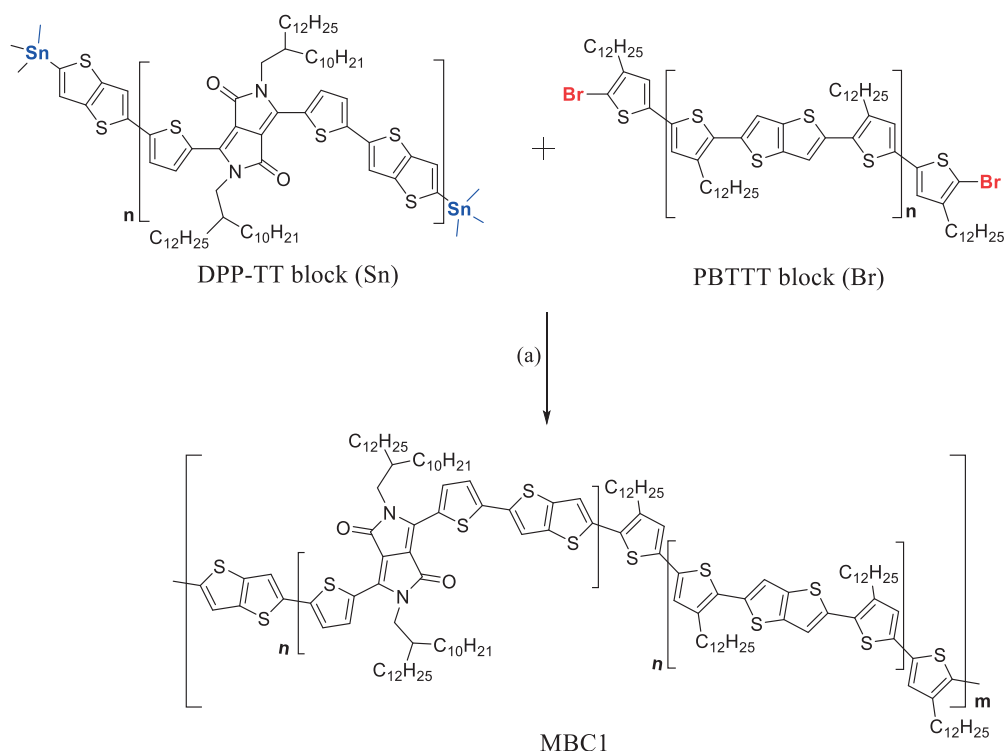


**Figure 10-6b** MALDI spectra of DPP-Tin functionalized in reflectron mode

**Scheme 10-13** . Synthetic path for the synthesis of the alternated multi block copolymer MBC1 ( $M_n = 51$  kDa, PDI 1.2) after purification by prep-SEC. Typical values of  $m = 5-7$  repeating units.



**MBC1** A molar ratio of 1:1 of DPP-TT block (5 mg) and PBTTT-Br block (10 mg) was chosen. The reaction was run at 100°C in chlorobenzene (1 ml) under inert atmosphere using tris(dibenzylideneacetone)dipalladium (2 mg) and excess of tri(*o*-tolyl)-phosphine (6 mg) as catalyst for 1h. The crude polymer fraction was analyzed through an analytical size exclusion chromatography column (SEC) at 80°C using chlorobenzene as mobile phase at 1 mL min<sup>-1</sup>. Successive fractionation by preparative SEC (in 80°C, chlorobenzene, 6 mL min<sup>-1</sup>, 40.0 x 250 mm column, linear M packing, Polymer Standards Service GmbH) afforded to selective isolate the high molecular weight fraction with a  $M_n$  of 51 kDa and a PDI of 1.2 (vs. PS standards)

## 10.3 Curriculum Vitae

### Education

- 2012-2016** PhD thesis on “ Tailoring self-assembly and optoelectronic properties of organic semiconductors via macromolecular engineering” under the supervision of Prof. Kevin Sivula at the Faculty of Basic Science, Institute of chemistry and chemical Engineering, EPFL, Switzerland
- 2012** Master thesis on “Recombination dynamics and charge transport in solid state DSSC studied by time resolved spectroscopy and Time of Flight measurements” under the supervision of Prof Jacques-Edouard Moser, EPFL, Switzerland
- 2010-2012** Master studies in molecular and biological chemistry at EPFL, Switzerland
- 2007-2010** Bachelor studies in Industrial Chemistry at University of Bologna, Italy
- 2002-2007** Maturità Scientifica al Liceo Fulcieri Paolucci di Calboli

### Teaching Experience

- 2013-2015 Teaching assistant for practical courses of “Introduction to Chemical Engineer” given by Prof. K. Sivula at EPFL

### Awards

1. SCNAT/SCS travel award 2014
2. Best poster award at ICOE, Grenoble 2013
3. Mention prize for innovative idea at “New ideas, new enterprises” contest in 2010

### Publications

1. Effect of molecular weight on *microstructure and charge transport* in a semicrystalline poly(thieno)thiophene A. Gasperini and K. Sivula *Macromolecules* **2013**, 46 (23), pp 9349–9358
2. Controlling conjugated polymer morphology and charge carrier transport with a flexible-linker approach A. Gasperini, S. Bivaud and K. Sivula *Chem. Sci.* **2014**, 5, 4922-4927
3. Enhancing thermal stability of solution-processed small molecule semiconductor thin films using a flexible linker approach A. Gasperini, X. Jeanbourquin, A. Rahmanudin, X. Yu and K. Sivula *Advanced Materials*, **2015** 27(37) 5541-5546

4. Role of fractionation on the electronic and lm formation properties of *NIR* diketo-pyrrolopyrrole conjugated polymers A. Gasperini, X. Jeanbourquin and K. Sivula Cryst. Eng. Comm. **2016**, in press
5. Synthesis of fully conjugated alternating multi-block copolymers A. Gasperini, X. Jeanbourquin, N. Guijarro and K. Sivula Manuscript under preparation **2016**

### Languages

1. **Italian** Mother tongue
2. **English** Fluent written and spoken level
3. **French** Fluent written and spoken level

